Universitat de Lleida

Emerging Techniques for Inorganic Metal Speciation and Bioavailability

Federico Quattrini

http://hdl.handle.net/10803/664422

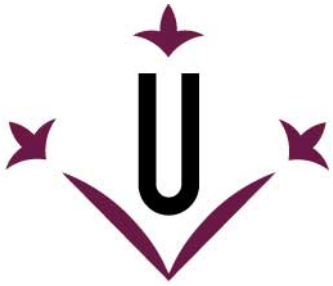

Universitat de Lleida

TESI DOCTORAL

Emerging Techniques for Inorganic Metal Speciation and Bioavailability

Federico Quattrini

Memòria presentada per optar al grau de Doctor per la Universitat de Lleida
Programa de Doctorat en Enginyeria i Tecnologíes de la Informació

Directors
Josep Galceran Nogués
Carlos Rey Castro

2018

No man is an island, and no scientific work is the product of one individual

For your help, knowledge and love - my deepest gratitude

SUMMARY

A deep knowledge of heavy metal ions speciation is key to assessing their toxicity and bioavailability in the environment. In this regard, data about concentrations (equilibrium speciation) should be complemented with data about the supplied fluxes (dynamic speciation), where kinetics and transport properties of the metal species are intertwined. Several analytical techniques have been recently developed to this purpose, and a number of them (*e.g.* the DGT, Diffusion Gradient in Thin films, and the IET, Ion Exchange Technique) exploit properties of Ion-Exchange (or chelating) Resins such as their selectivity and efficacy of binding.

The contributions of the present thesis to this field of work are mainly two. On the one hand, it studies the rate of metal ions uptake on Chelex 100 resin, both experimentally and by providing a theoretical interpretative framework. The simpler case of metal accumulation in absence of competing ligands is modelled as a case of pure diffusion, explicitly including the contribution of both the internal and external diffusion steps. This model is able to predict the influence of a plurality of environmentally relevant factors, such as pH and ionic strength of the medium. Formulating an interpretation with a sound physical basis also allows describing the effect of competing ligands and determining the dissociation constants of the complexes, casting some light as well on debated aspects of the DGT theory.

On the other hand, two new analytical techniques are developed. The first one stems from IET, a technique commonly used at equilibrium, but it is aimed at extracting dynamic information from it (and is thus denoted as DIET). In particular, it allows the determination of the lability degree of a number of metal complexes. The second one is a modification of the well-known DGT, devised so as to provide information once the equilibrium with the solution has been attained (and is thus denoted as eDGT). A model with a small number of assumptions was used to interpret the results of the accumulation and to perform speciation studies on systems of different metal ions and ligands.

RESUMEN

El conocimiento profundo de la especiación de los metales pesados es clave para determinar su toxicidad y biodisponibilidad en el medio ambiente. Por esta razón es necesario complementar la información sobre las concentraciones de iones metálicos (especiación en equilibrio) con la información sobre los flujos de dichos iones (especiación dinámica), donde se interrelacionan las propiedades cinéticas y de transporte de cada especie. Diversas técnicas analíticas han sido recientemente desarrolladas con este fin, y varias (como el DGT, *Diffusion Gradient in Thin films* y la IET, *Ion Exchange Technique*) aprovechan propiedades de las resinas de intercambio iónico (o quelantes) como su selectividad y gran afinidad.

Las contribuciones de la presente tesis a este tema son esencialmente dos. Por un lado, se investiga la velocidad de acumulación de iones metálicos en la resina Chelex 100, tanto experimentalmente, como a través de un modelo interpretativo teórico. El caso más sencillo de acumulación de metal en ausencia de ligandos competidores es modelizado como un caso de pura difusión, incluyendo explícitamente la contribución de la difusión interna y externa. Este modelo puede prever la influencia de una multitud de factores medioambientales, como el pH y la fuerza iónica. Formular una interpretación con una sólida base física permite, asimismo, describir los efectos de los ligandos competidores y determinar las constantes de disociación de los complejos, contribuyendo también a la dilucidación de aspectos controvertidos de la teoría del DGT.

Por otro lado, dos nuevas técnicas analíticas han sido desarrolladas. La primera deriva de la IET, una técnica comúnmente utilizada en condiciones de equilibrio, pero con el objetivo de extraer información dinámica de ella (y por ello se denomina DIET). En particular, permite la determinación del grado de labilidad de varios complejos metálicos. La segunda es una modificación del popular DGT, que se ha empleado para extraer información una vez el sistema ha alcanzado el equilibrio (y por ello se llama eDGT). Un modelo basado en un reducido número de hipótesis ha sido utilizado para interpretar los resultados de acumulación y efectuar estudios de especiación sobre sistemas de diferentes metales y ligandos.

RESUM

El coneixement profund de la especiació dels metalls pesants és clau per a determinar la seva toxicitat i biodisponibilitat en el medi ambient. Per això cal complementar la informació sobre les concentracions d'ions metàl·lics (especiació en equilibri), amb la informació sobre els fluxos d'aquests ions (especiació dinàmica), on s'interrelacionen les propietats cinètiques i de transport de cada espècie. Diverses tècniques analítiques han estat desenvolupades amb aquesta fi, i algunes d'elles (com el DGT, *Diffusion Gradient in Thin films* i la IET, *Ion Exchange Technique*) aprofiten les propietats de les resines d'intercanvi iònic (o quelants) com la seva selectivitat i gran afinitat.

Les contribucions d'aquesta tesi a aquest tema són essencialment dues. D'una banda, s'investiga la velocitat d'acumulació d'ions metàl·lics a la resina Chelex 100, sigui experimentalment o a través d'un model interpretatiu teòric. El cas més senzill d'acumulació de metall en absència de lligands competidors s'ha modelitzat com un cas de pura difusió, incloent-hi explícitament la contribució de la difusió interna i externa. Aquest model pot preveure la influència d'una multitud de factors mediambientals com el pH i la força iònica. Formular una interpretació amb una sòlida base física permet descriure els efectes dels lligands competidors i determinar les constants de dissociació dels complexes, contribuint també a la dilucidació d'aspectes controvertits de la teoria del DGT.

D'altra banda, dues noves tècniques analítiques han estat desenvolupades. La primera deriva de la IET, una tècnica comunament utilitzada en condicions d'equilibri, però cercant d'extreure'n informació dinàmica (i per això s'anomena DIET). En particular, permet la determinació del grau de labilitat de diversos complexos metàl·lics. La segona és una modificació del popular DGT, que s'ha emprat per a extreure informació un cop el sistema ha assolit l'equilibri (i per això s'anomena eDGT). Un model basat en un reduït nombre d'hipòtesis ha estat utilitzat per a interpretar resultats d'acumulació i efectuar estudis d'especiació sobre sistemes de diferents metalls i lligands.

CONTENTS

3. Dynamics of metal uptake to a chelating resin in absence of ligands

4. Dynamics of metal uptake to a chelating resin in presence of a ligand

Symbols

Bi_{m}	mass transfer Biot number, $Bi_{\mathrm{m}} = D_{\mathrm{M}} r_0 \big/ \left(\widetilde{D} \delta \kappa \right)$
c_{DGT}	DGT-labile concentration (mol L^{-1})
c_{DIET}	DIET-labile concentration (mol L^{-1})
c_{i}	concentration of species *i* (mol L^{-1})
c_{i}^{*}	concentration of species *i* in the bulk (mol L^{-1})
$\tilde{c}_{\mathrm{i}}$	concentration of species *i* in the resin (mol L^{-1})
$\tilde{c}_{\mathrm{i}}^{-}$	concentration of species *i* on the inner face of the bead (mol L^{-1})
c_{i}^{+}	concentration of species *i* on the outer face of the bead (mol L^{-1})
$\tilde{c}_{\mathrm{M,free}}$	concentration of free metal inside the resin (mol L^{-1})
$\tilde{c}_{\mathrm{MR}}$	concentration of metal bound to the resin groups (mol L^{-1})
$\tilde{c}_{\mathrm{R}}$	concentration of binding groups in the resin phase (mol L^{-1})
$\tilde{D}$	overall diffusion coefficient in the resin phase (m^2 s^{-1})
D_{M}	diffusion coefficient of free metal in water (m^2 s^{-1})
$\tilde{D}_{\mathrm{M}}$	diffusion coefficient of free metal in the resin phase (m^2 s^{-1})
f	fractional attainment of equilibrium
F	virtual flux at the interface (mol m^{-2} s^{-1})
g_1	virtual volume of the DBL at metal concentration equal to $c_{\mathrm{M}}\left(r_0^{+}, t\right)$ (m^3)
g_2	virtual volume of the DBL at metal concentration equal to $c_{\mathrm{M}}^{*}(t)$ (m^3)
h_1	resin-subdomain grid width (m)
h_2	solution-subdomain grid width (m)
I	ionic strength (mol L^{-1})
J_{i}	flux of species *i* (mol m^{-2} s^{-1})

K	stability constant (L mol^{-1})
K'	effective stability constant, $K'=Kc_L$
k_a	association rate constant (L mol^{-1} s^{-1})
k_a'	effective association rate constant (s^{-1})
k_d	dissociation rate constant (s^{-1})
L	generic ligand
m	effective reaction layer parameter, $m=\sqrt{\frac{D_M}{k_a'+k_d}}$ (m s^{-1})
M	generic metal
ML	generic complex with stoichiometry 1:1
n	number of moles (mol)
$\tilde{n}$	number of moles in the resin phase (mol)
n_{film}	moles of metal in the film (mol)
$\tilde{n}_{MR}$	moles of metal bound to the resin (mol)
n_{sol}	moles of metal in the solution (mol)
n_T	total moles of metal in the system (mol)
$\tilde{q}$	density of charges in the resin phase (mol L^{-1})
Q	flow rate (mL min^{-1})
r	radial variable (m)
r_0	radius of the bead (m)
r_1	distance from the centre of the bead at which bulk conditions are attained (m)
R	generic resin site
s	variable of the Laplace transform (s^{-1})
S	section of column (m^2)

t	time (s)
T,L	total ligand
T,M	total metal
v	interstitial velocity (m s^{-1})
V_{disc}	volume of the resin disc (volume of the polymeric matrix + V_R) (m^3)
V_R	volume of the resin (m^3)
V_T	total volume (m^3)
w	partition ratio (capacity parameter), $w = V_R \kappa / (V_T - V_R)$
$\overline{y}(s)$	Laplace transform of variable $y(t)$
z	distance from the inlet of the column (m)
z_{char}	characteristic column bed length (m)
z_{max}	column bed length (m)
z_i	charge of species i
α	effective exchange area per unit of column length (m)
β_{npex}	exchange coefficient
β_{npint}	intrinsic exchange coefficient
γ_z	activity coefficient of species with charge z
δ	effective thickness of the DBL (m)
ε	fraction of volume in the column occupied by the solution (discounting the DBL surrounding the beads)
κ	(global) partition coefficient
λ	penetration parameter, $\lambda = \sqrt{\frac{D_M}{k_d}}$ (m s^{-1})
μ_i	rc_i (mol m^{-2})
ν	normalised volume (V_R/V_T)
ξ	lability degree

Ξ system retention degree

ρ volume of beads per unit length of column (m^2)

χ Boltzmann factor relating concentrations in the resin and the solution at the bead surface

Acronyms

BLM	Biotic Ligand Model
CM	Complete Model
DBL	Diffusive Boundary Layer
DGT	Diffusion Gradients in Thin films
DIET	Dynamic Ion Exchange Technique
dSS	Diffusive steady state approximation
eDGT	Equilibrium DGT
EDTA	Ethylenediaminetetraacetic acid
eff	effluent
en	Ethylendiamine
FDM	Film Diffusion Model
FIAM	Free Ion Activity Model
ICP-OES	Inductively Coupled Plasma Atomic Emission Spectroscopy
ICP-MS	Inductively Coupled Plasma Mass Spectrometry
IDA	Iminodiacetic Acid
IDM	Intraparticle Diffusion Model
IET	Ion Exchange Technique
ISE	Ion-Selective Electrode
MCM	Mixed Control Model
MES	2-(N-morpholino)ethanesulfonic acid
MIDA	Methyliminodiacetic Acid
MOPS	3-(N-morpholino)propanesulfonic acid
NTA	Nitrilotriacetic acid

SM	Simplified Model
SS	Steady State
UM	Ultra-Simplified Model

1. Introduction

1.1. Why to study metal speciation?

It has been known for centuries that it is the dose that makes the poison. Assessing the toxicity of a chemical cannot, therefore, obviate the determination of its concentration in the environment, and in particular in the aqueous phase. Contaminants dissolved in water are a primary source of intoxication, as they can be most readily assimilated by living beings.

A class of contaminants of relevant importance are heavy metals. Normally present at trace-level concentration in soil, water and organisms, their concentration can increase above the usual level as a consequence of both anthropogenic (mining, atmospheric pollution, industrial activity, etc.) and natural causes (volcanic eruptions, etc.). Being highly reactive species, heavy metals can interact with metal transporters on the cell membrane and block them or, once internalised, they can catalyse the production of free radicals and generate oxidative stress, affect the metabolic processes of the cell and even DNA replication. Among the metals that are going to be studied in the present work, cadmium causes kidney damage[1] and bone demineralisation,[2,3] while Ni is a known carcinogenic agent[4] and Cu mainly affects the liver and the central nervous system, especially in subjects with reduced ability to excrete copper (Wilson disease).[5]

The study of heavy metals has been an important chapter in the history of aquatic chemistry in the previous century.[6] Historically, water quality criteria were based simply on the total dissolved metal concentration, without taking the chemistry of the contaminants into consideration. The realisation that toxicity was strongly influenced by parameters such as water hardness, pH and presence of complexing substances caused a paradigm shift in the seventies,[7] and led to the formulation of the principle on which all the subsequent models were based: it is the concentration of the free ion, instead of the total, that best predicts toxicity and bioavailability. The most successful models to predict metal toxicity have been the Free Ion Activity Model (FIAM)[8] and the Gill

Surface Interaction Model (GSIM),[9] which constitute also the basis for the Biotic Ligand Model (BLM).[10,11]

Although the development of this theoretical framework has greatly contributed to improve the definitions of bioavailability and toxicity (the US Environment Protection Agency adopted the BLM for establishing water quality criteria[12]), the assumptions on which it is based are not universally applicable.[13,14]

In particular, the hypothesis that bioavailability is related uniquely to the free metal fraction holds only if internalization (the process through which the metal crosses the cell membrane) is the rate determining step of the whole process, which means that metal transport and complex dissociation are fast enough to prevent metal depletion in the region surrounding the cell. Said otherwise, the supply of metal ions should be larger than the biouptake flux. If this is true in most cases, there are many well-documented exceptions.

This is the case, for example, of the accumulation of Cd in periphyton,[15] or of the effect of the dissociation of AgCl on the uptake in *Chlamydomonas reinhardtii*[16,17] or of the accumulation of Fe hydroxides in phytoplankton.[18] When metal transport cannot keep the pace with the internalisation, the concentration of free ions decreases in the proximity to the cell, perturbing the equilibrium of the metal complexes and forcing their dissociation. In this case, the bioavailability would not be related anymore to the free metal concentration, but rather to the overall metal flux, taking into account the contribution of the labile species as well.

As complex dissociation and association kinetics is recognised as a crucial factor in the prediction of bioavailability, it is worth spending a few words about the concept of complex lability and inertness. A complex is considered labile if, in a specific system, it reaches equilibrium everywhere within the experimental timescale and relevant spatial domain; on the contrary, if complex dissociation stays negligible at all relevant times, the system is labelled as inert. Lability depends on factors such as the geometrical aspects of the sensor or the composition of the sample. The intermediate cases are termed semi-labile. A suitable way to quantify the lability of complex is through the lability degree ξ,[19,20] defined as the ratio of the contribution of a complex to the metal flux over the maximum possible contribution:

$$\xi = \frac{J - J_{\text{free}}}{J_{\text{labile}} - J_{\text{free}}} \tag{1.1}$$

J_{free} is the flux if only free metal was in the system and J_{labile} is the flux that would result if the complex was fully labile. For inert complexes ξ=0, whereas ξ=1 for fully labile ones.

The brief excursus of the previous paragraphs should have clarified the rationale behind the present work: so as to better understand metal speciation in natural waters, the present equilibrium models need to be improved by taking into account also the dynamics of the system or, as it is called in the literature, the "dynamic speciation".[21,22] The first step in this direction will be to study the effects of metal transport and of complex dissociation on artificial devices (or their basic components) that can mimic biouptake. To keep the pace with a field of research that is becoming more and more sophisticated, novel and more refined analytical techniques are demanded, as well as improving and adapting the existing ones. Essential to the development of new theoretical frameworks, the experimental work to guide and validate it will be the subject of a large part of this thesis; its importance will be further stated in the following section.

1.2. How to study metal speciation?

A large number of analytical methods has been developed along the years with the purpose of selectively targeting only a narrow range of species. Among the most classical ones, we can quote Ion Selective Electrode (ISE) potentiometry, which started to be widely applied in the seventies[23] and it is now a staple of speciation studies. More recent years saw the rise of such techniques as Absence of Gradients and Nernstian Equilibrium Stripping (AGNES),[24] Polymer Inclusion Membranes (PIM),[25] Donnan Membrane Technique (DMT),[26] the Ion Exchange Technique (IET),[27] methods based on dialysis membranes[28,29] and ion-exchange resins.[30,31] As the techniques in this list only provide information about the thermodynamic aspect of the system (the free metal concentration), the need of knowledge of the contribution of the labile species to bioaccumulation led to the development of analytical techniques that could give access to metal fluxes. A widely known example, which will be addressed in detail later, is the DGT (Diffusive Gradient in Thin films)[32] passive sampler. An alternative approach employs ion-exchange and chelating resins; a good deal of work has been conducted on this topic by the group of Chakrabarti,[33–37] which took the accumulation on the Chelex 100 chelating resin as a model for biouptake. These studies deserve a mention also because Chelex 100 is the sorbent material at the core of the DGT passive sampler,

whose properties and applications have been thoroughly studied in several thesis works carried out in Lleida group.[38–42] A better insight into the mechanisms that regulate the uptake on the resin will, therefore, contribute to the understanding of the DGT; this will require, however, the development of models with a stronger physical basis than the one found in the works by Chakrabarti.

The resin Chelex 100 is an interesting chemical system in itself and has been extensively applied to metal speciation studies by Pavia group.[43,44] The conclusions of their work, basically devoted to the description of the resin at equilibrium, can be extended to account for the effect of pH and ionic strength in explaining deviation to the typical behaviour of DGT accumulation.[38] Anomalous behaviour is also attributable to specificities in the complex dissociation in the sampler, an aspect on which some further light could be shed by extending the knowledge of the mechanism of Chelex uptake.

A complete review of the techniques of speciation analysis is clearly outside the scope of this text. In the following sections we will review some of the techniques that, in various ways, are relevant to this work: the voltammetric technique AGNES, developed by Lleida group;[45] the column-equilibration technique IET; and, to conclude, a brief excursus about the passive sampling devices, a field of research met with particular success in the last decades thanks to its cost-efficiency and accuracy.

1.2.1. AGNES (Absence of Gradient Nernstian Equilibrium Stripping)

AGNES[46] is an electrochemical stripping technique designed for the direct determination of free metal ion concentrations in solution. Although the use made of AGNES in the present work is limited, a short introduction to the principles of this technique is convenient.

The analytical procedure consists of two stages. In the first one, a suitable potential is applied to preconcentrate the ion of interest within the working electrode, by a known factor *Y*, dubbed “gain”. The deposition time must be long enough to reach Nernstian equilibrium across the interface between the electrode and the bulk solution and flat concentration profiles. So as to allow the penetration of the metal in the electrode a HDME (Hanging Drop Mercury Electrode) is the choice of preference, although experiments have been carried out with thin mercury microelectrodes,[47] mercury film electrodes,[48] screen-printed electrodes[49], bismuth electrode[50] or microwire gold electrodes.[51]

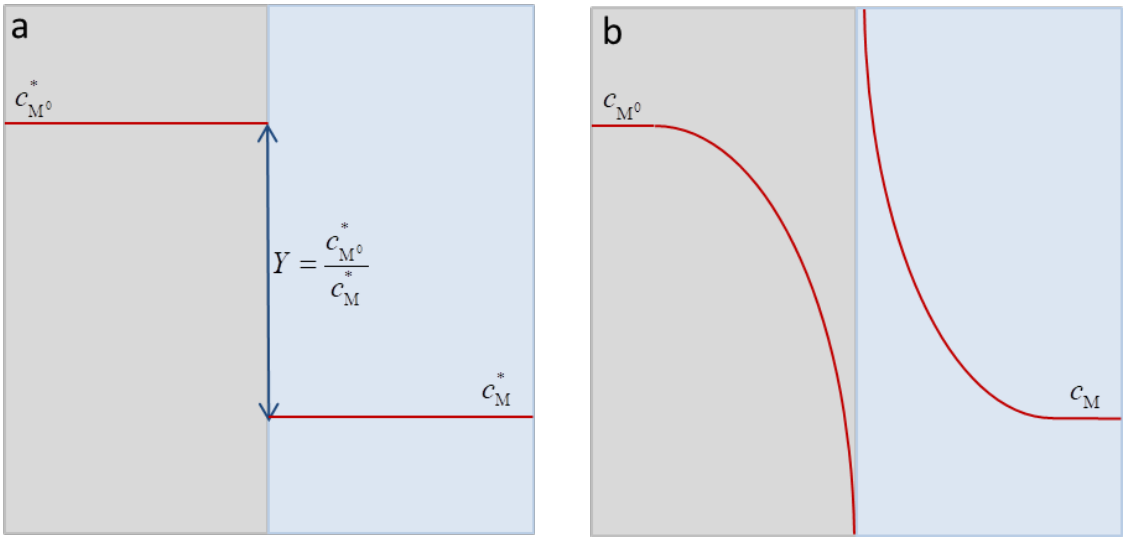

Figure 1.1. Concentration profiles inside the mercury electrode (grey) and in the solution (blue), once Nernstian equilibrium in AGNES has been attained (a) and during the stripping step (b)

Once flat concentration profiles have been established inside and outside the electrode, the gain can be related through Nernst relationship to the difference between the applied potential E_1 and the formal standard redox potential $E^{0\prime}$ of the target ion:

$$Y = \frac{c^0_{M^0}}{c^0_M} = \exp\left[-\frac{nF}{RT}\left(E_1 - E^{0\prime}\right)\right] \tag{1.2}$$

In the second step, the metal accumulated is electrochemically stripped from the electrode. The response can be quantified in terms of the resulting faradaic current or the stripped charge,[52] both of which are directly proportional to the free metal concentration in solution.

The main advantage presented by AGNES over traditional Anodic Stripping Voltammetry (ASV) techniques is that it allows a much easier interpretation of the results, not dissimilar from ISE (Nernstian response), while allowing to reach much lower concentration than ISE potentiometry thanks to the pre-concentration step. The minimum needed deposition time changes with the desired *Y*, with the caution that very large gains may require excessively long times. Different potential programs ("2 pulses") can be applied to reduce the deposition time.[53] As said before, several alternatives implementations that do not use mercury have been proposed to obviate the main drawback of the classical AGNES, its reliance on the HDME.

AGNES has been successfully applied to the analysis of Cd,[45] Cu,[51] In,[54] Pb[55] and Zn[53] in different matrices: from freshwater[56] to humic acid solutions[57] and seawater,[58] from nanoparticles dispersions[59] to wine.[60]

1.2.2. IET (Ion Exchange Technique)

The IET (Ion Exchange Technique) was developed by Cantwell[27] to perform metal speciation studies on wastewater, and later on applied by many others, including Campbell and Fortin.[61] In its most classical form, it involves flushing a sample solution through a column packed with an ion exchanger (generally, Dowex 50 sulphonic resin) until the attainment of equilibrium. The amount of metal accumulated, determined after eluting the column, can then be related to the corresponding free metal concentration in solution through a conditional constant, the distribution coefficient λ, determined calibrating the system in the conditions of interest.

In most cases IET was found to give results of comparable quality with those of ISE potentiometry; positively charged or neutral complexes are a major source of interference, as they accumulate in the resin along with the free metal.[62] The determination of λ in the experimental conditions may pose several problems as well, especially in complex matrices. A way to obviate it is to correlate λ with parameters such as the ionic strength of the sample. A particularly good correspondence was found with the concentration of the major divalent cations (Ca^{2+} and Mg^{2+}),[63] to which the sulphonic resin is known to show some selectivity. Empirical models have been developed to predict the distribution coefficient, which comported a relevant simplification and even allowed IET to be used for field measurements; a passive sampling device was specifically designed to this purpose.[63]

An alternative approach was recently tried by the group of Wilkinson:[64] instead of waiting for equilibrium, they seek a relationship between the free metal fraction in solution and the rate at which the metal accumulates in the resin along the first phases of the experiment. The results, albeit of difficult interpretation, are promising and deserve further attention.

1.2.3. Passive Samplers

Since being employed for the first time in 1927 for the semi-quantitative determination of CO,[65] passive sampling has found innumerable applications. An extensive bibliography about the topic can be found in the reviews by Seethapathy[66] and Peijnenburg.[67] In principle, a passive sampling device should carry out the three main

operations constituting a traditional sampling technique: the collection of the sample, the isolation of the analyte from the matrix and its preconcentration. The difference between a sampler and a sensor lies in the fact that these devices do not measure the analyte themselves, but they require a complementary technique to analyse it once retrieved from the sampler.

Following the definition of Górecki,[68] a sampler is constituted by a collecting phase, separated from the outside by a barrier that has the two-fold function of defining the uptake rate and minimising the influence of external factors. For the sampler to be "passive" the analyte should flow freely from the sampled phase to the collecting phase, purely as a result of the difference in its chemical potentials between the two phases.

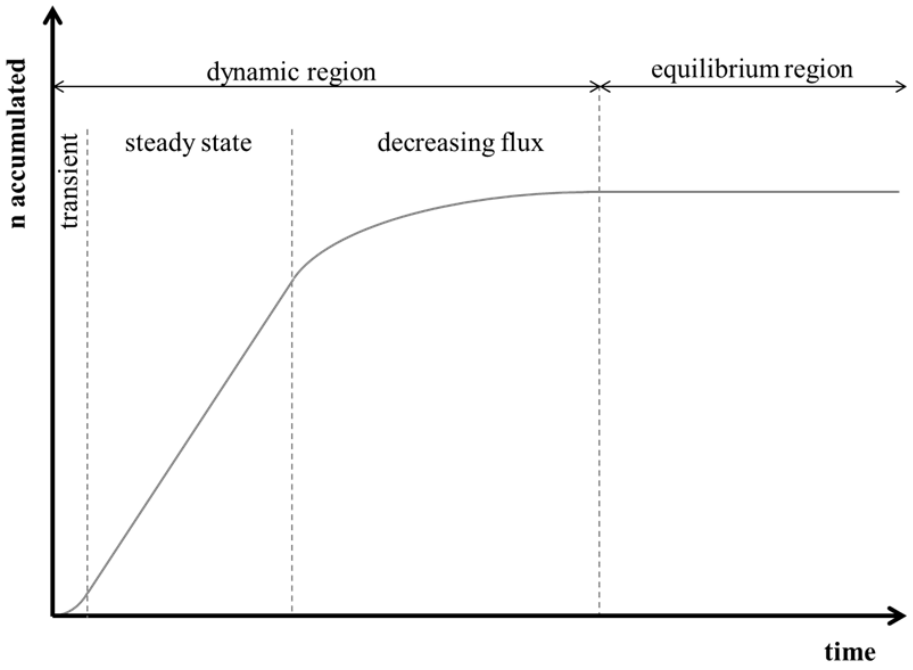

Figure 1.2. Scheme of the accumulation of an analyte in the collecting phase of a passive sampler as a function of time.

A first classification criterion relies on the choice of the moment when the sampling session is interrupted by the operator: if this takes place before the analyte equilibrates between the two media ("dynamic region" in Fig.1.2.) we will talk of Dynamic Passive Samplers (DPS); if equilibrium has already been attained ("equilibrium region"), of Equilibrium Passive Samplers (EPS). While the response of an EPS will be related to the free metal concentration, a DPS will provide information related to the flux.

From the definition above it comes as a logic conclusion that all passive samplers can be employed in both dynamic or equilibrium mode and what makes the difference is

how much time is left to pass. Clearly, an efficient sampler should be optimised in order to work in one mode or the other: for example, typical DPS like the DGT[32] or the Chemcatcher[69] have a thick barrier (in polyacrylamide and cellulose acetate, respectively) that defines the length of the diffusive boundary layer, allowing an accurate control over the analyte flux. On the contrary for an EPS like the DET[70] (Diffusive Equilibration in Thin films) or the Gellyfish,[71] the determination of the flux is irrelevant, while they require large exposed surfaces to shorten the equilibration time. Further details about these techniques are given in the following sections.

DGT (DIFFUSIVE GRADIENT IN THIN FILMS)

Diffusive Gradients in Thin films technique (DGT) is an established technique for measuring metal concentrations and speciation in natural waters, originally presented in the nineties by Bill Davison and Hao Zhang of Lancaster University.[32] In its most classical form, the DGT consists of a binding agent in which solutes accumulate quantitatively after passing through a well-defined diffusion layer. The DGT has been applied principally to the analysis of heavy metals, although an increasing portion of the most recent literature has been devoted to the study of organic pollutants.[72,73] The binding agent most commonly used for trace metals is the iminodiacetic resin Chelex-100; the resin beads are incorporated in a hydrogel, while a second gel membrane of known thickness constitutes the diffusion layer. Polyacrylamide is generally chosen for the hydrogel matrix, although other polymers (typically agarose) are used in special cases.[74] The gel layers are covered by a cellulose filter to prevent their fouling and encased in a purposely devised plastic holder (as shown in Fig. 1.3).

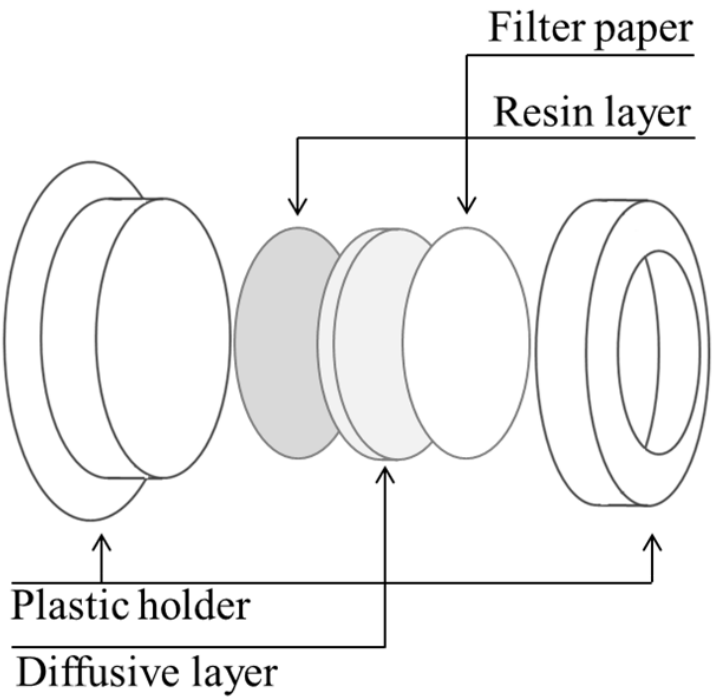

Figure 1.3. Exploded view drawing of the DGT.

The fundamental equation of the DGT, which gives the value of the bulk concentration of free metal, is directly derived from Fick's first law, and reads as follows:

$$c_{\mathrm{DGT}} = \frac{n_{\mathrm{DGT}}\delta^{\mathrm{g}}}{D_{\mathrm{M}}At} \tag{1.1}$$

where n_{DGT} are the moles of metal accumulated in the binding layer at time t, δ^{g} is the thickness of the diffusive layer, D_{M} the diffusive coefficient of the metal in the gel and A the surface area of the exposure window. As δ^{g} and A are fixed and known from the manufacturing process, while the values of D_{M} for each metal can be retrieved in the literature, c_{DGT}, the concentration of "labile" metal in solution can be directly linked to n_{DGT}, whose value is easily determined by eluting the binding layer in acidic conditions. Among the principal advantages of the DGT technique, we count the reduced analysis time (if compared to equilibrium techniques such as the DET), the lack of need for calibration and the "simple" interpretation of the results. It must be said, though, that the mentioned simplicity can be somewhat deceptive, based as it is on a plurality of assumptions (purely diffusional transport, perfect sink conditions, negligible contribution of the complexed metal to the accumulation in the binding layer) that are, more often than not, overlooked.[76–78]

THE CHEMCATCHER

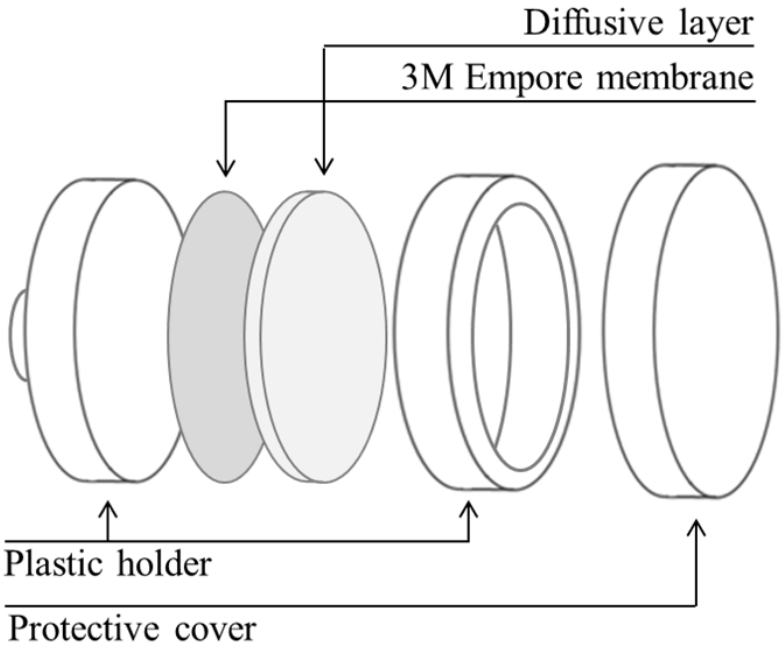

Figure 1.4. Exploded view of the Chemcatcher passive sampler.

The "Chemcatcher" is a kind of passive sampler developed by Kingston *et al.*,[69] rather similar in shape and operational principle to the DGT, the major difference being that its exposed surface is much larger. It consists of a two-pieces Teflon holder designed to house a 47 mm diameter disk of sorbent material (for the analysis of metal ions, the choice of preference is a 3M Empore membrane[79]) covered by a cellulose acetate membrane, which both defines the length of the diffusive layer and protects the sorbing layer. According to the usual procedure, the Chemcatcher is deployed in the natural medium for a certain period of time, after which the analyte accumulated in the sampler is retrieved and measured. Much like the DGT, the Chemcatcher gives a time-weighted average of the concentration of the analytes, measuring a certain labile fraction. For the Chemcatcher, it is common practice to determine the relationship between the analyte in solution and the sorbed one by calibrating the sampler in the experimental conditions, instead of relying on tabulated values of the diffusion coefficient as usually done with the DGT.

There are several works[80,81] describing how the Chemcatcher may be left to equilibrate with the surrounding medium on purpose, in order to determine the partitioning factor at the interface of the sorbent material. In one case,[81] the sampler was deployed without

the diffusive membrane; this setup was called “naked-disk” or “fast” Chemcatcher, since the absence of the membrane facilitates the transport of the analyte to the sorbent and reduces the equilibration time.

THE GELLYFISH

The original design of the “Gellyfish”[71] was quite simple, being constituted only by a small amount of an iminodiacetate cation-exchange resin, Toyopearl AF-Chelate 650M dispersed in a polyacrylamide gel matrix. A newer, improved version[82] added a polyester backbone, has larger exposed surface (from 3 to 20 cm^2) and has the gel matrix encased in a plastic support. In a typical experiment the gels are left to equilibrate in the solution of interest and then they are retrieved and eluted to determine the amount of metal complexed. The authors of the original paper developed a simple spreadsheet-based numerical model that allows relating the accumulated amount to the concentration of free metal in solution through the stability constant of the M-iminodiacetate complexes, as found in the literature. This model takes into account the change in the number of free resin sites due to protonation and metal binding.

1.3. Objectives

In the previous paragraphs we mentioned the important role played by ion-exchange resins in speciation studies, and how a deeper knowledge of the mechanisms of metal accumulation (including metal transport and kinetics of complex dissociation) will help to interpret the experimental results more rigorously. With this work we aim at providing an in-depth study of this phenomenon, with particular attention devoted to the influence of relevant factors like the pH and the ionic strength of the medium, as well as the stirring rate and the amount of sorbent.

The assessment of the contribution of metal transport to metal accumulation is preliminary to the study of complex dissociation kinetics in presence of an ion-exchange resin. As the chelating resin Chelex 100 is the binding core of the DGT, this knowledge will be also pivotal in understanding the non-Eigen dissociation mechanism[83] displayed by labile complexes when interacting with the sampler, a particularly puzzling phenomenon that defies the traditional DGT theory. The so-called “ligand-assisted mechanism”, introduced to explain this phenomenon, still awaits confirmation.

As already stated throughout this introductory chapter, in the study of metal speciation a good deal of work must be dedicated to the elaboration and fine-tuning of novel methods of analysis. Taking a well-known experimental technique and approaching it from a radically different perspective is often a good strategy in the development of new methods. By force of this reasoning, in this work we will start from a well-known dynamic technique, the DGT, and we will turn it into an equilibrium one, while trying to extract dynamic information from the IET, a technique commonly used at equilibrium.

1.4. Outline of this thesis

After the current introduction (**Chapter 1**), which presented the background and rationale, a rapid presentation of the experimental techniques involved and the general methodology will be given in **Chapter 2**. The main results of our work will then be addressed in the following four chapters, which constitute the body of the thesis.

We will tackle our subject on two fronts: on one side (**Chapters 3** and **4**) we will try to shed some light on the DGT theory by stripping it down to its very core: the accumulation of metal on loose resin beads. On the other side (**Chapters 5** and **6**) we will develop two new analytical techniques, both based on ion-exchange resins but with very different operational principles.

In **Chapter 3** we will focus on the uptake in absence of a competing ligand in solution, seeking to describe the effects of a plurality of variables via a comprehensive physicochemical model. This preludes to the work undertaken in **Chapter 4** where we extend the topic of our research to the systems in presence of a competing ligand. These experiments aim to elucidate the “ligand-assisted mechanism” hypothesis developed for DGT. **Chapter 5** will present the general outline of DIET, the column-based dynamic technique that we have fine-tuned and whose results have been extensively interpreted. A second brand new equilibrium technique, the eDGT, was developed, calibrated and applied to a synthetic water sample; this will constitute the topic of **Chapter 6**. A general discussion of the results and conclusions of this work constitute **Chapter 7**.

1.5. References

(1) Barbier, O.; Jacquillet, G.; Tauc, M.; Cougnon, M.; Poujeol, P. Effect of heavy metals on, and handling by, the kidney. *Nephron Physiol.* **2005**, *99*, 105–110.

(2) Staessen, J. A.; Roels, H. A.; Emelianov, D.; Kuznetsova, T.; Thijs, L.; Vangronsveld, J.; Fagard, R. Environmental exposure to cadmium, forearm bone density, and risk of fractures: prospective population study. Public Health and Environmental Exposure to Cadmium (PheeCad) Study Group. *Lancet* **1999**, *353* (9159), 1140–1144.

(3) Honda, R.; Tsuritani, I.; Noborisaka, Y.; Suzuki, H.; Ishizaki, M.; Yamada, Y. Urinary cadmium excretion is correlated with calcaneal bone mass in Japanese women living in an urban area. *Environ. Res.* **2003**, *91* (2), 63–70.

(4) Chervona, Y.; Arita, A.; Costa, M. Carcinogenic metals and the epigenome: understanding the effect of nickel, arsenic, and chromium. *Metallomics* **2012**, *4* (7), 619–627.

(5) Bush, J. A.; Mahoney, J. P.; Markowitz, H.; Gubler, C. J.; Cart-Wright, G. E.; Wintrobe, M. M. Studies on copper metabolism. XVI. Radioactive copper studies in normal subjects and in patients with hepatolenticular degeneration. *J. Clin. Invest.* **1955**, *34* (12), 1766–1778.

(6) Buffle, J.; DeVitre, R. R. *Chemical and Biological Regulation of Aquatic Systems*; CRC Press: Boca Raton, FL, 1993.

(7) Albaster, J. S.; Lloyd, R. *Water Quality Criteria for Freshwater Fish, 2nd Ed*; Butterworth Scientific: London, 1980.

(8) Morel, F. M. M. *Principles of Aquatic Chemistry*; John Wiley & Sons Ltd: New York, 1983.

(9) Pagenkopf, G. K. Gill Surface Interaction Model for trace-metal toxicity to fishes - role of complexation, pH, and water hardness. *Env. Sci.Technol.* **1983**, *17*, 342–347.

(10) Paquin, P. R.; Gorsuch, J. W.; Apte, S. C.; Batley, G. E.; Bowles, K. C.; Campbell, P. G. C.; Delos, C. G.; Di Toro, D. M.; Dwyer, R. L.; Galvez, F.; et al. The Biotic Ligand Model: A historical review. *Comp. Biochem. Physiol. C* **2002**, *133*, 3–35.

(11) Niyogi, S.; Wood, C. M. Biotic ligand model, a flexible tool for developing site-specific water quality guidelines for metals. *Environ. Sci. Technol.* **2004**, *38* (23),

6177–6192.

(12) U.S. Environmental Protection Agency. Quality criteria for water - 1986. U.S. EPA: Washington, DC 1986.

(13) Campbell, P. G. C. Interactions between trace metals and aquatic organisms: a critique of the free-ion activity model. In *Metal speciation and bioavailability in aquatic systems*; Tessier, A., Turner, D., Eds.; Wiley: New York, 1995; 45–102.

(14) Zhao, C. M.; Campbell, P. G. C.; Wilkinson, K. J. When are metal complexes bioavailable? *Environ. Chem.* **2016**, *13*, 425–433.

(15) Bradac, P.; Behra, R.; Sigg, L. Accumulation of Cadmium in periphyton under various freshwater speciation conditions. *Environ. Sci. Technol.* **2009**, *43* (19), 7291–7296.

(16) Fortin, C.; Campbell, P. G. C. Silver uptake by the green alga Chlamydomonas reinhardtii in relation to chemical speciation: Influence of chloride. *Environ. Toxicol. Chem.* **2000**, *19* (11), 2769–2778.

(17) Pinheiro, J. P.; Galceran, J.; van Leeuwen, H. P. Metal speciation dynamics and bioavailability: Bulk depletion effects. *Environ. Sci. Technol.* **2004**, *38* (8), 2397–2405.

(18) Hudson, R. J. M.; Morel, F. M. M. Lron transport in marine phytoplankton: Kinetics of cellular and medium coordination reactions. *Limnol. Oceanogr.* **1990**, *35* (5), 1002–1020.

(19) Galceran, J.; Puy, J.; Salvador, J.; Cecília, J.; van Leeuwen, H. P. Voltammetric lability of metal complexes at spherical microelectrodes with various radii. *J. Electroanal. Chem.* **2001**, *505* (1–2), 85–94.

(20) Puy, J.; Galceran, J. Theoretical aspects of dynamic metal speciation with electrochemical techniques. *Curr. Opin. Electrochem.* **2017**.

(21) van Leeuwen, H. P.; Town, R.; Buffle, J.; Cleven, R.; Davison, W.; Puy, J.; van Riemsdijk, W.; Sigg, L. Dynamic speciation analysis and bioavailabilty of metals in aquatic systems. *Environ. Sci. Technol.* **2005**, *39* (22), 8545–8556.

(22) Town, R. M.; Chakraborty, P.; van Leeuwen, H. P. Dynamic DGT speciation analysis and applicability to natural heterogeneous complexes. *Environ. Chem.* **2009**, *6* (2), 170–177.

(23) Frant, M. S. Where did Ion Selective Electrodes come from? The story of their development and commercialization. *J. Chem. Educ.* **1997**, *74*, 159.

(24) Companys, E.; Galceran, J.; Pinheiro, J. P.; Puy, J.; Salaün, P. A review on

electrochemical methods for trace metal speciation in environmental media. *Curr. Opin. Electrochem.* **2017**, *3*, 144–162.

(25) Vera, R.; Fontàs, C.; Galceran, J.; Serra, O.; Anticó, E. Polymer inclusion membrane to access Zn speciation: Comparison with root uptake. *Sci. Total Environ.* **2018**, *622*, 316–324.

(26) Temminghoff, E. J. M.; Plette, A. C. C.; van Eck, R.; van Riemsdijk, W. H. Determination of the chemical speciation of trace metals in aqueous systems by the Wageningen Donnan Membrane Technique. *Anal. Chim. Acta* **2000**, *417*, 149–157.

(27) Cantwell, F. F.; Nielsen, J. S.; Hrudey, S. E. Free nickel ion concentration in sewage by an ion exchange column-equilibration method. *Anal. Chem.* **1982**, *54* (9), 1498–1503.

(28) Franklin, N. M.; Rogers, N. J.; Apte, S. C.; Batley, G. E.; Gadd, G. E.; Casey, P. S. Comparative toxicity of nanoparticulate ZnO, bulk ZnO and $ZnCl_2$ to a freshwater microalga (Pseudokirchneriella subcapitata): The importance of particle solubility. *Env. Sci.Technol.* **2007**, *41*, 8484–8490.

(29) Berggren, D. Speciation of Aluminium, Cadmium, Copper and Lead in humic soil solutions - a comparison of the ion-exchange column procedure and equilibrium dialysis. *Int. J. Environ. Anal. Chem.* **1989**, *41*, 1–15.

(30) Pesavento, M.; Sturini, M.; D'Agostino, G.; Biesuz, R. Solid phase extraction of copper(II) by fixed bed procedure on cation exchange complexing resins. *J. Chromatogr. A* **2010**, *1217* (8), 1208–1218.

(31) Alberti, G.; Biesuz, R. EmporeTM membrane vs. Chelex 100: Thermodynamic and kinetic studies on metals sorption. *React. Funct. Polym.* **2011**, *71* (5), 588–598.

(32) Davison, W.; Zhang, H. In situ speciation measurements of trace components in natural waters using thin-fil gels. *Nature* **1994**, *367*, 546–548.

(33) Guthrie, J. W.; Mandal, R.; Salam, M. S. A.; Hassan, N. M.; Murimboh, J.; Chakrabarti, C. L.; Back, M. H.; Grégoire, D. C. Kinetic studies of nickel speciation in model solutions of a well-characterized humic acid using the competing ligand exchange method. *Anal. Chim. Acta* **2003**, *480* (1), 157–169.

(34) Shi, Z.; Wang, P.; Peng, L.; Lin, Z.; Dang, Z. Kinetics of heavy metal dissociation from natural organic matter: roles of the carboxylic and phenolic sites. *Environ. Sci. Technol.* **2016**, *50* (19), 10476–10484.

(35) Yapici, T.; Fasfous, I. I.; Zhao, J.; Chakrabarti, C. L. Effects of various competing ligands on the kinetics of trace metal complexes of Laurentian Fulvic Acid in model solutions and natural waters. *Anal. Chim. Acta* **2009**, *636* (1), 6–12.

(36) Chakrabarti, C. L.; Yanjia, L.; Grégoire, D. C.; Back, M. H.; Schroeder, W. H. Kinetic studies of metal speciation using Chelex cation exchange resin: Application to cadmium, copper, and lead speciation in river water and snow. *Environ. Sci. Technol.* **1994**, *28* (11), 1957–1967.

(37) Mandal, R.; Salam, M. S. A.; Murimboh, J.; Hassan, N. M.; Chakrabarti, C. L.; Back, M. H.; Grégoire, D. C. Competition of Ca(II) and Mg(II) with Ni(II) for binding by a well- characterized fulvic acid in model solutions. *Environ. Sci. Technol.* **2000**, *34* (11), 2201–2208.

(38) Mongin, S. Contribution to the availability of metal ions in aquatic systems. Doctoral thesis, Universitat de Lleida, 2012.

(39) Uribe, R. Availability of metal cations in aquatic systems from DGT measurements. Doctoral thesis, Universitat de Lleida, 2012.

(40) Cruz-González, S. Availability of metal ions and ZnO nanoparticles in aqueous media. Doctoral thesis, Lleida, 2014.

(41) Jiménez-Piedrahita, M. Interpreting DGT measurements beyond steady-state and perfect-sink conditions. Doctoral thesis, Universitat de Lleida, 2017.

(42) Altier, A. Diffusive Gradient in Thin Films (DGT) beyond perfect sink conditions. Doctoral thesis, Universitat de Lleida, 2018.

(43) Pesavento, M.; Biesuz, R.; Gallorini, M.; Profumo, A. Sorption mechanism of trace amounts of divalent metal ions on a chelating resin containing iminodiacetate groups. *Anal. Chem.* **1993**, *65* (18), 2522–2527.

(44) Pesavento, M.; Biesuz, R. Sorption of divalent metal ions on an iminodiacetic resin from artificial seawater. *Anal. Chim. Acta* **1997**, *346* (3), 381–391.

(45) Galceran, J.; Companys, E.; Puy, J.; Cecilia, J.; Garcés, J. L. AGNES: a new electroanalytical technique for measuring free metal ion concentration. *J. Electroanal. Chem.* **2004**, *566*, 95–109.

(46) Galceran, J.; Companys, E.; Puy, J.; Cecilia, J.; Garces, J. L. AGNES: A new electroanalytical technique for measuring free metal ion concentration. *J. Electroanal. Chem.* **2004**, *566* (1), 95–109.

(47) Huidobro, C.; Companys, E.; Puy, J.; Galceran, J.; Pinheiro, J. P. The use of

microelectrodes with AGNES. *J. Electroanal. Chem.* **2007**, *606* (2), 134–140.

(48) Rocha, L. S.; Companys, E.; Galceran, J.; Carapuça, H. M.; Pinheiro, J. P. Evaluation of thin mercury film rotating disk electrode to perform absence of gradients and Nernstian equilibrium stripping (AGNES) measurements. *Talanta* **2010**, *80* (5), 1881–1887.

(49) Parat, C.; Aguilar, D.; Authier, L.; Potin-Gautier, M.; Companys, E.; Puy, J.; Galceran, J. Determination of free metal ion concentrations using screen-printed electrodes and AGNES with the charge as response function. *Electroanalysis* **2011**, *23* (3), 619–627.

(50) Rocha, L. S.; Galceran, J.; Puy, J.; Pinheiro, J. P. Determination of the free metal ion concentration using AGNES implemented with environmentally friendly bismuth film electrodes. *Anal. Chem.* **2015**, *87* (12), 6071–6078.

(51) Domingos, R. F.; Carreira, S.; Galceran, J.; Salaün, P.; Pinheiro, J. P. AGNES at vibrated gold microwire electrode for the direct quantification of free copper concentrations. *Anal. Chim. Acta* **2016**, *920*, 29–36.

(52) Galceran, J.; Chito, D.; Martínez-Micaelo, N.; Companys, E.; David, C.; Puy, J. The impact of high Zn° concentrations on the application of AGNES to determine free Zn (II) concentration. *J. Electroanal. Chem.* **2010**, *638* (1), 131–142.

(53) Companys, E.; Cecília, J.; Codina, G.; Puy, J.; Galceran, J. Determination of Zn^{2+} concentration with AGNES using different strategies to reduce the deposition time. *J. Electroanal. Chem.* **2005**, *576* (1), 21–32.

(54) Tehrani, M. H.; Companys, E.; Dago, A.; Puy, J.; Galceran, J. Free indium concentration determined with AGNES. *Sci. Total Environ.* **2018**, *612*, 269–275.

(55) Alberti, G.; Biesuz, R.; Huidobro, C.; Companys, E.; Puy, J.; Galceran, J. A comparison between the determination of free Pb(II) by two techniques: Absence of Gradient and Nernstian Equilibrium Stripping and Resin Titration. *Anal. Chim. Acta* **2007**, *599*, 41–50.

(56) Zavarise, F.; Companys, E.; Galceran, J.; Alberti, G.; Profumo, A. Application of the new electroanalytical technique AGNES for the determination of free Zn concentration in river water. *Anal. Bioanal. Chem.* **2010**, *397* (1), 389–394.

(57) Companys, E.; Puy, J.; Galceran, J. Humic acid complexation to Zn and Cd determined with the new electroanalytical technique AGNES. *Environ. Chem.* **2007**, *4* (5), 347–354.

(58) Galceran, J.; Huidobro, C.; Companys, E.; Alberti, G. AGNES: A technique for determining the concentration of free metal ions. The case of Zn(II) in coastal Mediterranean seawater. *Talanta* **2007**, *71* (4), 1795–1803.

(59) David, C. A.; Galceran, J.; Rey-Castro, C.; Puy, J.; Companys, E.; Salvador, J.; Monné, J.; Wallace, R.; Vakourov, A. Dissolution kinetics and solubility of ZnO nanoparticles followed by AGNES. *J. Phys. Chem. C* **2012**, *116* (21), 11758–11767.

(60) Companys, E.; Naval-Sánchez, M.; Martínez-Micaelo, N.; Puy, J.; Galceran, J. Measurement of free zinc concentration in wine with AGNES. *J. Agric. Food Chem.* **2008**, *56* (18), 8296–8302.

(61) Fortin, C.; Campbell, P. G. G. An ion-exchange technique for free-metal ion measurements (Cd^{2+}, Zn^{2+}): Applications to complex aqueous media. *Int. J. Environ. Anal. Chem.* **1998**, *72* (3), 173–194.

(62) Sweileh, J. A.; Lucyk, D.; Kratochvil, B.; Cantwell, F. F. Specificity of the ion exchange/atomic absorption method for free copper(II) species determination in natural waters. *Anal. Chem.* **1987**, *59* (4), 586–592.

(63) Crémazy, A.; Leclair, S.; Mueller, K. K.; Vigneault, B.; Campbell, P. G. C.; Fortin, C. Development of an in situ Ion-Exchange Technique for the determination of free Cd, Co, Ni, and Zn concentrations in freshwaters. *Aquat. Geochemistry* **2015**, *21* (2–4), 259–279.

(64) Nduwayezu, I.; Mostafavirad, F.; Hadioui, M.; Wilkinson, K. J. Speciation of a lanthanide (Sm) using an ion exchange resin. *Anal. Methods* **2013**, *8*, 6774–6781.

(65) Gordon, C. S.; Lowe, J. T. Carbon-monoxide detector. US1644014A, 1927.

(66) Seethapathy, S.; Górecki, T.; Li, X. Passive sampling in environmental analysis. *J. Chromatogr. A* **2008**, *1184* (1–2), 234–253.

(67) Peijnenburg, W. J. G. M.; Teasdale, P. R.; Reible, D.; Mondon, J.; Bennett, W. W.; Campbell, P. G. C. Passive sampling methods for contaminated sediments: State of the science for metals. *Integr. Environ. Assess. Manag.* **2014**, *10* (2), 179–196.

(68) Górecki, T., Namienik, J. Passive sampling. *Trends Anal. Chem.* **2002**, *21* (4), 276–291.

(69) Kingston, J. K.; Greenwood, R.; Mills, G. A.; Morrison, G. M.; Björklund Persson, L. Development of a novel passive sampling system for the time-averaged measurement of a range of organic pollutants in aquatic environments.

J. Environ. Monit. **2000**, *2* (5), 487–495.

(70) Davison, W. The solubility of iron sulfides in synthetic and natural waters at ambient temperature. *Aquat. Sci.* **1991**, No. 53, 309.

(71) Senn, D. B.; Griscom, S. B.; Lewis, C. G.; Galvin, J. P.; Chang, M. W.; Shine, J. P. Equilibrium-based sampler for determining Cu^{2+} concentrations in aquatic ecosystems. *Environ. Sci. Technol.* **2004**, *38* (12), 3381–3386.

(72) Chen, C. E.; Zhang, H.; Jones, K. C. A novel passive water sampler for in situ sampling of antibiotics. *J. Environ. Monit.* **2012**, *14* (6), 1523–1530.

(73) Challis, J. K.; Hanson, M. L.; Wong, C. S. Development and calibration of an organic-Diffusive Gradients in Thin Films aquatic passive sampler for a diverse suite of polar organic contaminants. *Anal. Chem.* **2016**, *88* (21), 10583–10591.

(74) Wang, Y.; Ding, S.; Gong, M.; Xu, S.; Xu, W.; Zhang, C. Diffusion characteristics of agarose hydrogel used in diffusive gradients in thin films for measurements of cations and anions. *Anal. Chim. Acta* **2016**, *945*, 47–56.

(75) Davison, W.; Grime, G. W.; Morgan, J. a. W.; Clarke, K. Distribution of dissolved iron in sediment pore waters at submillimetre resolution. *Nature* **1991**, *352* (6333), 323–325.

(76) Davison, W.; Zhang, H. Progress in understanding the use of diffusive gradients in thin films (DGT) back to basics. *Environ. Chem.* **2012**, *9* (1), 1–13.

(77) Galceran, J.; Puy, J. Interpretation of diffusion gradients in thin films (DGT) measurements: A systematic approach. *Environ. Chem.* **2015**, *12* (2), 112–122.

(78) Puy, J.; Galceran, J.; Rey-Castro, C. Interpreting the DGT Measurement. In *Diffusive Gradients in Thin-Films for Environmental Measurements*; Cambridge University Press: Cambridge (UK), 2016; 93–122.

(79) Björklund Blom, L.; Morrison, G. M.; Kingston, J.; Mills, G. A.; Greenwood, R.; Pettersson, T. J. R.; Rauch, S. Performance of an in situ passive sampling system for metals in stormwater. *J. Environ. Monit.* **2002**, *4* (2), 258–262.

(80) Stephens, B. S.; Kapernick, A.; Eaglesham, G.; Mueller, J. Aquatic passive sampling of herbicides on naked particle loaded membranes: Accelerated measurement and empirical estimation of kinetic parameters. *Environ. Sci. Technol.* **2005**, *39* (22), 8891–8897.

(81) Stephens, B. S.; Kapernick, A. P.; Eaglesham, G.; Mueller, J. F. Event monitoring of herbicides with naked and membrane-covered Empore disk integrative passive sampling devices. *Mar. Pollut. Bull.* **2009**, *58* (8), 1116–1122.

(82) Dong, Z.; Lewis, C. G.; Burgess, R. M.; Shine, J. P. The Gellyfish: An in situ equilibrium-based sampler for determining multiple free metal ion concentrations in marine ecosystems. *Environ. Toxicol. Chem.* **2015**, *34* (5), 983–992.

(83) Puy, J.; Galceran, J.; Cruz-González, S.; David, C. A.; Uribe, R.; Lin, C.; Zhang, H.; Davison, W. Measurement of metals using DGT: Impact of ionic strength and kinetics of dissociation of complexes in the resin domain. *Anal. Chem.* **2014**, *86* (15), 7740–7748.

2. Methodology

2.1. Analytical methods

It is now convenient to introduce the techniques that have been employed to carry out this work, with a special focus on their applicative details. We will start from two of the instrumental techniques most widely used in speciation and elemental analysis, Potentiometry based on Ion Selective Electrode (ISE) and Inductive Coupled Plasma Spectrometry (ICP). For the description of the new techniques developed and fine-tuned during this work (the aforementioned DIET and eDGT) the reader is referred to the specific chapters, 5 and 6.

A necessary digression will be, thus dedicated to the resin Chelex 100, and to the determination of its physical characteristics.

2.2. ISE (Ion Selective Electrodes)

2.2.1. Basis of the technique

Potentiometry is a method of analysis based on measuring the potential of an electrochemical cell when negligible current is drawn. Its relative speed and easiness of use, in comparison to the majority of the analytical techniques, has determined its general success across a wide range of disciplines. The only equipment required is an indicator electrode (the real sensing device), a reference electrode (with respect to which the potential difference is measured) and a potentiometer to measure the potential difference between the two; in a well-designed potentiometric cell this difference can be related to the activity of the target analyte through Nernst equation.

The reference electrodes of widest practical application are the calomel electrode and the silver chloride electrode, which present a potential known and independent from the composition of the medium. The choice of the indicator electrode is instead determined by the nature of the target analyte, which implies the existence of a very large variety of

electrode designs; among them, the membrane electrodes are probably those of broadest application.

In the membrane electrode a potential difference is created across a membrane designed to be sensitive only to a small set of ions (ideally to only one). One of the sides of the membrane is in contact with the solution to be analysed, while the other faces a reference solution, normally contained in the body of the electrode, at a fixed concentration of the target ion. A Nernst-like equation can be derived to relate the potential difference across the membrane ΔE and a_M, the activity of the analyte in solution:

$$\Delta E = \frac{RT}{nF} \ln a_M \tag{2.1}$$

where R is the gas constant, T the absolute temperature and n the number of electrons exchanged in the redox process. Given their ability to specifically target a certain analyte, membrane electrodes are generally known under the name of ISE, Ion Selective Electrode.

The ISE can be further classified according to the type of membrane, which also defines the type of target analytes – liquid membrane, glass membrane or crystal membrane. In liquid-membrane electrodes, the sensing element is a hydrophobic membrane containing a liquid organic complexant (such as an ionophore or an ion-exchanger) that reacts selectively with the analyte. Among the most common electrodes of this kind we can quote the K^+ electrode[1] (that exploits the selectivity of the ionophore valinomicine) and the Ca^{2+} electrode[2] (based on an aliphatic ester of phosphoric acid).

While in the present work we have not dealt with liquid membrane electrodes, we extensively used two electrodes that will be taken as a model for the other two kinds: the glass pH electrode and the Cd crystalline electrode.

The glass pH electrode sensing element is a thin layer of a glass of special composition, whose silicate groups can exchange protons with the bulk solution, originating a difference of charge between the faces of the membrane.

The Cd electrode is based on a similar principle, with the difference that the sensing membrane, instead of glass, is constituted by a crystalline solid, being a mixture of AgS and CdS.

2.2.2. Implementation of ISE in this work

Figure 2.1. Electrodes used for the potentiometric measurements: Cd-ISE Crison 9658S7, Separate pH electrode Metrohm 6.0133.100 and Ag/AgCl reference electrode Metrohm 6.0726.100.

A characteristic of ISE that must be always kept in mind is that they are not really specific to only one analyte, but rather selective to several: if the interfering elements are present at high concentration in the solution of interest, they may alter or even suppress the signal due to the main target. For example, the well-known "alkaline error" displayed by the pH glass electrode (systematic underestimation of the pH in strongly basic environments), arises from the interference of Na^+ cations. The membrane of the Cd-ISE, on the other hand, is responsive to Ag^+, Hg^{2+} and Cu^{2+},[3] which will therefore have to be absent from the samples. The presence of interfering elements may constitute a crippling obstacle to the application of potentiometric techniques: this will be shown in Chapter 5, where the use of an ISE for the on-line monitoring of Cu^{2+} in the effluent of a packed column was prevented by the high concentration of chlorides in the medium.

In the experimental part of the present work we used both a traditional pH electrode (Metrohm 6.0133.100) and a combination probe, which comes paired with the reference electrode (Crison 5203). When using the separate one, the electrostatic cell was completed with a silver chloride electrode (Metrohm 6.0726.100).

Two different models of Cd-ISE were used (Metrohm 6.0502.110 and Crison 9658S7); they delivered equally good performances, with some minor differences ascribable to their different age (see Fig. 2.1). The average slope of Eq. (2.1) for the Metrohm electrode is 28.5(6) (12 replicates), while for the Crison one is 29.5(9) (16 replicates); an ideal behaviour of the electrodes at 25 ºC would result in a slope of 29.6.

All the electrodes were connected to a potentiometer Orion 920A+ or, alternatively, to an Orion 720A+; the main advantage of this last model was that it could be controlled by an external computer through an appositely written MATLAB routine.

2.2.3. Calibration of the ISE at low concentration

Even though the limit of detection of the Cd-ISE reported by the manufacturer is 1×10^{-7} M,[3] it is known[4–6] that the ISE can show linear response even at much lower activities, provided that $c_{T,M}$ is much higher.

This was the case handled in Chapter 4, where the electrode was used to follow the metal uptake to a complexing resin in presence of a competing ligand. We calibrated the Cd-ISE by making small additions of NTA to a solution containing a fixed Cd(II)concentration, at the same I used for the experiments (Fig. 2.2), and, in these conditions, the electrode displayed linear behaviour down to at least 1×10^{-9} M, the concentration corresponding to the last point of the calibration.

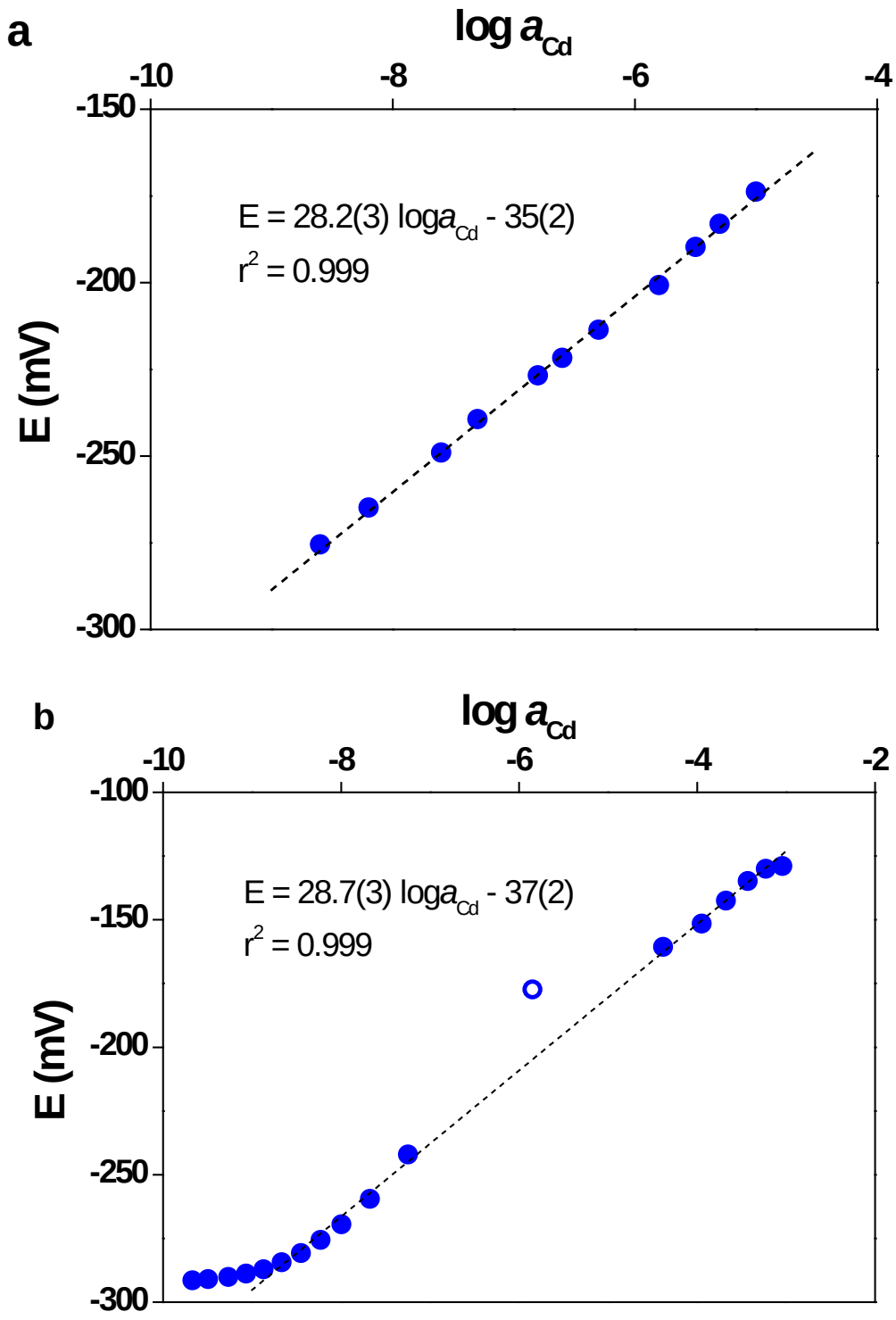

Figure 2.2. Calibration plots of Metrohm Cd-ISE in presence of a competing ligand (NTA), obtained: by adding aliquots of ligand standard to a solution at fixed $c_{T,M}$ *(Panel* a, $c_{T,M}$*= 1×10^{-5} M, I= 0.1 M in NaNO$_3$, pH 6.4) and by adding aliquots of metal standard to a solution at fixed* $c_{T,L}$ *(Panel* b, $c_{T,L}$*= 8.3×10^{-5} M, I= 0.1 M in NaNO$_3$, pH 7.5. The empty point was not taken for the regression).*

Alternatively, the electrode could be calibrated by making progressive additions of metal standard to a solution at known ligand concentration.[6] This procedure, in principle exactly equivalent, actually presents the flaw that, when the ligand is close to be saturated, even the smallest additions of metal standard will cause a sudden increase in the free metal concentration, resulting in the loss of details around the equivalence point. Of course, this does not affect the limit of detection.

2.3. ICP (Inductive Coupled Plasma spectroscopy)

2.3.1. Implementation of ICP in this work

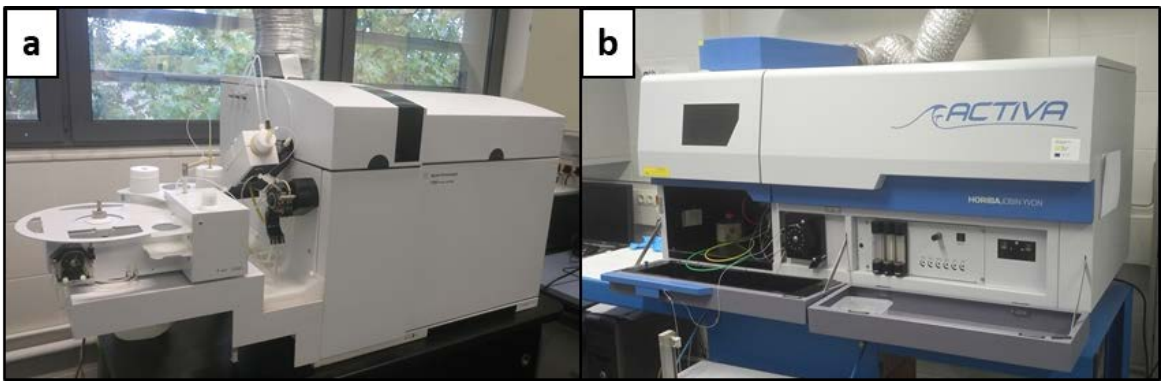

Figure 2.3. ICP-MS Agilent 7700x and ICP-OES Horiba Jobin Yvon ACTIVA, the two models used in the experimental part of this work.

Inductive Coupled Plasma Spectrometry (ICP) has become the most common technique for elemental analysis at trace level, thanks to its extremely low detection limits, relative usability and the possibility of being automatized.

The core of an ICP Spectrometer is a plasma torch, which plays the two-fold role of atomising the sample and bringing the atoms to their excited state. The torch is coupled to a detector system, which can be a mass spectrometer (ICP-MS) or a spectrophotometer (ICP-OES).

In ICP-MS, the ions, after passing through a series of cones, are separated according to their mass/charge ratio by a mass analyser, generally a quadrupole, and redirected to an ion detector. ICP-OES, on the contrary, exploits the spectra emitted by the excited atoms upon coming back to their original state. The models used for this work were an ICP-MS Agilent 7700x and an ICP-OES Horiba Jobin Yvon ACTIVA (Fig. 2.3).

Our choice of preference was the ICP-MS, because it guarantees for most of the elements of our interest limits of detection at least one order of magnitude lower than

ICP-OES. We resorted to the latter in the few cases where the ICP-MS performs poorly, namely for the analysis of Ca and Li. A major problem when analysing Ca is that its most abundant isotope, ^{40}Ca, shares the atomic mass with the majoritarian isotope of argon, ^{40}Ar. Since the gas argon is the main constituent of the plasma, as well as being used to contain it and to carry the sample into the torch, it is present in very large amount and causes a high background noise. Even if it can be subtracted from the total signal, fluctuations in the argon flux may cause errors in the background correction. To obviate this problem, the isotope chosen for the analysis is usually ^{44}Ca; the drawback in this case is that it constitutes only the 2% of the total Ca, which implies higher detection limits.

Another element whose analysis is difficult is Li, as it is typically used as internal standard (along with Bi, Ge, In, Sc, Tb and Y): it is added in equal amount to all samples and standards, and by monitoring how its concentration varies eventual matrix effects or instrument malfunctioning can be spotted. Even though other internal standard mixtures are commercially available it was generally handier to work with the optical instrument, which does not require by default the use of the internal standard.

In order to be injected into the plasma torch, the samples need to be liquid, and they had sometimes to be filtrated to avoid the presence of suspended particles. To prevent precipitation or adsorption on the walls of the plasticware all the samples were acidified to 1% in HNO_3. The samples with a higher percentage of HNO_3, such as those coming from the elution of the resin layers of the DGT, had to be diluted accordingly, as too acidic solutions may wear the tubing of the equipment.

In many experiments the range of concentrations of a single metal was very wide, up to 4 orders of magnitude. Instead of diluting the samples, we generally preferred to calibrate the instrument over the whole range of concentrations and, if needed, to split the calibration line in two, in order to reduce the uncertainty on the regression.

2.3.2. Comparison between ISE and ICP results

ISE and ICP measure two different physical quantities (the activity of a species and the total concentration of an element) and, rather than being alternative, can provide complementary information. When speciation is negligible, though, the results of the two techniques substantially coincide, as shown for the case of Cd(II)in Fig. 2.4 at least for concentrations ranging between 5×10^{-5} M and 1×10^{-6} M.

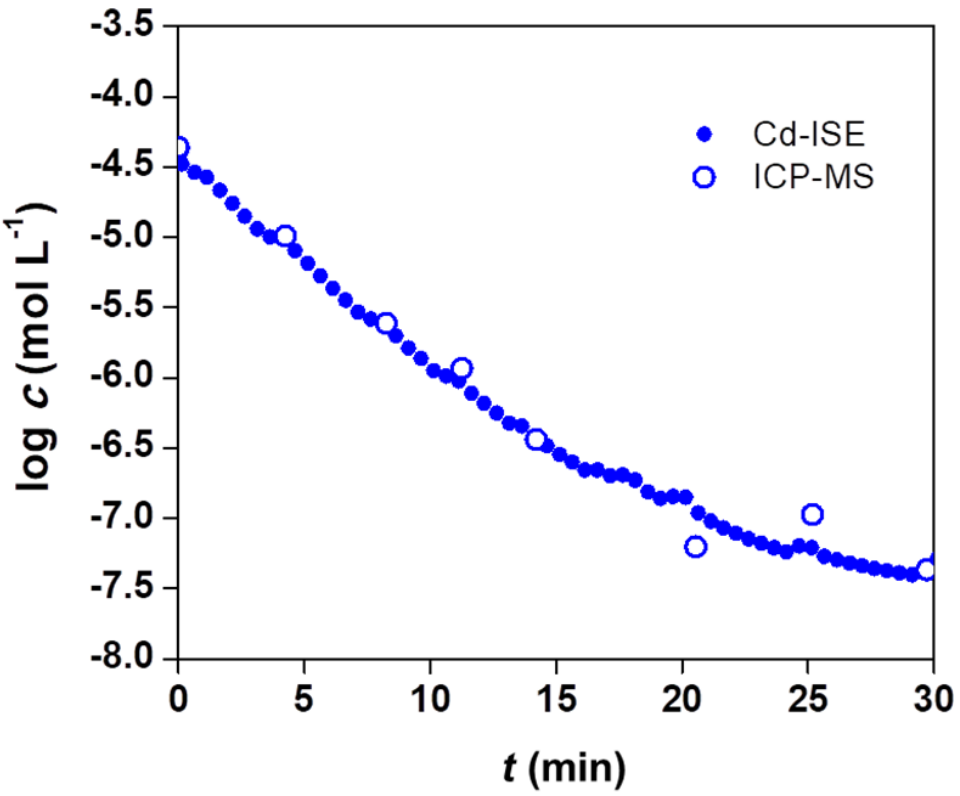

Figure 2.4. Uptake curves of Cd(II) on Chelex 100, measured with Cd-ISE (dots) and ICP-MS (circles). Experimental conditions: $c_{T,M}$*=* 5×10^{-5} *M, I= 0.1 M in* $NaNO_3$*,* $m_{dry\ resin}$*= 24.5 mg, pH 7.5, suspension buffered with 1 mM MOPS.*

As the results of the two techniques are consistent with each other, the choice of preference could be taken on the basis of such factors as the operational simplicity, cost and fastness of response – and under these aspects the ISE is clearly preferable to the ICP.

On the other hand, when the levels of free metal are very low, such as in the experiments in presence of ligands presented in Chapter 4, we found that the results from the ICP were generally more reliable, as the response time of the electrode tended to increase. The ICP was also the best choice when dealing with multiple analytes, as in the experiments of Chapter 6, since it is capable of multielemental analysis.

2.4. Chelex 100 chelating resin

2.4.1. General features of the beads

The core of the DGT is the Chelex 100 chelating resin, a styrene divinylbenzene copolymer containing paired iminodiacetate moieties which act as chelating groups in

binding polyvalent metal ions. Chelex 100 stands out among the other ion exchangers for the strength and selectivity for divalent cations of its functional groups. Thanks to these advantageous features it has found numerous applications in different fields, such as DNA purification,[7] removal of hazardous materials from wastewater,[8,9] recovery of precious metals from leachates,[10] chemical speciation studies in environmental matrices,[11–15] or extraction and pre-concentration of ions of analytical interest.[16]

Chelex 100 appears as a slightly wet white powder. It is highly hygroscopic, and upon wetting it increases up to 4 times its volume. It generally sinks in distillate water, although a fraction of beads may float as a consequence of bubbles of air trapped inside the beads. The amount of the floating fraction is inconsistent among batches, most likely because it depends on differences in the manufacturing. In Tab. 2.1 below some general features of the resin are given.

Table 2.1. General features of the Chelex 100 chelating resin used in this work, as provided by the manufacturer.

Matrix	Styrene divinylbenzene, 1% crosslinkage [17]
Functional groups	Sodium salt of iminodiacetic acid [17]
Capacity	1.90 mmol g^{-1} [18]
Approx. MW exclusion	3500 [17]
Particle size	100-200 mesh [17]
Nominal density	0.65 Kg L^{-1} [17]

Being weakly acidic (pK_{a1}: 9.12, pK_{a2}: 3.20),[19] the protonated fraction of functional groups in the resin may change widely according to the environmental conditions (pH and ionic strength). This affects not only its sorption capacity, but also its volume and water content, as a consequence of the repulsion of the charged groups. For our purposes we generally need more accurate information about the bead size (radius r_0 and volume V_R) than the one found in the technical literature, and the determination of these parameters will have to be taken into account together with their dependence on the external conditions.

2.4.2. Determination of the bead size

It is known that the size of the hydrated beads changes with the nature of the counterion, swelling 100% in going from the H^+ to the Na^+ form,[17] thus correlating the bead size

with the external pH was a necessary challenge. We started by determining the average radius of two batches of resin at two radically different pH (2.51 and 7.50, *I*= 0.1 M) by direct observation with a microscope (Fig. 2.5 and Fig. 2.6). A Navitar Zoom 6000 optical system equipped with a 10x objective lens (Mitutoyo) was used. The microscope, combined with a camera (Lumenera INFINITY2-1digital), was mounted on a Linear Motor Positioning Stage (Standa), capable of a resolution of ≈ 0.16 μm.

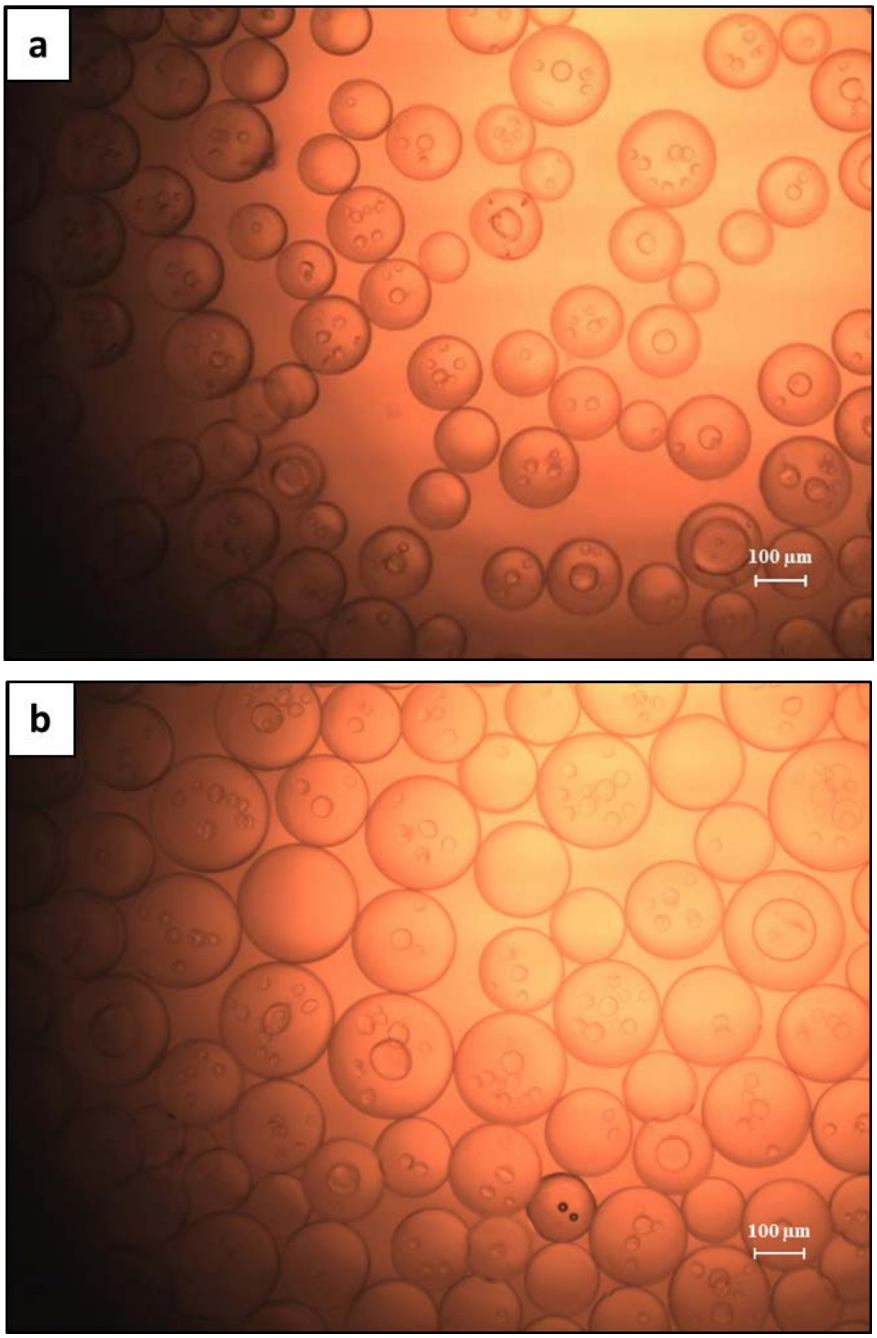

Figure 2.5. Representative microscopic photo (magnification: 100x) of the beads suspended at pH 2.51 (Panel a*) and 7.50 (Panel* b*) in 0.1 M $NaNO_3$. A total of 12 photos were taken at each pH.*

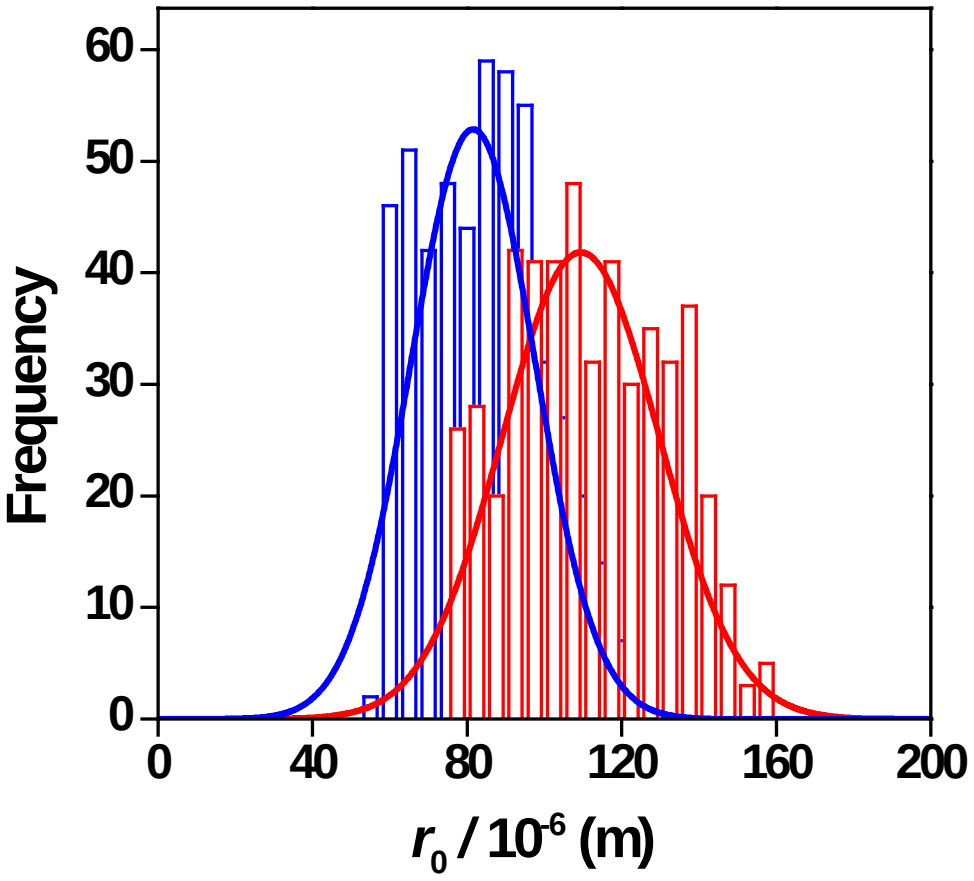

Figure 2.6. Frequency histograms of the radii of Chelex 100 beads (100-200 mesh) at pH 2.51 and 7.50, both at an ionic strength of 0.1 M in $NaNO_3$. Lines: Gaussian distribution fits.

The total volume of the resin (V_R, as it will be called in the following chapters) can be safely approximated to its water content, and then determined by letting equilibrate a small amount of Chelex 100 in a $NaNO_3$ solution at the desired pH and ionic strength. The resin was then separated from the supernatant by rapid filtration on vacuum funnel; the fraction that could be recovered from the filter was accurately weighted and then dried in oven at 60° C overnight. The water content was estimated as the difference in mass before and after drying; at pH 2.51 and pH 7.50, the computed V_R values were 2.7×10^{-8} m^3 and 7.6×10^{-8} m^3, respectively. From the linear interpolation of the average radii of the batches between pH 2.51 and 7.50 it was then possible to determine the relationship between r_0 and V_R at constant mass of dry resin.

2.5. References

(1) Moss, S. D.; Janata, J.; Johnson, C. C. Potassium ion-sensitive field effect transistor. *Anal. Chem.* **1975**, *47* (13), 2238–2243.

(2) Craggs, A.; Moody, G.; Thomas, J. PVC matrix membrane ion-selective electrodes. *J. Chem. Educ* **1974**, *51* (8), 541–544.

(3) Metrohm. Ion Selective Electrode: Instructions for use. Metrohm Ltd.: Herisau, Switzerland.

(4) Avdeef, A.; Zabronsky, J.; Stuting, H. H. Calibration of copper Ion Selective Electrode response to pCu 19. *Anal. Chem.* **1983**, *55* (2), 298–304.

(5) Milne, C. J.; Kinniburgh, D. G.; de Wit, J. C. M.; van Riemsdijk, W. H.; Koopal, L. K. Analysis of metal-ion binding by a peat humic acid using a simple electrostatic model. *J. Colloid Interface Sci.* **1995**, *175*, 448–460.

(6) Serrano, N.; Díaz-Cruz, J. M.; Ariño, C.; Esteban, M.; Puy, J.; Companys, E.; Galceran, J.; Cecilia, J. Full-wave analysis of stripping chronopotentiograms at scanned deposition potential (SSCP) as a tool for heavy metal speciation: Theoretical development and application to Cd(II)-phthalate and Cd(II)-iodide systems. *J. Electroanal. Chem.* **2007**, *600* (2), 275–284.

(7) Walsh, P. S.; Metzger, D. A.; Higuchi, R. Biotechniques 30th anniversary gem Chelex 100 as a medium for simple extraction of DNA for PCR-based typing from forensic material. *Biotechniques* **2013**, *54* (3), 506–513.

(8) Zagorodni, A. *Ion Excahge Materials: Properties and Applications*; Elsevier: Oxford, 2007.

(9) Inamuddin; Luqman, M. (Eds). *Ion-Exchange Technology. I, Theory and Materials*; Inamuddin, Luqman, M., Eds.; Springer: Dordrecht, 2012.

(10) Cortina, J. L.; Warshawsky, A.; Kahana, N.; Kampel, V.; Sampaio, C. H.; Kautzmann, R. M. Kinetics of goldcyanide extraction using ion-exchange resins containing piperazine functionality. *React. Funct. Polym.* **2003**, *54* (1–3), 25–35.

(11) Pesavento, M.; Biesuz, R. Simultaneous determination of total and free metal-ion concentration in solution by sorption on iminodiacetate resin. *Anal. Chem.* **1995**, *67* (19), 3558–3563.

(12) Pohl, P. Application of ion-exchange resins to the fractionation of metals in water. *TrAC - Trends Anal. Chem.* **2006**, *25* (1), 31–43.

(13) Manouchehri, N.; Besançon, S.; Bermond, A. Kinetic characterizing of soil trace

metal availability using Soil/EDTA/Chelex mixture. *Chemosphere* **2011**, *83* (7), 997–1004.

(14) Leguay, S.; Campbell, P. G. C.; Fortin, C. Determination of the free-ion concentration of rare earth elements by an ion-exchange technique: Implementation, evaluation and limits. *Environ. Chem.* **2016**, *13* (3), 478–488.

(15) Shi, Z.; Wang, P.; Peng, L.; Lin, Z.; Dang, Z. Kinetics of heavy metal dissociation from natural organic matter: roles of the carboxylic and phenolic sites. *Environ. Sci. Technol.* **2016**, *50* (19), 10476–10484.

(16) Pesavento, M.; Profumo, A.; Biesuz, R.; Alberti, G. Ion exchange complexing resins as sensors for the determination of free metal Ion concentration at a low level. *Solvent Extr. Ion Exch.* **2008**, *26* (3), 301–320.

(17) Biorad. *Chelex® 100 and Chelex 20 Chelating Ion Exchange Resin Instruction Manual*; Hercules, CA.

(18) Pesavento, M.; Biesuz, R.; Cortina, J. L. Sorption of metal ions on a weak acid cation-exchange resin containing carboxylic groups. *Anal. Chim. Acta* **1994**, *298* (2), 225–232.

(19) Pesavento, M.; Biesuz, R. Sorption of divalent metal ions on an iminodiacetic resin from artificial seawater. *Anal. Chim. Acta* **1997**, *346* (3), 381–391.

3. Dynamics of metal uptake to a chelating resin in absence of ligands

Part of this this chapter has been published in:

Chemical Engineering Journal, 317, **2017**, 810-820

3.1. Introduction

In the previous chapter we have mentioned the advantageous features of the chelating ion exchange resin Chelex 100 and its numerous applications, among them being the binding agent of the DGT passive sampler. An increasing number of works has been devoted to study the physicochemical mechanisms that regulate the metal accumulation in the DGT in varying environmental conditions (pH, ionic strength, etc.).[1–4] Despite existing work, the mechanisms that govern the kinetics of metal uptake by the free resin beads still need further study.

We will start by formulating some general hypotheses to better define our field of work: (*i*) Although many works assimilate the accumulation to the resin as a pseudo-first order reaction,[5] we will assume that the chemical reaction step between the metal ion of interest and the functional groups in the resin is very fast if compared to the diffusion of the trace ion. (*ii*) We will also treat our problem as if it was a case of pure self-diffusion, which means that we will treat the diffusing species as if they had the same charge and diffusion coefficient. Strictly speaking this hypothesis is valid only when dealing with isotopes, while in this chapter we study the exchange of divalent cations with the monovalent counterions of the resin. As a consequence the two species will have an interdiffusion coefficient that evolves with the course of the exchange reaction, and taking this into account requires solving the Nernst-Planck equation.[6] However, since the change takes place between a trace metal and a major (background) cation, it is safe to assume that the ratio of concentrations trace/background ions remains very low, and the diffusion coefficient stays constant throughout the experiment. The electrostatic

effects will be taken into account by introducing an accumulation factor at the resin/solution interface. (*iii*) Regarding the perturbation of the system introduced by the presence of the ion exchanger, we can distinguish between two cases: in the first one the size of the metal reservoir is huge in comparison with the capacity of the sorbent material, so that, notwithstanding the sorption process, the bulk metal concentration remains practically constant (infinite volume conditions). In the other one, on the contrary, metal uptake is large enough to cause an appreciable variation in the bulk concentration (finite volume conditions). Since the readiest way to study the dynamic behaviour of ion exchangers is to monitor the decay in the trace metal bulk concentration with time, our model will necessarily assume finite volume conditions. (*iv*) Once accepted that the uptake is controlled essentially by metal transport, it is left to decide whether the rate-determining step is the diffusion through the film surrounding the resin bead or the diffusion inside the particle.

The former case, denoted here as Film Diffusion Model (FDM), was solved by Boyd *et al.*[7] and it shows good agreement with experimental kinetic data for relatively small uptake values. As it will be shown, though, FDM fails at long times and, what is more important, it does not provide a theoretical support for the observed influence of pH and ionic strength on the kinetic data. On the other hand, the model assuming the ion exchange process as controlled by internal diffusion in finite volume conditions (solved by Paterson[8] and here called IDM, Intraparticle Diffusion Model) has the obvious disadvantage of being unable to account for the observed impact of stirring rate in batch experiments. Further information about these models, which constitute the theoretical antecedents of our work, is given in the Appendices to this chapter.

Although some authors have reported a transition from external film to intraparticle diffusion regimes during the kinetic experiments,[9] examples of application of mixed-control diffusion models to ion exchange in bulk depletion conditions are still very scarce.[10] One reason for this gap may be the relative mathematical complexity of the available analytical solutions, which are expressed as infinite series (see references[11] and[12] for the cases of infinite and finite volume conditions, respectively).

Furthermore, while the thermodynamic description of pH and ionic strength effects on the Chelex binding properties at equilibrium is well developed (see Section 3.7.5 below), there is still a need for the incorporation of such effects into consistent kinetic models.

In this chapter we try to fill this gap in four ways. First, we report an approximate (but very accurate) analytical solution to the Mixed Control Model (MCM) for finite volume conditions, which compares favourably with the infinite series expression (16-112) listed by Le Van[12] in terms of simplicity of implementation and convergence. Secondly, the model reported here incorporates the estimation of the thermodynamic solution/resin partition coefficients for the metal ions through the Gibbs-Donnan model.[13,14] Thirdly, the overall internal diffusion coefficients is interpreted in terms of fast, reversible binding of metal ions to the Chelex 100 functional groups within the resin phase. Finally, the model is used to describe experimental data of Cd(II) sorption on Chelex 100 and proves successful at describing the effects of experimental conditions (stirring rate, pH, ionic strength, volume of sorbent, etc.) with a minimum number of fitted empirical variables (basically, the thickness of the diffusion boundary layer).

3.2. The Mixed Control Model (MCM)

3.2.1. Derivation of the Mixed Control Model

Let us consider the sorbent material as constituted by an ensemble of perfectly spherical beads, homogeneous in size and composition, with radius r_0.

At time t=0, the beads (initially without any metal) are plunged into a uniformly stirred metal ion solution at a given concentration $c_{\mathrm{M}}^{*}(t=0)$, where the superscript * represents the local value of the concentration at a sufficiently large distance from the beads, *i.e.:* $c_{\mathrm{M}}^{*}(t)=c_{\mathrm{M}}(t, r>r_1)$ (see Fig. 3.1). In solution, the metal is present exclusively as free hydrated metal cations.

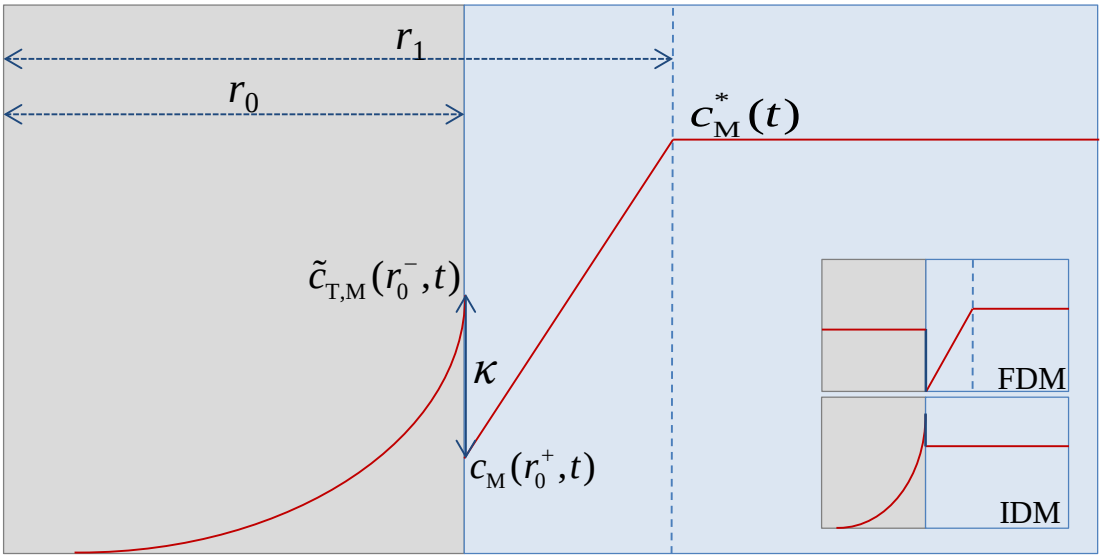

Figure 3.1. Schematic representation of the radial concentration profiles in the resin (grey background) and aqueous solution (blue background) phases, as expected in the Mixed Control Model (MCM). The metal partitions between the two sides of the interface according to the coefficient κ, which depends only on pH and ionic strength. The diffusive boundary layer (DBL) extends from r_0 to r_1. The insets represent the concentration profiles as described by the Film Diffusion Model (FDM) and the Intraparticle Diffusion Model (IDM). Profiles are not in scale.

As time proceeds, the metal ions in solution diffuse into the beads. Since the solution volume is finite, $c_M^*(t)$ diminishes. The rate of metal depletion in bulk solution derives from the following treatment in the solution and particle domains.

FILM DOMAIN

Due to the stirring, we assume that bulk concentrations are restored at a fixed distance r_1 from the centre of the bead, defining a film domain. Migration applies whenever there is a drop of the electrostatic potential created by the charges of the resin bead. The "effective" distance of the potential drop from the resin solution interface is of the order of the Debye length[15] which is less than 10 nm for the smallest ionic strength considered in our work. The thickness of the film domain depends on the stirring, but is assumed to be of the order of 10^{-6} m. Thus, migration is implicitly included in this model via Donnan partitioning (see Eq. (3.20) below), which is a reasonable approximation when the concentration of the metal cation is negligible with respect to the salt background. We also assume that diffusion in the boundary solution film in contact with the beads reaches instantaneously a quasi-steady state[16,17] (*i.e.* diffusion across the film is much

faster than the concentration changes in bulk solution due to depletion). The flux (J) can be computed as

$$J = D_{\mathrm{M}} \frac{c_{\mathrm{M}}^{*}(t) - c_{\mathrm{M}}\left(r_0^{+}, t\right)}{\delta} \tag{3.1}$$

where r_0^{+} denotes the position at the solution side of the bead/solution interface, D_{M} is the diffusion coefficient of the free metal in solution, and δ is the effective thickness of the Diffusive Boundary Layer (DBL). If bulk concentrations are assumed to be restored at a distance r_1 from the centre of the bead (see Fig. 3.1), then

$$\delta = \frac{r_0}{r_1}\left(r_1 - r_0\right) \tag{3.2}$$

PARTICLE DOMAIN

As in the film domain, the Donnan model assumes that the electrostatic potential is constant inside the bead so that transport is only due to diffusion. We also assume that diffusion of the trace ion is not distorted by the exchangeable counterions, because the Na^{+} ions present in the resin and solution phases are in great excess with respect to the trace metal.

For the sake of simplicity we assume that the metal forms only one kind of complex with the resin sites, with stoichiometry 1:1. Let us anticipate that, in Chapter 6, the binding to the resin will be described in a more sophisticated way that takes into account different possible stoichiometries. Let us also assume that the $\widetilde{\mathrm{MR}}$ complexes are labile; as a consequence the following relation holds:

$$\tilde{c}_{\mathrm{MR}}(r,t) = \tilde{K}_{\mathrm{MR}}\, \tilde{c}_{\mathrm{R}}(r,t)\, \tilde{c}_{\mathrm{M,free}}(r,t) \tag{3.3}$$

where $\tilde{K}_{\mathrm{MR}}$ is the conditional stability constant of the complex between the metal ion and the active groups of the resin, and $\tilde{c}_{\mathrm{R}}$ is the instantaneous local concentration of free resin active sites (in general, the tilde denotes parameters referred to the resin phase).

Now, the continuity equation for the free metal inside the beads reads as follows:

$$\frac{\partial \tilde{c}_{\mathrm{M,free}}(r,t)}{\partial t} = \tilde{D}_{\mathrm{M}} \nabla^2 \tilde{c}_{\mathrm{M,free}}(r,t) + \tilde{k}_{\mathrm{d}}\, \tilde{c}_{\mathrm{MR}}(r,t) - \tilde{k}_{\mathrm{a}}\, \tilde{c}_{\mathrm{R}}\, \tilde{c}_{\mathrm{M,free}}(r,t) \qquad r < r_0 \tag{3.4}$$

while the continuity equation for the bound metal can be written as

$$\frac{\partial \tilde{c}_{\mathrm{MR}}(r,t)}{\partial t} = \tilde{D}_{\mathrm{MR}} \nabla^2 \tilde{c}_{\mathrm{MR}}(r,t) - \tilde{k}_{\mathrm{d}}\, \tilde{c}_{\mathrm{MR}}(r,t) + \tilde{k}_{\mathrm{a}}\, \tilde{c}_{\mathrm{R}}\, \tilde{c}_{\mathrm{M,free}}(r,t) \qquad r < r_0 \tag{3.5}$$

The addition of the previous two equations cancels out the kinetic terms and yields:

$$\frac{\partial \tilde{c}_{\mathrm{M,free}}(r,t)}{\partial t} + \frac{\partial \tilde{c}_{\mathrm{MR}}(r,t)}{\partial t} = \tilde{D}_{\mathrm{M}} \nabla^2 \tilde{c}_{\mathrm{M,free}}(r,t) + \tilde{D}_{\mathrm{MR}} \nabla^2 \tilde{c}_{\mathrm{MR}}(r,t) \qquad r < r_0 \tag{3.6}$$

Let $\tilde{c}_{\mathrm{T,M}}(r,t) = \tilde{c}_{\mathrm{M,free}}(r,t) + \tilde{c}_{\mathrm{MR}}(r,t)$ denote the local total metal concentration inside the resin at time *t* and distance *r* from the centre of the bead.

Assuming excess of resin sites (*i.e.* $\tilde{c}_{\mathrm{R}}(r,t) \approx$ constant), and taking into account that the bound metal ion is immobile (*i.e.* $\tilde{D}_{\mathrm{MR}} = 0$), Eq. (3.6) becomes

$$\frac{\partial \tilde{c}_{\mathrm{T,M}}(r,t)}{\partial t} = \nabla^2 \left(\tilde{D}_{\mathrm{M}} \tilde{c}_{\mathrm{M,free}}(r,t) + \tilde{D}_{\mathrm{MR}} \tilde{c}_{\mathrm{MR}}(r,t) \right) = \tilde{D}_{\mathrm{M}} \left(\frac{1}{1 + \tilde{K}_{\mathrm{MR}} \tilde{c}_{\mathrm{R}}} \right) \nabla^2 \tilde{c}_{\mathrm{T,M}}(r,t) = \tilde{D}\, \nabla^2 \tilde{c}_{\mathrm{T,M}}(r,t) \tag{3.7}$$

where

$$\tilde{D} = \frac{\tilde{D}_{\mathrm{M}}}{1 + \tilde{K}_{\mathrm{MR}} \tilde{c}_{\mathrm{R}}} \tag{3.8}$$

is the overall (total metal) diffusion coefficient inside the resin, *i.e.* the "effective" diffusion coefficient for the ensemble of metal species inside the bead.

Eq. (3.7) indicates that the diffusion and reaction of the free metal ions inside the bead can be re-formulated as a diffusion problem where the total metal species $\tilde{c}_{\mathrm{T,M}}(r,t)$ has an effective diffusion coefficient given by Eq. (3.8), which is lower than that of the free ions. This approximation is valid whenever the reaction is fast enough to assume local instantaneous equilibrium and there is excess of resin sites.

The initial condition for Eq. (3.7) is:

$$\tilde{c}_{\mathrm{T,M}}(r, t=0) = 0 \qquad \forall r \le r_0 \tag{3.9}$$

and one boundary condition is null flux at the centre of the bead

$$\left(\frac{\partial \tilde{c}_{\mathrm{T,M}}}{\partial r} \right)_{r=0} = 0 \qquad r = 0 \quad \forall t \tag{3.10}$$

Due to the coupling with the solution domain, the second boundary condition (at $r = r_0$), splits into two parts, the first associated with the concentration and another with the flux.

The concentration relationship corresponds to an instantaneous equilibrium at the solid-liquid interface, determined by the partition coefficient κ[7] which accounts for the electrostatic partitioning associated to the potential drop at $r = r_0$ and the chemical binding to the resin sites in equilibrium conditions (see below, Section 3.2.2):

$$\tilde{c}_{\mathrm{T,M}}\left(r_0^-,t\right) = \kappa\, c_{\mathrm{M}}\left(r_0^+,t\right) \tag{3.11}$$

where $\tilde{c}_{\mathrm{T,M}}\left(r_0^-,t\right)$ and $c_{\mathrm{M}}\left(r_0^+,t\right)$ are the (total and free) metal concentrations at the interface in the resin and in the aqueous phase, respectively. The value of κ depends on pH and ionic strength, but not on the local metal concentration, as it is assumed that the amount of resin functional groups is in excess with respect to the total moles of metal.

The flux condition prescribes continuity of fluxes at the interface:

$$J = \tilde{D}\left(\frac{\partial \tilde{c}_{\mathrm{T,M}}}{\partial r}\right)_{r=r_0^-} = D_{\mathrm{M}}\left(\frac{\partial c_{\mathrm{M}}}{\partial r}\right)_{r=r_0^+} = D_{\mathrm{M}}\frac{c_{\mathrm{M}}^*(t) - c_{\mathrm{M}}\left(r_0^+,t\right)}{\delta} \tag{3.12}$$

Finally, the finite volume conditions are ensured through the mass balance constrain (where V_{T} and V_{R} are, respectively, the total volume and the volume of the resin phase):

$$\left(V_{\mathrm{T}} - V_{\mathrm{R}}\right)c_{\mathrm{M}}^*(0) = \frac{3V_{\mathrm{R}}}{r_0^3}\int_0^{r_0} \tilde{c}_{\mathrm{T,M}}(r,t)\, r^2 dr + c_{\mathrm{M}}^*(t)\left(V_{\mathrm{T}} - V_{\mathrm{R}}\right) \tag{3.13}$$

This equation assumes that the average concentration of metal in the DBL is approximately equal to the bulk value (a discussion on the accuracy of this assumption is included in the Appendices, see Section 3.7.2).

MATHEMATICAL SOLUTIONS

The continuity equation (3.7), with initial condition (3.9) and boundary conditions associated to (3.10), (3.11) and (3.12) can be solved via numerical inversion of the expression for the concentration in the Laplace space (see details in the Appendices, Section 3.7.1).

To obtain a simple analytical expression one can take the approximation:

$$\coth\left(\sqrt{\frac{s}{\tilde{D}}}r_0\right) \approx 1 \tag{3.14}$$

(*s* being the variable in the Laplace transform) which is clearly valid for $\tilde{D} \ll \frac{r_0^2}{t}$. Note that, in the least favourable conditions, we estimate a value of $\frac{r_0^2}{\tilde{D}} = 19\ \text{h}$, which is much greater than the largest time recorded during the kinetic experiments. Eq. (3.14) is parallel to other approaches where semi-infinite diffusion in the spherical domain is assumed.[18–20]

In this way, the following equation can be derived:

$$c_{\text{M}}^{*}(t) = \frac{c_{\text{M}}^{*}(0)}{3Bi_{\text{m}}w}\left[\frac{(Bi_{\text{m}}-1)R_1+1}{R_1(R_1-R_2)(R_1-R_3)}F\left(-\frac{\sqrt{\tilde{D}t}}{r_0R_1}\right)+\right.$$
$$+\frac{(Bi_{\text{m}}-1)R_2+1}{R_2(R_1-R_2)(R_3-R_2)}F\left(-\frac{\sqrt{\tilde{D}t}}{r_0R_2}\right)$$
$$\left.+\frac{(Bi_{\text{m}}-1)R_3+1}{R_3(R_1-R_3)(R_2-R_3)}F\left(-\frac{\sqrt{\tilde{D}t}}{r_0R_3}\right)\right] \qquad (3.15)$$

where the factors R_1, R_2 and R_3 are the roots of:

$$x^3 - x^2 + \frac{1-Bi_{\text{m}}}{3Bi_{\text{m}}w}x - \frac{1}{3Bi_{\text{m}}w} = 0 \qquad (3.16)$$

the mass transfer Biot number is defined as

$$Bi_{\text{m}} = \frac{D_{\text{M}}r_0}{\delta\tilde{D}\kappa} \qquad (3.17)$$

and

$$F(x) = \text{e}^{x^2}\ \text{Erfc}(x) \qquad (3.18)$$

Throughout this chapter, the sorption data are expressed in terms of the fractional attainment of equilibrium *f*, which is defined as the ratio between the instantaneous and final (at equilibrium) amounts of metal sorbed in the resin.[7] It can be directly computed from the experimental data as:

$$f = \frac{\left\langle \tilde{c}_{\text{M}}(t) \right\rangle}{\tilde{c}_{\text{M}}(\infty)} = \frac{c_{\text{M}}^{*}(0) - c_{\text{M}}^{*}(t)}{c_{\text{M}}^{*}(0) - c_{\text{M}}^{*}(\infty)} \quad ; \quad 0 \le f \le 1 \qquad (3.19)$$

where $\left\langle \tilde{c}_{\text{M}}(t) \right\rangle$ represents the average metal concentration in the resin. This parameter *f* has the advantage that normalizes the kinetic data with respect to the initial and

equilibrium bulk concentrations, which is useful for comparison among experiments. The main drawback of this notation is that it does not show properly the details of the experimental curves at relatively long times (close to equilibrium), which may be inconvenient for fitting purposes. For this reason, the results will be represented as $\ln(1-f)$ *vs*. time, where the starting point of the experiments is $\ln(1-f)=0$ and equilibrium is asymptotically reached at $\ln(1-f)\to-\infty$. An additional advantage of this representation is that, according to the FDM model, $\ln(1-f)$ depends linearly on time, thus discriminating between MCM and FDM.

Fig. 3.2 compares several solutions of the MCM for a typical set of parameters. Note that the numerical inversion of the Laplace solution agrees with the exact analytical solution given in Le Van and Carta,[12] Eq. (A3.23), as expected. One of the drawbacks of this exact analytical solution is the long computation times required for some sets of parameters. For instance, with a standard personal computer, it took 7 minutes to calculate the 300 points used to draw the curve in Fig. 3.2, with $\kappa=3.63\times10^{3}$, while several hours were needed for $\kappa=10^{8}$.

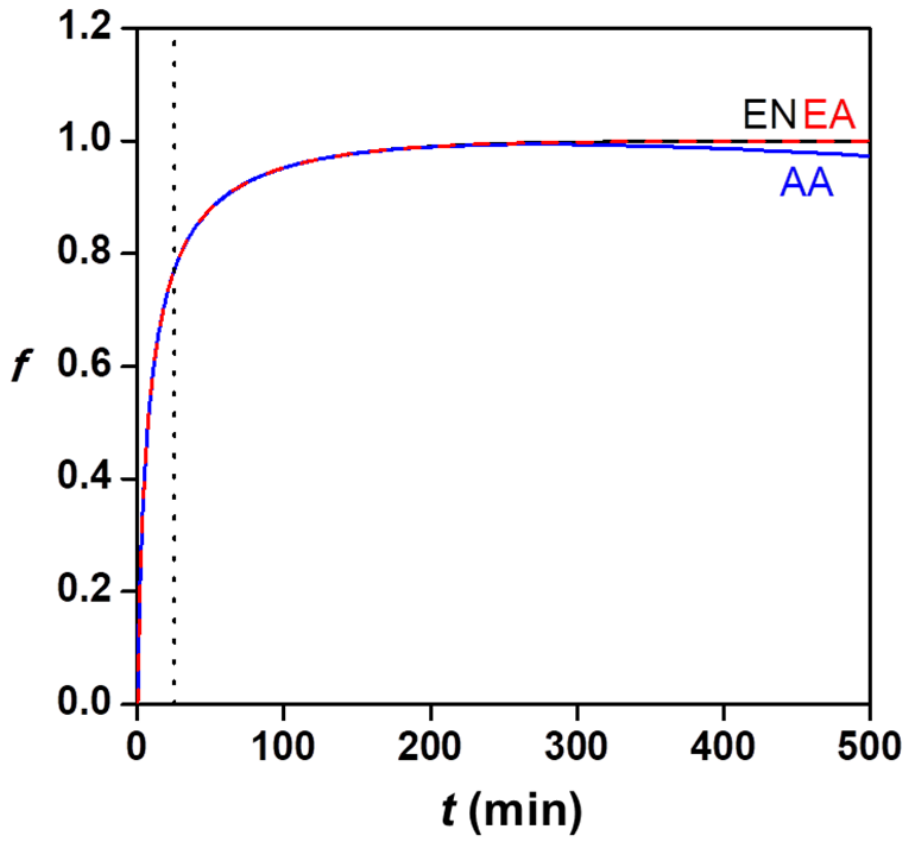

Figure 3.2. Comparison of the fractional approach to equilibrium f, Eq. (3.19) according to the Approximate Analytical solution (AA, Eq. (3.15)), the Exact Numerical solution (EN, numerical inversion of Eq. (A3.22) and the Exact Analytical solution (EA,Eq. (A3.35)) of MCM. The parameters used for the computation are listed in Tab. 3.2, experiment 1 (pH 3.48). The vertical dashed line at t= 25 min corresponds to the typical timescale considered in the experiments.

On the other hand, the new approximate solution (3.15) required less than 1 minute to complete the same calculations. Moreover, the accuracy of this approximate expression is excellent at relatively short times, while the deviations from the exact solution are only relevant when approaching equilibrium (f > 0.99), but still below the order of magnitude of the experimental uncertainty, and without practical consequences in our testing conditions.

3.2.2. Theoretical interpretation of $\widetilde{D}$

As the polymer in the beads bears negative charge, a Donnan potential will develop at the bead/solution interface. The Donnan partitioning factor, χ, can be expressed as:

$$\chi^2 = \frac{\tilde{c}_{\mathrm{M,free}}\left(r_0^-,t\right)}{c_{\mathrm{M}}\left(r_0^+,t\right)} = \frac{\tilde{c}_{\mathrm{T,M}}\left(r_0^-,t\right)\Big/\left(1+\tilde{K}_{\mathrm{MR}}\tilde{c}_{\mathrm{R}}\right)}{c_{\mathrm{M}}\left(r_0^+,t\right)} \tag{3.20}$$

where the exponent takes into account the divalent nature of Cd^{2+} ions.

In this way, the global partitioning factor κ can be interpreted as the product of an electrostatic and a chemical binding term:[21]

$$\kappa = \chi^2 \left(1 + \tilde{K}_{MR} \tilde{c}_R\right) \tag{3.21}$$

Thus, Eq. (3.8) becomes

$$\tilde{D} = \frac{\chi^2 \tilde{D}_M}{\kappa} \tag{3.22}$$

The polymeric matrix is expected to reduce the mobility of the metal ion ($\tilde{D}_M$) in the bead with respect to the value in solution. We assumed $\tilde{D}_M / D_M = 1/14$, in agreement with the ratios reported by Fernández *et al.*[22] for divalent cations such as Cu^{2+} and Co^{2+} in a similar iminodiacetic resin (see Tab. A3.2) or by Dykstra *et al.*[6] for a variety of species. The calculation of κ and χ from the thermodynamic Gibbs-Donnan model is detailed in Section 3.7.5 below. The validity of Eq. (3.22) was tested by comparing its results with freely fitted $\tilde{D}$ values, as shown in Section 3.7.6 of the Appendices to this chapter.

3.2.3. Influence of the parameters on model predictions

A series of theoretical calculations are first presented to describe the effects of the parameters V_R, r_0, κ, and $\tilde{D}$ on the modelled kinetic data. The corresponding plots of ln(1-*f*) *vs*. time (Figs. 3.3, 3.4 and 3.5) were calculated by varying each of these parameters systematically around the values used to model the experimental data.

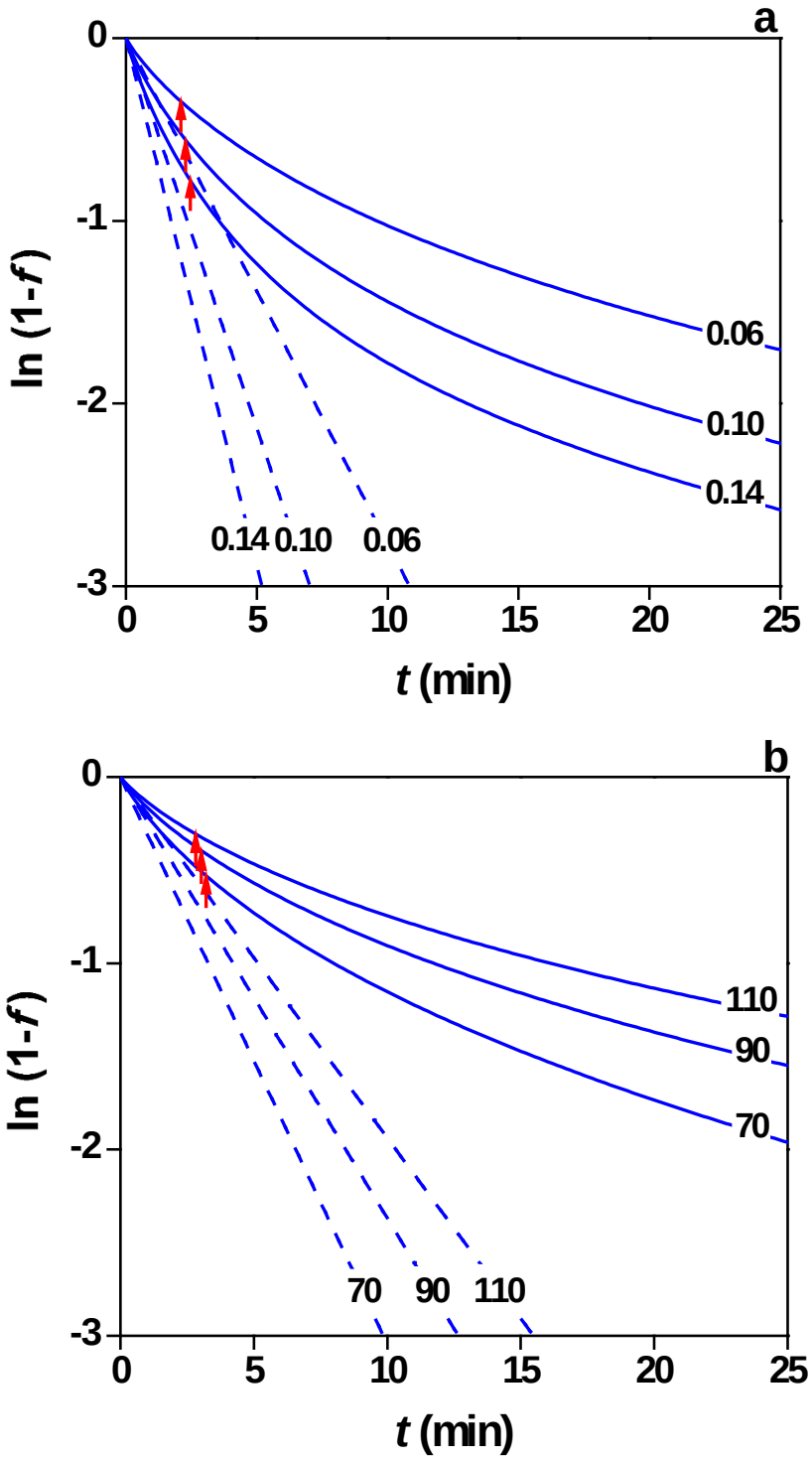

Figure 3.3. Effect of V_R (a) and r_0 (b) on the sorption kinetics according to MCM (continuous lines) and FDM (dashed lines). The arrows indicate the points where the predominant transport mechanism changes from external film to internal diffusion (i.e. values of t and f corresponding to equal values of the metal flux according to FDM and IDM). The labels on the lines represent the values of $V_R \times 10^6$ (in m^3) and $r_0 \times 10^6$ (in m), respectively. The rest of parameters are listed in Tab. 3.2, experiment 1 (pH 3.48).

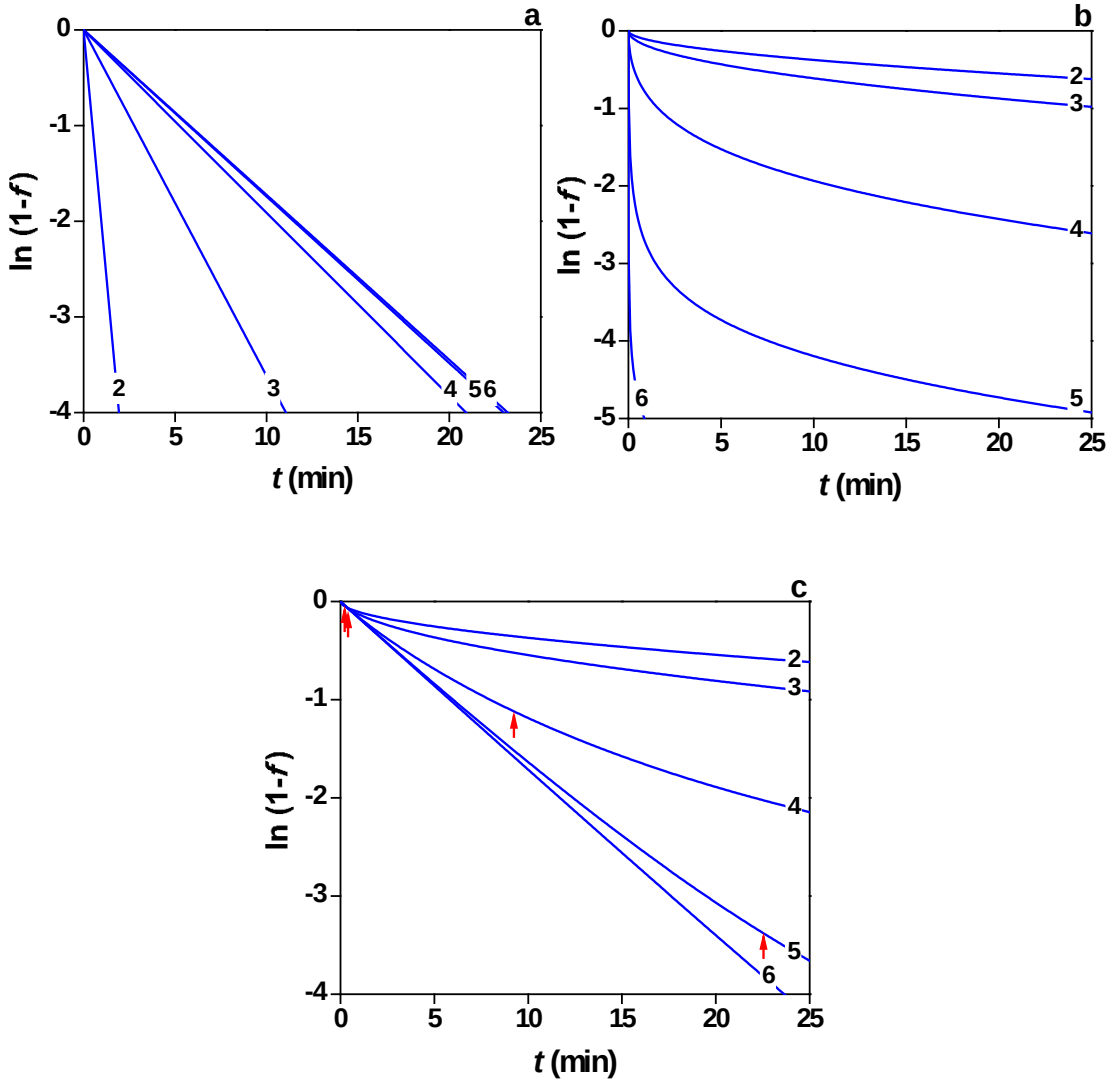

Figure 3.4. Effect of κ on the sorption kinetics, as described by FDM (a), IDM (b) and MCM (c), at constant D̃. The labels on the lines represent the values of log Ø. The rest of parameters are listed in Tab. 3.2, experiment 1 (pH 3.48). Note that the curves of log κ=5 and log κ=6 in (a) are overlapped. The arrows in (c) indicate the points where the predominant transport mechanism changes from external film to internal diffusion.

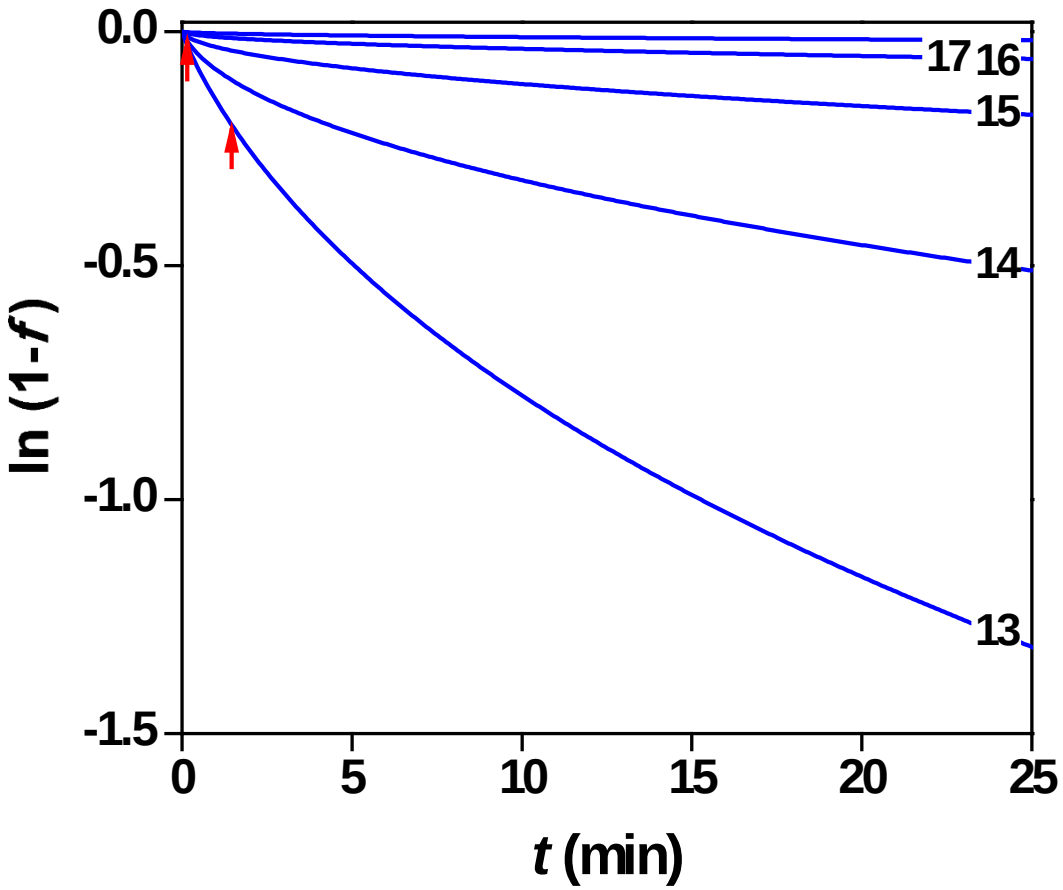

Figure 3.5. Effect of $\widetilde{D}$ on the sorption kinetics according to MCM. The labels on the lines represent the values of $-log\left(\widetilde{D}/m^2s^{-1}\right)$. The rest of parameters are listed in Tab. 3.2, experiment 1 (pH 3.48). The arrows indicate the points where the predominant transport mechanism changes from external film to internal diffusion. In the cases of $-log\left(\widetilde{D}/m^2s^{-1}\right)$ = 15, 16 and 17, the points lay too close to the origin to be displayed.

A first inspection reveals that the plots differ from each other essentially in two aspects, the initial slope and the degree of nonlinearity (concavity). During the initial stages of the experiments, the rate of metal sorption is mostly controlled by external film diffusion. Since FDM predicts a linear behaviour of ln(1-*f*) over the entire time domain (see Eq. (A3.56)), the presence of nonlinearity in the MCM is a result of the increasing limitation of the overall sorption rate due to intraparticle diffusion. The comparison of the theoretical fluxes of metal ion across the bead/solution boundary, calculated according to FDM, IDM and MCM, allows the approximate assessment of the point of maximum concavity. Indeed, at this point, the main controlling mechanism of the

sorption rate switches from film diffusion to intraparticle diffusion. The position of this crossover point is estimated as the intersection of the fluxes predicted by FDM and IDM (see Fig. 3.6).

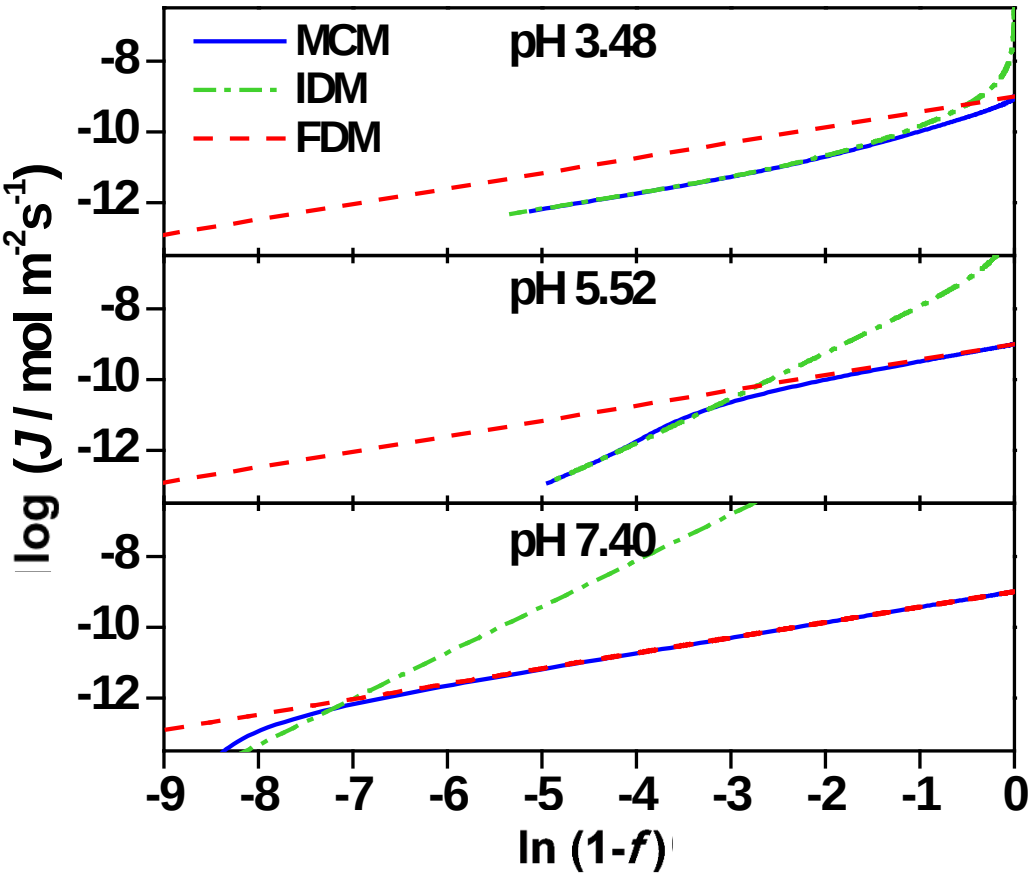

Figure 3.6. Fluxes J (in mol m^{-2} s^{-1}) at the particle/solution interface, expressed as a function of f, computed according to MCM (blue continuous line), IDM (green dotted line) and FDM (red dashed line) at pH 3.48, 5.52 and 7.40. The parameters used for the computations are listed in Tab. 3.2.

Let us now review the influence of the different model parameters.

The effect of the volume of resin, V_R, is shown in Fig. 3.3a. As observed, the increase in V_R leads to a faster sorption rate, which is a straightforward result of the mass balance. In fact, an increasing volume of resin, at a constant bead radius, implies an increment in the number of particles, which means that each bead is depleting a proportionally smaller "cell" of bulk solution (while the metal ion flux and the interfacial area per bead remain constant) and, therefore, a given fractional uptake (f) is reached in a shorter time. The opposite behaviour is predicted when the bead radius is varied at constant V_R: larger values of r_0 and constant total volume imply a smaller number of beads, a larger volume to be depleted by each bead and, consequently, longer equilibration times (Fig. 3.3b). In

this case, the onset of the control by internal diffusion is also shifted to shorter times as the size increases, due to the growing thickness of the intraparticle domain.

In the previous two cases, both FDM and MCM predict the same trend of the initial slope with the parameters being varied (V_R or r_0).

The case of κ (Fig. 3.4), however, is more involved. In order to analyse the effect of this parameter alone (*i.e.* at constant values of $\tilde{D}$), let us consider first the two limiting cases (represented by FDM and IDM). If transport is exclusively controlled by diffusion through the external film, the time needed to reach a given value of *f* increases with the value of κ since the amount of metal required for equilibrium is also progressively larger. In FDM, the slope of ln(1-*f*) *vs.* *t* tends asymptotically to a constant value (see the collapsing curves of log κ = 5 and log κ = 6 in Fig. 3.4a), which depends only on the V_R / V_T ratio (see Eq. (A3.53)) and not on κ. This can be interpreted as the bead surface acting as a perfect sink for the metal ion.

On the other hand, in the limiting case where transport is exclusively controlled by internal diffusion, the metal ion concentration in aqueous solution at the interface is equal to the bulk value at all times (see inset for FDM in Fig. 3.1), and the sorption flux is determined by the gradient of the internal concentration profile at $r = r_0$ and the intraparticle diffusion coefficient. As κ increases, the local gradient of concentration at the interface becomes progressively steeper and, consequently, the flux of metal ion is enhanced (recall that these simulations are performed at constant $\tilde{D}$), which leads to increasingly faster sorption kinetics. It is, thus, evident that FMD and IDM predict opposite trends of the kinetic profiles with κ.

In the mixed control situation, the net flux will be controlled by the slowest mechanism. Indeed, as observed in Fig. 3.4c, MCM predicts kinetic profiles that range between a predominantly FDM behaviour at large κ values, especially at short times (where ln(1-*f*) *vs.* *t* is almost linear) and a mostly intraparticle diffusion-limited kinetics at low κ values (where the partition coefficient is not high enough to induce a relevant decline of the metal ion concentration at the interface). As a consequence, MCM foresees an inverse trend with κ of the ln(1-*f*) slope, to the one found with FDM.

The relative predominance of the external film or internal particle diffusion controls is obviously affected also by the value of the internal diffusion coefficient, as seen in Fig. 3.5, which represents the effect on the kinetic profiles of varying values of $\tilde{D}$ at constant κ. In this case, the effect is straightforward: at small values of the internal

diffusion coefficient, the simulated curves approach the IDM results, whereas at large values of $\tilde{D}$ the intraparticle diffusion becomes faster (not limiting) and the behaviour tends to be better described by FDM.

Finally, one can assess the impact of the inverse relationship between κ and $\tilde{D}$ (Eq. (3.22)) due to cation complexation inside the resin. According to this relationship, the increase in κ has opposite effects on the relative contribution of the intraparticle diffusion mechanism to the mass transport: it leads to a simultaneous increase in the concentration gradient at the interface and a decrease in the internal diffusion coefficient.

3.3. Materials and Methods

Chelex 100 resin (100-200 mesh) was purchased from BioRad Laboratories. Prior to the experiments, the resin was soaked in methanol solution to remove any possible free iminodiacetic moieties, then carefully rinsed with Milli-Q water, filtered and stored in a closed pot. All solutions were prepared in Milli-Q water.

Either a Metrohm or a Crison Cd-ISE was used to monitor the concentration of Cd^{2+} in solution during the sorption experiments. The reproducibility and reliability of these measurements were also checked by comparison with ICP-MS analysis (see Section 2.3.2). The Cd-ISEs were calibrated with standard Cd(II) solutions in the same ionic media as used in the kinetic experiments. At least two calibration curves were performed, before and after each sorption experiment.

For each experimental condition tested, an accurately weighted amount of resin, previously dried in oven at 60º C, was equilibrated in a $NaNO_3$ solution at the desired pH and ionic strength. For experiments at circumneutral pH, the solutions were buffered with 1 mM 3-(N-morpholino)propanesulfonic acid (MOPS) (which has been reported not to complex Cd[23]) and the pertinent small additions of NaOH or HNO_3.

The sorption batch experiments were performed at 25 ± 0.1 ºC in thermostated polypropylene vessels (the resin beads adhere to glass surfaces). Since the prolonged usage of a magnetic stirrer may deteriorate the beads, the suspension was stirred from above using an OrionStar Series Automatic Stirrer Probe.

After the initial contact of the equilibrated resin with the standard Cd(II) solution, the values of Cd^{2+} concentration were recorded in continuous mode by measuring the Cd-ISE potentials at each time with a computer program specifically written in MATLAB.[24]

Each experiment was performed in duplicate, and the error bars in the ln(1-*f*) data were computed from the standard deviation of the measured concentrations.

3.4. Selection of model parameters

Most parameters required by the MCM are experimentally accessible (D_M, V_R and r_0), while others were estimated indirectly from theoretical models ($\widetilde{D}$ and κ) or directly fitted from the kinetic sorption data (δ).

The value of the diffusion coefficient of Cd^{2+} ion in water, D_M, was taken from the literature,[25] as 7×10^{-10} m^2 s^{-1} (25º C). The values of V_R and r_0 must take into account the variation of the bead size due to the swelling/shrinking of Chelex 100,[26] which is highly sensitive to pH and ionic strength of the surrounding solution. Therefore, they were directly determined at the same experimental conditions of the sorption data, through dedicated experiments. V_R is assumed equal to the water content in the resin beads and it was determined by measuring the loss of mass of an aliquot of resin previously equilibrated in aqueous solutions at the corresponding pH and ionic strength and, then, oven-dried at 60°C until constant weight (considering the water density equal to 1 g mL^{-1}). We assume that V_R stays constant during the experiment, notwithstanding the progressive substitution of the counterion Na^+ with Cd^{2+}.

The radius of the resin beads, $r_{0,}$ was interpolated for each experimental condition (pH, *I*) from values determined by optical microscopy, as detailed in Section 2.4.2.

The ratio κ between the concentration of metal sorbed in the resin and that in bulk solution at equilibrium can, in principle, be calculated from experimental equilibrium data, using the following expression, derived from Eq. (3.11) and the mass balance:

$$\kappa = \frac{(V_T - V_R)(c_M^*(0) - c_M^*(\infty))}{V_R c_M^*(\infty)} \tag{3.23}$$

However, the use of this equation is not convenient at acidic pH values, where the amount of sorbed metal ion is negligible, or at high pH values (>6), and relatively large V_R/V_T ratios, where the values of $c_M^*(\infty)$ are affected by a large uncertainty due to analytical detection limits and/or excessively long equilibration times. Therefore, the values of κ were computed from the Gibbs-Donnan equilibrium model.[13] According to this model, the sorbent is represented as a concentrated solution phase, separated from the external solution by an interface through which water, neutral molecules and ions can diffuse, but the active groups, permanently linked to the solid matrix, cannot. The

partition coefficient of the metal ions between the two phases (*K**, in the Gibbs-Donnan nomenclature, which corresponds to κ in the present notation), is computed from the intrinsic protonation and complexation constants of the metal ion with the active groups of the resin, the pH and ionic strength (*I*) of the solution and the concentration of the counterion in both phases, as reported in the literature[13,14,27–29] (see details in the Appendices to this chapter, Section 3.7.5). Once κ is computed, the values of $c_{\mathrm{M}}^{*}(\infty)$ required for the calculation of *f* in Eq. (A3.36) are obtained from Eq. (3.23).

The effective thickness of the DBL,[16,30] (δ) was considered as a fitted parameter, with the only constraint of being lower than the radius of the bead, and it was assumed to be dependent on the stirring rate only.

χ was estimated from the Donnan model using the values of the ionic strength (*I*) and the concentration of charged sites in the resin ($\tilde{q}$), as:

$$\chi = \frac{\tilde{q}}{2I} + \sqrt{\left(\frac{\tilde{q}}{2I}\right)^2 + 1} \tag{3.24}$$

The values of $\tilde{q}$ at each value of pH and *I* were computed as the amount of free sites (not bound to protons or Cd(II) ions) per volume of resin, according to the Gibbs-Donnan model. The total number of sites was taken equal to 1.90 mmol g^{-1}, as determined by acid-base titrations of the resin.[31] We refer to Section 4.6.2 for further details about the determination of the Boltzmann factor.

3.5. Results and Discussion

This section analyses the ability of the MCM to describe the effect of the different variables (metal ion concentration, amount of resin, size of beads, stirring rate, pH and ionic strength) on the sorption kinetics by comparison with experimental data.

3.5.1. Influence of $c_{\mathrm{M}}^{*}(0)$ and V_{R}.

The present derivation of the MCM assumes that the total functional groups of the resin are in excess with respect to the amount of metal ion bound at equilibrium. This condition is necessary to ensure that κ (and, consequently, $\widetilde{D}$) is invariant with respect to $\tilde{c}_{\mathrm{T,M}}(r,t)$). Under these conditions, the bulk metal ion concentration at each time, $c_{\mathrm{M}}^{*}(t)$, is strictly proportional to the initial concentration, $c_{\mathrm{M}}^{*}(0)$, which leads to the fractional attainment of equilibrium f being independent of the initial metal ion concentration. This expectation was confirmed from experiments at different initial Cd(II) concentrations (while keeping constant all other conditions) in the range 1×10^{-6} M to 1×10^{-4} M. In these conditions, the kinetic profiles collapsed on the same master curve, which demonstrates that the sorption data can be effectively normalised using the descriptor f. For instance, Fig. 3.7a shows how the effect of a 2.5-fold increase in $c_{\mathrm{M}}^{*}(0)$ leads to negligible differences in f within the experimental uncertainty. As a reference, at $c_{\mathrm{M}}^{*}(0) = 5\times10^{-5}$ M and with the amount of resin used in the experiments, the ratio bound metal ion/Chelex 100 groups at equilibrium is estimated as 0.05. The experimental data also show a good reproducibility in the whole range selected for model fitting. Uncertainty increases significantly as f gets closer to 1, due to accumulated experimental errors and the constraint of the analytical limit of detection.

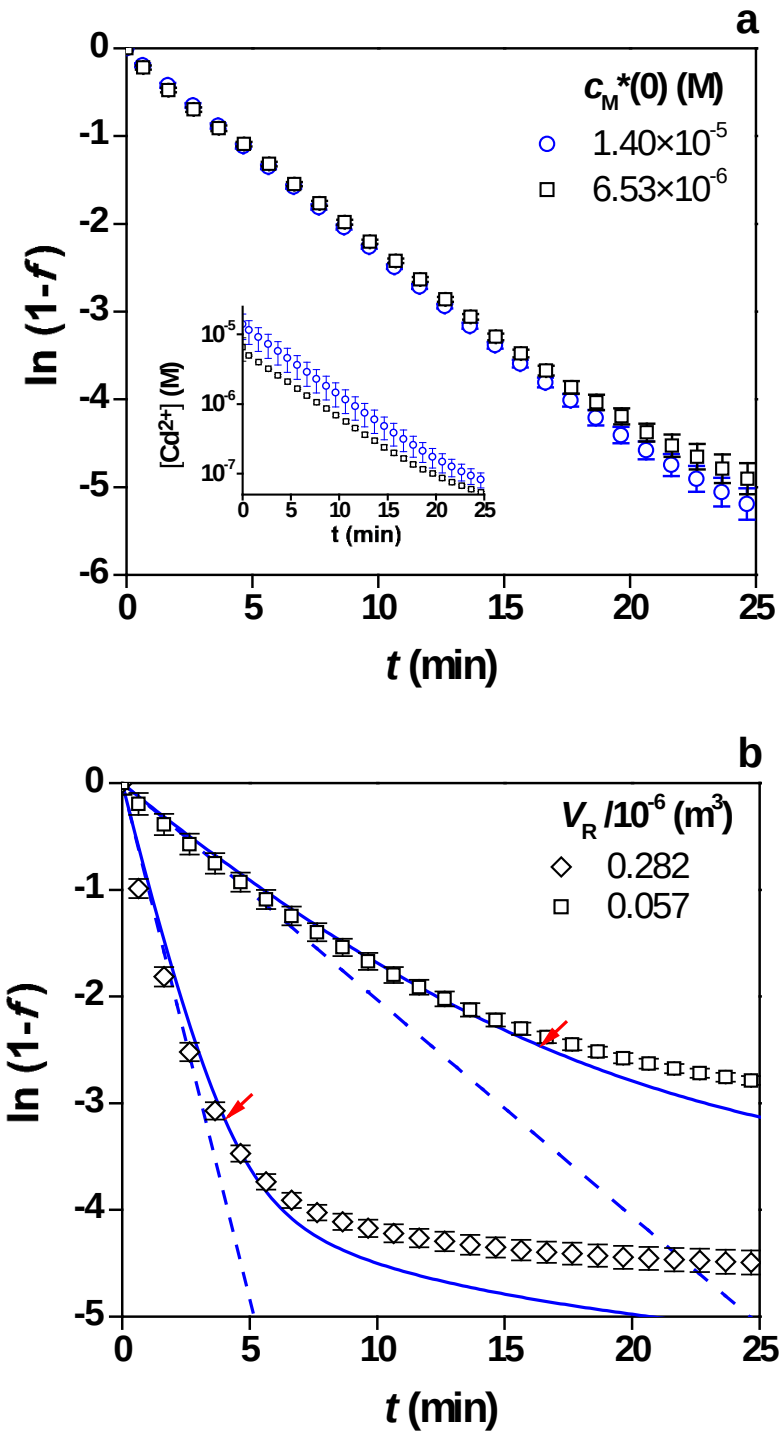

Figure 3.7. Effects of the initial metal concentration (a) and resin volume (b) on the sorption curves of Cd(II) on Chelex-100 in 0.1 M $NaNO_3$. Symbols: experimental data (average of two replicates); solid lines: MCM fits; dashed lines: FDM fittings with the same parameters. (a): $c_M^*(0)$= 1.40×10-5 M (blue circles) and 6.53×10-6 M (black squares); $m_{dry\ resin}$= 24.5 mg; pH 7.4; the inset shows the experimental raw data (error bars correspond to standard deviation of the replicates). (b): pH 4.55; $c_M^*(0)$= 5×10-5 M; $m_{dry\ resin}$= 24.5 mg (squares) and 121.2 mg (diamonds). The internal legend reports the values of V_R×10^6 (in m^3).

Let us now comment on the ability of the MCM to account for the influence of the amount of resin on the experimental kinetic profiles. As discussed in Section 3.2.3, the effect of V_R arises as a direct consequence of the mass balance constrain. Fig. 3.7b shows a representative example of the influence of a 5-fold increase in the amount of resin, compared with MCM predictions involving V_R as the only varied parameter. As expected, the increase in the volume of resin leads to an increase in the initial slope of the ln(1-*f*) plot (in absolute value), reflecting a faster kinetics. The crossover point between the predominant mechanisms of external and internal diffusion control is reached at higher *f* values, but shorter times in the experiment with the largest V_R, which is reflected by the greater curvature of the plot. In both cases, there is a good agreement between data and MCM predictions within the experimental uncertainty.

3.5.2. Impact of the stirring rate

To evaluate the influence of the hydrodynamic conditions on the sorption kinetics, a series of five experiments were performed at exactly the same experimental conditions except for the rate of the stirrer probe. A relatively high pH value (7.3) was chosen for this set of experiments to ensure conditions close to the regime of external diffusion control (see Section 3.5.3 below for details of the consequences of pH changes).

As shown in Fig. 3.8, the sorption rate increases with the stirring speed, which indicates that the overall mass transport process is, at least partially, controlled by diffusion across the external film. This effect is accurately described by the MCM (see continuous lines in Fig. 3.8) as a monotonic decrease of the DBL thickness, δ, from 43.5 to 7 μm (values listed in Tab. 3.1). Note that δ is the only fitted parameter in this series of kinetic profiles.

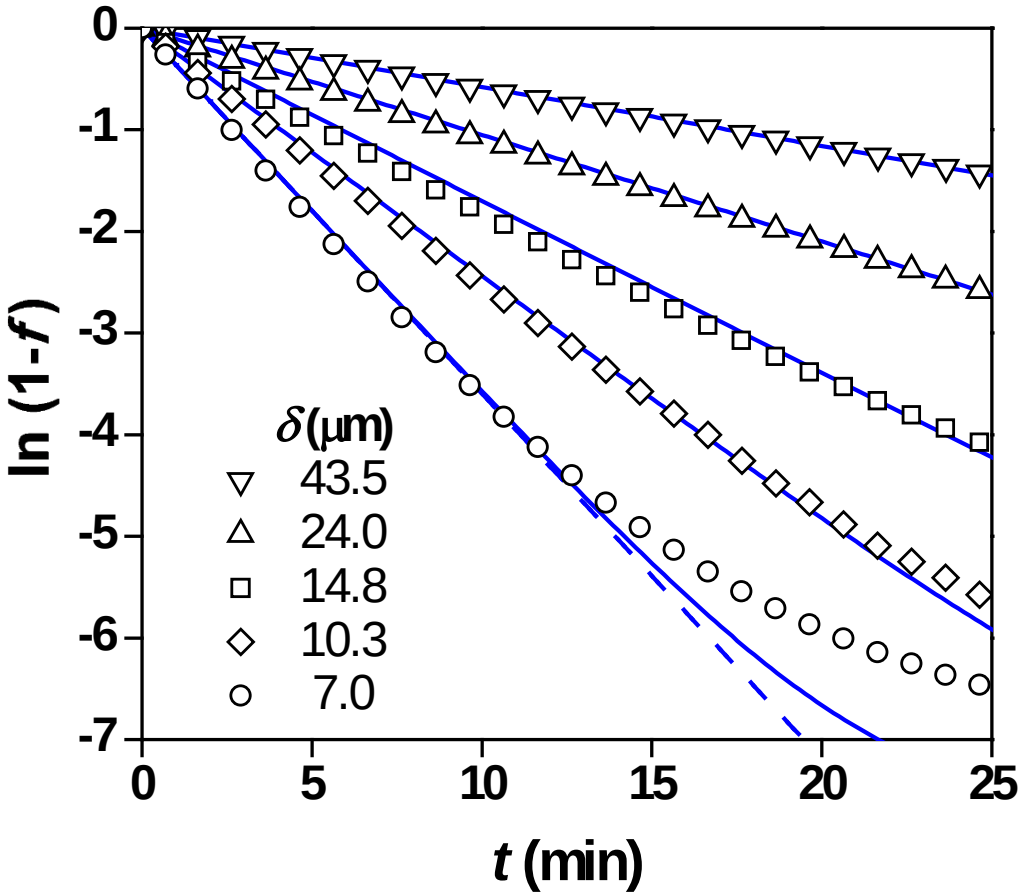

Figure 3.8. Sorption curves of Cd(II) on Chelex 100 at different stirring rates. Symbols: experimental data. Solid lines: MCM fittings. In the legend the fitted values of δ, expressed in μm, are reported, each of them corresponding to one of the available settings of the stirrer. For the sake of comparison, the curve corresponding to the highest stirring rate was also calculated with FDM, using the same parameters (dashed line). Experimental conditions: pH 7.3, I= 0.1 M in $NaNO_3$, $m_{\text{dry resin}}$= 36 mg, $c_M^*(0) = 5\times10^{-5}$ M. Experiments performed under N_2 atmosphere.

The increasing trend of the slope of ln(1-*f*) *vs*. *t* (in absolute value) with the stirring rate is due to the increased concentration gradient across the DBL (and, consequently, a larger metal flux) associated with the decline in δ, which is obviously consistent also with the predictions of FDM. However, some deviation from linearity is observed at the highest stirring speeds, where the relative contribution of the internal mass transfer resistance is largest; this behaviour can only be described by the MCM.

3.5.3. Impact of pH and ionic strength (*I*)

The influences of pH and ionic strength on the metal ion sorption kinetics are related to each other, as both variables regulate the degree of protonation of the resin which, in turn, determines: (*i*) the variation in the physical structure of the beads due to the swelling/shrinking phenomena (reflected on the values of V_R and r_0); and (*ii*) the effective metal binding properties of the resin (κ) and, indirectly, the internal diffusion coefficient $\widetilde{D}$ (see Section 3.2.3 above).

The effect of pH was first studied through a series of experiments performed at the same ionic strength and mass of dry resin in the range $3.5 \leq pH \leq 7.4$, since at pH < 3.5 the fraction of metal ion sorbed on the resin is too low (less than 1% of total Cd(II)) to allow accurate measurements of the depletion rate in bulk solution. The upper limit of pH 7.4 was selected to prevent precipitation of Cd(II) hydroxides or Cd(II) carbonates taking into account thermodynamic predictions of Visual MINTEQ.[32] This upper limit could be moved to 7.5 in the case of the experiment under N_2 atmosphere (see Fig. 3.8). The experimental results are shown in Fig. 3.9, together with MCM calculations using the parameter values listed in Tab. 3.2.

Table 3.1. Values of the parameters used to fit the curves of Fig. 3.8. All the experiments were carried out with the same mass of dry resin (36.0 mg); the stirring rates correspond to the settings of the OrionStar Series Automatic Stirrer Probe.

stirring rate	*I* (M)	*pH*	κ	D_M (m^2/s)	χ	$\tilde{D}$(m^2/s)	V_T (m^3) /10^{-6}	V_R (m^3) /10^{-6}	r_0 (m) /10^{-6}	δ (m) /10^{-6}
1	*0.1*	*7.3*	3.15×10^{8}	7×10^{-10}	6.9	7.67×10^{-18}	50.53	0.108	107	43.5
2	*0.1*	*7.3*	3.15×10^{8}	7×10^{-10}	6.9	7.67×10^{-18}	50.53	0.108	107	24.0
3	*0.1*	*7.3*	3.15×10^{8}	7×10^{-10}	6.9	7.67×10^{-18}	50.54	0.108	107	14.8
4	*0.1*	*7.3*	3.15×10^{8}	7×10^{-10}	6.9	7.67×10^{-18}	50.51	0.108	107	10.3
5	*0.1*	*7.3*	3.15×10^{8}	7×10^{-10}	6.9	7.67×10^{-18}	50.50	0.108	107	7.0

Table 3.2. Parameters used to draw the MCM curves of Figs. 3.9 and 3.10. All the experiments were carried out with the same mass of dry resin (24.5 mg) and at the same stirring rate (5).

experiment n°	*I* (M)	*pH*	κ	D_M (m^2/s)	χ	$\tilde{D}$(m^2/s)	V_T (m^3) /10^{-6}	V_R (m^3) /10^{-6}	r_0 (m) /10^{-6}	δ (m) /10^{-6}
1	*0.1*	*3.48*	3.63×10^{3}	7×10^{-10}	3.1	1.34×10^{-13}	50.65	0.046	95	7.0
2	*0.1*	*4.56*	1.21×10^{5}	7×10^{-10}	5.5	1.27×10^{-14}	50.43	0.057	101	7.0
3	*0.1*	*5.52*	5.40×10^{5}	7×10^{-10}	6.8	4.41×10^{-15}	50.46	0.064	104	7.0
4	*0.1*	*6.48*	5.55×10^{6}	7×10^{-10}	6.8	4.26×10^{-16}	50.53	0.069	107	7.0
5	*0.1*	*7.40*	3.45×10^{8}	7×10^{-10}	6.9	6.88×10^{-18}	50.30	0.069	107	7.0
6	*0.0015*	*5.52*	6.46×10^{7}	7×10^{-10}	147.2	1.70×10^{-14}	50.50	0.070	109	7.0

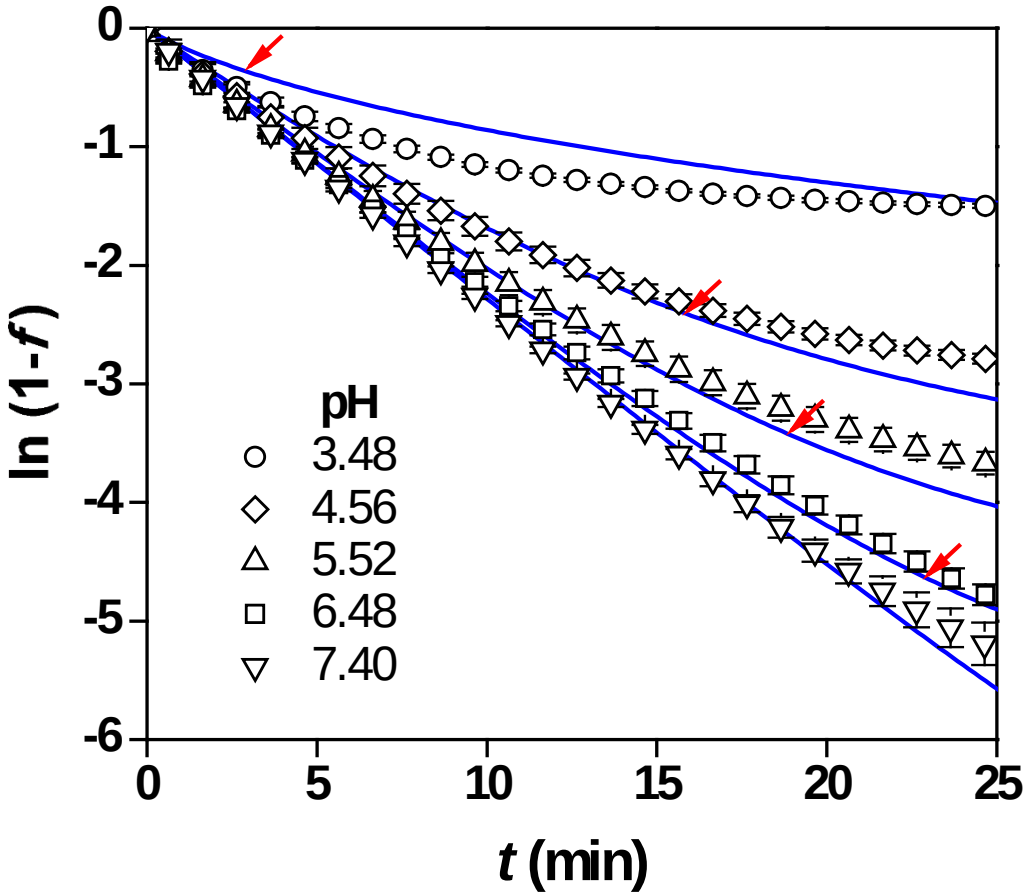

Figure 3.9. Sorption curves of Cd on Chelex 100 at different pH values (shown in the internal legend). Symbols: experimental data. Lines: MCM predictions using parameter values listed in Tab. 3.2 subject to Eq. (3.22) constraint. Experimental conditions: $c_M^*(0)$ *= 5×10-5 M (except for pH 7.40, where a concentration of 1.4×10-5 M was used to prevent precipitation), I= 0.1 M in* $NaNO_3$*,* $m_{\text{dry resin}}$ *= 24.5 mg. The experiments at pH 6.48 and 7.40 were performed in solutions buffered with 1 mM MOPS. Each experiment was performed in duplicate, and the error bars represent the standard deviation of the measurements. The arrows indicate the points where the predominant transport mechanism changes from external film to internal diffusion (i.e. values of t and f corresponding to equal values of the metal flux according to FDM and IDM).*

As seen in this figure, the overall repeatability of the measurements was good. The predictive ability of the model is remarkable, taking into account that none of the MCM parameters was specifically fitted to these data, as discussed in the following paragraphs.

The values of V_R and r_0 were determined experimentally, in absence of Cd(II), at each pH and ionic strength (as explained in Section 3.4 above), and supposed to be constant within the timescale of the experiments (consistently with the low metal/resin group

ratios experimentally tested). The values of κ and $\widetilde{D}$ were calculated at each pH as detailed in the previous sections. Finally, the diffusion layer thickness (δ = 7 μm) was taken equal to the value fitted at the corresponding stirring rate in the experiments discussed in Section 3.5.2 above. No evidences of variations of δ with pH or ionic strength were found.

The physicochemical interpretation (according to MCM) of the observed influence of pH on the sorption profiles in Fig. 3.9 follows the general ideas presented in Section 3.2.3 above. The kinetic data present a monotonic behaviour with pH, where the most sensitive parameters are κ and $\widetilde{D}$. At low pH values, the sorption rates are low with a distinct nonlinear behaviour of ln(1-*f*) *vs*. *t*. In these conditions, the net flux of metal across the resin/solution interface reaches a situation of control by internal diffusion at the early stages of the kinetic process, due to the relatively small values of $\widetilde{D}$ and concentration gradient inside the beads. The resulting kinetic profile resembles the simulations plotted in Fig. 3.4b for IDM. As pH increases, the sorption rates increase and, in the limit of high pH, they approach the linear behaviour predicted by FDM at large κ (see Figs. 3.4a and 3.4c). The relative influence of external film and internal diffusion controls throughout each kinetic run can be evidenced by the position of the crossover point between the FDM and IDM theoretical fluxes pointed by red arrows in Fig. 3.9, which are shifted to larger values of *t* and *f* as pH increases. Notice that according to FDM the slope of ln(1-*f*) should decrease with pH (the larger the number of protonated sites, the shorter the time needed to fill up the resin), while the experiments showed otherwise; this represents an important support for the application of MCM to the Cd(II)/Chelex 100 system.

The effects of the ionic strength were investigated by keeping the pH and the mass of dry resin constant, but changing the concentration of background electrolyte. Due to the preliminary nature of this study we chose to work only at two, radically different levels of *I*: 0.1 M and 0.0015 M in $NaNO_3$. A pH equal to 5.5 was selected since, according to the Gibbs-Donnan model (see Section 3.7.5 below), the largest variation in the protonation degree of Chelex 100, due to the change in *I*, takes place between pH 4.5 and 6.5. The resulting experimental curves are shown in Fig. 3.10, while the fitting parameters are listed in Tab. 3.2 (experiments 3 and 6).

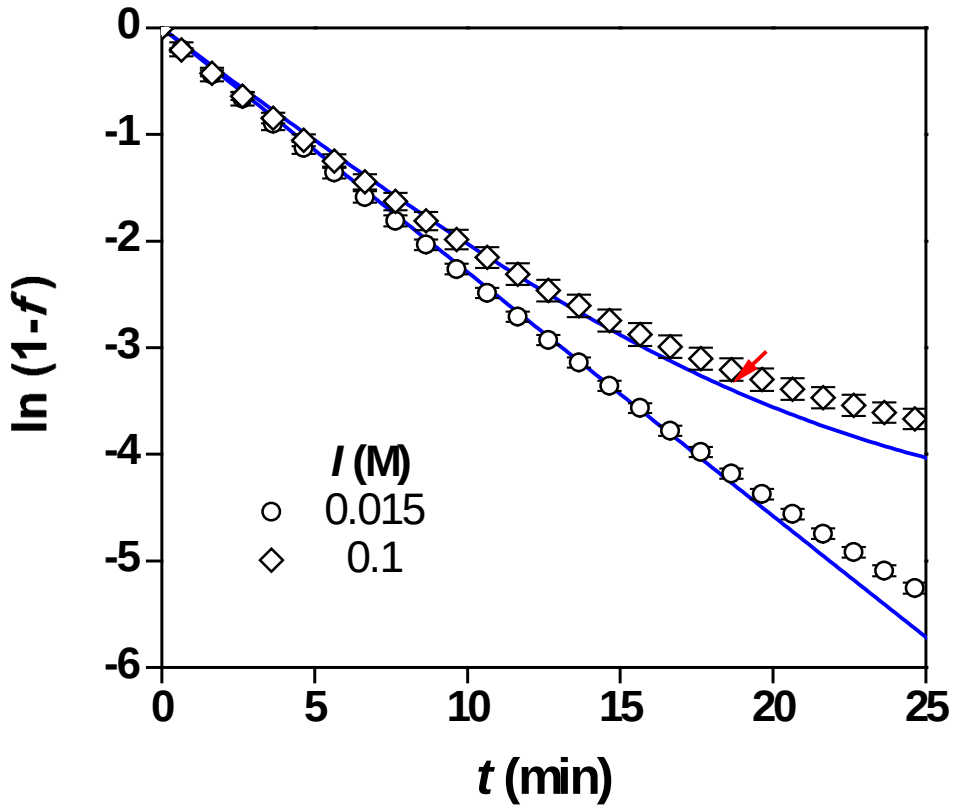

Figure 3.10. Sorption curves of Cd(II) on Chelex 100 at different ionic strengths (shown in the internal legend). Symbols: experimental data. Lines: model predictions with MCM. Experimental conditions: pH= 5.52; $m_{\text{dry resin}}$= 41.1 mg, $c_M^*(0)$= 5×10^{-5} M, background electrolyte: $NaNO_3$. The arrow indicates the point where the predominant transport mechanism changes from external film to internal diffusion. At I= 0.0015 M, the transition point lies beyond the timescale of the experiments.

At low concentration of background electrolyte, the ln(1-*f*) function behaves almost linearly (especially at short times), with a high sorption rate. This can be explained as a consequence of the reduced electrostatic screening inside the resin. The lower ionic strength induces swelling of the beads due to increased repulsion among the negatively charged iminodiacetic groups of Chelex 100 and, consequently, slightly increased values of V_R and r_0 are obtained (Tab. 3.2). These parameters have an opposite impact on the sorption rates (see Fig. 3.3) and, consequently, their combined influence on the observed effect is secondary. On the other hand, the reduced electrolyte screening at low ionic strength leads to stronger interactions of the metal ions with the active sites of the resin and, thus, to a larger partitioning coefficient at the interface (κ), which seems to be the prevailing effect (a change in two orders of magnitude is observed, as listed in Tab. 3.2). As a consequence, the kinetic curve at low ionic strength approaches the

FDM behaviour, in a similar way to the sorption rates found at higher pH. Indeed, it must be noted that the model parameters for κ and $\widetilde{D}$ at I= 0.0015 M and pH 5.52 could (from interpolation of the data listed in Tab. 3.2) correspond to those at I= 0.1 M and an approximate pH of 7.

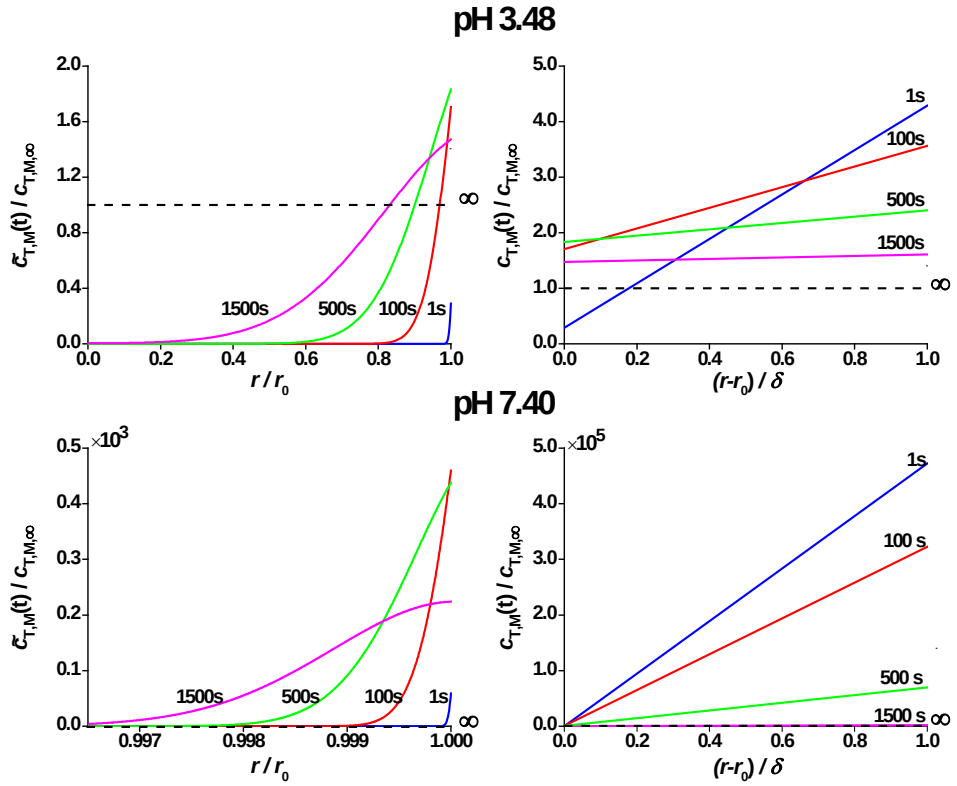

Figure 3.11. Concentration profiles of Cd(II) in the resin bead (left) and DBL (right) at pH= 3.48 (above) and 7.40 (below) at 1, 100, 500 and 1500 s. The profiles in the bead were calculated using Eq. (A3.16), while the bulk concentration was given by Eq. (A3.22). The values of the parameters are reported in Tab. 3.2. The concentration values are normalised with respect to the local equilibrium concentration, computed from Eq. (3.11) at $t \to \infty$ (dashed line).

The study of the dynamics of the local metal concentration in the system provides further insight into the controlling transport mechanisms behind the process of accumulation. Fig. 3.11 shows the normalized concentration profiles in the resin phase and in the adjacent diffusive boundary layer as a function of contact time at the lowest and highest pH values. Note that, from previous discussion, the profiles at the highest pH are also representative of equivalent systems at low ionic strength at lower pH values.

At pH= 7.40 (lower panels in Fig. 3.11) the binding affinity of the resin groups is large enough for the local concentration in the solution region adjacent to the interface to remain effectively exhausted throughout the timescale of the experiments. This means that the hypothesis of perfect sink behaviour holds and the sorption rate remains close to the value predicted by the film diffusion model. It must be pointed out that in some cases (*e.g.* 100 s and 500 s in the external layer of the resin) the local concentration reaches values not physically compatible with the number of sites. The lack of an upper concentration limit given by the saturation of the resin is an inherent flaw of the model, which may possibly explain some of the deviations from the trends experimentally observed.

The concentration profiles calculated at pH= 3.48 (upper panels in Fig. 3.11) are characteristic of a system that exhibits a transition between external film and internal diffusion control. In very initial stages (*e.g.* 1 s) there is an almost complete exhaustion of metal ions in the solution region adjacent to the interface ($c_{\mathrm{M}}\left(r_0^+, t\right) \approx 0$), and, thus, the resin bead acts as a perfect sink. As time proceeds, the increase of the concentration at $r = r_0^+$ leads to a flattening of the gradient in the DBL (see *e.g.* the profile at 100 s), which is also facilitated by the metal ion depletion in bulk solution. At subsequent stages, the metal ion profile along the DBL becomes almost flat (see *e.g.* the concentration profile at 1500 s) and the resistance to the mass transport in the external film becomes progressively smaller, whereas the internal concentration gradient is still significant and, therefore, the overall flux converges to the limiting value under control by internal diffusion.

3.6. Conclusions

An approximate analytical solution for the Mixed Control Model (MCM) (Eq. (3.15)) is here reported to describe the rate of metal ion sorption by a chelating sorbent in finite volume conditions, where the transport is limited by both internal and external diffusion. This analytical expression is accurate up to relatively large values of fractional attainment of equilibrium, and it can be easily computed even with a standard spreadsheet application.

The proposed MCM has a good descriptive and predictive capability, being able to account for the effects of several experimental variables such as pH and ionic strength with just one empirical parameter (the DBL thickness). A substantial improvement over

the classical film diffusion model (FDM) was obtained by considering the intraparticle diffusion, which can account for the deviation from the theoretical linear behaviour at low pHs and gives some insights about the physicochemical mechanisms of sorption. The effective diffusion coefficient in the resin can be computed from thermodynamic resin/solution partition ratios calculated by the Gibbs-Donnan model (see Eqs.(3.8) and (3.22)).

Precaution is advised against the extrapolation of these results to more complex systems (*e.g*. large concentrations of electrolytes leading to resin saturation, or presence of non-labile metal-ligand complexes in solution). However, the model used to describe the competition of the protons could be extended to take into account the effect of other competing ions, such as Mg(II) and Ca(II).

3.7. Appendices

3.7.1. Mathematical formulation of the mixed control model (MCM)

ASSUMPTIONS OF THE MODEL

a) Diffusion in the film around the particle instantaneously reaches steady state at any moment from upon introduction of the resin beads (of radius r_0) into the solution with initial bulk concentration $c_{\mathrm{M}}(t=0, r>r_1) = c_{\mathrm{M}}^{*}(t=0)$. The metal concentration profile in the film is

$$c_{\mathrm{M}}(r) = \frac{1}{r}\left(\frac{c_{\mathrm{M}}^{*} - c_{\mathrm{M}}(r_0)}{1/r_0 - 1/r_1}\right) + \frac{r_1 c_{\mathrm{M}}^{*} - r_0 c_{\mathrm{M}}(r_0)}{r_1 - r_0} \qquad \text{(A3.1)}$$

where r_1 is the distance at which bulk concentration is restored (*i.e.* the film thickness is r_1-r_0).

Thus, the flux is given by

$$J = D_{\mathrm{M}}\left(\frac{1}{r_0} + \frac{1}{r_1 - r_0}\right)\left(c_{\mathrm{M}}^{*}(t) - c_{\mathrm{M}}^{0}\right) = D_{\mathrm{M}}\frac{c_{\mathrm{M}}^{*}(t) - c_{\mathrm{M}}(r_0, t)}{\delta} \qquad \text{(A3.2)}$$

where D_{M} is the diffusion coefficient of free metal in solution and δ is the effective thickness of the Diffusive Boundary Layer (DBL).

b) The concentrations of the free metal inside the beads, $\tilde{c}_{\mathrm{M,free}}(r,t)$, and of the metal bound to the resin functional groups, $\tilde{c}_{\mathrm{MR}}(r,t)$, are related via an equilibrium relationship (*i.e.* MR species acts as a fully labile complex):

$$\tilde{c}_{\mathrm{MR}}(r,t) = \tilde{K}_{\mathrm{MR}}\,\tilde{c}_{\mathrm{R}}(r,t)\,\tilde{c}_{\mathrm{M,free}}(r,t) \qquad \text{(A3.3)}$$

where $\tilde{c}_{\mathrm{R}}(r,t)$ stands for the concentration of free resin sites.

c) The resin sites are in excess with respect to the metal concentration, so that $\tilde{c}_{\mathrm{R}}(r,t) \approx \tilde{c}_{\mathrm{R}}$ can be taken as constant.

The total concentration can be expressed as

$$\tilde{c}_{\mathrm{T,M}}(r,t) = \tilde{c}_{\mathrm{M,free}}(r,t) + \tilde{c}_{\mathrm{MR}}(r,t) = \tilde{c}_{\mathrm{M,free}}(r,t)\left(1 + \tilde{K}_{\mathrm{MR}}\,\tilde{c}_{\mathrm{R}}\right) \qquad \text{(A3.4)}$$

DERIVATION OF THE RULING EQUATION FOR MCM

The continuity equation for the free metal inside the beads can be written as

$$\frac{\partial \tilde{c}_{\mathrm{M,free}}(r,t)}{\partial t} = \tilde{D}_{\mathrm{M}} \nabla^2 \tilde{c}_{\mathrm{M,free}}(r,t) + \tilde{k}_{\mathrm{d}}\, \tilde{c}_{\mathrm{MR}}(r,t) - \tilde{k}_{\mathrm{a}}\, \tilde{c}_{\mathrm{R}}\, \tilde{c}_{\mathrm{M,free}}(r,t) \qquad r < r_0 \tag{A3.5}$$

while the continuity equation for the bound metal can be written as

$$\frac{\partial \tilde{c}_{\mathrm{MR}}(r,t)}{\partial t} = \tilde{D}_{\mathrm{MR}} \nabla^2 \tilde{c}_{\mathrm{M,free}}(r,t) - \tilde{k}_{\mathrm{d}}\, \tilde{c}_{\mathrm{MR}}(r,t) + \tilde{k}_{\mathrm{a}}\, \tilde{c}_{\mathrm{R}}\, \tilde{c}_{\mathrm{M,free}}(r,t) \qquad r < r_0 \tag{A3.6}$$

where $\tilde{D}_{\mathrm{M}}$, the diffusion coefficient in the resin phase, is defined as in (3.8). By combining the two previous equations, the kinetic terms cancel out:

$$\frac{\partial \tilde{c}_{\mathrm{T,M}}(r,t)}{\partial t} = \left(\frac{\tilde{D}_{\mathrm{M}}}{1 + \tilde{K}_{\mathrm{MR}} \tilde{c}_{\mathrm{R}}} \right) \nabla^2 \tilde{c}_{\mathrm{T,M}}(r,t) = \tilde{D}\, \nabla^2 \tilde{c}_{\mathrm{T,M}}(r,t) \tag{A3.7}$$

which will be solved with the initial condition

$$\tilde{c}_{\mathrm{T,M}}(r, t=0) = 0 \qquad \forall r \le r_0 \tag{A3.8}$$

and the following boundary conditions:

i) at the centre of the bead:

$$\left(\frac{\partial \tilde{c}_{\mathrm{T,M}}}{\partial r} \right)_{r=0} = 0 \qquad r = 0 \quad \forall t \tag{A3.9}$$

ii) the partitioning of metal concentration at the bead surface:

$$\tilde{c}_{\mathrm{T,M}}(r_0^-, t) = \kappa\, c_{\mathrm{M}}(r_0^+, t) \tag{A3.10}$$

iii) the continuity of fluxes at the bead surface:

$$J = \tilde{D} \left(\frac{\partial \tilde{c}_{\mathrm{T,M}}}{\partial r} \right)_{r=r_0^-} = D_{\mathrm{M}} \left(\frac{\partial c_{\mathrm{M}}}{\partial r} \right)_{r=r_0^+} = D_{\mathrm{M}} \frac{c_{\mathrm{M}}^*(t) - c_{\mathrm{M}}(r_0^+, t)}{\delta} \tag{A3.11}$$

Introducing the variable

$$\mu(r,t) = r\, \tilde{c}_{\mathrm{T,M}}(r,t) \tag{A3.12}$$

and applying Laplace transform to Eq.(3.7) with the initial condition (3.9) yields

$$s \bar{\mu}(r;s) = \tilde{D} \frac{d^2 \bar{\mu}(r;s)}{dr^2} \tag{A3.13}$$

where variables with overbar belong to the Laplace space.

The boundary condition (3.10) becomes

$$\bar{\mu}(0;s) = 0 \tag{A3.14}$$

and the boundary condition (3.11) becomes

$$\bar{\mu}\left(r_0^-;s\right) = \kappa\, r_0 \bar{c}_{\mathrm{M}}\left(r_0^+;s\right) \tag{A3.15}$$

The solution of the differential equation (A3.13) is

$$\bar{\tilde{c}}_{\mathrm{T,M}}\left(r;s\right) = \frac{r_0}{r}\kappa \bar{c}_{\mathrm{M}}\left(r_0^+;s\right)\frac{\sinh\left(\sqrt{\frac{s}{\tilde{D}}}r\right)}{\sinh\left(\sqrt{\frac{s}{\tilde{D}}}r_0\right)} \tag{A3.16}$$

So, the number of moles inside the resin is given by the integral:

$$\bar{\tilde{n}}(s) = z\int_0^{r_0} r_0\kappa \bar{c}_{\mathrm{M}}\left(r_0^+;s\right)\frac{\sinh\left(\sqrt{\frac{s}{\tilde{D}}}r\right)}{\sinh\left(\sqrt{\frac{s}{\tilde{D}}}r_0\right)}4\pi r dr = 3V_{\mathrm{R}}\kappa \bar{c}_{\mathrm{M}}\left(r_0^+;s\right)\frac{\sqrt{\frac{s}{\tilde{D}}}r_0\cosh\left(\sqrt{\frac{s}{\tilde{D}}}r_0\right)-\sinh\left(\sqrt{\frac{s}{\tilde{D}}}r_0\right)}{\frac{s}{\tilde{D}}r_0^2\sinh\left(\sqrt{\frac{s}{\tilde{D}}}r_0\right)} \tag{A3.17}$$

where z is the number of resin beads, so that $V_{\mathrm{R}} = z\frac{4}{3}\pi r_0^3$.

Now, substituting (A3.16) into the relation of the equality of fluxes (3.12), we can write:

$$D_{\mathrm{M}}\frac{\bar{c}_{\mathrm{M}}^*(s)-\bar{c}_{\mathrm{M}}\left(r_0^+;s\right)}{\delta} = \tilde{D}\frac{d}{dr}\left(\frac{r_0}{r}\kappa \bar{c}_{\mathrm{M}}\left(r_0^+;s\right)\frac{\sinh\left(\sqrt{\frac{s}{\tilde{D}}}r\right)}{\sinh\left(\sqrt{\frac{s}{\tilde{D}}}r_0\right)}\right)_{r=r_0} \tag{A3.18}$$

which can be rearranged to obtain the concentration in bulk solution:

$$\bar{c}_{\mathrm{M}}^*(s) = \bar{c}_{\mathrm{M}}\left(r_0^+;s\right)\left\{1+\frac{\tilde{D}\delta\kappa}{D_{\mathrm{M}}}\left[\sqrt{\frac{s}{\tilde{D}}}\coth\left(\sqrt{\frac{s}{\tilde{D}}}r_0\right)-\frac{1}{r_0}\right]\right\} \tag{A3.19}$$

Due to the consideration of a finite volume of solution, an additional constrain is the mass balance, which can be written as

$$\left(V_{\mathrm{T}}-V_{\mathrm{R}}\right)c_{\mathrm{M}}^*(0) = \frac{3V_{\mathrm{R}}}{r_0^3}\int_0^{r_0}\tilde{c}_{\mathrm{T,M}}(r,t)\,r^2 dr + c_{\mathrm{M}}^*(t)\left(V_{\mathrm{T}}-V_{\mathrm{R}}\right) \tag{A3.20}$$

if one assumes that the free metal concentration is constant for any $r>r_0$. A more detailed consideration of the mass balance is discussed in Section 3.7.2 below.

Taking into account (A3.17) and (A3.19), we can write:

$$\left(V_{\mathrm{T}}-V_{\mathrm{R}}\right)\frac{c_{\mathrm{M}}^{*}(0)}{s}=3V_{\mathrm{R}}\kappa\overline{c}_{\mathrm{M}}\left(r_{0}^{+};s\right)\left\{\frac{\sqrt{\frac{s}{\tilde{D}}}r_{0}\cosh\left(\sqrt{\frac{s}{\tilde{D}}}r_{0}\right)-\sinh\left(\sqrt{\frac{s}{\tilde{D}}}r_{0}\right)}{\frac{s}{\tilde{D}}r_{0}^{2}\sinh\left(\sqrt{\frac{s}{\tilde{D}}}r_{0}\right)}\right\}+ \tag{A3.21}$$

$$+\left(V_{\mathrm{T}}-V_{\mathrm{R}}\right)\overline{c}_{\mathrm{M}}\left(r_{0}^{+};s\right)\left\{1+\frac{\tilde{D}\delta\kappa}{D_{\mathrm{M}}}\left[\sqrt{\frac{s}{\tilde{D}}}\coth\left(\sqrt{\frac{s}{\tilde{D}}}r_{0}\right)-\frac{1}{r_{0}}\right]\right\}$$

which can be rearranged to obtain the Laplace transform of the bulk concentration:

$$\overline{c}_{\mathrm{M}}^{*}(s)=\frac{\left(V_{\mathrm{T}}-V_{\mathrm{R}}\right)c_{\mathrm{M}}^{*}(0)}{s\left\{\frac{3V_{\mathrm{R}}\kappa\left[\frac{\coth\left(\sqrt{\frac{s}{\tilde{D}}}r_{0}\right)}{\sqrt{\frac{s}{\tilde{D}}}r_{0}}-\frac{\tilde{D}}{sr_{0}^{2}}\right]}{1+\frac{\tilde{D}\delta\kappa}{D_{\mathrm{M}}r_{0}}\left[r_{0}\sqrt{\frac{s}{\tilde{D}}}\coth\left(\sqrt{\frac{s}{\tilde{D}}}r_{0}\right)-1\right]}+V_{\mathrm{T}}-V_{\mathrm{R}}\right\}} \tag{A3.22}$$

This equation can be inverted numerically (in the body of this chapter we have referred to the corresponding solution as the "numerical solution of the exact equation").
The analytical inversion of Eq. (A3.22) has been reported as:[12]

$$f\left(t\right)=1-6\sum_{n=1}^{\infty}\frac{\mathrm{e}^{-\frac{\tilde{D}t}{r_{0}^{2}}p_{n}^{2}}}{9w+\frac{1}{w+1}\left(p_{n}^{2}+\frac{p_{n}^{4}}{Bi_{\mathrm{m}}^{2}}\right)-\left(\frac{6w+1}{w+1}\right)\frac{p_{n}^{2}}{Bi_{\mathrm{m}}}} \tag{A3.23}$$

where p_n is the nth positive root of

$$\frac{\tan\left(p_{n}\right)}{p_{n}}=\frac{3-\frac{p_{n}^{2}}{wBi_{\mathrm{m}}}}{3+\frac{\left(Bi_{\mathrm{m}}-1\right)p_{n}^{2}}{wBi_{\mathrm{m}}}} \tag{A3.24}$$

Bi_{m} is the mass transfer Biot number,[33] which compares the relative influence of intraparticle and external film resistance to the metal diffusion:

$$Bi_{\mathrm{m}}=\frac{D_{\mathrm{M}}r_{0}}{\delta\tilde{D}\kappa} \tag{A3.25}$$

and w is the capacity parameter or partition ratio:[34,35]

$$w \equiv \frac{\textit{moles in beads at equilibrium}}{\textit{moles still in solution at equilibrium}} = \frac{V_R \kappa}{V_T - V_R} \tag{A3.26}$$

In some instances, in particular for large values of κ, the computation of the exact analytical solution (A3.23) takes a relatively long time.

NEW ANALYTICAL APPROXIMATION

If we take

$$\coth\left(\sqrt{\frac{s}{\widetilde{D}}} r_0\right) \approx 1 \tag{A3.27}$$

Eq. (A3.22) simplifies to:

$$\overline{c}_M^*(s) = \frac{\left(V_T - V_R\right) c_M^*(0)}{s\left\{\dfrac{3V_R\kappa\left[\dfrac{1}{r_0}\sqrt{\dfrac{\widetilde{D}}{s}} - \dfrac{\widetilde{D}}{s r_0^2}\right]}{1 + \dfrac{\widetilde{D}\delta\kappa}{D_M r_0}\left[r_0\sqrt{\dfrac{s}{\widetilde{D}}} - 1\right]} + V_T - V_R\right\}} \tag{A3.28}$$

The Eq. above simplifies to

$$\overline{c}_M^*(s) = \frac{1}{s}\frac{(1 - Bi_m)x - 1}{3Bi_m w x^3 - 3Bi_m w x^2 + (1 - Bi_m) - 1} \tag{A3.29}$$

in terms of the dimensionless parameters Bi_m from (3.17), w defined in (A3.26) and

$$x = \frac{\sqrt{\widetilde{D}}}{r_0\sqrt{s}} \tag{A3.30}$$

The factorization of the denominator of (A3.29) leads to the summation:

$$\overline{c}_M^*(s) = \frac{c_M^*(0)}{3Bi_m w}\left[\frac{(1 - Bi_m)R_1 - 1}{s(R_1 - R_2)(R_1 - R_3)(x - R_1)} + \frac{1 - (1 - Bi_m)R_2}{s(R_1 - R_2)(R_2 - R_3)(x - R_2)} + \right.$$
$$\left. + \frac{(1 - Bi_m)R_3 - 1}{s(R_1 - R_3)(R_3 - R_2)(x - R_3)}\right] \tag{A3.31}$$

where the factors R_1, R_2 and R_3 are the roots of:

$$x^3 - x^2 + \frac{1 - Bi_m}{3Bi_m w}x - \frac{1}{3Bi_m w} = 0 \tag{A3.32}$$

Now, if s is made explicit through (A3.30), each of the three terms composing (A3.31) can be exactly inverted, as it is detailed here for the first term:

$$L^{-1}\left\{\frac{(Bi_{\mathrm{m}}-1)R_1+1}{R_1(R_1-R_2)(R_1-R_3)}\frac{1}{s-\frac{\sqrt{\widetilde{D}s}}{r_0R_1}}\right\}=\frac{(Bi_{\mathrm{m}}-1)R_1+1}{R_1(R_1-R_2)(R_1-R_3)}\mathrm{e}^{\frac{\widetilde{D}}{r_0^2R_1^2}t}\,\mathrm{Erfc}\left(-\frac{\sqrt{\widetilde{D}t}}{r_0R_1}\right) \quad \text{(A3.33)}$$

For the sake of simplicity in the notation, we define:

$$F(x)=\mathrm{e}^{x^2}\,\mathrm{Erfc}(x) \quad \text{(A3.34)}$$

From the linearity property of the Laplace transform, (A3.31) can, thus, be rewritten as:

$$\begin{aligned}c_{\mathrm{M}}^{*}(t)=\frac{c_{\mathrm{M}}^{*}(0)}{3Bi_{\mathrm{m}}w}\Bigg[&\frac{(Bi_{\mathrm{m}}-1)R_1+1}{R_1(R_1-R_2)(R_1-R_3)}F\left(-\frac{\sqrt{\widetilde{D}t}}{r_0R_1}\right)+\\&+\frac{(Bi_{\mathrm{m}}-1)R_2+1}{R_2(R_1-R_2)(R_3-R_2)}F\left(-\frac{\sqrt{\widetilde{D}t}}{r_0R_2}\right)\\&+\frac{(Bi_{\mathrm{m}}-1)R_3+1}{R_3(R_1-R_3)(R_2-R_3)}F\left(-\frac{\sqrt{\widetilde{D}t}}{r_0R_3}\right)\Bigg]\end{aligned} \quad \text{(A3.35)}$$

In the codes given at the end of this chapter we refer to this equation as the "analytical solution of the approximate equation".

The fractional attainment of equilibrium is defined as the ratio between the instantaneous and final (at equilibrium) amounts of metal sorbed in the resin:

$$f=\frac{c_{\mathrm{M}}^{*}(0)-c_{\mathrm{M}}^{*}(t)}{c_{\mathrm{M}}^{*}(0)-c_{\mathrm{M}}^{*}(\infty)} \quad \text{(A3.36)}$$

The analytical approximate equation for *f* in MCM can be readily derived:

$$\begin{aligned}f(t)=\frac{w+1}{w}\Bigg\{1-\frac{1}{3Bi_{\mathrm{m}}w}\Bigg[&\frac{(Bi_{\mathrm{m}}-1)R_1+1}{R_1(R_1-R_2)(R_1-R_3)}F\left(-\frac{\sqrt{\widetilde{D}t}}{r_0R_1}\right)+\\&+\frac{(Bi_{\mathrm{m}}-1)R_2+1}{R_2(R_1-R_2)(R_3-R_2)}F\left(-\frac{\sqrt{\widetilde{D}t}}{r_0R_2}\right)+\frac{(Bi_{\mathrm{m}}-1)R_3+1}{R_3(R_1-R_3)(R_2-R_3)}F\left(-\frac{\sqrt{\widetilde{D}t}}{r_0R_3}\right)\Bigg]\Bigg\}\end{aligned} \quad \text{(A3.37)}$$

The flux across the interface can be derived from the equality between the number of moles entering the beads and the variation in the number of moles in solution:

$$zJ\,4\pi r_0^2=\left(V_{\mathrm{T}}-V_{\mathrm{R}}\right)\frac{dc_{\mathrm{M}}^{*}(t)}{dt} \quad \text{(A3.38)}$$

So, from the exact solution (A3.23), the following equation can be readily derived:

$$J = \frac{2\tilde{D}\left(V_{\mathrm{T}} - V_{\mathrm{R}}\right)}{r_0 V_{\mathrm{R}}}\left(c_{\mathrm{M}}^{*}(0) - c_{\mathrm{M}}^{*}(\infty)\right)\sum_{n=1}^{\infty}\frac{p_n^2\, \mathrm{e}^{-\frac{\tilde{D}t}{r_0^2}p_n^2}}{9w + \frac{1}{w+1}\left(p_n^2 + \frac{p_n^4}{Bi_{\mathrm{m}}^2}\right) - \left(\frac{6w+1}{w+1}\right)\frac{p_n^2}{Bi_{\mathrm{m}}}} \qquad \text{(A3.39)}$$

3.7.2. Contribution of the metal in the DBL to the mass balance according to two variants of the MCM

The variant of the MCM used in the previous sections (which could be called the "simple MCM") assumes that the concentration of metal is constant from the bead/solution interface to the bulk solution (*i.e.* $c_{\mathrm{M}}(r,t) = c_{\mathrm{M}}^{*}(t)$ for $r \geq r_0$). This translates into the number of moles in solution participating in the mass balance equation (A3.20). This assumption is obviously correct when the amount of metal ions in the DBL is negligible in comparison with the total amount of metal in solution. Although this can be true in most experimental cases, we detail now a "refined" MCM that circumvents this assumption.

The total number of moles in the boundary films can be obtained by integrating Eq. (A3.1) between r_0 and r_1 and multiplying by z, the number of beads:

$$n_{\mathrm{film}} = \frac{2}{3}z\pi r_0(2r_0 + r_1)(r_1 - r_0)c_{\mathrm{M}}(r_0) + \frac{2}{3}z\pi r_1(r_0 + 2r_1)(r_1 - r_0)c_{\mathrm{M}}^{*} \qquad \text{(A3.40)}$$

The coefficients $\frac{2}{3}z\pi r_0(2r_0 + r_1)(r_1 - r_0)$ and $\frac{2}{3}z\pi r_1(r_0 + 2r_1)(r_1 - r_0)$ can be physically interpreted as two virtual volumes, which will be called g_1 and g_2, where the metal concentration is constant and equal, respectively, to $c_{\mathrm{M}}\left(r_0^{+}, t\right)$ (metal concentration at the interface outside the bead) and to $c_{\mathrm{M}}^{*}(t)$ (metal concentration in the bulk), see Fig. A3.1.

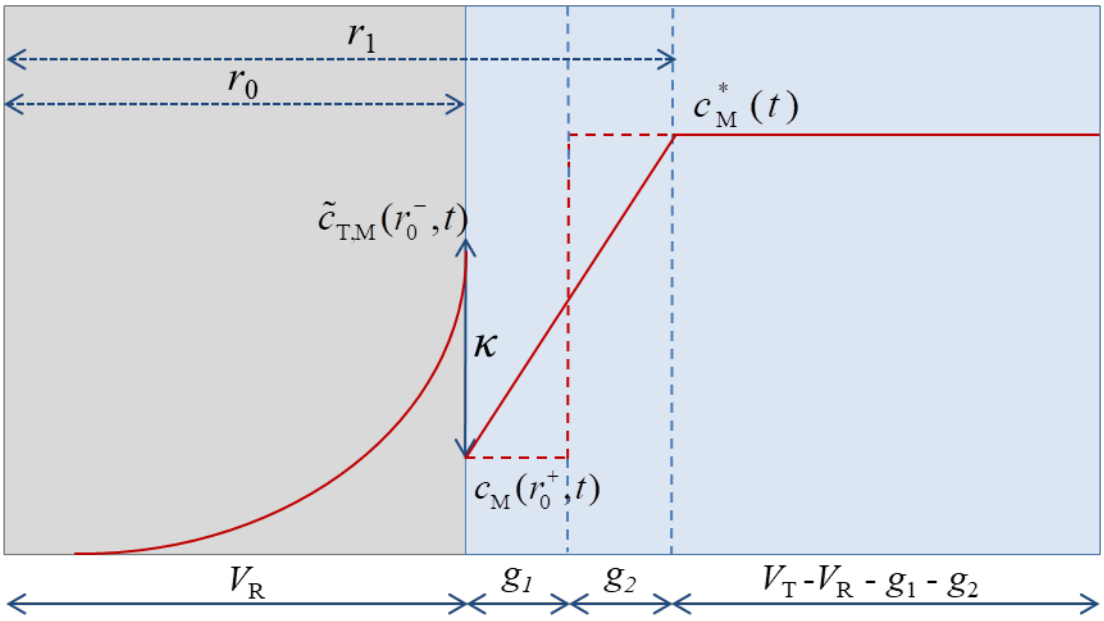

Figure A3.1. Outline of concentration profiles inside and outside the resin bead. The solid red line represents the actual concentration, while the dashed red line represents the concentration modelled considering the virtual volumes g_1 *and* g_2*. The bottom line indicates the volume of each region.*

If the moles present in the film are taken into account in the mass balance, (A3.22) becomes:

$$\bar{c}_M^*(s) = \frac{(V_T - V_R)c_M^*(0)}{s\left\{\dfrac{g_1 + 3V_R\kappa\left[\dfrac{\coth\left(\sqrt{\dfrac{s}{\tilde{D}}}r_0\right)}{\sqrt{\dfrac{s}{\tilde{D}}}r_0} - \dfrac{\tilde{D}}{sr_0^2}\right]}{1 + \dfrac{\tilde{D}\delta\kappa}{D_M r_0}\left[r_0\sqrt{\dfrac{s}{\tilde{D}}}\coth\left(\sqrt{\dfrac{s}{\tilde{D}}}r_0\right) - 1\right]} + V_T - V_R - g_1\right\}} \qquad \text{(A3.41)}$$

This equation for the metal concentration in the bulk, in the Laplace space, can be back-transformed numerically or analytically, under the assumption (A3.27). The form of the approximate solution is exactly the same as in the "simplified MCM" (Eq. (A3.35)) except that the third degree equation to be solved (Eq. (A3.42)) to find the roots R_1, R_2 and R_3 is more involved than (3.16). Additionally, the use of g_1 precludes the exclusive use of dimensionless grouping of constants such as the Biot number (Bi_m) or the partition ratio w. Specifically, R_1, R_2 and R_3 to be used in the "refined MCM" are the roots of the equation:

$$x^3 - x^2 + \left[\frac{v-1}{3\kappa v} - \frac{\varepsilon\rho}{3}\left(\frac{3\rho - 2\rho^2}{2(1-\rho)^2} + \frac{v-1}{v} \right) \right] x + \frac{\varepsilon\rho}{3}\left(\frac{3\rho - 2\rho^2}{2(1-\rho)^2} + \frac{v-1}{v} \right) = 0 \qquad \text{(A3.42)}$$

where $v = \frac{V_R}{V_T}$, $\varepsilon = \frac{\widetilde{D}}{D_M}$ and $\rho = \frac{\delta}{r_0}$.

The code to implement these analytical solutions is given in Section 3.8 below).

Despite taking into account the contribution of the metal in the DBL, even this refined solution carries one inconsistency. In fact, according to this model, at t= 0 the metal concentration in g_1 is assumed to be 0, which means that the DBL is already partially depleted. As a consequence, a certain amount of metal is missing from the mass balance, which causes the bulk concentration to have slightly negative values at very short times, although this fact is not relevant for actual experimental conditions.

The contribution of g_1 was found to be negligible in all the real cases considered so far; however, it could be significant for large values of δ and volume of sorbent material, as exemplified in the following figures:

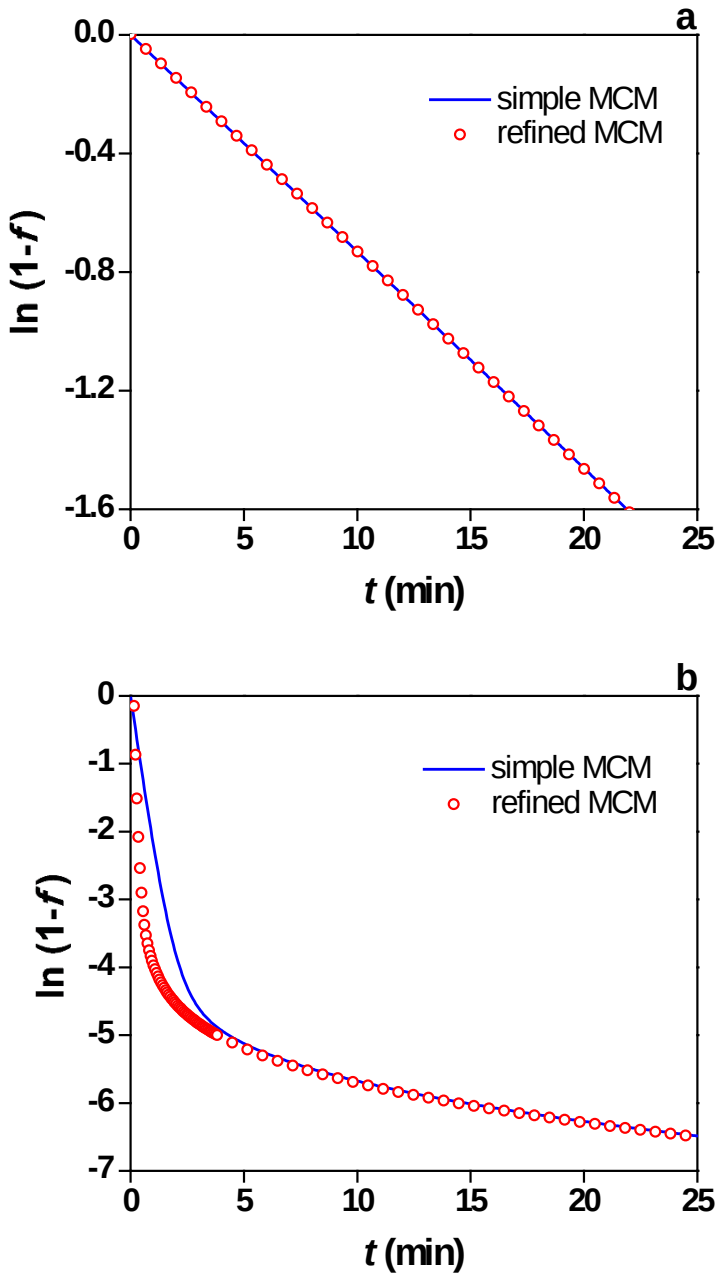

Figure A3.2. Sorption curves of Cd on Chelex 100, computed with the "refined" MCM, which takes into account the contribution of g_1 (red circles) or the "simple" one (solid blue line). In panel a, the parameters selected for the computations are those corresponding to the experiment performed at the lowest stirring rate and largest δ (rate "1", reported in Tab. 3.1); in panel b, the parameters are those of experiment nº1 (Tab. 3.2), but with $\delta = 7\times10^{-5}$ m and $V_R = 4.6\times10^{-6}$ m^3.

While conditions like those represented in figure A3.2b can be difficultly met working with stirred batch solutions, they may become realistic in the case of packed columns with sufficiently slow flow rate.

3.7.3. FDM (Film Diffusion Model)

FDM assumes that intraparticle diffusion is not limiting, and the overall transport rate is just determined by diffusion through the DBL. As a result, the concentration profiles $\tilde{c}^{*}_{\mathrm{T,M}}(t)$ for the total metal inside the bead are flat. Two variants of the model are available, one for infinite volume conditions (proposed by Boyd to describe isotopic exchange on organic zeolites[7]) and the other for finite volume conditions (with parallels in the works of Pinheiro[36] and Hajdu[37]).

INFINITE VOLUME CONDITIONS

As depletion in solution is negligible, the bulk condition at distance r_1 is independent from time:

$$c_{\mathrm{M}}(r_1,t) = c^{*}_{\mathrm{M}} \tag{A3.43}$$

Diffusion in the "film" instantaneously reaches steady state (SS). Thus, the flux is given by

$$J = D_{\mathrm{M}}\left(\frac{1}{r_0}+\frac{1}{r_1-r_0}\right)\left(c^{*}_{\mathrm{M}} - c_{\mathrm{M}}\left(r_0^{+},t\right)\right) = D_{\mathrm{M}}\frac{c^{*}_{\mathrm{M}} - c_{\mathrm{M}}\left(r_0^{+},t\right)}{\delta} \tag{A3.44}$$

The partition at the interface prescribes

$$c_{\mathrm{M}}\left(r_0^{+},t\right) = \frac{\tilde{c}^{*}_{\mathrm{T,M}}(t)}{\kappa} \tag{A3.45}$$

Inside the particle, the concentration is uniform:

The variation with time in the number of moles inside the particle equals the product of the flux times the area of the particle:

$$\frac{d}{dt}\left(\frac{4}{3}\pi r_0^{3}\tilde{c}^{*}_{\mathrm{T,M}}(t)\right) = \frac{D_{\mathrm{M}}\left(c^{*}_{\mathrm{M}} - \dfrac{\tilde{c}^{*}_{\mathrm{T,M}}(t)}{\kappa}\right)}{\delta}4\pi r_0^{2} \tag{A3.46}$$

Integrating from t= 0 to t it leads to:

$$1 - \frac{\tilde{c}^{*}_{\mathrm{T,M}}(t)}{\kappa c^{*}_{\mathrm{M}}} = \exp\left(-\frac{3D_{\mathrm{M}}}{\delta r_0 \kappa}t\right) \tag{A3.47}$$

Given the absence of depletion, the definition of “fractional attainment of equilibrium” (Eq. (A3.36)) becomes:

$$f \equiv \frac{\tilde{c}^*_{\mathrm{T,M}}(t)}{\tilde{c}^*_{\mathrm{T,M}}(\infty)} = \frac{\tilde{c}^*_{\mathrm{T,M}}(t)}{\kappa c^*_{\mathrm{M}}} \tag{A3.48}$$

Combining previous Eqs. (A3.47) and (A3.48) leads to:

$$\ln(1-f) = -\frac{3D_{\mathrm{M}}}{\delta r_0 \kappa} t \tag{A3.49}$$

FINITE VOLUME CONDITIONS

As the bulk metal concentration changes with time we will need to consider the complete mass balance (neglecting the depletion of free metal in the DBL, as in the simple MCM, see Section 3.7.2):

$$(V_{\mathrm{T}} - V_{\mathrm{R}}) c^*_{\mathrm{M}}(t=0) = (V_{\mathrm{T}} - V_{\mathrm{R}}) c^*_{\mathrm{M}}(t) + V_{\mathrm{R}} \bar{c}^*_{\mathrm{T,M}}(t) \tag{A3.50}$$

While, with the introduction of the time dependence, Eq. (A3.46) becomes:

$$\frac{d}{dt}\left(\frac{4}{3}\pi r_0^3 \tilde{c}^*_{\mathrm{T,M}}(t)\right) = \frac{D_{\mathrm{M}}\left(c^*_{\mathrm{M}}(t) - \dfrac{\tilde{c}^*_{\mathrm{T,M}}(t)}{\kappa}\right)}{\delta} 4\pi r_0^2 \tag{A3.51}$$

Use of the mass balance in (A3.51) leads to:

$$J = \frac{d}{dt}\left(\frac{r_0}{3}\tilde{c}^*_{\mathrm{T,M}}(t)\right) = \frac{D_{\mathrm{M}}\left(c^*_{\mathrm{M}}(t=0) - \left(\dfrac{V_{\mathrm{R}}}{V_{\mathrm{T}} - V_{\mathrm{R}}} + \dfrac{1}{\kappa}\right)\tilde{c}^*_{\mathrm{T,M}}(t)\right)}{\delta} = \frac{D_{\mathrm{M}}\left(c^*_{\mathrm{M}}(t=0) - \dfrac{\tilde{c}^*_{\mathrm{T,M}}(t)}{\kappa'}\right)}{\delta} \tag{A3.52}$$

where

$$\frac{1}{\kappa'} = \frac{V_{\mathrm{R}}}{V_{\mathrm{T}} - V_{\mathrm{R}}} + \frac{1}{\kappa} \tag{A3.53}$$

Much alike to the case of infinite volume, the solution of the differential Eq. (A3.51), with initial condition $\tilde{c}^*_{\mathrm{T,M}}(t) = 0$ (and neglecting transient effects in the DBL) is

$$1 - \frac{\tilde{c}^*_{\mathrm{T,M}}(t)}{\kappa' c^*_{\mathrm{M}}(t=0)} = \exp\left(-\frac{3D_{\mathrm{M}}}{\delta r_0 \kappa'} t\right) \tag{A3.54}$$

By applying the definition of *f* given in Eq. (A3.48) the solution (A3.54) can be re-casted as:

$$\ln(1-f) = -\frac{3D_{\mathrm{M}}}{\delta r_0 \kappa'} t \tag{A3.55}$$

Combining Eqs. (A3.52) and (A3.54), we find a very convenient way to write the flux in terms of *f*

$$J = \frac{r_0}{3}\frac{d\tilde{c}^*_{\mathrm{T,M}}(t)}{dt} = \frac{D_{\mathrm{M}} c^*_{\mathrm{M}}(t=0)}{\delta}(1-f) \tag{A3.56}$$

3.7.4. IDM (Intraparticle Diffusion Model)

The solution to this problem was first found by Paterson while studying heat transfer in a solid sphere.[8] IDM assumes that diffusion through the DBL is not limiting. In this case, the concentration profiles in solution are flat, *i.e.*: $c^*_{\mathrm{M}}(r,t) = c^*_{\mathrm{M}}(t) \quad \forall r \geq r_0$.

The mass balance is:

$$(V_{\mathrm{T}} - V_{\mathrm{R}}) c^*_{\mathrm{M}}(t=0) = (V_{\mathrm{T}} - V_{\mathrm{R}}) c^*_{\mathrm{M}}(t) + z\int_0^{r_0} \tilde{c}^*_{\mathrm{T,M}}(r,t) 4\pi r^2 dr \tag{A3.57}$$

The differential equation (3.7) must be solved with the initial condition (3.9) and boundary conditions (3.10) and

$$\tilde{c}_{\mathrm{T,M}}(r_0^-, t) = \kappa\, c^*_{\mathrm{M}}(t) \tag{A3.58}$$

The exact analytical solution, given by Paterson,[8,38] is

$$f(t) = 1 - \frac{2}{3w}\sum_{n=1}^{\infty} \frac{\mathrm{e}^{-\frac{\tilde{D}t}{r_0^2} S_n^2}}{1 + \frac{S_n^2}{9w(w+1)}} \tag{A3.59}$$

where S_n are the roots of

$$x\cot(x) = 1 + \frac{x^2}{3w} \tag{A3.60}$$

For short times, this series solution converges very slowly.

An approximate analytical solution (derived by assuming (A3.27) in the Laplace transformed of (3.7)) can be written as

$$c^*_{\mathrm{M}}(t) = \frac{c^*_{\mathrm{M}}(0)}{2\sqrt{m(2+m)}}\left\{\left(m+\sqrt{m(2+m)}\right) F\left(\left(m+\sqrt{m(2+m)}\right)\frac{\sqrt{\tilde{D}t}}{r_0}\right) - \right.$$
$$\left. -\left(m-\sqrt{m(2+m)}\right) F\left(\left(m-\sqrt{m(2+m)}\right)\frac{\sqrt{\tilde{D}t}}{r_0}\right)\right\} \tag{A3.61}$$

where $m = \frac{3}{2} w$ and $F(x) = \mathrm{e}^{x^2}\ \mathrm{Erfc}(x)$.

Eq.(A3.61) is equivalent to the approximation also derived by Paterson[8] (Eq. 27):

$$f(t) = \frac{w+1}{w}\left\{1 - \frac{1}{\alpha - \beta}\left[\alpha\, F\left[\alpha\ \frac{\sqrt{\widetilde{D}t}}{r_0}\right] - \beta\, F\left[\beta\ \frac{\sqrt{\widetilde{D}t}}{r_0}\right]\right]\right\} \tag{A3.62}$$

where α and β are the roots of

$$x^2 + 3wx - 3w = 0 \tag{A3.63}$$

as correctly reported in some works.[35,38] A wrong plus sign appeared in front of the independent term in other works.[34,39] The approximation (A3.62) is accurate for short and intermediate times. Accuracy fails at long times, where -at least for the parameters assayed here- *f* is already practically 1. In fact, Paterson approximation is equivalent to consider that the diffusion inside the particle is semi-infinite (instead of finite volume).

The flux across the interface can be computed using the same approach adopted in the case of the MCM; and thus combining (A3.38) with the exact solution (A3.59), leads to

$$J = \frac{2\tilde{D}\left(V_{\mathrm{T}} - V_{\mathrm{R}}\right)}{9 w r_0 V_{\mathrm{R}}}\left(c_{\mathrm{M}}^{*}(0) - c_{\mathrm{M}}^{*}(\infty)\right)\sum_{n=1}^{\infty}\frac{S_n^2\, \mathrm{e}^{-\frac{\tilde{D}t}{r_0^2} S_n^2}}{1 + \frac{S_n^2}{9w(w+1)}} \tag{A3.64}$$

If one uses the approximate expression (A3.61), the flux in IDM can be computed as:

$$\begin{aligned} J = c_{\mathrm{M}}^{*}(0)\frac{\kappa\widetilde{D}}{4 r_0 m\sqrt{m(2+m)}}\Bigg\{&\left(m + \sqrt{m(2+m)}\right)^3 F\left(\left(m + \sqrt{m(2+m)}\right)\frac{\sqrt{\widetilde{D}t}}{r_0}\right) - \\ -&\left(m - \sqrt{m(2+m)}\right)^3 F\left(\left(m - \sqrt{m(2+m)}\right)\frac{\sqrt{\widetilde{D}t}}{r_0}\right) - \frac{4 m r_0\sqrt{m(2+m)}}{\sqrt{\pi\widetilde{D}t}}\Bigg\} \end{aligned} \tag{A3.65}$$

This equation was used to draw the fluxes in Fig. 3.6.

3.7.5. Applications of the Gibbs-Donnan model

Before coming to the computation of κ it will be necessary to introduce the main concepts and the nomenclature used in the literature about the Gibbs-Donnan model, [13,14,27–29] to which the reader is referred for further information.

The Gibbs-Donnan model has been widely employed to describe the sorption of metal ions on chelating resins. The sorbent is represented as a liquid phase separated from the external solution by an interface across which water, neutral molecules and ions can

diffuse, while the active groups, permanently linked to the resin, cannot; as a consequence of the separation of charge, a Donnan potential arises at the interface.

A metal ion M of charge *z* interacts with the resin sites $\widetilde{H_hR}$ (the tilde represents the resin phase) according to the following ion-exchange reaction (charges are omitted for simplicity):

$$M + n\ \widetilde{H_hR} \rightleftharpoons \widetilde{MH_pR_n} + q\ H \tag{A3.66}$$

(in the case considered, the uptake of Cd^{2+} on Chelex, the complex formed is $CdHR^+$, which means that n= 1, h= 2, p= 1 and q= 1 as $n \times h = p + q$ from the balance of protons and 2= 1+q from the balance of charges). For this equilibrium the corresponding exchange coefficient is defined as:

$$\beta_{np\mathrm{ex}} = \frac{\left[\widetilde{MH_pR_n}\right][H]^q}{[M]\left[\widetilde{H_hR}\right]^n} \tag{A3.67}$$

The exchange coefficients are not intrinsic thermodynamic parameters and must be experimentally determined at the conditions of interest (in particular, at specific pH and ionic strength *I*). In order to work with constants independent from the experimental conditions, a further parameter, called intrinsic complexation constant, is introduced and defined as:

$$\beta_{np\mathrm{int}} = \beta_{np\mathrm{ex}} \frac{\gamma_H^q \cdot \gamma_C^{(z-q)}}{\gamma_M} \frac{[C]^{(z-q)}}{[\tilde{C}]^{(z-q)}} \tag{A3.68}$$

where $[C]$ and $[\tilde{C}]$ stand for the concentration of counterions in the bulk solution and in the resin phase, while γ_H^q, $\gamma_C^{(z-q)}$ and γ_M are the activity coefficients of, respectively, protons, counterions and metal ions. All these variables can be known (or approximated): the activity coefficients can be computed applying the classical models (*i.e.* Debye-Hückel, Davis or SIT equations); in presence of a large concentration of (monovalent) background electrolyte $[C]$ is constant and equal to *I*, while $[\tilde{C}]$ can be computed from the Donnan partitioning equation, which assumes electroneutrality within the resin phase.

In this way, from a corpus of $\beta_{np\mathrm{ex}}$ experimentally obtained in different conditions, it is possible to find the values of the intrinsic constants, specific to each sorbent material and universally applicable.

The exchange of protons between resin and solution can be defined in a similar way, by introducing an intrinsic protonation constant:

$$K_{ar\,\mathrm{int}} = K_{ar\,\mathrm{ex}} \frac{\gamma_{\mathrm{C}}}{\gamma_{\mathrm{H}}} \frac{[\mathrm{C}]}{[\tilde{\mathrm{C}}]} \tag{A3.69}$$

paired to the conditional protonation constant:

$$K_{ar\,\mathrm{ex}} = \frac{\left[\widetilde{\mathrm{H}_r\mathrm{R}}\right]}{[\mathrm{H}]\left[\widetilde{\mathrm{H}_{(r-1)}\mathrm{R}}\right]} \tag{A3.70}$$

In this chapter the Gibbs-Donnan model was applied to obtain an estimate of the partition coefficient κ. Here we will assume the fraction of free Cd^{2+} ions inside the resin is negligible, and so that $\kappa \approx \frac{\left[\widetilde{\mathrm{MH}_p\mathrm{R}_n}\right]}{[\mathrm{M}]}$. This ratio can be easily computed from the intrinsic extraction coefficient, the proton concentration (experimentally determined from the pH in the bulk solution), and the amount of protonated sites in the resin $\left[\widetilde{\mathrm{H}_h\mathrm{R}}\right]$ (which can be computed at a certain pH and external *I* through the conditional protonation constant).

On the other hand, κ can be also computed from the experimental concentrations of metal ion at equilibrium. However, in the system studied here this is only feasible at relatively low pH values, where the concentrations in solution are far above the limit of detection of the analytical technique. In those cases, the κ values obtained from both sources are in good agreement with each other (at pH= 3.48, $\log\kappa_{\mathrm{theor}}$: 3.56, $\log\kappa_{\mathrm{exp}}$: 3.59; at pH= 4.56, $\log\kappa_{\mathrm{theor}}$: 5.08, $\log\kappa_{\mathrm{exp}}$: 4.25; at pH= 5.52, $\log\kappa_{\mathrm{theor}}$: 5.73, $\log\kappa_{\mathrm{exp}}$: 4.76).

As a further application, the Gibbs-Donnan model was used to determine the best pH at which the effects of *I* on the resin could be studied or, in other words, the pH at which a change in *I* will produce the largest change possible in the protonation degree of the resin. In Fig. A3.3 below the concentration of counterions in the resin phase (directly related to the protonation degree) is represented as a function of pH at the levels of *I* chosen for the experiments.

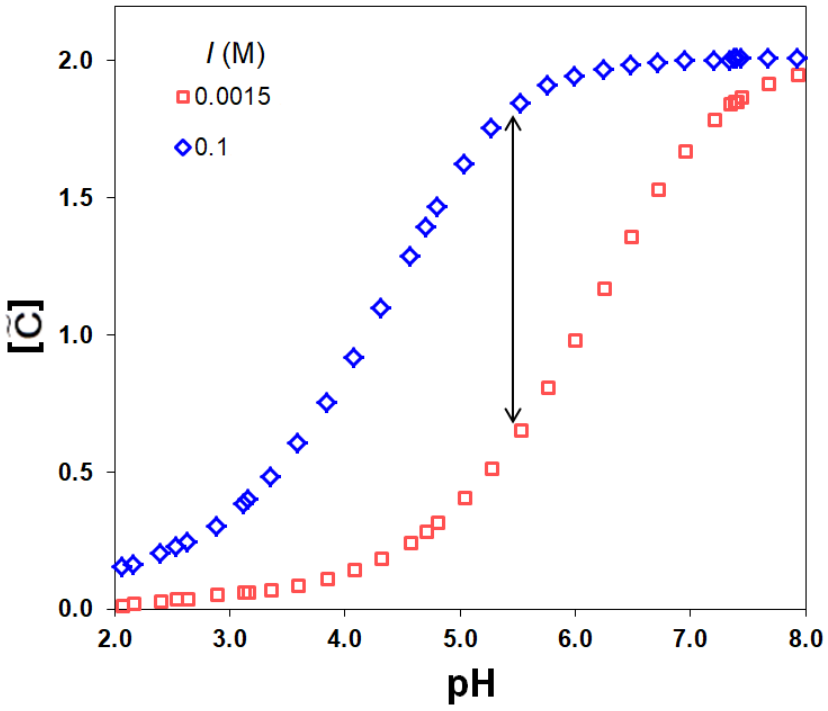

Figure A3.3. Counterion concentration in the resin phase as a function of pH, at two levels of ionic strength, as computed with the Gibbs-Donnan model. The arrow indicates the largest difference between the two curves, corresponding to pH= 5.5.

In order to maximise the effect of *I* it is recommendable to work between pH= 5 and 6, where the change in the protonation degree is the largest; finally, the experiments reported in Fig. 3.10 were performed at pH= 5.5.

3.7.6. Comparison between modelled and fitted values of the internal diffusion coefficient

The values of $\tilde{D}$ computed from the theoretical values of κ were found to be very close to the best-fit values obtained from the minimization of square residuals in ln(1-*f*) using the Nelder-Mead simplex algorithm.[40] The following figure compares the fitted and theoretical values related to the experiments shown in Fig. 3.9:

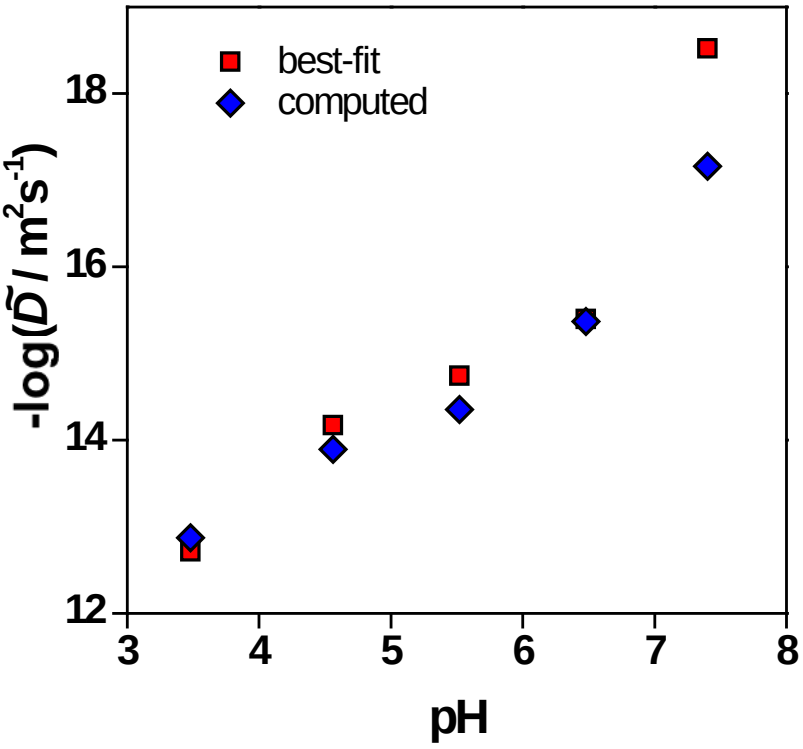

Figure A3.4. Comparison of the values of $\tilde{D}$ computed with Eq.(3.22) (blue diamonds) and fitted (red squares), for the experiments described in Fig. 3.9.

Table A3.1. Values of $\tilde{D}$ computed with Eq. (3.22) and fitted, for the experiments described in Fig. 3.9.

pH	$\tilde{D}_{\mathbf{computed}}$ ($m^2\ s^{-1}$)	$\tilde{D}_{\mathbf{fitted}}$ ($m^2\ s^{-1}$)
3.48	1.34×10^{-13}	1.93×10^{-13}
4.56	1.27×10^{-14}	6.70×10^{-15}
5.52	4.41×10^{-15}	1.80×10^{-15}
6.48	4.26×10^{-16}	4.00×10^{-16}
7.40	6.88×10^{-18}	3.00×10^{-19}

The use of the best-fit values instead of the theoretical ones does not improve significantly the agreement between the experimental data and the modelled curves, as can be noted from Fig.A3.5 below.

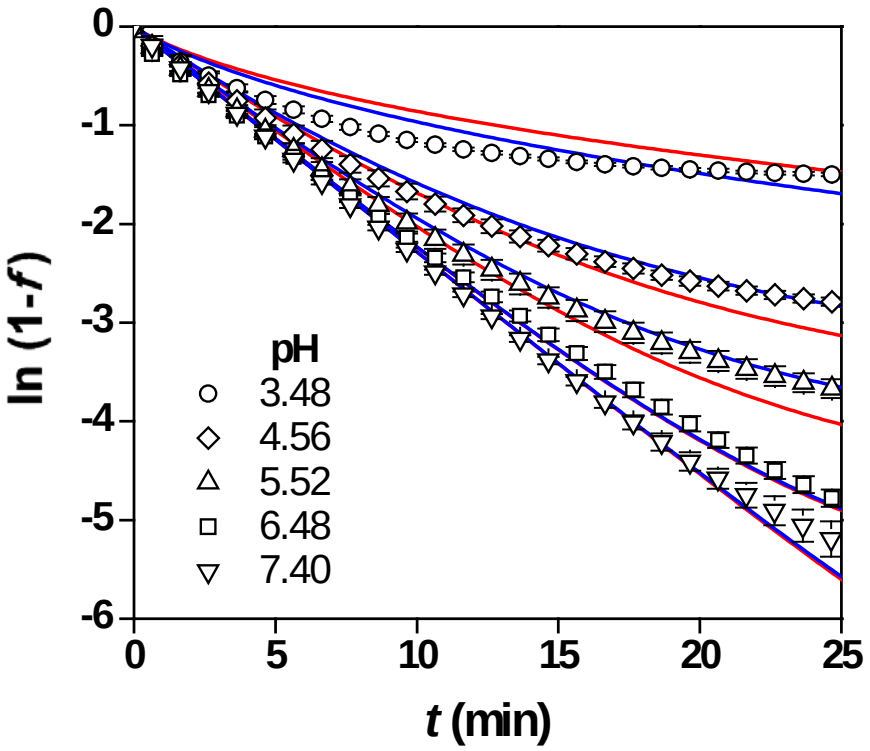

Figure A3.5. Sorption curves of Cd(II) on Chelex 100 at different pH values. The modelled curves in red were drawn using the theoretical values of $\tilde{D}$ computed with Eq. (3.22), while for those in blue the internal diffusion coefficient was fitted freely.

3.7.7. Metal diffusion coefficients in ion-exchange resins

The following table summarises the published values of the diffusion coefficient of free metal ($\widetilde{D}_{\mathrm{M}}$) found in the literature for Chelex 100 and Lewatit TP-207, two ion-exchange resins which share similar polymer structure and functionalities. The models applied by the authors of the quoted papers for determining the diffusion coefficients are reported as well.

Table A3.2. Published values of the diffusion coefficient of free metal ($\widetilde{D}_{\mathrm{M}}$).

Ion	**Model**	**Resin**	**log $\tilde{D}_{\mathrm{M}}$**	**D_{M} / $\tilde{D}_{\mathrm{M}}$**	**Reference**
Cu^{2+}	*Unreacted core*	*Lewatit TP-207*	-10.3	0.08	[22]
	Pore diffusion	*Lewatit TP-207*	-10.5	0.05	[22]
	Pore diffusion	*Lewatit TP-207*	-9.9	0.17	[41]
	Pore diffusion	*Chelex 100*	-10.6	0.03	[42]
Co^{2+}	*Unreacted core*	*Lewatit TP-207*	-10.3	0.07	[22]
	Pore diffusion	*Lewatit TP-207*	-10.5	0.04	[22]
Zn^{2+}	*Pore diffusion*	*Lewatit TP-207*	-9.9	0.17	[41]
	Pore diffusion	*Chelex 100*	-10.7	0.03	[42]

3.8. Codes

In this section we report the codes to implement the numerical solution of the analytical solution of the approximate equation (A3.35) and numerical inversion of the exact equation (A3.22) in:

- Mathematica. The numerical inversion of the Laplace transform is carried out with the Stehfest Method, applying the code reported in Cheng *et al*..[43]

```
(*Mathematica code to implement the analytical solution of the
 approximate equation ,not taking into *)
(*account the contribution of the amount of metal in the DBL (Eq.A3.35)*)
(*Legend :*)
(*DDbar_: Effective diffusion coefficient in resin phase (m^2/s)*)
(*DDM_: Diffusion coefficient in water (m^2/s)*)
(*rr0_: Radius of the bead (m)*)(*tt_: time (s)*)
(*VVR_: Volume of the resin (m^3)*)
(*VVT_: Total volume (volume of solution +VR) (m^3)*)
(*δδ_:Effective diffusion layer thickness (m)*)
(*κκ_: Partition coefficient *)
af[DDbar_, DDM_, rr0_, tt_, VVR_, VVT_, δδ_, κκ_] :=
 Block[{Dbar = DDbar, DM = DDM, r0 = rr0, t = tt, VR = VVR, VT = VVT, δ = δδ,
   κ = κκ, Bim, w, Sols, R1, R2, R3, NormalizedBulkConcentration, fractional, sol},
  Bim = (DM r0)/(Dbar δ κ);
  w = (VR κ)/(-VR + VT);
  Sols = Solve[-1/(3 Bim w) + ((1 - Bim) x)/(3 Bim w) - x^2 + x^3 == 0, x];
  R1 = Sols[[1]][[1]][[2]];
  R2 = Sols[[2]][[1]][[2]];
  R3 = Sols[[3]][[1]][[2]];
  NormalizedBulkConcentration =
   Re[(1)/(3 Bim w)
     (((1 - R1 + Bim R1) E^((Dbar t)/(r0^2 R1^2)) Erfc[-Sqrt[Dbar t]/(r0 R1)])/
        (R1 (R1 - R2) (R1 - R3)) +
       ((1 - R2 + Bim R2) E^((Dbar t)/(r0^2 R2^2)) Erfc[-Sqrt[Dbar t]/(r0 R2)])/
        ((R1 - R2) R2 (R3 - R2)) +
       ((1 - R3 + Bim R3) E^((Dbar t)/(r0^2 R3^2)) Erfc[-Sqrt[Dbar t]/(r0 R3)])/
        ((R1 - R3) R3 (R2 - R3)))];
  fractional = (1 - NormalizedBulkConcentration)/
    (1 - ((VT - VR))/((VT - VR) + κ VR));
  sol = Log[1 - fractional];
  Return[sol]          (*Returns the value of ln(1-f)*)] (*Block *)
```

```
(*Mathematica code to implement the numerical solution of the
 exact equation ,not taking into *)
(*account the contribution of the amount of metal in the DBL
 (Eq .A3 .22 )*)
(*Legend :*)
(*DDbar_: Effective diffusion coefficient in resin phase (m^2/s)*)
(*DDM_: Diffusion coefficient in water (m^2/s)*)
(*rr0_: Radius of the bead (m)*)(*tt_: time (s)*)
(*VVR_: Volume of the resin (m^3)*)
(*VVT_: Total volume (volume of solution +VR) (m^3)*)
(*δδ_:Effective diffusion layer thickness (m)*)
(*κκ_: Partition coefficient *)
nf[DDbar_, DDM_, rr0_, tt_, VVR_, VVT_, δδ_, κκ_] :=
 Block[{Dbar = DDbar, DM = DDM, r0 = rr0, t = tt, VR = VVR, VT = VVT,
   δ = δδ, κ = κκ, i, F, n, s, ccMbbar, csteh, NLInvSteh,
   NormalizedBulkConcentration, fractional, sol}, (*Stehfest Method *)
  (*Stehfest ,H.,Numerical inversion of Laplace transforms *)
  (*Comm .ACM ,v.13 ,47-49 and Y,1970. *)
  (*All credits for the implementation on Mathematica go to*)
  (*Cheng ,A.H-D.,Sidauruk ,P.and Abousleiman ,Y.,
  Approximate inversion of the Laplace transform *)
  (*Mathematica Journal ,Vol .4 ,No .2 ,1994 *)
  csteh[n_, i_] :=
   (-1)^(i + n/2)
     Sum[k^(n/2) (2 k)!/((n/2 - k)! k! (k - 1)! (i - k)! (2 k - i)!),
      {k, Floor[(i + 1)/2], Min[i, n/2]}] // N;
  NLInvSteh[F_, s_, t_, n_] :=
   Log[2]/t Sum[csteh[n, i] F /. s → i Log[2]/t, {i, 1, n}] // N;
  ccMbbar[s_] :=
   (VT - VR)/
    (s
      ((3 VR κ (-(Dbar/(r0^2 s)) +
            (Sqrt[Dbar] Coth[(r0 Sqrt[s])/Sqrt[Dbar]])/(r0 Sqrt[s])))/
        (1 + (Dbar δ κ)/(DM r0)
           ((r0 Sqrt[s] Coth[(r0 Sqrt[s])/Sqrt[Dbar]])/(Sqrt[Dbar] -
             1)) + (-VR + VT)));
  NormalizedBulkConcentration = NLInvSteh[ccMbbar[s], s, t, 14];
  fractional = (1 - NormalizedBulkConcentration)/
    (1 - ((VT - VR))/((VT - VR) + κ VR));
  sol = Log[1 - fractional];
  Return[sol]          (*Returns the value of ln(1-f)*)]
 (*Block *)
```

- MATLAB or GNU Octave. The numerical inversion of the Laplace transform is carried out with the Talbot method, applying the code reported in Abate *et al.*.[44] The code to implement (A3.23), from Le Van and Carta,[12] is included as well.

```
% MATLAB codes for calculating the fractional attainment of
equilibrium according
% to the Mixed Control Model (MCM) using 3 different methods.

clear all
%% Declaration of variables
VR=0.027*10^-6; % volume of the resin (m3)
VT=51.33*10^-6; % total volume (m3)
Dt=9.53*10^-14; % overall diffusion coefficient in the resin phase
(m2/s)
DM=7*10^-10; % diffusion coefficient of free metal in water (m2/s)
r0=82*10^-6; % radius of the bead (m)
kappa=1000; %(global) partition coefficient
delta=7*10^-6; % effective thickness of the DBL (m)

Bim=(DM*r0)/(Dt*delta*kappa); % mass transfer Biot number
w= (VR*kappa)/(VT-VR); % partition ratio
lamda=w/(w+1);

t=10:10:10000; % Time (s)

%% Numerical solution of the exact equation. It calculates the inverse
of Laplace of
%(Eq. A2.21) with Talbot's method (Abate, Joseph, and Ward Whitt. "A
Unified Framework for Numerically
% Inverting Laplace Transforms." INFORMS Journal of Computing, vol.
18.4
% (2006): 408-421)

F=@(s) 1/(s*((3*w*(coth(r0*(s/Dt)^0.5)/(r0*(s/Dt)^0.5)-
Dt/(s*r0^2)))/...
    (1+1/Bim*(r0*(s/Dt)^0.5*coth(r0*(s/Dt)^0.5)-1))+1));

cMt=talbot_inversion(F, t)'; %bulk concentration in the solution
(mol/L)
c_Mf=1/(1+w);
f_t=(1-cMt)/(1-c_Mf); %fractional attainment of equilibrium

plot(t,real(log(1-f_t)),'g')

%% Analytical solution of the approximate equation (Eq. 2.13)
syms x
tic
R=vpasolve(x^3-x^2 +(1-Bim)*x/(3*Bim*w)-1/(3*Bim*w) == 0, x);
toc
n1=[1 2 3 1 2];
c_Ms=0;

for l=1:3
    c_Ms=c_Ms+(1/(3*Bim*w)*exp(Dt*t/(r0^2*R(n1(l))^2)).*...
        erfc(-((Dt*t).^0.5)/(r0*R(n1(l))))*(1-
R(n1(l))+Bim*R(n1(l)))...
```

```
        /(R(n1(l))*(R(n1(l))-R(n1(l+1)))*(R(n1(l))-R(n1(l+2)))));
end
toc

c_M=double(real(c_Ms)); %bulk concentration in the solution (mol/L)
c_Mf=1/(1+w);
f_F=(1-c_M)/(1-c_Mf);%fractional attainment of equilibrium
plot(t,log(1-f_F),'r')

%% Analytical solution (from Perry and Green, page 16-29, chapter by
LeVan and others)(Eq. A2.22)
no_sol=10000;
R1(1:no_sol)=0;

sp=4;
f2=0;
for n=1:no_sol
    R1(n)=vpasolve(tan(x)/x==(3-(1-lamda)*x^2/(lamda*Bim))/(3+(1-
lamda)*(Bim-1)*x^2/(lamda*Bim)),x,sp);
    sp=double(R1(n))+pi;
    f1=1-6*sum(exp(-Dt/r0^2*(R1(1:n).^2).*10)./...
        (9*lamda/(1-lamda)+(1-lamda)*R1(1:n).^2-...
        (5*lamda+1)*R1(1:n).^2/Bim+(1-lamda)*R1(1:n).^4/Bim^2),2);
    if abs(log(f1)-log(f2))<10^-3
        break;
    end
    f2=f1;
end

pn=R1(1:n)';
t_mat=repmat(t,size(pn));
pn_mat=repmat(pn,size(t));
f=1-6*sum(exp(-Dt/r0^2*(pn_mat.^2).*t_mat)./...
    (9*lamda/(1-lamda)+(1-lamda)*pn_mat.^2-...
    (5*lamda+1)*pn_mat.^2/Bim+(1-lamda)*pn_mat.^4/Bim^2),1);
%fractional attainment of equilibrium
plot(t,log(1-f),'k')
```

We also include a MATLAB program for calculating the metal flux through the interface according to MCM, FDM and IDM.

```
%MATLAB Codes for computing the metal flux through the interface
according to MCM, FDM and IDM;
%these codes were used to draw Figure 2.6.
clear all
syms x t
%% Declaration of experimental variables
pHi=[3.5 4.5 5.5 6.5 7.5];
VRi=1*[0.046 0.057 0.064 0.069 0.069]*10^-6; % volume of the resin
(m3)
VTi=[50.65 50.43 50.46 50.53 50.52]*10^-6;  % total volume (m3)
Dti=[1.34*10^-13 1.27*10^-14 4.41*10^-15 4.26*10^-16 4.40*10^-18]; %
overall diffusion coefficient in the resin phase (m2/s)
r0i=[95 101 104 107 107]*10^-6; % radius of the bead (m)
kappai=[3.63*10^3 1.21*10^5 5.4*10^5 5.55*10^6 5.47*10^8]; %(global)
partition coefficient
DM=7*10^-10; % diffusion coefficient of free metal in water (m2/s)
delta=7*10^-6; %effective thickness of the DBL (m)
%% Choose the variables of an experiment
j=1; % 1 to 5
pH=pHi(j);
VR=VRi(j);
VT=VTi(j);
Dt=Dti(j);
r0=r0i(j);
kappa=kappai(j);
Bim=DM*r0/(Dt*delta*kappa);% mass transfer Biot number
w= (VR*kappa)/(VT-VR); % partition ratio

g=0;
g1=g/(VTi(j)-VRi(j)); % virtual volume of the DBL at metal
concentration equal to the one at the interface outside the bead (m3)

ti=10.^(-3:0.1:4); % time range (s)

for i=1:size(ti,2)
    % Mixed Control Model MCM
    F= @(s) 1/(s*(((3*w*(coth(r0*(s/Dt)^0.5)/(r0*(s/Dt)^0.5)-
Dt/(s*r0^2)))+g1)/...
    (1+1/Bim*(r0*(s/Dt)^0.5*coth(r0*(s/Dt)^0.5)-1))+1-g1));
    c_Ms(i)=talbot_inversion(F,  ti(i)); % bulk concentration in the
solution (mol/L)

    G=@(s) 1/(s*(3*w*(coth(r0*(s/Dt)^0.5)/(r0*(s/Dt)^0.5)-
Dt/(s*r0^2))+g1+...
        (1-g1)*(1+1/Bim*(r0*(s/Dt)^0.5*coth(r0*(s/Dt)^0.5)-1))));
    cM_0(i)=talbot_inversion(G,  ti(i));% metal concentration at the
interface outside the bead (mol/L)

    % Intraparticle Diffusion Model IDM
    Gi=@(s) r0^2/(3*w*Dt*(r0*(s/Dt)^0.5*coth(r0*(s/Dt)^0.5)-
1+s*r0^2/(3*w*Dt)));
    cMb0(i)=talbot_inversion(Gi,  ti(i));% bulk concentration in the
solution (mol/L)
end
```

```
f_mix=(1-c_Ms)/(w/(1+w)); %fractional attainment of equilibrium MCM
f_in=(1-cMb0)/(w/(1+w)); %fractional attainment of equilibrium IDM
f_pm=(f_in(2:end)+f_in(1:end-1))/2;

dcdt=real(cMb0(2:end)-cMb0(1:end-1))./(ti(2:end)-ti(1:end-1)); %first
derivative of the bulk concentration with respect to time

J=DM/delta*(real(c_Ms)-real(cM_0));% metal flux through the interface
(mol/m2/s) MCM (Eq. A2.2)
J_in=r0*kappa/(3*w)*dcdt;% metal flux through the interface (mol/m2/s)
IDM (Eq. SI.59)


% Film Diffusion Model FDM
f=0.0001:0.0001:0.9999; %fractional attainment of equilibrium FDM
kappa_p=1/(VR/(VT-VR)+1/kappa);
t_ex=-log(1-f)*delta*r0/(3*DM)*kappa_p;
J_F=DM/delta*(1-f);% metal flux through the interface (mol/m2/s) FDM
(Eq. A2.50)
```

3.9. References

(1) Puy, J.; Galceran, J.; Cruz-González, S.; David, C. A.; Uribe, R.; Lin, C.; Zhang, H.; Davison, W. Measurement of metals using DGT: Impact of ionic strength and kinetics of dissociation of complexes in the resin domain. *Anal. Chem.* **2014**, *86* (15), 7740–7748.

(2) Jiménez-Piedrahita, M.; Altier, A.; Cecilia, J.; Rey-Castro, C.; Galceran, J.; Puy, J. Influence of the settling of the resin beads on diffusion gradients in thin films measurements. *Anal. Chim. Acta* **2015**, *885*, 148–155.

(3) Puy, J.; Galceran, J.; Rey-Castro, C. Interpreting the DGT Measurement. In *Diffusive Gradients in Thin-Films for Environmental Measurements*; Davison, W., Ed.; Cambridge University Press: Cambridge (UK), 2016; 93–122.

(4) Altier, A.; Jiménez-Piedrahita, M.; Rey-Castro, C.; Cecilia, J.; Galceran, J.; Puy, J. Accumulation of Mg to Diffusive Gradients in Thin Films (DGT) devices: kinetic and thermodynamic effects of the ionic strength. *Anal. Chem.* **2016**, *88* (20), 10245–10251.

(5) Chakrabarti, C. L.; Yanjia, L.; Grégoire, D. C.; Back, M. H.; Schroeder, W. H. Kinetic studies of metal speciation using Chelex cation exchange resin: Application to cadmium, copper, and lead speciation in river water and snow. *Environ. Sci. Technol.* **1994**, *28* (11), 1957–1967.

(6) Dykstra, J. E.; Biesheuvel, P. .; Bruning, H.; Ter Heijne, A. Theory of ion transport with fast acid-base equilibrations in bioelectrochemical systems. *Phys. Rev. E* **2014**, *90*.

(7) Boyd, G. E.; Adamson, A. W.; Myers, L. S. The exchange adsorption of ions from aqueous solutions by organic zeolites .2. Kinetics. *J. Am. Chem. Soc.* **1947**, *69*, 2836–2848.

(8) Paterson, S. The heating or cooling of a solid sphere in a well-stirred fluid. *Proc. Phys. Soc.* **1947**, *59* (1), 50–58.

(9) Hosseini-Bandegharaei, A.; Hosseini, M. S.; Sarw-Ghadi, M.; Zowghi, S.; Hosseini, E.; Hosseini-Bandegharaei, H. Kinetics, equilibrium and thermodynamic study of Cr(VI) sorption into toluidine blue o-impregnated XAD-7 resin beads and its application for the treatment of wastewaters containing Cr(VI). *Chem. Eng. J.* **2010**, *160* (1), 190–198.

(10) Petruzzelli, D.; Liberti, L.; Passino, R. Chloride sulfate exchange kinetics -

Solution for combined film and particle diffusion. *React. Polym.* **1987**, *5*, 219–226.

(11) Grossman, J. J.; Adamson, A. W. The diffusion process for organolite exchangers. *J. Phys. Chem.* **1952**, *56* (7), 97–100.

(12) Le Van, M. D.; Carta, G. Adsorption and ion exchange. In *Perry's chemical engineers' handbook*; Green, D. W., Perry, R. H., Eds.; McGraw-Hill: New York, 2008; 1–69.

(13) Alberti, G.; Amendola, V.; Pesavento, M.; Biesuz, R. Beyond the synthesis of novel solid phases: Review on modelling of sorption phenomena. *Coord. Chem. Rev.* **2012**, *256* (1–2), 28–45.

(14) Pesavento, M.; Biesuz, R.; Gallorini, M.; Profumo, A. Sorption mechanism of trace amounts of divalent metal ions on a chelating resin containing iminodiacetate groups. *Anal. Chem.* **1993**, *65* (18), 2522–2527.

(15) Ohshima, H. *Theory of Colloid and Interfacial Electric Phenomena, 1st Ed.*; Elsevier Academic Press: Cambridge (MA), 2006.

(16) Galceran, J.; van Leeuwen, H. Dynamics of biouptake processes: The role of transport, adsorption and internalisation. In *Physicochemical Kinetics and Transport at Biointerfaces*; van Leeuwen, H. P., Köster, W., Eds.; John Wiley & Sons Ltd, 2004; 147.

(17) Galceran, J.; Monné, J.; Puy, J.; van Leeuwen, H. P. Transient biouptake flux and accumulation by microorganisms: The case of two types of sites with Langmuir adsorption. *Mar. Chem.* **2006**, *99* (1–4), 162–176.

(18) Brumleve, T. R.; Osteryoung, J. Spherical diffusion and shielding effects in Reverse Pulse Volltammetry. *J. Phys. Chem.* **1982**, *86* (10), 1794–1801.

(19) Park, S. Y.; Aoki, K.; Tokuda, K.; Matsuda, H. Determination of diffusion coefficients of metals dissolved in mercury by double potential step chronoamperometry at hanging mercury drop electrodes. *Bull. Chem. Soc. Jpn* **1983**, *56*, 2133–2137.

(20) Galceran, J.; Salvador, J.; Puy, J.; Mas, F.; Gimenez, D.; Esteban, M. Amalgamation effects in reverse pulse polarography at spherical electrodes. Influence on speciation measurements. *J. Electroanal. Chem.* **1998**, *442*, 151–167.

(21) Fatin-Rouge, N.; Milon, A.; Buffle, J.; Goulet, R. R.; Tessier, A. Diffusion and partitioning of solutes in agarose hydrogels: The relative influence of electrostatic

and specific interactions. *J. Phys. Chem. B* **2003**, *107* (44), 12126–12137.

(22) Fernández, A.; Díaz, M.; Rodrigues, A. Kinetic mechanism in ion exchange processes. *Chem. Eng. J.* **1995**, *57*, 17–25.

(23) Ferreira, C. M. H.; Pinto, I. S. S.; Soares, E. V.; Soares, H. M. V. M. (Un)suitability of the use of pH buffers in biological, biochemical and environmental studies and their interaction with metal ions - a review. *RSC Adv.* **2015**, *5*, 30989–31003.

(24) The MathWorks Inc. MATLAB Release 2012b. Natick, Massachusetts, USA 2012.

(25) *CRC Handbook of Chemistry and Physics*, 97th ed.; CRC Press: Boca Raton (FL), 2016.

(26) Krasner, J.; Marinsky, J. A. The dissociation of iminodiacetic acid groups incorporated in a chelating ion-exchange resin. *J. Phys. Chem.* **1963**, *67* (12), 2559–2561.

(27) Pesavento, M.; Profumo, A.; Biesuz, R.; Alberti, G. Ion exchange complexing resins as sensors for the determination of free metal Ion concentration at a low level. *Solvent Extr. Ion Exch.* **2008**, *26* (3), 301–320.

(28) Alberti, G.; Biesuz, R. EmporeTM membrane vs. Chelex 100: Thermodynamic and kinetic studies on metals sorption. *React. Funct. Polym.* **2011**, *71* (5), 588–598.

(29) Pesavento, M.; Biesuz, R.; Alberti, G.; Sturini, M. Separation of copper (II) and aluminium (III) from fresh waters by solid phase extraction on a complexing resin column. *J. Sep. Sci.* **2003**, *26*, 381–386.

(30) Pinheiro, J. P.; Domingos, R. F. Impact of spherical diffusion on labile trace metal speciation by electrochemical stripping techniques. *J. Electroanal. Chem.* **2005**, *581* (2), 167–175.

(31) Pesavento, M.; Biesuz, R.; Cortina, J. L. Sorption of metal ions on a weak acid cation-exchange resin containing carboxylic groups. *Anal. Chim. Acta* **1994**, *298* (2), 225–232.

(32) Gustafsson, J. P. Visual MINTEQ. Stockholm 2013.

(33) Inglezakis, V. J.; Poulopoulos, S. G. *Adsorption and Ion Exchange*; Elsevier: Amsterdam, 2006.

(34) Helfferich, F. G. *Ion Exchange*; Dover Publications: New York, 1995.

(35) Atun, G.; Hisarli, G.; Kurtoğlu, A. E.; Ayar, N. A comparison of basic dye

adsorption onto zeolitic materials synthesized from fly ash. *J. Hazard. Mater.* **2011**, *187* (1–3), 562–573.

(36) Pinheiro, J. P.; Galceran, J.; van Leeuwen, H. P. Metal speciation dynamics and bioavailability: Bulk depletion effects. *Environ. Sci. Technol.* **2004**, *38* (8), 2397–2405.

(37) Hajdu, R.; Pinheiro, J. P.; Galceran, J.; Slaveykova, V. I. Modeling of Cd uptake and efflux kinetics in metal-resistant bacterium cupriavidus metallidurans. *Environ. Sci. Technol.* **2010**, *44* (12), 4597–4602.

(38) Popelt, P.; Kohler, J.; Pilchowski, K. Determination of diffusion coefficients in solids from sorption data. 9. Numerical-calculation of diffusion-coefficients using Paterson series development. *Z. Phys. Chem.* **1977**, *258*, 1081–1087.

(39) Krongauz, V. V.; Kocher, C. W. Kinetics of ion exchange in monodisperse resin. *J. Appl. Polym. Sci.* **1997**, *65* (7), 1271–1283.

(40) Lagarias, J. C.; Reeds, J. A.; Wright, M. H.; Wright, P. E. Convergence properties of the Nelder-Mead simplex method in low dimensions. *Siam J Optim.* **1998**, *9*, 112–147.

(41) Valverde, J. L.; De Lucas, A.; Carmona, M.; González, M.; Rodríguez, J. F. Model for the determination of diffusion coefficients of heterovalent ions in macroporous ion exchange resins by the zero-length column method. *Chem. Eng. Sci.* **2005**, *60* (21), 5836–5844.

(42) Lin, L. C.; Juang, R. S. Ion-exchange kinetics of Cu(II) and Zn(II) from aqueous solutions with two chelating resins. *Chem. Eng. J.* **2007**, *132* (1–3), 205–213.

(43) Cheng, A. H. D.; Sidauruk, P.; Abousleiman, Y. Approximate inversion of the Laplace transform. *Math. J.* **1994**, *4*, 76–82.

(44) Abate, J.; Whitt, W. A unified framework for numerically inverting Laplace transforms. *Informs J Comput* **2006**, *18*, 408–421.

4. Dynamics of metal uptake to a chelating resin in presence of a ligand

4.1. Introduction

Determining the bioavailable fraction of a metal in the natural medium is paramount to understand its effects on the biota and to predict its toxicity. Since working with living organisms comports intrinsic difficulties, the most accessible strategy implies using artificial systems that can mimic the uptake process. This ability to act as a surrogate for biouptake is one of the recognised advantages of the DGT technique.[1,2]

A large portion of the literature about the chelating resin Chelex 100 is devoted to its use in the study of metal biouptake, which began with seminal work that showed the correlation between the Chelex-batch-labile fraction of cadmium and its toxicity to salmon.[3]

Since then, kinetic measurements of metal accumulation on ion-exchange resins have been widely used *e.g.* by the group of Chakrabarti and others[4–6] to characterize humic acids and to determine the labile metal fraction in natural waters. In their approach the rate-determining step is the dissociation of the metal from the ligand, while the binding on the resin is assumed to be much faster; the contribution of metal transport to the whole process is neglected.[7,8] On the basis of these assumptions, the whole uptake can be modelled as the summation of a number of first order or pseudo-first order reactions, one for each ligand or complexing site of a polyelectrolyte. Other works take a more empirical approach,[9,10] and discriminate between labile, semi-labile and inert complexes simply on the basis of the amount of metal accumulated in the resin after a fixed period of time. This kind of methods, albeit fast and readily implementable, requires complete control over the parameters of the systems to guarantee comparable results. On the contrary, the development of a rigorous theoretical framework to describe the kinetics of metal uptake would allow the use of methods based on ion exchange/chelating resins

in a wider range of working conditions, such as different concentrations of background electrolyte, amount of sorbent material, total metal concentration, etc.

In this chapter we aim at filling this gap by proposing a newly developed model with a sound physical basis, which allows the characterisation of the metal-ligand complexes by determining the value of their kinetics dissociation constant. Successive simplifications of the model are proposed, which adapt to different experimental conditions: inert complexes in short timescales far away from equilibrium, inert complexes in a wider timescale approaching equilibrium and labile complexes whose dissociation takes place in the same timescale of metal transport.

The complexing agent chosen was NTA (nitrilotriacetic acid), a ligand known to bind divalent cations to mostly generate negatively charged complexes with 1:1 stoichiometry. To cover complexes with a broad range of kinetic behaviours, we focused on Ni(II) and Cd(II) which are known to form, respectively, relatively inert and labile complexes with NTA.[11]

Another goal of the present chapter is to gain a better understanding of the mechanism of complex dissociation in the resin phase of the DGT passive sampler. It is known that, in bulk water solutions, the association or dissociation of a complex involves the exchange of one of the water molecules coordinated to the metal ion with a ligand. According to the widely accepted Eigen model,[12,13] the exchange reaction involves two steps: in the first one, the ligand reacts with the hydrated ion, forming the so-called outer-sphere complex (divalent cations of transition metals normally coordinate with 6 water molecules):

$$\mathrm{M(H_2O)_6^{2+}} + \mathrm{L^{n-}} \underset{}{\overset{K_{os}}{\rightleftharpoons}} \mathrm{M(H_2O)_6, L^{(2-n)+}} \tag{4.1}$$

This first reaction reaches equilibrium instantaneously and it is ruled by the stability constant K_{os}, which depends on the charges of the ions and the ionic strength I. Then, the rate-limiting step consists in the loss of a molecule of water from the inner hydration sphere:

$$\mathrm{M(H_2O)_6, L^{(2-n)+}} \xrightarrow{k_{-w}} \mathrm{M(H_2O)_5\, L^{(2-n)+}} + \mathrm{H_2O} \tag{4.2}$$

where k_{-w} is the rate constant for water exchange and is characteristic of each metal cation. The overall rate association constant is, then, given by the product:

$$k_a = K_{os} k_{-w} \tag{4.3}$$

and it is related to the corresponding dissociation rate constant by the stability constant of complex formation *K*:

$$k_d = \frac{k_a}{K} \tag{4.4}$$

It is worth pointing out that, since K_{os} and *K* show the same dependence on *I*, according to this mechanism of reaction, the dissociation rate constant should be independent from the ionic strength.

A recent paper[11] has suggested that, when interacting with the DGT resin, labile and inert complexes dissociate following two different pathways: while the labile ones (like CdNTA) follow closely an Eigen-like mechanism as the one described, the most inert ones (like NiNTA) show a remarkable influence of *I* on the dissociation rate constant, a feature that can be explained only by means of an alternative hypothesis, the so-called "ligand-assisted mechanism". According to this model, the inert complexes penetrate inside the resin layer without dissociating and, instead, react directly with the resin sites:

$$\mathrm{ML}^{z_{\mathrm{ML}}} + \mathrm{R}^{z_{\mathrm{R}}} \underset{\tilde{k}_a}{\overset{\tilde{k}_d}{\rightleftharpoons}} \mathrm{MR}^{z_{\mathrm{MR}}} + \mathrm{L}^{z_{\mathrm{L}}} \tag{4.5}$$

When both reacting species are charged, the reaction rate will depend on the ionic strength through a Debye-Hückel-like relationship:[14]

$$\log \tilde{k}_d = \log \tilde{k}_d^{o} + 1.02 z_R z_{ML} \tilde{I}^{1/2} \tag{4.6}$$

where $\tilde{k}_d^{o}$ is the value of the dissociation rate constant at infinite dilution, while $z_R z_{ML}$ is the product of the charges of the ions. z_{NiNTA} is -1 and z_R is the effective (negative) charge of the resin functional groups, which we assume that form 1:1 complexes with Ni(II) (see Chapter 6).

The rationale of this chapter derives from the fact that working in a system simpler than the DGT should make the different behaviours of the complexes more understandable.

4.2. The model

As anticipated, we aim at describing the experimental data with three variants of the same model: for the most general case we will apply the Complete Model (CM), while the Simplified Model (SM) and the Ultra-Simplified Model (UM) have limited applicability, but easier implementation.

4.2.1. Complete Model (CM)

The model stems from two key assumptions, the first one being that the fraction of free metal in solution is negligible ($c^0_{\mathrm{T,M}} \approx c^0_{\mathrm{ML}}$, where the superscript "0" indicates time 0 before starting the experiment) and the accumulation of metal in the resin is ruled only by the penetration and subsequent dissociation of the complexes inside the bead (see Fig. 4.1). The dissociation of the complex follows the equation:

$$\mathrm{ML}^{z_{\mathrm{ML}}} \underset{\tilde{k}_{\mathrm{a}}}{\overset{\tilde{k}_{\mathrm{d}}}{\rightleftharpoons}} \mathrm{M}^{z_{\mathrm{M}}} + \mathrm{L}^{z_{\mathrm{L}}} \tag{4.7}$$

The second key assumption, is that, inside the resin, the free and the bound metal are related by a fast exchange equilibrium and can be "lumped" together under the common name $\tilde{c}_{\mathrm{M}}$:

$$\tilde{c}_{\mathrm{M}} \equiv \tilde{c}_{\mathrm{MR}} + \tilde{c}_{\mathrm{M,free}} = \tilde{c}_{\mathrm{M,free}} \left(1 + \tilde{K}'_{\mathrm{R}}\right) \tag{4.8}$$

where $\tilde{K}'_{\mathrm{R}}$ is the conditional stability constant of the metal-resin complex; the tilde indicates parameters referred to the resin phase. The charged complexes distribute across the resin/solution interface according to the Donnan partitioning equation:

$$\tilde{c}_{\mathrm{ML}}\left(r_0^-\right) = \chi^{z_{\mathrm{ML}}} c_{\mathrm{ML}}\left(r_0^+\right) \tag{4.9}$$

For the sake of simplicity, we neglect any concentration profile inside the bead. The resistance to mass transport due to intraparticle diffusion is expected to be comparatively low, as the timescale of the experiments is much larger than $r_0^2 / \tilde{D}_{\mathrm{ML}}$. As done for the MCM in Chapter 3, the beads are modelled as spheres of fixed radius r_0, surrounded by an effective diffusion layer of effective thickness δ. All the models consider finite volume of the solution.

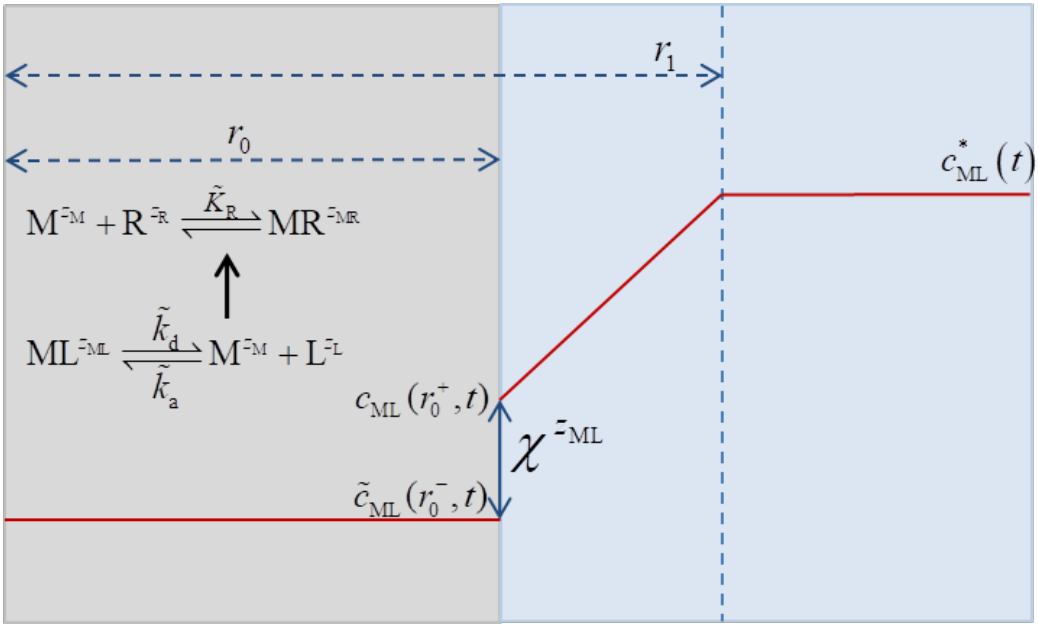

Figure 4.1. Schematic representation of the radial concentration profiles in the resin (grey background) and aqueous solution (blue background), as per the hypotheses of the Complete Model (CM). The metal complex distributes between the two sides of the interface according to the Donnan partitioning factor χ. The effective thickness of the diffusive boundary layer (DBL) is δ. We neglect any concentration gradient inside the bead, where the exchange reaction between the ML complex and the resin takes place.

For the mathematical formulation of the model, we address the reader to the Appendices (Section 4.6.1). It can be demonstrated that the evolution of the bulk concentration with time can be described by the following equation:

$$c^*_{ML}(t) = c^\infty_{ML} + \vartheta\, e^{\lambda_1 t} + \left(c^0_{ML} - c^\infty_{ML} - \vartheta\right) e^{\lambda_2 t} \tag{4.10}$$

where c^∞_{ML} is the bulk concentration at equilibrium, c^0_{ML} is the initial total metal concentration and λ_1 and λ_2 are, respectively, the two eigenvalues:

$$\lambda_1 = \frac{1}{2}\left(-\tilde{k}'_a + p - \sqrt{\left(\tilde{k}'_a + p\right)^2 + 4\tilde{k}_d s}\right) \tag{4.11}$$

$$\lambda_2 = \frac{1}{2}\left(-\tilde{k}'_a + p + \sqrt{\left(\tilde{k}'_a + p\right)^2 + 4\tilde{k}_d s}\right) \tag{4.12}$$

In the previous equations, to simplify the notation, we introduced the following groups of parameters:

$$p \equiv -\frac{3D_{\mathrm{ML}}}{r_0\delta}\left(\frac{v}{1-v}+\frac{1}{\chi^{z_{\mathrm{ML}}}}\right)+\tilde{k}_{\mathrm{d}} \tag{4.13}$$

$$s \equiv \tilde{k}'_{\mathrm{a}} - \frac{3D_{\mathrm{ML}}}{r_0\delta}\frac{v}{1-v} \tag{4.14}$$

$$\vartheta = -\frac{v}{1-v}\frac{\tilde{k}_{\mathrm{d}}}{(\lambda_1-\lambda_2)\lambda_1}d + \frac{v}{1-v}\frac{\tilde{k}'_{\mathrm{a}}+\lambda_1}{(\lambda_1-\lambda_2)\lambda_1}d \tag{4.15}$$

$$d \equiv \frac{3D_{\mathrm{ML}}}{r_0\delta}c^0_{\mathrm{ML}} \tag{4.16}$$

where v is the ratio between V_{R} (the volume of resin) and V_{T} (the total volume), $\tilde{k}'_{\mathrm{a}}$ is the effective association constant of ML in the resin domain ($\tilde{k}'_{\mathrm{a}} \equiv \frac{\tilde{k}_{\mathrm{a}}\tilde{c}_{\mathrm{L}}}{1+\tilde{K}'_{\mathrm{R}}}$) while $\tilde{k}_{\mathrm{d}}$ is the dissociation constant of the ML complex.

4.2.2. Simplified Model (SM)

It is reasonable to assume that, when dealing with complexes of particularly slow dissociation kinetics, the contribution of metal transport will be practically negligible (see Fig. A4.2) and the only variation in the concentration profile will be given by the Donnan partitioning at the interface. It can be demonstrated (see Section 4.6.1) that the equation describing this model is:

$$\ln\left(\frac{c^*_{\mathrm{ML}}(t)-c^{\infty}_{\mathrm{ML}}}{c^0_{\mathrm{ML}}-c^{\infty}_{\mathrm{ML}}}\right) = -\left(\tilde{k}'_{\mathrm{a}}+\upsilon\chi^{z_{\mathrm{ML}}}\,\tilde{k}_{\mathrm{d}}\right)t \tag{4.17}$$

where:

$$\upsilon \equiv \frac{v}{1-v+v\chi^{z_{\mathrm{ML}}}} \tag{4.18}$$

Eq. (4.17) is formally equivalent to the classical solution of a first-order reversible reaction, where the corresponding forward and backward rate constants correspond to constant (excess) ligand concentrations and are corrected for Donnan partitioning and resin/solution volume ratio. It must also be noted that the argument of the logarithm is equal to 1-*f*, where *f* is the fractional uptake, as defined in Eq. (3.19) of Chapter 3. The relationship between the initial and the equilibrium bulk concentration is given by the following equation:

$$c_{\mathrm{ML}}^{\infty} = \frac{c_{\mathrm{ML}}^{0}}{\frac{v}{1-v}\left(\frac{1}{\tilde{K}'}+1\right)\chi^{z_{\mathrm{ML}}}+1} \tag{4.19}$$

where $\tilde{K}'$ is the effective stability constant of the complex in the resin phase, defined as:

$$\tilde{K}' = \frac{\tilde{c}_{\mathrm{ML}}}{\tilde{c}_{\mathrm{M}}} = \frac{\tilde{k}_{\mathrm{a}}'}{\tilde{k}_{\mathrm{d}}} \tag{4.20}$$

Note that $\tilde{K}'$ can be computed from the initial and equilibrium bulk concentration by rearranging Eq. (4.19):

$$\tilde{K}' = \frac{c_{\mathrm{ML}}^{\infty} v \chi^{z_{\mathrm{ML}}}}{\left(c_{\mathrm{ML}}^{0} - c_{\mathrm{ML}}^{\infty}\right)(1-v) - c_{\mathrm{ML}}^{\infty} v \chi^{z_{\mathrm{ML}}}} \tag{4.21}$$

4.2.3. Ultra-simplified Model (UM)

In the first phase of the uptake, when the amount of dissociated metal in the resin phase is still very low, the backward reaction of (4.7) can be reasonably neglected. Under this assumption, Eq. (4.17) may undergo a further simplification resulting in the simple solution of a first-order reaction:

$$\ln\left(\frac{c_{\mathrm{ML}}^{*}(t)}{c_{\mathrm{ML}}^{0}}\right) = -at \tag{4.22}$$

where

$$a = \upsilon \tilde{k}_{\mathrm{d}} \chi^{z_{\mathrm{ML}}} \approx v \tilde{k}_{\mathrm{d}} \chi^{z_{\mathrm{ML}}} \tag{4.23}$$

is the first-order rate constant, corrected for resin/solution volume ratio and Donnan partitioning. If the results are plotted as $\ln\left(\frac{c_{\mathrm{ML}}^{*}(t)}{c_{\mathrm{ML}}^{0}}\right)$ *vs. t*, they will lie on a straight line, whose slope can be used to estimate the dissociation rate constant.

4.3. Experimental method

All the experiments were performed following a procedure similar to the one applied to the study of metal accumulation to the resin in absence of ligand (see Chapter 3), but with a few important differences. An accurately weighted amount of resin Chelex-100 (previously dried at 60º C) was left to equilibrate overnight in a solution at the desired pH and *I*. While the ionic strength was one of the main factors to be studied, and was changed accordingly to the experiment, the pH has always been 7.4, kept constant with

MOPS 1 mM. This pH is close to the one used in a similar series of experiments with DGT;[11] as the free metal concentration is very low, the risk of precipitation is negligible. The same mass of dry resin (24.5 mg) was used for all the experiments, unless specified otherwise. The suspension was stirred from above using an OrionStar Series Automatic Stirrer Probe, at the highest rate allowed by the probe. Then, a concentrated solution of metal in presence of NTA was prepared, buffered at the same pH and *I* of the resin suspension.

A typical experiment was started with the addition of an aliquot of the concentrated M/NTA standard solution to the resin suspension. The total metal concentration in the bulk was ~2.5×10^{-5} M, while the total NTA concentration was ~8×10^{-5} M; under these conditions, the percentage of free metal in solution was ~1%, as confirmed by direct measurements with the Cd-ISE. Due to the extremely long equilibration times, the vessel could not be exactly thermostated (at 25 ± 0.1 ºC) throughout the whole experiments, but only during the first few hours. However, no relevant changes in the uptake rate were observed after leaving the suspension to equilibrate at room temperature (23 ± 2 ºC).

The uptake was mainly followed by collecting samples of the supernatant, later analysed by ICP-MS. Special care had to be taken during the sampling to avoid sucking the suspended resin beads along with the liquid. To do so, different strategies were employed: at first, we tried interrupting the stirring for about 30 s to let the beads settle. We realised, though, that this was not a viable option in the cases where the uptake was particularly fast, as it caused visible “jumps” in the results, as a consequence of the loss of homogeneity. We finally adopted the procedure of not interrupting the stirring and to systematically filter the samples right after being taken (pore size of the filter: 0.45 μm). The amount of resin accidentally removed from the suspension in this way is negligible in comparison to the total. Regardless of the procedure, the samples were acidified to 1% v/v with ultrapure nitric acid.

Several of the systems studied here displayed an overtly sluggish kinetics and, as a consequence, it was practically impossible to follow the uptake process until equilibrium was fully attained.

4.4. Results and Discussion

4.4.1. An inert complex: NiNTA

The complex NiNTA is known to be inert in the DGT timescale[11] and all the more so in the free resin beads timescale. It is reasonable to assume, then, that its dissociation is the rate-determining step of the whole accumulation. Preliminary experiments conducted at different stirring rates confirmed that the effect of metal transport is, in fact, negligible, provided that the suspension is homogeneous and there is no clustering of the beads. Actually, in the experiments at I= 0.01 M and 0.025 M (see Fig. 4.5 later on), the stirring was interrupted after a few days, without causing any significant variation in the slope. If the hypotheses mentioned above are correct, we will not need to resort to the complete model to have a full understanding of the results, but we could apply UM (in a short timescale, far from equilibrium) and SM (in the cases where equilibrium is approached).

In the following sections, the parameters under scrutiny will be the total metal concentration, the ratio of volumes v and the ionic strength I.

DEPENDENCE ON c_{ML}^{0} AND v

A way to verify whether the UM can be applied to the case of NiNTA consists in performing two experiments in the same conditions, but with different total Ni(II) concentrations; if Eq. (4.22) holds, c_{ML}^{*} must be linear with the total metal concentration, since neither the metal transport nor the re-association reaction play a relevant role, at least in the first phase of the uptake. The results showed that, not only the model applies, but also that, due to the extremely slow dissociation kinetics of the complex, the linear portion of the curve extends to very long times, in the scale of several hundreds of hours (see Fig. 4.2).

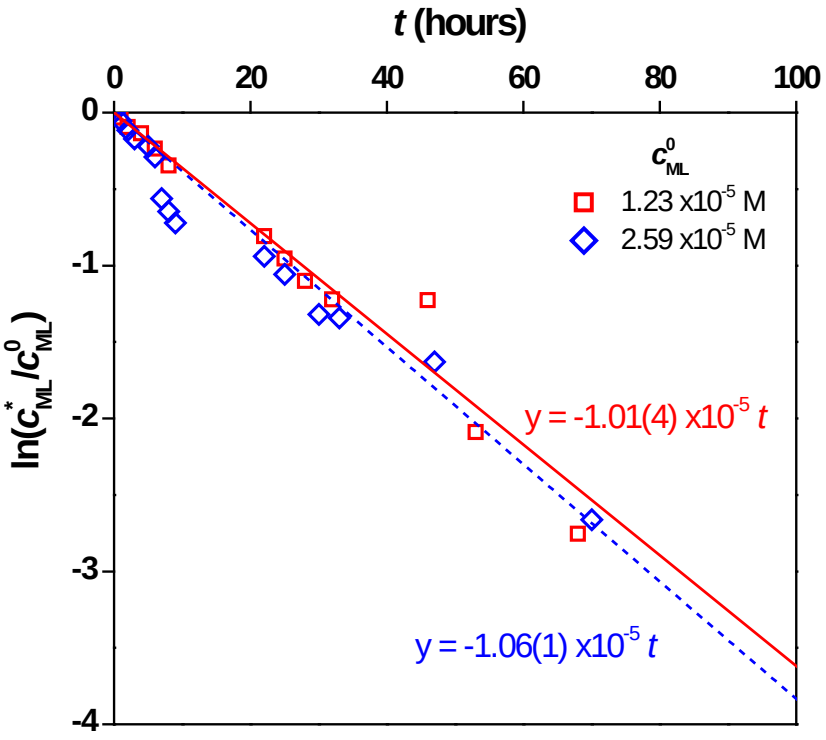

Figure 4.2. Accumulation curves of Ni(II) in Chelex 100 in presence of NTA, at two different total metal concentrations (2.59×10^{-5} M and 1.23×10^{-5} M). I= 0.1 M, pH= 7.4, $\nu = 6.5\times10^{-4}$, $c_{NTA} = 8\times10^{-5}$ M.

This feature is particularly convenient as it allows an accurate determination of the slope of the curve (the parameter *a* in the equations), key to estimate the dissociation constants.

A second way to validate the UM is to verify whether the slope *a* linearly depends on the ratio of volumes, as predicted by Eq. (4.23). A total of four experiments were performed, increasing the value of *ν* up to 50 times by changing the amount of resin or the volume of supernatant.

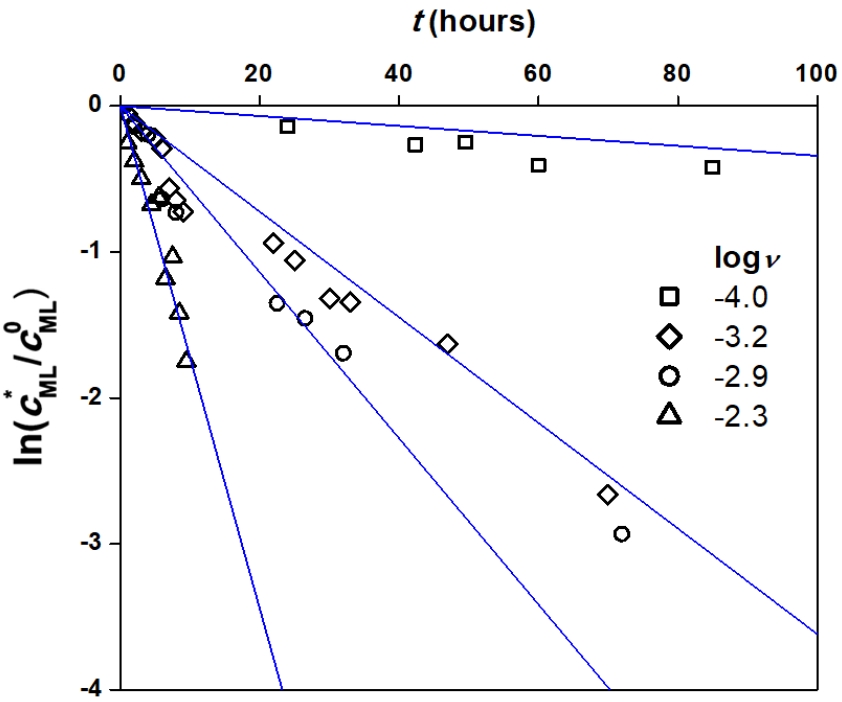

Figure 4.3. Accumulation curves of Ni(II) in Chelex-100 in presence of NTA, at four different V_R/V_T ratios, reported in the legend as log ν. Symbols: experimental data; lines: regression lines. I= 0.1 M, pH= 7.4, c_{NTA}= 8×10^{-5} M.

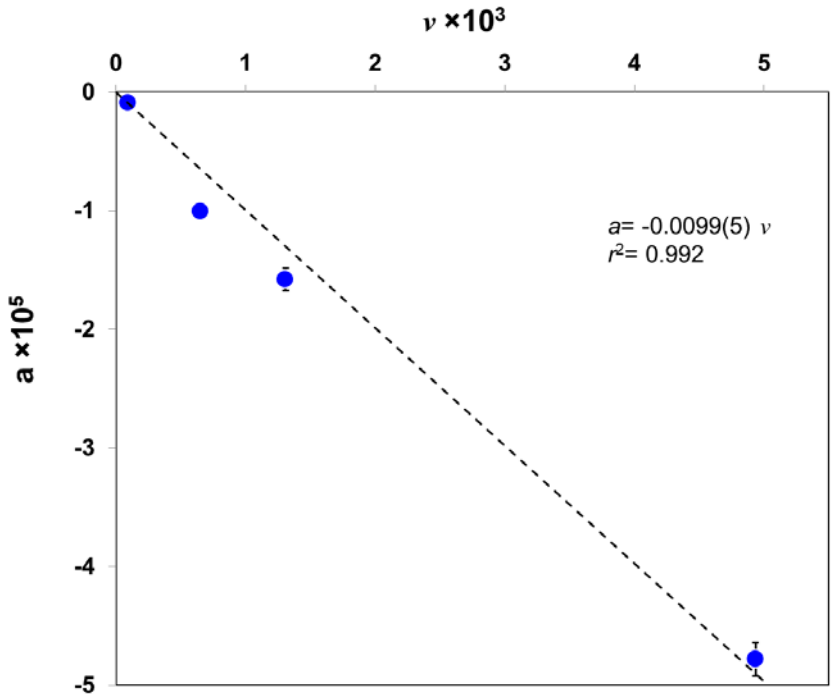

Figure 4.4. Dependence of the slope a of the uptake curves in Fig. 4.3 on the ratio of volumes.

It is now patent the linear relationship that holds between *a* and *v*. For the sake of completeness, it must be said that the linearity between c^*_{ML} and c^0_{ML} and between *a* and *v* can also be explained by models based on different premises, such as the FDM described in Chapter 3. A model based uniquely on metal transport such as FDM could not be applied to the present case, though, as it is not consistent with the negligible influence of the stirring speed that was observed experimentally.

A further consideration is that, according to Eq. (4.23), the slope of the regression line of Fig. 4.4 is equal to $\tilde{k}_d \chi^{z_{ML}}$; this would allow the computation of the dissociation rate constant, if a good estimate of the Boltzmann factor was available. To this purpose we will apply the Donnan model, following the example of Chapter 3 (Eq. (3.24)); the concentration of charges in the resin phase $\tilde{q}$ will be taken equal to the average number of iminodiacetic sites of Chelex,[15] since at pH= 7.4 practically all the resin sites are monoprotonated (total charge -1). For further details on the determination of χ, both experimental and theoretical, we refer to the Appendices (Section 4.6.2).

As the value of the slope in Fig. 4.4 is 9.9×10^{-3} s^{-1} and the estimated Boltzmann factor at *I*= 0.1 M is 5.77, we find that $\log\left(\tilde{k}_d / s^{-1}\right)$= -1.24. The value of $\log \tilde{k}_d$ predicted by the Eigen model (Eqs. (4.3) and (4.4)) for NiNTA is -5.11, several orders of magnitude lower than the one just obtained; this difference will be more thoroughly discussed in the following section.

DEPENDENCE ON THE IONIC STRENGTH

The study of the effects of the ionic strength on the kinetics of uptake is less straightforward. Looking at Eq. (4.23), we see that *I* can affect the kinetics in three ways: through a variation in the Boltzmann factor, in the volume of the resin phase (as shown in Chapter 3) or in the dissociation rate constant. Assessing the dependence of this last parameter on *I* is of particular interest, as it would shed some light on the dissociation mechanism in the resin phase of DGT that has been discussed in a previously published paper.[11] On the one hand, lower *I* should correspond to higher pre-concentration factors, longer equilibration times, and, consequently, to larger (more negative) values of *a*. On the other hand, the resin beads swell at low *I*, slowing down the metal transport; this effect, though, is probably negligible in comparison with the other one. In addition, if the ligand-assisted mechanism hypothesis holds, the

dissociation rate constant should decrease with *I*, due to the decreased electrostatic repulsion between the negative charges on the complexes and the resin sites.

The results of a series of experiments performed in similar conditions, but with *I* ranging from 0.01 to 0.5 M, are presented in Fig. 4.5. The horizontal axis was cut after 200 hours for the sake of readability, even though much longer times were required for the full attainment of equilibrium.

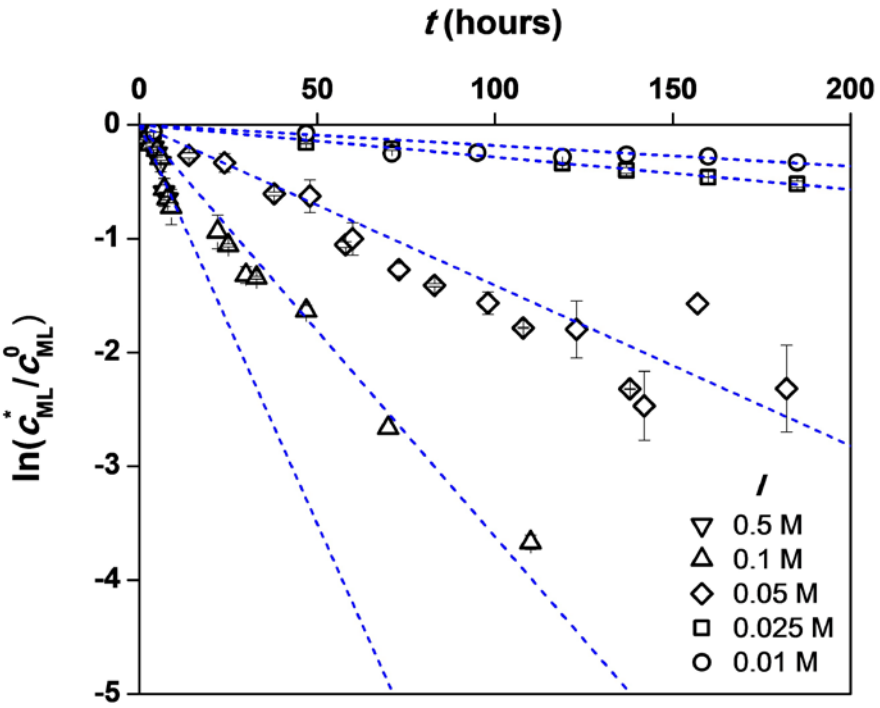

Figure 4.5. Accumulation curves of Ni(II) in Chelex 100 in presence of NTA, at five ionic strengths. The exact values of I are: 0.507 M, 0.098 M, 0.050 M, 0.025 M, 0.010 M. Markers: experimental data; solid lines: UM fittings (slopes reported in Tab. 4.1). The error bars correspond to the standard deviation of the replicates.

As expected, the uptake rate increases with the ionic strength. The linearity of the curves strongly suggests that the overall process is entirely under kinetic control, even at the highest concentrations of background electrolyte. It is, therefore, reasonable to apply Eq. (4.22) to fit the initial part of the curves and, then, to estimate the value of $\tilde{k}_d$ for each case. In order to do so, though, the values of the parameters *v* and χ have to be known. *v* was estimated following the procedure detailed in Chapter 3 to determine the water content of the resin, by measuring its mass loss after being equilibrated at the corresponding pH and ionic strength and, then, oven-dried at 60º C. From the value of *a*, as given by the linear regression of the curves in Fig. 4.5, the dissociation rate

constant in the resin phase could be computed (Tab. 4.1). As indicated in the previous paragraph, the Eigen model predicts $\log\left(\tilde{k}_d/s^{-1}\right)$ = -5.11.

Table 4.1. $\log\tilde{k}_d$ obtained by applying Eq. (4.23)with values of the slope *a* from the regression curves in Fig. 4.5 All the experiments were carried out with the same mass of dry resin (24.5 mg).

***I* (M)**	***a* (s^{-1})**	$\tilde{q}$ **(M)**	***v***	χ_{theo}	$\log\left(\tilde{k}_d/s^{-1}\right)$
0.500	$-4.5(1)\times10^{-5}$	0.55	6.5×10^{-4}	1.68	-0.93
0.100	$-1.01(4)\times10^{-5}$	0.55	6.5×10^{-4}	5.77	-1.05
0.050	$-4.1(2)\times10^{-6}$	0.54	6.7×10^{-4}	10.82	-1.18
0.025	$-7.9(3)\times10^{-7}$	0.53	6.8×10^{-4}	20.89	-1.61
0.010	$-4.29(8)\times10^{-7}$	0.53	6.8×10^{-4}	51.14	-1.49

The uptake is much faster than predicted by the Eigen model, as the experiments with the DGT[11] had already shown. In addition, there is a general decrease of $\tilde{k}_d$ as *I* decreases, which supports the "ligand-assisted mechanism" hypothesis. This mechanism will be confirmed if the variation in the kinetics constant could be related to the variation in *I* through Eq. (4.6). Since the reaction takes place in the resin phase, the ionic strength will have to be corrected accordingly, by applying the following equation, based on the Donnan model (we neglect the amount of Na^+ provided by the resin as counterions):

$$\tilde{I} = \frac{1}{2} I \left(\frac{1}{\chi} + \chi \right) \tag{4.24}$$

Contrary to the prediction of (4.6), no linear relationship between $\log\tilde{k}_d$ and $\tilde{I}^{1/2}$ can be seen in Fig. 4.6.

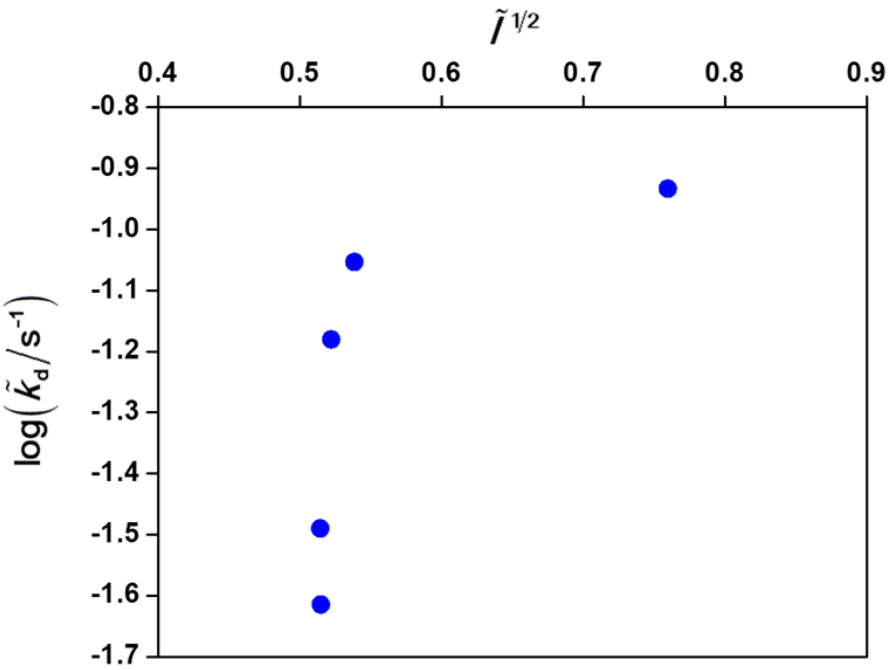

Figure 4.6. Dependence of the dissociation constant with the ionic strength inside the resin. The Debye-Hückel law predicts a linear relationship between $\log\left(\tilde{k}_d/s^{-1}\right)$ *and* $\tilde{I}^{1/2}$ *(Ionic strength expressed in M).*

What Fig. 4.6 does show is that the high concentration of charges inside the resin is buffering $\tilde{I}$, which becomes practically independent from the external *I*, unless in cases where the concentration of background electrolyte is extremely large (as in the point at *I*= 0.5M). Since all the experiments were performed at virtually the same $\tilde{I}$, it is impossible to spot a clear relationship with the rate constant. Even though the dependence on the ionic strength would have been the conclusive evidence, the large difference between the experimental $\tilde{k}_d$ and the Eigen-predicted one strongly suggests that the ligand-assisted hypothesis is still valid.

THE ATTAINMENT OF EQUILIBRIUM

We move on now to the study of the region close to equilibrium. From all the experiments listed in the previous section, only four are taken into consideration in Fig. 4.7, as the quality of the data was sometimes poor at long times.

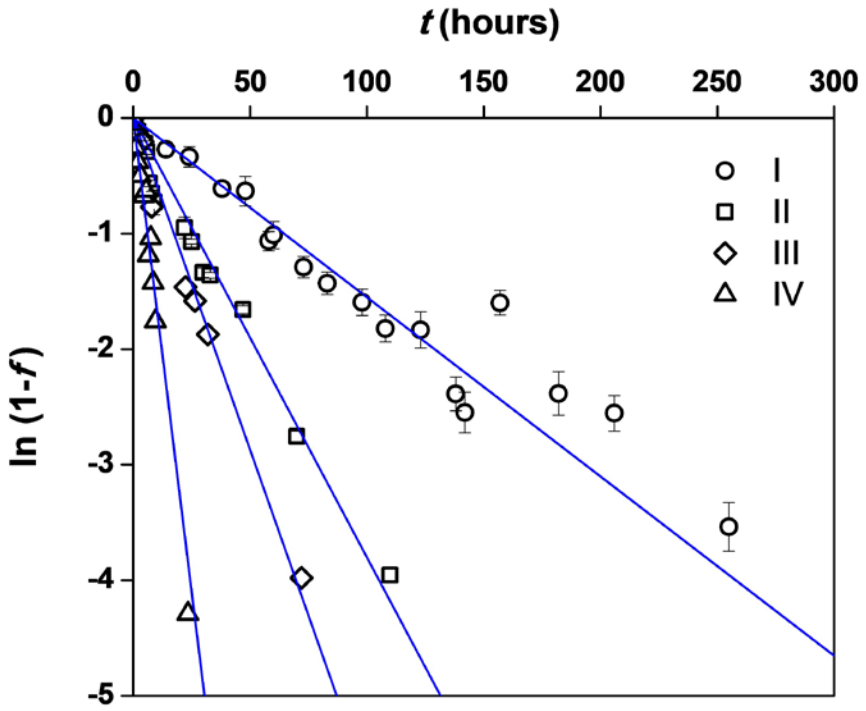

Figure 4.7. Comparison of four NiNTA uptake experiments at different ν and I, with special focus on the region at long times. Sorption data expressed in terms of the fractional attainment of equilibrium. Markers: experimental data; solid lines: SM fits (Eq. (4.17)). The error bars correspond to the standard deviation of the replicates (for III and IV only one replicate was available).

As in this region the contribution of the back reaction (metal-ligand association) cannot be neglected any longer, by fitting the data with the intermediate model (SM), we can estimate not only the dissociation rate constant, but also $\tilde{k}'_a$ and, through Eq. (4.21), the effective stability constant of the complex. The values of $\tilde{K}'$ computed from the data of Fig. 4.7 are given in Tab. 4.2:

Table 4.2. Computation of the effective stability constant $\tilde{K}'$ for the four experiments considered in Fig. 4.7.

Experiment	***I* (M)**	***ν***	**log $\tilde{K}'$**
I	0.050	6.7×10^{-4}	-6.4
II	0.100	6.6×10^{-4}	-6.3
III	0.100	1.3×10^{-3}	-5.1
IV	0.100	4.9×10^{-3}	-5.8

We expect $\tilde{K}'$ to be independent from *ν*, but to be affected by the ionic strength. Actually, no particular trend of $\log\tilde{K}'$ can be spotted, either related to *ν* o to *I*: all the

experiments gave quite similar results. Most likely, the variation in the ionic strength among the experiments is not large enough to have a visible effect (also keeping in mind the buffering effect discussed in the previous paragraph), while the variability among the retrieved values of $\log \tilde{K}'$ is simply a consequence of the experimental uncertainty.

4.4.2. A labile complex: CdNTA

As mentioned before, in the case of a labile complex, the contribution of metal transport cannot be neglected *a priori*. For this reason, apart from the influence of the ionic strength, in this section we will study the effect of the stirring rate, and we will try to describe it by applying the Complete Model.

DEPENDENCE ON THE STIRRING RATE

To verify how the thickness of the DBL affects the overall metal uptake process, two experiments were carried out in identical conditions, but at two radically different rates of the stirrer probe (which correspond to δ= 43.5 µm and 7 µm, as per the results reported in Tab. 3.1).

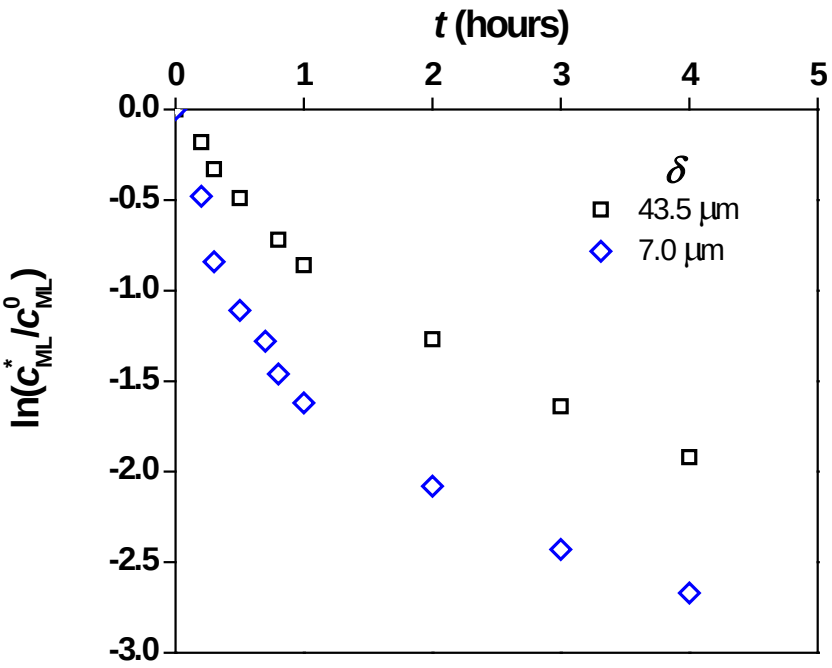

Figure 4.8. Uptake curves of Cd(II) on Chelex-100 in presence of NTA, at different stirring rates (corresponding to δ= 43.5 µm and 7 µm). I= 0.1 M, pH= 7.4, ν= 6.5×10⁻⁴.

A clear increase of the sorption rate was observed at the higher stirring speed (see Fig. 4.8), so confirming the contribution of metal transport in the accumulation of Cd(II) in the resin.

DEPENDENCE ON THE IONIC STRENGTH

Similarly to what shown in the previous section, a series of experiments was performed at different ionic strengths. So as to keep the accumulation rate relatively low we chose to work with rather dilute solutions, with I ranging from 0.100 to 0.007 M in $NaNO_3$. In the following figure the experimental results were fitted with SM (dashed lines) and with CM (solid lines), imposing no restrictions to any of the fitted parameters ϑ, λ_1 and λ_2.

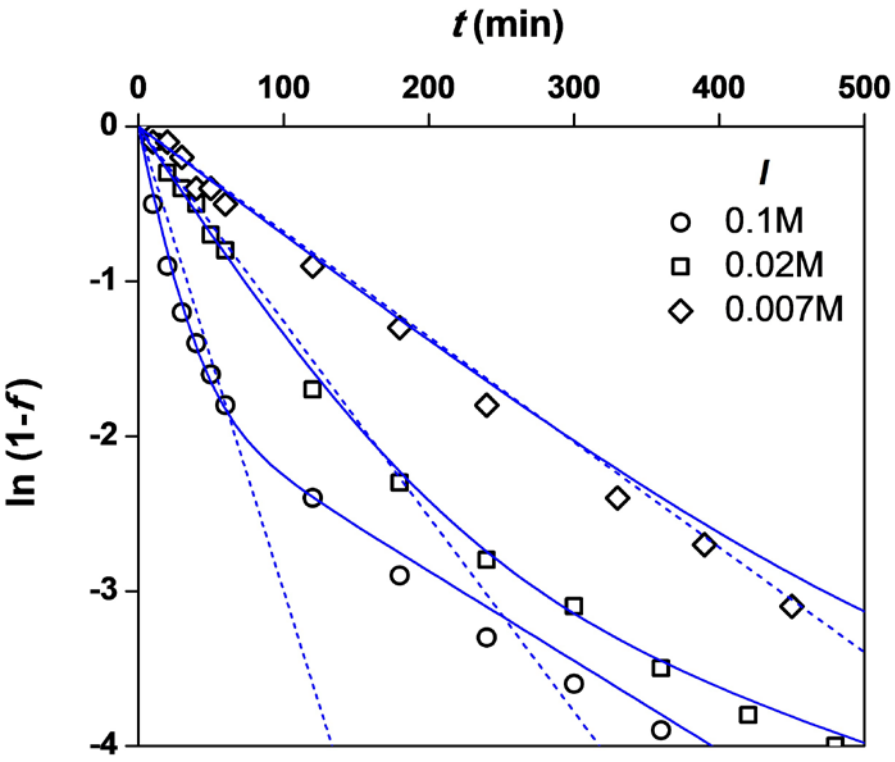

Figure 4.9. Uptake curves of Cd(II) on Chelex-100 in presence of NTA, at three ionic strengths. Markers: experimental results; lines: best-fitting curves, obtained with the Complete Model (solid, Tab. 4.4) and the Simplified Model (dashed).

The experiment at I= 0.007 M can be fitted reasonably well by the SM, but only CM is able to describe the results at the higher ionic strengths. This may be evidence that, in the conditions where the uptake is particularly fast (as it is at high I), it may take place in the same timescale of metal transport, whose contribution cannot therefore be neglected any longer. However, to confirm that this is the reason why the SM fails, it will be necessary to verify that the best-fit values of ϑ, λ_1 and λ_2, the parameters which

describe the effect of metal transport, are consistent. For this purpose it was required to attribute reliable values to the variables of the model, in particular to $\tilde{k}_d$, δ and r_0.

Let us assume that the contribution of metal transport is negligible at least in the experiment at I= 0.007 M. We can then obtain the value of $\tilde{k}_d$ by fitting the initial part of its curve with UM, as done before for NiNTA. The resulting $\log\left(\tilde{k}_d / s^{-1}\right)$ is equal to 0.91 (see the last line of Tab. 4.3), rather close to the value provided by the Eigen model, 0.62.

Table 4.3. Parameters used for computing $\log \tilde{k}_d$ from the slope a of the regression curves for the CdNTA systems in Fig. 4.9. All the experiments were carried out with the same mass of dry resin (24.5 mg).

I (M)	a (s^{-1})	$\tilde{q}$ (M)	v	χ	$\log\left(\tilde{k}_d / s^{-1}\right)$
0.100[a]	-5.90×10^{-4}	0.55	6.5×10^{-4}	5.84	0.73
0.020[a]	-2.1×10^{-4}	0.53	6.8×10^{-4}	32.9	0.98
0.007	-1.2×10^{-4}	0.43	8.4×10^{-4}	60.8	0.91

[a] in the experiments at I= 0.1 and 0.02 M a non-negligible role of metal transport is hypothesized and as a consequence the UM could not be applied. The corresponding values of $\log \tilde{k}_d$ are given just for comparison purposes.

From this result and previous measurements with the DGT,[11] it can be concluded that the dissociation of CdNTA follows the Eigen mechanism, meaning that $\tilde{k}_d$ is not influenced by I.

The thickness of the diffusive layer was not directly accessible; it was taken equal to 7×10^{-6} m, the value fitted at this stirring rate in the experiments in absence of ligand (see Tab. 3.1.). r_0 was taken as 5×10^{-5} m, the average radius of the particle, thus neglecting the variation due to the swelling, most likely not significant. $\tilde{k}'_a$ was calculated from the fitted value of $\tilde{k}_d$ and the effective stability constant $\tilde{K}'$, as given by Eq. (4.21). The values of ϑ, λ_1 and λ_2 computed from these parameters by applying Eqs. (4.11), (4.12) and (4.15) are reported in Tab. 4.4, along with those coming from the fitting of the curves in Fig. 4.9.

Table 4.4. Comparison of the values of the parameters of CM (ϑ, λ_1 and λ_2) obtained by fitting the experimental data reported in Fig. 4.9 (Fitted) and by direct computation applying Eqs. (4.11), (4.12) and (4.15) (Computed).

	Fitted			**Computed**		
IS (M)	ϑ	λ_1	λ_2	ϑ	λ_1	λ_2
0.100	-2.32×10^{-5}	-8.92×10^{-4}	-9.65×10^{-5}	-9.98×10^{-9}	-33	-6.88×10^{-4}
0.020	-2.64×10^{-5}	-2.55×10^{-4}	-5.70×10^{-5}	-6.58×10^{-10}	-142	-1.70×10^{-4}
0.007	---	---	-1.13×10^{-4}	-4.45×10^{-10}	-256	-1.19×10^{-4}

The computed values are strikingly different from the best-fit ones. In particular, the so negative values of λ_1 in the "computed" column cause the first exponential of Eq. (4.10) to drop practically to zero and, as a result, the CM *de facto* reverts into the linear SM. The model is still able to describe the trend with respect to *I*, but the fitting of the central part is very poor, as made clear in Fig. 4.10:

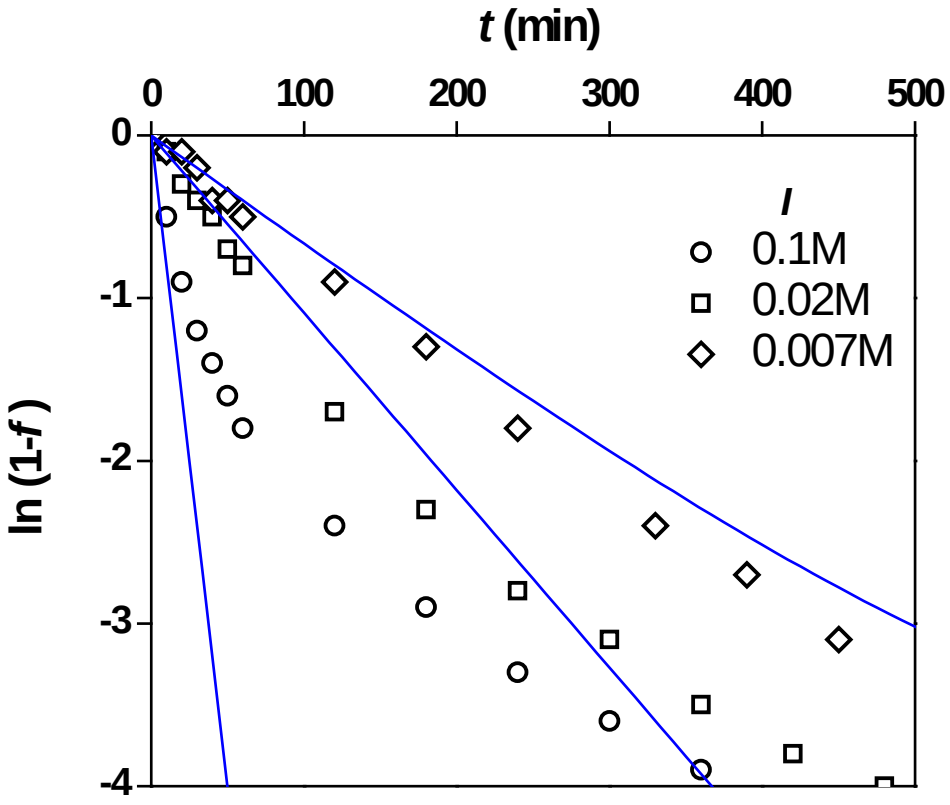

Figure 4.10. Experimental data presented in Fig.4.9 (symbols), compared with the results of CM, implemented using the computed values of ϑ, λ_1 and λ_2.

The experiments at different stirring rates suggested that the contribution of metal transport may be not negligible in some situations, and the poor performance of the SM

at high *I* seemed to point in the same direction; we have just found, though, that apparently CM is not an accurate option either.

A tentative explanation might invoke the contribution of the free metal to the whole flux, an aspect not considered by the model; it must be rejected, though, as it is likely to be negligible and, even if it played a significant role, it would make the uptake faster, rather than slower as observed. Further options that could be assayed are the influence of internal diffusion or the dissociation of the complexes in the stagnant layer.

4.5. Conclusions

A model, valid for a broad range of labilities and timescales, was developed to describe the accumulation with time of metal ions on a chelating sorbent, in presence of a competing ligand. Although the resulting expression, in its simplest incarnation, is formally similar to other semi-empirical models,[7] it stems from a stronger theoretical basis that allows to describe the dependence on the ionic strength and also includes the possibility of control by external diffusion. Even though a full understanding of the contribution of metal transport is yet to come, some light might be shed by performing numerical simulations of the uptake, taking into account a larger number of factors (*e.g.* the influence of control of internal diffusion, the contribution of free metal or the dissociation of the complex in the DBL).

The resin-based methods to assess the labile metal fraction assume that the dissociation of the complexes is the rate-determining step of the whole accumulation. There are cases (like NiNTA) where this assumption was proved to be correct, but the rate constant inside the resin phase is several orders of magnitude higher than in the bulk solution, as the dissociation follows different pathways in the two media. Most kinetic constants derived with this method should, then, be refined in order to extrapolate the behaviour of metal complexes in water. The ligand-assisted mechanism hypothesis, which may help in this regard, has been substantially confirmed, as the $\tilde{k}_{\mathrm{d}}$ experimentally determined for NiNTA were found to increase with the ionic strength.

The dissociation of labile complexes (like CdNTA), on the contrary, was found to follow quite closely the Eigen model, apart from some deviations in the experiments at higher *I*, whose reason is still under debate.

4.6. Appendices

4.6.1. Mathematical formulation of the models

COMPLETE MODEL

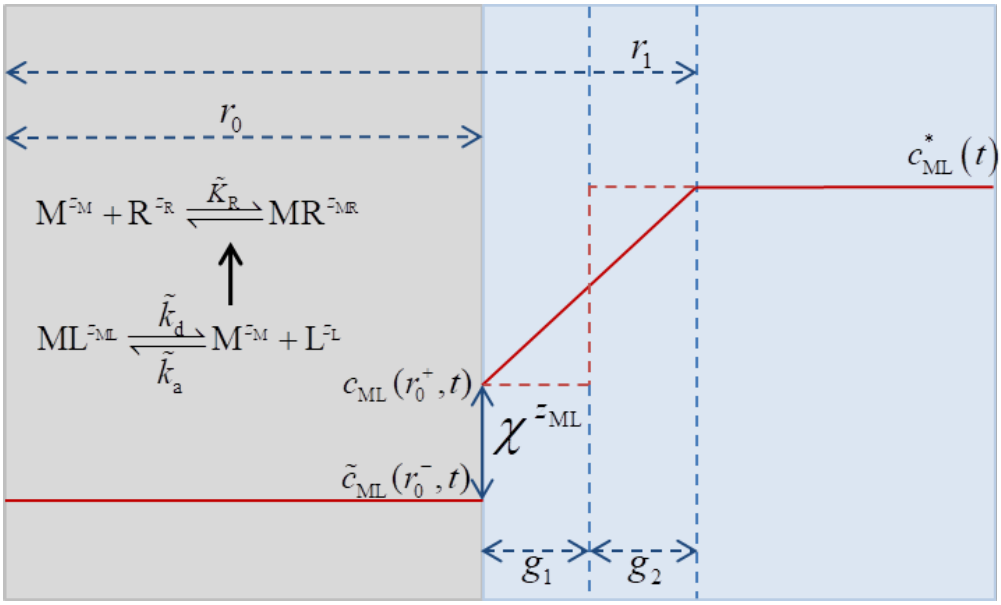

Figure A4.1. Schematic representation of the radial concentration profiles in the resin (grey background) and aqueous solution (blue background) phases, as per the hypotheses of the complete model. The solid red line represents the actual concentration, while the dashed red line represents the concentration modelled considering the virtual volumes g_1 and g_2.

The complete model is based on the following assumptions:

1. The supply to an individual bead results from diffusion in spherical geometry. The beads are spheres of fixed radius r_0. Diffusion in the solution surrounding the bead extends just to a finite distance r_1.
2. There is excess of ligand conditions, so that c_L (and $\tilde{c}_L$) are constant throughout the experiment and in solution all the metal is present as complex. The complex only dissociates inside the bead.
3. In the resin phase, the concentration of free metal is lumped with the concentration of metal bound to the resin, as the equilibrium equation holds:

$$\tilde{c}_M \equiv \tilde{c}_{MR} + \tilde{c}_{M,free} = \tilde{c}_{M,free}\left(1 + \tilde{K}'_R\right) \quad \text{(A4.1)}$$

4. Any gradient in the concentration profile inside the bead is neglected
5. There is instantaneous equilibrium at the bead surface, across which the complexes distribute according to the Boltzmann partitioning factor χ^{z_j}.

$$\tilde{c}_{\mathrm{ML}}\left(r_0^-,t\right)=\chi^{z_{\mathrm{ML}}}c_{\mathrm{ML}}\left(r_0^+,t\right) \tag{A4.2}$$

The continuity equation for ML in one bead can be written as:

$$\frac{4}{3}\pi r_0^2\frac{d\tilde{c}_{\mathrm{ML}}(t)}{dt}=\frac{4}{3}\pi r_0^2\left(\tilde{k}_{\mathrm{a}}c_{\mathrm{L}}\frac{\tilde{c}_{\mathrm{M}}(t)}{1+K'_{\mathrm{R}}}-\tilde{k}_{\mathrm{d}}\tilde{c}_{\mathrm{ML}}(t)\right)+4\pi r_0^2J_{\mathrm{ML}} \tag{A4.3}$$

Equation (A4.3) can be recast as:

$$\frac{d\tilde{c}_{\mathrm{ML}}(t)}{dt}=\tilde{k}'_{\mathrm{a}}\tilde{c}_{\mathrm{M}}(t)-\tilde{k}_{\mathrm{d}}\tilde{c}_{\mathrm{ML}}(t)+\frac{3}{r_0}J_{\mathrm{ML}} \tag{A4.4}$$

Where the effective association rate constant $\tilde{k}'_{\mathrm{a}}$ is introduced:

$$\tilde{k}'_{\mathrm{a}}\equiv\frac{\tilde{k}_{\mathrm{a}}\tilde{c}_{\mathrm{L}}}{1+K'_{\mathrm{R}}} \tag{A4.5}$$

For $\tilde{k}'_{\mathrm{a}}$ to be a constant, we are assuming excess of ligand (constant $\tilde{c}_{\mathrm{L}}$) and excess of resin sites (constant K'_{R}).

By assuming steady state conditions the flux of complexed metal can be computed by applying Fick's first law:

$$J_{\mathrm{ML}}=\frac{D_{\mathrm{ML}}}{\delta}\left(c^*_{\mathrm{ML}}(t)-c_{\mathrm{ML}}\left(r_0^+,t\right)\right) \tag{A4.6}$$

The continuity equation for the "lumped" metal (that is, the ions bound to the resin and the free ones) in one bead:

$$\frac{d\tilde{c}_{\mathrm{M}}(t)}{dt}=-\tilde{k}'_{\mathrm{a}}\tilde{c}_{\mathrm{M}}(t)+\tilde{k}_{\mathrm{d}}\tilde{c}_{\mathrm{ML}}(t) \tag{A4.7}$$

As done in Section 3.7.2, let us ideally split the diffusive boundary layer into the virtual volumes g_1 and g_2, where the concentration profile is flat and equal to, respectively, $c_{\mathrm{ML}}\left(r_0^+,t\right)$ and $c^*_{\mathrm{ML}}(t)$.

With this division in mind, the total balance of metal in all the system is:

$$V_{\mathrm{R}}\left(\tilde{c}_{\mathrm{M}}(t)+\tilde{c}_{\mathrm{ML}}(t)\right)+g_1c_{\mathrm{ML}}\left(r_0^+,t\right)+\left(V_{\mathrm{T}}-V_{\mathrm{R}}-g_1\right)c^*_{\mathrm{ML}}(t)=\left(V_{\mathrm{T}}-V_{\mathrm{R}}\right)c^0_{\mathrm{T,M}} \tag{A4.8}$$

where $c^0_{\mathrm{T,M}}$ is the total metal concentration at t= 0.

Solving for $c^*_{\mathrm{ML}}(t)$ in (A4.8), and combining with (A4.6) and (A4.2), we obtain the following expression for the flux:

$$J_{\mathrm{ML}} = \frac{3D_{\mathrm{ML}}}{r_0\delta}\left(\frac{1-v}{1-v-\varpi_1 v}c^0_{\mathrm{T,M}} - \frac{v}{1-v-\varpi_1 v}\tilde{c}_{\mathrm{M}}(t) - \frac{1-v+v\chi^{z_{\mathrm{ML}}}}{(1-v-\varpi_1 v)\chi^{z_{\mathrm{ML}}}}\tilde{c}_{\mathrm{ML}}(t)\right) \qquad \text{(A4.9)}$$

where $\varpi_1 \equiv \frac{g_1}{V_{\mathrm{R}}}$. In most cases the term ϖ_1, which represents the contribution of the metal in the diffusive layer, could be neglected; the equations given in the body of the chapter do not take it into account.

From the equation of the mass balance (A4.8), the concentration at equilibrium can be derived:

$$c^{\infty}_{\mathrm{ML}} = \frac{c^0_{\mathrm{ML}}}{\frac{v}{1-v}\left(\frac{\tilde{k}_{\mathrm{d}}}{\tilde{k}'_{\mathrm{a}}}+1\right)\chi^{z_{\mathrm{ML}}}+1} \qquad \text{(A4.10)}$$

where $c_{\mathrm{T,M}}$ is the initial concentration (t= 0) in the solution, v is the ratio of V_{R} (the resin volume) and V_{T} (the total volume), $\tilde{k}_{\mathrm{d}}$ is the dissociation constant of the ML complex inside the resin and $\chi^{z_{\mathrm{ML}}}$ is the Donnan partitioning factor.

By introducing the following grouping of variables:

$$p \equiv -\left(\frac{3D_{\mathrm{ML}}v\left(1+\frac{\varpi_1}{\chi^{z_{\mathrm{ML}}}}\right)}{r_0\delta(1-v-\varpi_1 v)} + \frac{3D_{\mathrm{ML}}}{r_0\delta\chi^{z_{\mathrm{ML}}}} + \tilde{k}_{\mathrm{d}}\right) \qquad \text{(A4.11)}$$

$$s \equiv \tilde{k}'_{\mathrm{a}} - \frac{3D_{\mathrm{ML}}v}{r_0\delta(1-v-\varpi_1 v)} \qquad \text{(A4.12)}$$

$$d \equiv \frac{3D_{\mathrm{ML}}(1-v)}{r_0\delta(1-v-\varpi_1 v)}c^0_{\mathrm{ML}} \qquad \text{(A4.13)}$$

the Eqs (A4.4) and (A4.7) can be rewritten as:

$$\frac{d\tilde{c}_{\mathrm{ML}}(t)}{dt} = p\,\tilde{c}_{\mathrm{ML}}(t) + s\,\tilde{c}_{\mathrm{M}}(t) + d \qquad \text{(A4.14)}$$

$$\frac{d\tilde{c}_{\mathrm{M}}(t)}{dt} = \tilde{k}_{\mathrm{d}}\tilde{c}_{\mathrm{ML}}(t) - \tilde{k}'_{\mathrm{a}}\tilde{c}_{\mathrm{M}}(t) \qquad \text{(A4.15)}$$

that constitutes a system of ordinary differential equations whose initial conditions are:

$$\tilde{k}_{\mathrm{d}}\tilde{c}_{\mathrm{ML}}(t) = 0 \;;\; \tilde{c}_{\mathrm{M}}(t) = 0 \text{ at } t\text{= 0.} \qquad \text{(A4.16)}$$

The solution of the system, via the diagonalization method, can be written in terms of the eigenvalues:

$$\lambda_1 = \frac{1}{2}\left(-\tilde{k}'_a + p - \sqrt{\left(\tilde{k}'_a + p\right)^2 + 4\tilde{k}_d s} \right) \tag{A4.17}$$

$$\lambda_2 = \frac{1}{2}\left(-\tilde{k}'_a + p + \sqrt{\left(\tilde{k}'_a + p\right)^2 + 4\tilde{k}_d s} \right) \tag{A4.18}$$

as

$$c^*_{ML}(t) = c^\infty_{ML} + \vartheta\, e^{\lambda_1 t} + \left(c^0_{ML} - c^\infty_{ML} - \vartheta\right) e^{\lambda_2 t} \tag{A4.19}$$

where ϑ is a grouping of parameters defined as:

$$\vartheta = -\frac{v\tilde{k}_d}{(1 - v - \varpi_1 v)(\lambda_1 - \lambda_2)\lambda_1} d + \frac{v\left(1 + \frac{\varpi_1}{\chi^{z_{ML}}}\right)\left(\tilde{k}'_a + \lambda_1\right)}{(1 - v - \varpi_1 v)(\lambda_1 - \lambda_2)\lambda_1} d \tag{A4.20}$$

Eq. (A4.19) is Eq. (4.10) in the body of the chapter, which is the key equation of the CM. Also note that, when ϖ_1, Eqs. (A4.11), (A4.13), (A4.12) and (A4.20) revert to (4.13), (4.16), (4.14) and (4.15).

SIMPLIFIED MODEL (BACKWARD REACTION AND NO TRANSPORT)

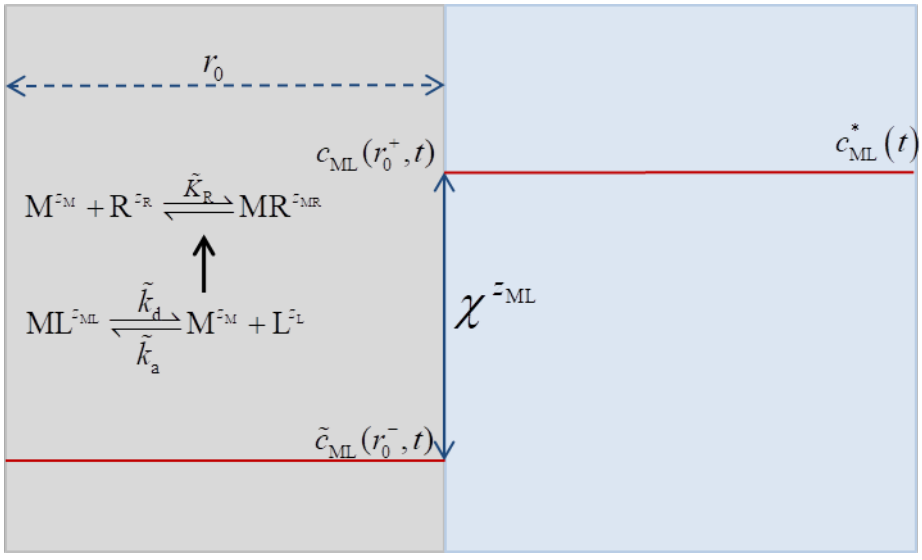

Figure A4.2. Schematic representation of the radial concentration profiles as per the hypotheses of the simplified model.

The main assumptions of the complete model are still valid, but the contribution of metal transport is negligible (the concentration at the interface is always the bulk one).

With this additional hypothesis, Eq. (A4.2) becomes

$$\tilde{c}_{\mathrm{ML}}\left(r_0^-,t\right)=\chi^{z_{\mathrm{ML}}}c_{\mathrm{ML}}^{*}\left(t\right) \tag{A4.21}$$

while the continuity equation for the complex becomes:

$$\left(V_{\mathrm{T}}-V_{\mathrm{R}}\right)\frac{dc_{\mathrm{ML}}^{*}\left(t\right)}{dt}=V_{\mathrm{R}}\left(\tilde{k}_{\mathrm{a}}'\tilde{c}_{\mathrm{M}}\left(t\right)-\tilde{k}_{\mathrm{d}}\chi^{z_{\mathrm{ML}}}c_{\mathrm{ML}}^{*}\left(t\right)\right)-V_{\mathrm{R}}\chi^{z_{\mathrm{ML}}}\frac{dc_{\mathrm{ML}}^{*}\left(t\right)}{dt} \tag{A4.22}$$

Equation (A4.7) becomes:

$$\frac{d\tilde{c}_{\mathrm{M}}\left(t\right)}{dt}=-\tilde{k}_{\mathrm{a}}'\tilde{c}_{\mathrm{M}}\left(t\right)+\tilde{k}_{\mathrm{d}}\chi^{z_{\mathrm{ML}}}c_{\mathrm{ML}}^{*}\left(t\right) \tag{A4.23}$$

The system constituted by Eqs. (A4.22) and (A4.23) is solved, leading to:

$$c_{\mathrm{ML}}^{*}\left(t\right)=c_{\mathrm{ML}}^{\infty}+\left(c_{\mathrm{ML}}^{0}-c_{\mathrm{ML}}^{\infty}\right)\mathrm{e}^{at} \tag{A4.24}$$

where:

$$a=-\left(\tilde{k}_{\mathrm{a}}'+\upsilon\chi^{z_{\mathrm{ML}}}\,\tilde{k}_{\mathrm{d}}\right) \tag{A4.25}$$

and:

$$\upsilon\equiv\frac{V_{\mathrm{R}}}{V_{\mathrm{T}}-V_{\mathrm{R}}+V_{\mathrm{R}}\chi^{z_{\mathrm{ML}}}}=\frac{v}{1-v+v\chi^{z_{\mathrm{ML}}}} \tag{A4.26}$$

for practical purposes υ will be very close to v which is $V_{\mathrm{R}}/V_{\mathrm{T}}$ (*i.e.* a very small number).

c_{ML}^{∞} is given by Eq. (A4.10) above. Eq. (A4.24) can be re-written as:

$$\ln\left(\frac{c_{\mathrm{ML}}^{*}\left(t\right)-c_{\mathrm{ML}}^{\infty}}{c_{\mathrm{ML}}^{0}-c_{\mathrm{ML}}^{\infty}}\right)=-at \tag{A4.27}$$

which is Eq. (4.17), the main equation of the SM.

ULTRA-SIMPLIFIED MODEL (NO BACKWARD REACTION AND NO TRANSPORT)

A further simplified version of the model is derived by neglecting the backward reaction in Eq. (A4.23), so as to obtain:

$$\left(V_{\mathrm{T}}-V_{\mathrm{R}}\right)\frac{dc_{\mathrm{ML}}^{*}\left(t\right)}{dt}=-V_{\mathrm{R}}\tilde{k}_{\mathrm{d}}\chi^{z_{\mathrm{ML}}}c_{\mathrm{ML}}^{*}\left(t\right)-V_{\mathrm{R}}\chi^{z_{\mathrm{ML}}} \tag{A4.28}$$

which, using the definition of υ given in Eq. (A4.26), becomes:

$$\frac{dc^*_{ML}(t)}{dt} = -\upsilon \tilde{k}_d \chi^{z_{ML}} c^*_{ML}(t) \quad \text{(A4.29)}$$

whose integration leads to:

$$\ln\left(\frac{c^*_{ML}(t)}{c^0_{ML}}\right) = -at \quad \text{(A4.30)}$$

where:

$$a = \upsilon \tilde{k}_d \chi^{z_{ML}} \approx v \tilde{k}_d \chi^{z_{ML}} \quad \text{(A4.31)}$$

4.6.2. Determination of χ

DETERMINATION FROM DONNAN PARTITIONING

The Boltzmann partitioning factor can be computed by applying the Donnan model. Let us assume that the resin is a volume separate from the external solution containing charged sites at concentration $\tilde{q}$. Then, in the hypothesis that there is only one monovalent background electrolyte (*i.e.* a salt that dissolves to give the anion A^- and the cation C^+), which distributes across the resin according to a partitioning factor χ:

$$\tilde{c}_{A^-} = \chi^{-1} c_{A^-} \text{ and } \tilde{c}_{C^+} = \chi c_{C^+} \quad \text{(A4.32)}$$

the charge balance in the resin phase reads as follows:

$$\tilde{q} + \tilde{c}_{A^-} = \tilde{c}_{C^+} \quad \text{(A4.33)}$$

As a first approximation, let us impose the activity coefficients of all species equal to 1, as done throughout the main text. Since there is only one monovalent background electrolyte the ionic strength is simply: $c_{A^-} = c_{C^+} = I$. By combining the Eqs. (A4.32) and (A4.33) and rearranging we obtain:

$$I\chi^2 - \tilde{q}\chi - I = 0 \quad \text{(A4.34)}$$

Eq. (A4.34) is a quadratic equation that can be readily solved to give:[16]

$$\chi = \frac{\tilde{q}}{2I} + \sqrt{\left(\frac{\tilde{q}}{2I}\right)^2 + 1} \quad \text{(A4.35)}$$

The relationship can be adapted to account for activity coefficients different from 1. It can be shown that the actual Boltzmann factor χ_{real}, given by the ratio of activities, is related to the effective Boltzmann factor (χ, from the ratio of concentrations) by the following relationship:

$$\chi_{\text{real}} = \frac{\gamma_1}{\tilde{\gamma}_1}\chi \qquad \text{(A4.36)}$$

where γ_1 and $\tilde{\gamma}_1$ are the activity coefficients of monovalent species in the solution and in the resin phase.

EXPERIMENTAL DETERMINATION

In order to determine experimentally the value of χ, three aliquots of resins were equilibrated in $NaNO_3$ solutions at different ionic strengths (0.1, 0.011 and 0.002 M), each of them containing a small concentration of Rb^+; χ is found as the ratio of the concentration of Rb^+ in the resin phase and in the supernatant. The metal bound to the resin was eluted with HNO_3 20%, as done for the DGT.[17] Rb^+ is not specifically bound by Chelex, and we suppose that it partitions between the two phases according to the Boltzmann factor alone. In the literature, it is argued[18] that, in the case of huge ions such as Rb^+, steric hindrance may also play a role in the partitioning. However, this possible source of bias was ruled out by another member of the Lleida group by carrying out analogue experiments with Na^+, an ion of much smaller size.[19]

In Tab. A4.1 below, the experimental values of χ are compared with those computed applying Eq. (A4.35):

Table A4.1. Comparison of the values of the Boltzmann factor computed with the Donnan model (χ_{calc}) and those estimated from the equilibration of the resin with Rb^+ (χ_{exp}).

***I* (M)**	**0.100**	**0.011**	**0.002**
χ_{calc}	5.77	51.1	350
χ_{exp}	7.1	53.1	168

With the exception of the point at lower ionic strength, the correspondence between experimental and theoretical data is very good; the difference in the values at I= 2 mM may be a consequence of the error on the estimation of V_R or by an effective deviation from the Donnan-predicted values.

This discrepancy aside, the experiments confirm the huge variation of χ predicted by the Donnan model, a consequence of the high charge density in the beads.

4.7. References

(1) Tusseau-Vuillemin, M. H.; Gilbin, R.; Bakkaus, E.; Garric, J. Performance of diffusion gradient in thin films to evaluate the toxic fraction of copper to Daphnia magna. *Environ. Toxicol. Chem.* **2004**, *23* (9), 2154–2161.

(2) Degryse, F.; Smolders, E.; Merckx, R. Labile Cd complexes increase Cd availability to plants. *Environ. Sci. Technol.* **2006**, *40* (3), 830–836.

(3) Buckley, J. A.; Yoshida, G. A.; Wells, N. R.; Aquino, R. T. Toxicities of total and chelex-labile cadmium to salmon in solutions of natural water and diluted sewage with potentially different cadmium complexing capacities. *Water Res.* **1985**, *19* (12), 1549–1554.

(4) Guthrie, J. W.; Mandal, R.; Salam, M. S. A.; Hassan, N. M.; Murimboh, J.; Chakrabarti, C. L.; Back, M. H.; Grégoire, D. C. Kinetic studies of nickel speciation in model solutions of a well-characterized humic acid using the competing ligand exchange method. *Anal. Chim. Acta* **2003**, *480* (1), 157–169.

(5) Shi, Z.; Wang, P.; Peng, L.; Lin, Z.; Dang, Z. Kinetics of heavy metal dissociation from natural organic matter: roles of the carboxylic and phenolic sites. *Environ. Sci. Technol.* **2016**, *50* (19), 10476–10484.

(6) Yapici, T.; Fasfous, I. I.; Zhao, J.; Chakrabarti, C. L. Effects of various competing ligands on the kinetics of trace metal complexes of Laurentian Fulvic Acid in model solutions and natural waters. *Anal. Chim. Acta* **2009**, *636* (1), 6–12.

(7) Chakrabarti, C. L.; Yanjia, L.; Grégoire, D. C.; Back, M. H.; Schroeder, W. H. Kinetic studies of metal speciation using Chelex cation exchange resin: Application to cadmium, copper, and lead speciation in river water and snow. *Environ. Sci. Technol.* **1994**, *28* (11), 1957–1967.

(8) Mandal, R.; Salam, M. S. A.; Murimboh, J.; Hassan, N. M.; Chakrabarti, C. L.; Back, M. H.; Grégoire, D. C. Competition of Ca(II) and Mg(II) with Ni(II) for binding by a well- characterized fulvic acid in model solutions. *Environ. Sci. Technol.* **2000**, *34* (11), 2201–2208.

(9) Alvarez, M. B.; Malla, M. E.; Batistoni, D. A. Performance evaluation of two chelating ion-exchange sorbents for the fractionation of labile and inert metal species from aquatic media. *Anal. Bioanal. Chem.* **2004**, *378* (2), 438–446.

(10) Bowles, K. C.; Apte, S. C.; Batley, G. E.; Hales, L. T.; Rogers, N. J. A rapid

Chelex column method for the determination of metal speciation in natural waters. *Anal. Chim. Acta* **2006**, *558* (1–2), 237–245.

(11) Puy, J.; Galceran, J.; Cruz-González, S.; David, C. A.; Uribe, R.; Lin, C.; Zhang, H.; Davison, W. Measurement of metals using DGT: Impact of ionic strength and kinetics of dissociation of complexes in the resin domain. *Anal. Chem.* **2014**, *86* (15), 7740–7748.

(12) Eigen, M.; Wilkins, R. G. The kinetics and mechanism of formation of metal complexes. In *Mechanisms of inorganic reactions*; Kleinberg, J., Murmann, R. K., Fraser, R. T. M., Bauman, J., Eds.; America Chemical Society: Washington (DC), 1965; 55–80.

(13) Morel, F. M. M. *Principles of Aquatic Chemistry*; John Wiley & Sons Ltd: New York, 1983.

(14) Atkins, P. W.; De Paula, J. *Physical Chemistry*, 8th ed.; Oxford University Press: Oxford, 2006.

(15) Pesavento, M.; Biesuz, R.; Gallorini, M.; Profumo, A. Sorption mechanism of trace amounts of divalent metal ions on a chelating resin containing iminodiacetate groups. *Anal. Chem.* **1993**, *65* (18), 2522–2527.

(16) Ohshima, H. *Theory of Colloid and Interfacial Electric Phenomena, 1st Ed.*; Elsevier Academic Press: Cambridge (MA), 2006.

(17) Altier, A. Diffusive Gradient in Thin Films (DGT) beyond perfect sink conditions. Doctoral thesis, Universitat de Lleida, 2018.

(18) Fatin-Rouge, N.; Milon, A.; Buffle, J.; Goulet, R. R.; Tessier, A. Diffusion and partitioning of solutes in agarose hydrogels: The relative influence of electrostatic and specific interactions. *J. Phys. Chem. B* **2003**, *107* (44), 12126–12137.

(19) Altier, A.; Jiménez-Piedrahita, M.; Rey-Castro, C.; Cecilia, J.; Galceran, J.; Puy, J. Accumulation of Mg to Diffusive Gradients in Thin Films (DGT) devices: kinetic and thermodynamic effects of the ionic strength. *Anal. Chem.* **2016**, *88* (20), 10245–10251.

5. Assessment of labilities of metal complexes with the Dynamic Ion Exchange Technique

Part of this this chapter has been submitted to *Environmental Chemistry*

5.1. Introduction

In Chapter 1, while reviewing the main techniques developed for the purpose of studying metal speciation, we mentioned the IET (Ion Exchange Technique), firstly employed by Cantwell[1] and later applied by many others, including Campbell and Fortin.[2] In brief, the IET is a column equilibration technique consisting of: (*i*) an accumulation step, where the sample solution is flushed through a column packed with an ion exchanger until equilibrium is attained, and (*ii*) a subsequent elution step where the amount of metal accumulated is measured with a suitable elemental analysis technique. This amount can, then, be related to the corresponding free metal concentration in solution *via* a conditional exchange constant determined by calibrating the system in the conditions of interest.

The knowledge acquired with the IET is related only to the thermodynamic aspects of the systems studied and, though valuable, in several cases is too limited;[3] dynamic speciation techniques, like the DGT (Diffusive Gradient in Thin films), aims at providing information beyond thermodynamics, such as rates of association/dissociation and mobility.

Recent work[4–6] has considered the possibility of extracting meaningful information from the time-resolved accumulations in IET columns. In this new approach, called Dynamic Ion Exchange Technique (DIET), the amount of metal accumulated by the resin is recorded as a function of the contact time. The initial slope of the curve of accumulated metal vs. time is then related to the free metal concentration in the sample

via an empirical relation.[4] The main advantage of DIET over IET is that it is much more economical both in terms of time and sample volume, as it does not require waiting for the full attainment of equilibrium. This can become critical when equilibration is particularly slow, as in the case of highly charged ions[5] or at low ionic strengths. Being the DIET in its early stages, there are many questions still awaiting an answer, in particular whether the slope actually reflects only the binding of free metal ion or if the labile species contribute as well.[4]

Most work about dynamic speciation with packed columns has just relied on semi-empirical fractionation schemes,[7–10] perhaps due to a limited interpretative framework. In addition, in most of these cases, the sorbent materials are weakly acidic, chelating resins like Chelex 100,[11] while little information is found about strongly acidic, ion-exchange resins like Dowex, which display a radically different behaviour.

For these reasons, in this chapter we will try to give a comprehensive interpretation of DIET, with a focus on retrieving information on the kinetic properties of the complexes. Four models are presented, (and derived in detail in the Appendices to this chapter):

- Model I describes the time-dependent accumulation in an individual bead.
- Model II describes accumulation in an individual bead at steady state. The solution to this model is formally similar to the one derived for complex penetration in the DGT[12,13] and allows the computation of ξ, the lability degree (see Eq. (1.1)).
- Model III describes the accumulation in the whole column considering the transient, predicting how the concentration in the effluent changes over time. A treatment to a similar problem had already been given in the classical engineering literature.[14]
- Model IV describes the accumulation in the whole column focusing on the initial (quasi) steady-state regime. A DIET-labile concentration (c_{DIET}), analogous to the DGT-labile concentration[15,16] is defined and practical formulas to compute it are proposed.

5.2. Materials and Methods

5.2.1. Equipment and reagents

The background solution for all the experiments has the major ion composition of a typical algal growth medium[17] (Ca(II): 6.8×10^{-5} M; Mg(II): 8.12×10^{-5} M; K(I) 4.22×10^{-3} M; all the cations were introduced as nitrate salts). In all the experiments the total ionic strength of the medium is $I = 4.4\times10^{-3}$ M, while the pH was fixed to 6.0 with 1×10^{-3} M 2-(N-morpholino)ethanesulfonic acid (MES).

5.2.2. The columns

Three different types of the strongly acidic cation exchange Dowex 50 sulphonic resin were used (nominal values):

- Dowex 50x2 200-400 mesh (38-75 µm) – crosslinking degree of 2%, 0.6 meq mL^{-1} capacity.
- Dowex 50x4 100-200 mesh (75-150 µm) – crosslinking degree of 8%, 1.1 meq mL^{-1} capacity.
- Dowex 50x8 50-100 mesh (150-300 µm) - crosslinking degree of 8%, 1.7 meq mL^{-1} capacity.

Before usage, the resin was pre-treated following the procedure detailed in Cantwell *et al.*.[1] At first, the impurities were removed by repeated decantation in water. Then, the resin was washed in a beaker with several aliquots of 4 M HCl until the supernatant was colourless and then rinsed with Milli-Q water (Millipore Sigma, Merck KGaA, Darmstadt, Germany). Next, it was converted to the K^+ form by leaving it in a 3 M KOH solution overnight, and then washed several times with Milli-Q water. The resin was, then, washed with methanol and again Milli-Q water, before being oven-dried at 45 ºC. The resin was stored in a screw cap polyethylene jar kept in a desiccator until use.

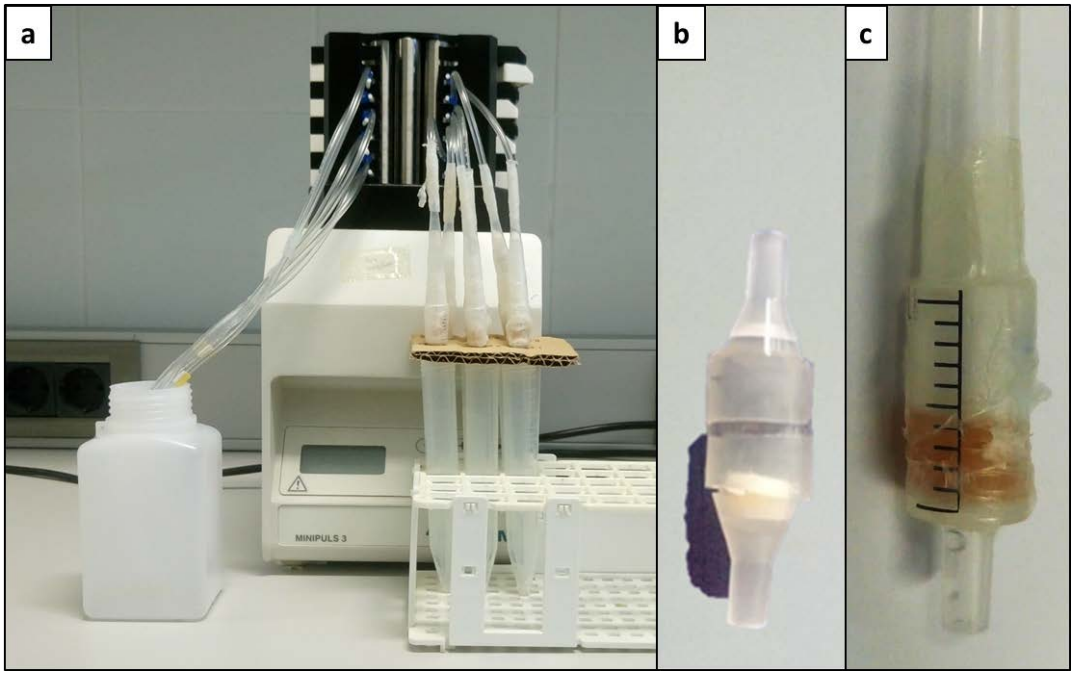

Figure 5.1. Apparatus required by a typical DIET (or IET) experiment. Panel a*, the sample reservoir, connected to the columns through the peristaltic pump. Panel* b*, detail of a packed column (design for small amounts of resin). Panel* c*, detail of a packed column (design for larger amounts of resin).*

Two kinds of minicolumns were built: the first one, (panel "b" of Fig. 5.1) employed in the experiments with smaller amount of resin (~10 mg), was constituted by two Polypropylene Luer Fittings (Kimble 420168-0000) for disposable chromatography columns held together by a section of Tygon tubing. The resin was kept in place by two Polyethylene (PE) Supports (Kimble 420162-0020); the internal radius of this kind of column was 2 mm. The second one (panel "c") was obtained from the end part of a 2 mL syringe (BD Discardit II), in which a micropipette tip was inserted (Gilson D1000); the resin was contained between two PE disks, cut to fit inside the syringe. In this design, the tip can be moved up and down to accommodate a larger volume of resin; the internal radius of this second column is 3.5 mm. In order to avoid contamination Dowex resin should be handled with plastic spatulas. It is recommendable to form a slurry first by adding Milli-Q water to the resin before pouring it into the column, so as to prevent the resin from sticking to the plasticware because of static. The column was then wrapped in Parafilm to hold the pieces together and prevent leaks.

5.2.3. Experimental setup

Before starting each DIET experiment, the resin is cleaned (with, in sequence: 1.5 M HNO_3 acid at 0.5 mL min^{-1} for 20 min, ultrapure water for 5 min, 0.1 M KOH at 4.5 mL

min^{-1} for 4 min and again ultrapure water for 5 min) and conditioned by flushing a solution identical to the sample background (with no trace metals or ligands), until the pH and ionic strength of the eluate are the same as those at the inlet. In our conditions, the stabilisation of the pH required about 20 min. The sample itself is, then, passed through the column for different periods of time (*e.g.* 5-10-30 min.). After each period, the resin is eluted with 1.5 M HNO_3 at 0.5 mL min^{-1} for 20 min and the eluate is collected. The column is then renewed by repeating the cleaning and reconditioning procedure and a new run can be started. Unless otherwise specified, the samples were flushed at 4.5 mL min^{-1}. Since the prolonged use causes the tubing to swell, the flow rate has to be checked periodically by measuring the volume of solution passed through the column in a certain period of time with a graduate cylinder.

The uptake can be also followed by measuring on-line the metal concentration in the effluent during the initial pumping of the test solution through the column, instead of eluting the metal accumulated in the beads.

5.2.4. Concentration measurements

All the sample aliquots were acidified to 1% in HNO_3. The aliquots from the highly acidic eluates had to be diluted accordingly before the analysis. All the samples were analysed with ICP-OES (Horiba Jobin Yvon) or ICP-MS (Agilent 7700x). Possible matrix effects due to the background electrolyte were taken into account during the calibration by spiking the standards with different volumes of Mg, Ca and K standard solution.

5.3. Results and Discussion

5.3.1. Accumulations and their trajectories

In this section, the experimental data obtained with DIET in synthetic solutions will be described. Let us analyse, first, the plots of accumulations in the resin beads *vs.* time (which will be labelled as trajectories) such as those presented in Fig. 5.2 (for a fixed amount of total metal and variable amounts of ligands).

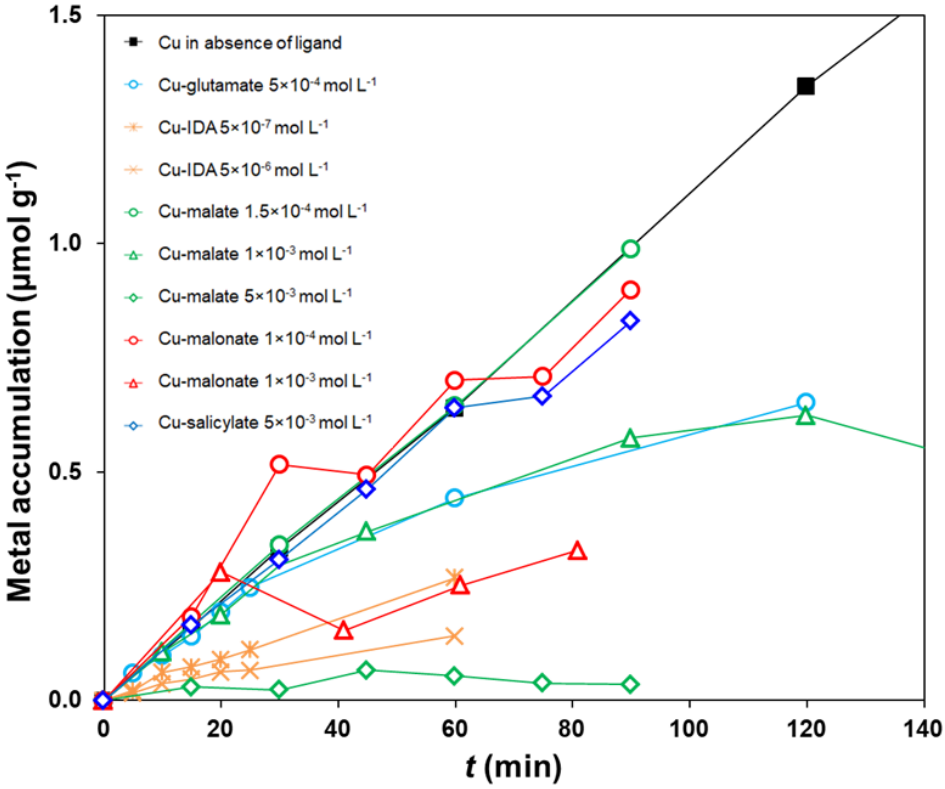

Figure 5.2. Trajectories showing Cu(II) accumulation in Dowex 50x4 (100-200 mesh) in presence of a series of different ligands. m_{resin}*= 100 mg; flow rate, Q= 4.5 mL min*$^{-1}$*;* $c_{T,Cu}$*= ~2.5×10*$^{-7}$ *M.*

We distinguish, in general, four different kinds of trajectories. First, those complexes (such as Cu-salicylate) that accumulate in the column following an initially linear trend over time, and with slope equal to that of the ligand-free metal solutions. The behaviour of this type of complex indicates (*i*) a high rate of dissociation within the column or a large direct binding of the complexes and (*ii*) conditions far away from equilibrium of the solution with the resin (*i.e.* far from the maximum capacity of the resin). Second, there are other complexes that display curved trajectories where the slope approaches the value in absence of ligands at initial stages, but it soon decays with time and tends to a constant value (see *e.g.* Cu-glutamate), indicative of resin-sample equilibrium. Depending on the lability of the metal complexes and the extent of the free metal ion buffering, the rate of metal binding may vary as can be seen by comparing the results of the Cu-malate complexes: with an increase of the ligand concentration from 1.5×10^{-4} M to 5×10^{-3} M, the time to attain equilibrium may decrease from several hours to a few minutes.

Third, there are other complexes (like Cu-IDA) that show linear trajectories with a slope smaller than that obtained with the ligand-free metal solutions (at the same total metal concentration). This indicates that the initial slope of DIET trajectories is not strictly proportional to the total concentration in all cases. In fact, the analysis of data obtained at varying ligand-to-metal ratios in these systems shows a monotonic trend of the slope with the concentration of free metal ion (see also the Ni-EDTA data in Fig.5.3).

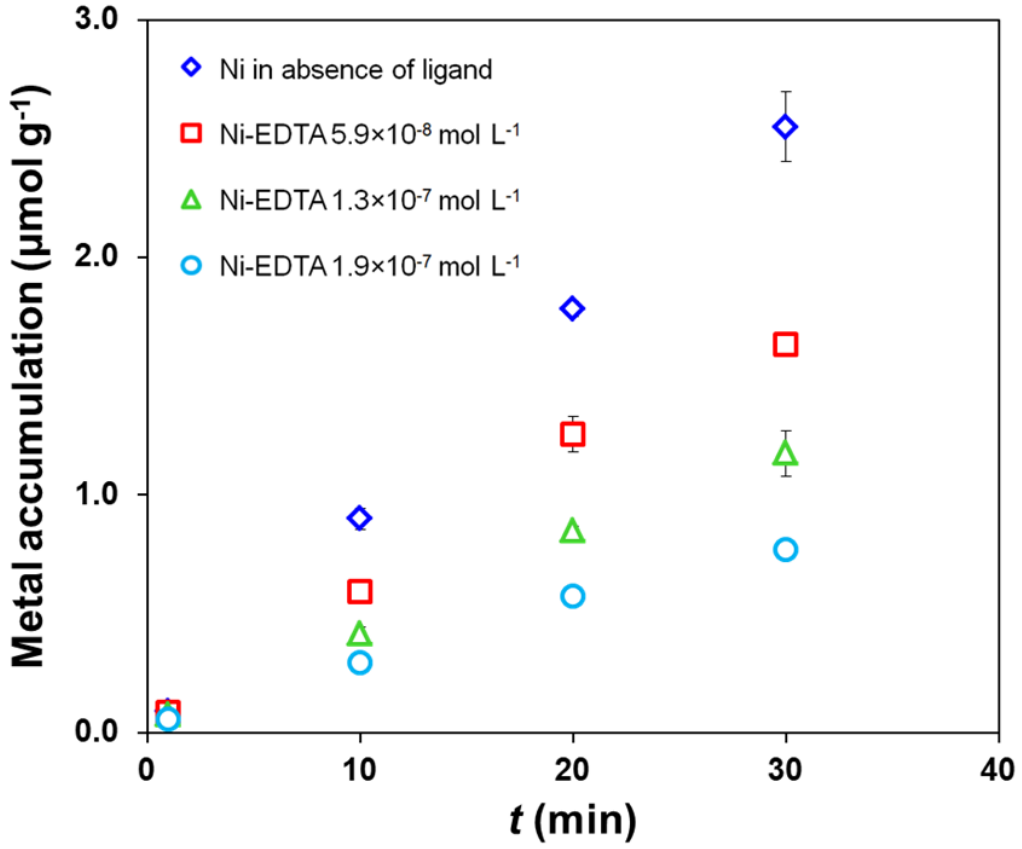

Figure 5.3. Trajectories related to Ni(II) accumulation on Dowex 50x4 (200-400 mesh) in presence of three different concentrations of EDTA. Each series corresponds to a different free Ni^{2+} concentration, reported in the legend (as M). The points stand for the average of three independent columns. $c_{T,Ni}$*= 2.5×10*$^{-7}$ *M, Q= 4.5 mL min*$^{-1}$*.*

Therefore, a question arises as to whether the slope at short stages depends exclusively on the value of the free metal ion concentration in the bulk sample or, rather, it reflects the effective rate of dissociation of the metal complexes inside the resin column under the experimental conditions (flow rate, resin particle size, length of bed, etc.) of the accumulation step. In the latter case, DIET results should not be interpreted as free metal fraction, but they would allow us to obtain information on the labile or inert character of the complexes (*i.e*. the *dynamic* speciation).

Finally, a fourth kind of system, typically under ligand excess conditions and very low free metal concentration (*e.g.*, Cu-malate at the highest ligand concentration, shown in Fig. 5.2) exhibits a constant (and very small) accumulation at all times, which results in the almost instantaneous attainment of equilibrium. In these cases, no information on the dissociation kinetics can be obtained from the accumulations at the experimental conditions.

5.3.2. Evolution of effluent concentrations

As done for the trajectories in the previous section, let us now move to the classification of the breakthrough curves, like those shown in Fig. 5.4b.

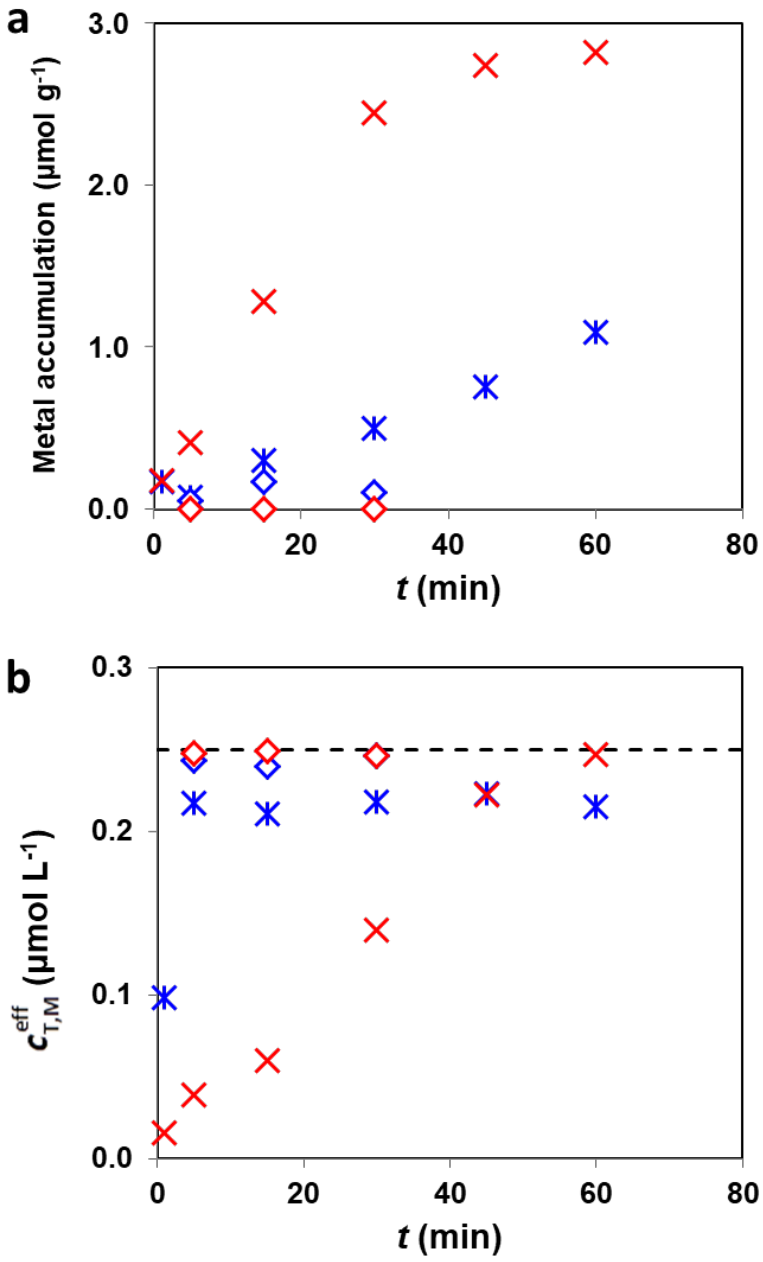

Figure 5.4. Accumulation of Ni(II), in presence and in absence of a competing ligand (citrate) on Dowex resin beads of different sizes ("large R": Dowex 50x8 50-100 mesh; "small R": Dowex 50x2 200-400 mesh). Panel a*: Trajectories; panel* b *Breakthrough curves. Blue stars: no ligand added, resin 50-100 Mesh; red crosses: no ligand added, resin 200-400 Mesh; blue diamond:* $c_{T,Cit}$*= 5×10*$^{-4}$ *M, resin 50-100 Mesh; red diamond:* $c_{T,Cit}$*= 5×10*$^{-4}$ *M, resin 200-400 Mesh. In panel* b *the dashed line stands for the eventual equilibrium value.*

The shape of the curve of Ni(II) in absence of ligand obtained with the smaller resin (blue *) is a typical example of the systems studied throughout this chapter: it exhibits an initial sudden increase followed by a stabilization (almost constant values below the equilibrium value), which we call “plateau”. This plateau might be the last observed feature of a breakthrough curve, instead of the eventual equilibrium value (indicated by the horizontal dashed line) and could be misinterpreted as the equilibrium itself. The two series with citrate complexes (diamonds) show that equilibrium has been practically reached after 10 minutes of exposure. The shape of the curve of Ni(II) in absence of ligand obtained with the large resin (red ×) illustrates another characteristic behaviour where the concentration rises with small slope up to $c_{T,M}$. The empirically observed “biphasic” behaviour (two stages: firstly fast increase, followed by slow increase) in the literature (*e.g.* Fig. 1 in Pesavento[18] or Figs 1b and S2 in Leguay[5]) will be usually interpreted here in terms of an “SS plateau”, for reasons discussed in detail in Section 5.3.4.1.

5.3.3. Individual beads models

We consider that a metal (M) reacts with a ligand (L) to produce complex (ML). Their charges are z_M (+2 for the metal ions studied here), z_L and z_{ML}. So:

$$z_{ML} = z_M + z_L \tag{5.1}$$

These charges are usually omitted in the notation of the species for the sake of simplicity.

As confirmed by the observation of the trajectories of Ni(II) and Cu(II), the binding of the metal ions to a strong acid cation exchange resin like Dowex can be assumed to be essentially electrostatic. As a first approximation, we neglect the steric interactions that are known to affect metal binding.[19] The affinity relationship was described by an equilibrium Donnan model. We call χ the Boltzmann factor given by the ratio of equilibrium concentrations of monovalent ions in the resin and aqueous domains (as done in the previous chapters, we neglect activity corrections as a first approximation):

$$\chi = \frac{c_{\text{monovalent}}\left(r = r_0^-\right)}{c_{\text{monovalent}}\left(r = r_0^+\right)} \tag{5.2}$$

where r_0^- and r_0^+ indicate the positions adjacent to the bead surface in the resin and in the solution, respectively. This Boltzmann factor depends on the density of charges in the resin phase and on the ionic strength, which in our experiments was essentially fixed

by KNO_3. The value taken for simulations, obtained from the experimental partitioning of Cu, was χ=128.

If we assume instantaneous equilibrium at the bead surface, then the concentrations of a given species *j* (of charge z_j) across the resin-solution interface are related with each other through:

$$c_j\left(r=r_0^-\right)=\chi^{z_j}c_j\left(r=r_0^+\right) \tag{5.3}$$

The large values of χ imply that the trace metal ion (with z_M=+2) is taken up by the resin phase right from the initial stages of contact and depleted from the solution boundary layer, so that $c_M\left(r=r_0^+\right)\approx 0$. Eventually, bulk equilibrium between the resin domain and the feed solution will be reached, so that $c_M\left(r=r_0^+\right)=c_M$ (no superscript is added to indicate the bulk conditions of the sample or solution mixture previous to its introduction in the column) and the total metal concentration inside the bead will be $\chi^{z_M}c_M+\chi^{z_{ML}}c_{ML}$. In passing, we notice that this expression quantifies the reported interference of positive complexes in IET.[20]

The charge of the complex is very relevant to its "penetration" inside the bead. Negatively charged complexes are excluded from the resin phase,[12,21] whereas the accumulation of the positively charged ones is particularly strong at short stages. At equilibrium, for z_M=+2 and z_{ML}=0, the expected amount of complexes relative to the total metal accumulated in the resin is negligible, since they are globally neutral (we neglect the possible presence of dipoles). Even if these complexes can penetrate into the resin they do not concentrate inside (because $c_{ML}\left(r=r_0^-\right)=c_{ML}\left(r=r_0^+\right)$), contrary to the metal ion. The lability of the complexes (of any charge), however, does have an impact in speeding up the overall metal uptake kinetics.

5.3.3.1. Time-dependent model of individual beads (Model I)

Model I is based on a set of general assumptions shared by all the models reported in this chapter:

1- The supply to an individual bead results from diffusion in spherical geometry. The beads are spheres of fixed radius r_0. Diffusion in the solution surrounding the bead extends just to a finite distance r_1, defining a diffusion layer of thickness δ.

2- Given that none of the complexes studied here are macromolecular, all metal species have a similar diffusion coefficient D_M (the same value in solution as inside the bead).

3- Penetration of the different metal species inside the beads is allowed. In time-dependent models, all species penetrate according to their charge. In steady-state models (II and IV), the penetration of some species is neglected.

4- There is instantaneous equilibrium at the bead surface, so that the partitioning equation (Eq. (5.3)) applies.

5.- In the reaction

$$\mathrm{M} + \mathrm{L} \underset{k_\mathrm{d}}{\overset{k_\mathrm{a}}{\rightleftharpoons}} \mathrm{ML} \tag{5.4}$$

there is an excess of ligand, so that the concentrations of free ligand in solution (c_L if $r > r_0$) and inside the bead ($c_\mathrm{L}^\mathrm{bead}$ if $r < r_0$) are constant over time or space (for both resin and solution domains).

The conditional (excess) stability constant (or coefficient) in solution is defined as:

$$K' = \frac{c_\mathrm{ML}}{c_\mathrm{M}} = \frac{k_\mathrm{a} c_\mathrm{L}}{k_\mathrm{d}} \tag{5.5}$$

where k_a and k_d are the association and dissociation rate constants in solution.

Model I, for the time-dependent accumulation in one bead, starts with null concentrations in both diffusion domains and it has the following boundary conditions: $c_\mathrm{ML}(r_1, t) = c_\mathrm{ML}$ and $c_\mathrm{M}(r_1, t) = c_\mathrm{M}$. Details on the model and its numerical resolution are given in Section 5.5.1.

5.3.3.2. Steady-state model of metal uptake by individual beads (Model II)

It can be seen that, after a short transient (generally less than half a second), the simulated uptake practically reaches a steady state. So, Model II assumes this regime in order to reproduce the accumulation during the initial stages of uptake.

A further simplification of Model II is that the surface of the bead acts as perfect sink for the diffusion of M in solution, because of the large concentration jump (with a partitioning χ^{z_M}) at the bead surface. This hypothesis is valid as long as the current accumulation in the bead is far away from equilibrium (which is relevant to explain the initial slope in the trajectories in the case of Model IV below). The assumption of perfect sink conditions and mass transport limited by diffusion in the boundary layer around the beads has been shown to hold during the initial stages of metal uptake in batch experiments with Chelex resins[22] and is the standard operation principle of DGT.

In SS, the flux can be computed as:[23–25]

$$J = \frac{D_M \left(1 + K'\xi\right)}{\delta} c_M \tag{5.6}$$

Where ξ is the lability degree of the metal complex, introduced in Chapter 1 (Eq. (1.1)), while δ is the thickness of the dbl.

The next subsections detail the values of the lability degree to be used in (5.6) for the different possible charges of the complex.

NEUTRAL COMPLEXES

Neutral complexes (with partitioning factor χ^0=1) can penetrate inside the beads. Given that at relatively short times (but once SS has settled according to Model I), the existing amounts of M and ML inside the beads are far from equilibrium with each other, we assume that there is no back-association of M and L inside the resin, but just dissociation of ML. Under excess ligand conditions, the contribution from complex dissociation inside the bead will be very relevant. This is parallel to the treatment of penetration in several DGT models[12,13,21] where the accumulation is essentially due to this dissociation inside the resin domain.

As shown in Section 5.5.2, the lability degree can be computed as

$$\xi = 1 - \frac{1 + K'}{K' + \frac{r_0\left(r_1 - r_0\right)}{r_1 m}\coth\left(\frac{r_1 - r_0}{m}\right) + \frac{r_1 - r_0}{r_1} + \frac{r_0\left(r_1 - r_0\right)\left(1 + K'\right)\chi^{z_{ML}}}{r_1 \lambda}\coth\left(\frac{r_0}{\lambda}\right)} \tag{5.7}$$

with

$$\lambda = \sqrt{\frac{D_{ML}}{k_d}} \tag{5.8}$$

and:

$$m = \sqrt{\frac{D_{ML}}{k_d + k_a c_L}} \tag{5.9}$$

where k_a and k_d are the association/dissociation rate constants of ML in the solution which, even though they might differ from the values inside the bead due to electrostatic effects,[13,21] are assumed here to be equal.

POSITIVELY CHARGED COMPLEXES

In this case, the bead acts as perfect sink not only for M, but also for ML:

$$J = \frac{D_M}{\delta} c_M + \frac{D_M}{\delta} c_{ML} = \frac{D_M \left(1 + K'\right)}{\delta} c_M \tag{5.10}$$

As a consequence, due to the direct accumulation of ML, a flux equivalent to the fully labile case ($\xi = 1$) is expected, even if the actual dissociation kinetics was slow.

NEGATIVELY CHARGED COMPLEXES

For the extreme case of negative charge and high Boltzmann factor χ, the overall flux of metal to the bead would essentially result from the free metal ions plus some contribution from the dissociation of the complex in the diffusion layer. Dedicated expressions, similar to those developed in voltammetry,[26] could be derived. However, the model for neutral complexes Eq. (5.7) still applies just using the suitable z_{ML}, because, at least in the initial stages, the concentrations of M in the resin phase are very far from the expected eventual equilibrium values (*i.e.* $c_M \chi^{z_M}$), so that there could be a net, albeit small, dissociation of ML.

5.3.4. Column models

The modelling of the column considers that the spherical beads receive a flux (see arrows in Fig. 5.5) that could be computed with Model I or Model II. As the transient period to reach SS for an individual bead has been shown (with Model I) to be much shorter than the typical timescale of column experiments, we will assume in the column models (III and IV) that diffusion towards the bead (in the region between r_0 and r_1) is always under SS. This has been called a "diffusional steady state" (dSS) approximation (see p. 170 in Galceran *et al.*[27]). Another assumption of the column models is that there is a flat concentration profile of M and ML inside the bead (this is also supported by simulations with Model I, see Fig. A5.1). This, again, is consistent with numerical simulation results of a combined particle and film diffusion control of metal uptake in Chelex resins,[22] which indicate that film diffusion is typically the most relevant resistance to mass transfer at the initial stages.

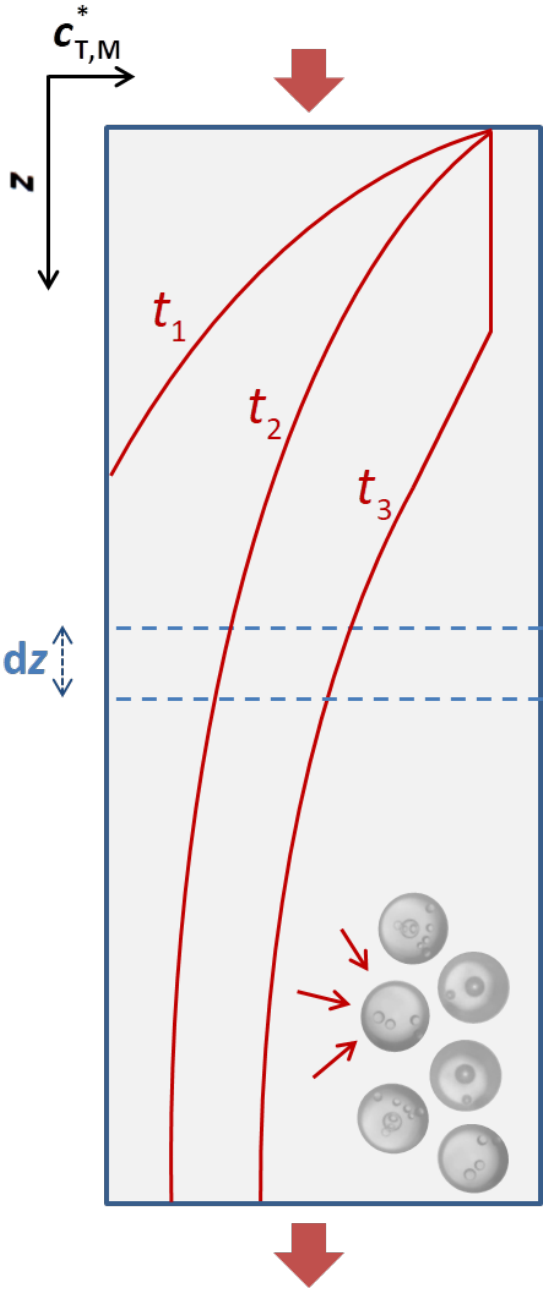

Figure 5.5. Schematic representation of the flux towards individual beads (arrows) and concentration profile of total metal along the column (continuous lines) at intervals of time t_1, t_2 and t_3. The column has bed length z_{max} (vertical axis). In each of the layers of infinitesimal thickness dz the solution is in SS.

The total concentration of M in the interstices of the column, outside the diffusion boundary layer, at a given height of the column (z) and a given time (t) since the beginning of the experiment, is denoted as $c^*_{T,M}(z,t)$ with a fixed inlet value (at z=0) of $c_{T,M}$ and an effluent value (at z=z_{max}) of $c^{eff}_{T,M}(t)$. Schematic concentration profiles of $c^*_{T,M}(z,t)$ are depicted in Fig. 5.5.

5.3.4.1. Transient model of metal uptake in the column (Model III)

Regardless of the charge of the complex, one can derive the following continuity equations:

$$S\varepsilon\frac{\partial c^{*}_{\mathrm{T,M}}(z,t)}{\partial t}=-\frac{D_{\mathrm{M}}\alpha}{\delta}\left(c^{*}_{\mathrm{T,M}}(z,t)-\frac{\tilde{c}_{\mathrm{ML}}(z,t)}{\chi^{z_{\mathrm{ML}}}}-\frac{\tilde{c}_{\mathrm{M}}(z,t)}{\chi^{z_{\mathrm{M}}}}\right)-S\varepsilon v\frac{\partial c^{*}_{\mathrm{T,M}}(z,t)}{\partial z} \tag{5.11}$$

$$\rho\frac{\partial\tilde{c}_{\mathrm{M}}(z,t)}{\partial t}=\frac{D_{\mathrm{M}}\alpha}{r_0(1+K')}\left[\left(\frac{\tilde{c}_{\mathrm{ML}}(z,t)}{\chi^{z_{\mathrm{ML}}}}-\frac{K'\tilde{c}_{\mathrm{M}}(z,t)}{\chi^{z_{\mathrm{M}}}}\right)\left(\frac{r_0}{m}\coth\left(\frac{r_1-r_0}{m}\right)+1\right)+\frac{r_1}{r_1-r_0}\left(c^{*}_{\mathrm{T,M}}(z,t)-\frac{\tilde{c}_{\mathrm{ML}}(z,t)}{\chi^{z_{\mathrm{ML}}}}-\frac{\tilde{c}_{\mathrm{M}}(z,t)}{\chi^{z_{\mathrm{M}}}}\right)\right]+$$
$$+\rho\left(k_{\mathrm{d}}\tilde{c}_{\mathrm{ML}}(z,t)-k_{\mathrm{a}}\tilde{c}_{\mathrm{L}}\tilde{c}_{\mathrm{M}}(z,t)\right) \tag{5.12}$$

$$\rho\frac{\partial\tilde{c}_{\mathrm{ML}}(z,t)}{\partial t}=\frac{D_{\mathrm{M}}\alpha}{r_0(1+K')}\left[-\left(\frac{\tilde{c}_{\mathrm{ML}}(z,t)}{\chi^{z_{\mathrm{ML}}}}-\frac{K'\tilde{c}_{\mathrm{M}}(z,t)}{\chi^{z_{\mathrm{M}}}}\right)\left(\frac{r_0}{m}\coth\left(\frac{r_1-r_0}{m}\right)+1\right)+\frac{K'r_1}{r_1-r_0}\left(c^{*}_{\mathrm{T,M}}(z,t)-\frac{\tilde{c}_{\mathrm{ML}}(z,t)}{\chi^{z_{\mathrm{ML}}}}-\frac{\tilde{c}_{\mathrm{M}}(z,t)}{\chi^{z_{\mathrm{M}}}}\right)\right]-$$
$$-\rho\left(k_{\mathrm{d}}\tilde{c}_{\mathrm{ML}}(z,t)-k_{\mathrm{a}}\tilde{c}_{\mathrm{L}}\tilde{c}_{\mathrm{M}}(z,t)\right) \tag{5.13}$$

where tilde denote concentrations inside the beads, ρ is the volume of beads per unit of column length, α is the effective bead area per unit of column length, S is the column section, ε is the volume fraction of the column occupied by the flowing solution (not affected by diffusion), and v is the interstitial velocity of the solution, defined as:

$$v=\frac{Q}{S\varepsilon} \tag{5.14}$$

where Q is the flow rate. ρ was set as the experimental ratio of resin volume over the bed length of the column, while α was computed from the height of the SS plateau as per Eq. (A5.102). While the perfect packing of equal spheres would predict a theoretical fractional interstitial volume of $\varepsilon \approx 0.26$, this value must be corrected for the finite volume of the diffusion layers surrounding the beads. We applied an effective volume ε of 0.18.

Table 5.1. Parameters used for fitting the trajectories and breakthrough curves of neutral complexes of Cu(II).

Parameter	Value	Source
z_{max} (m)	$6\pm1\times10^{-3}$	direct measurement (average over the 6 columns)
	1×10^{-3}	direct measurement
S (m^2)	3.85×10^{-5}	direct measurement
	1.26×10^{-5}	
r_0 (m)	1.12×10^{-4} (50-100 Mesh)	from nominal average size of the beads
	5.60×10^{-5} (100-200 Mesh)	
	2.80×10^{-5} (200-400 Mesh)	
ε	0.18	70% of the value given by the close packing of spheres of equal volume
ρ (m^2)	1.80×10^{-5}	from $\rho = \frac{V_R}{z_{max}}$, where V_R is the volume of the resin phase
	1.10×10^{-5}	
α (m)	0.234 (50-100 Mesh, S)	from Eq. (A5.102)
	0.499 (100-200 Mesh, S)	
	0.203 (200-400 Mesh, S)	
D_M ($m^2\ s^{-1}$)	7.14×10^{-10} (Cu) 6.61×10^{-10} (Ni)	from literature (values at 25ºC)
δ (m)	10×10^{-6} (50-100 Mesh) (flow rate 7.5×10^{-8} $m^3\ s^{-1}$)	fitted
	7×10^{-6} (100-200 Mesh) (flow rate 7.5×10^{-8} $m^3\ s^{-1}$)	
	5×10^{-6} (200-400 Mesh) (flow rate 7.5×10^{-8} $m^3\ s^{-1}$)	
	10×10^{-6} (200-400 Mesh) (flow rate 1.9×10^{-8} $m^3\ s^{-1}$)	

As seen in Fig. 5.8, the model reproduces the general shape of the experimental breakthrough curve of Cu-IDA. The values given to the model parameters are gathered in Tab. 5.1. r_0 was taken equal to the radius of the bead, while r_1 was fitted. The conditional complexation constant K' was computed directly from the species distribution using the speciation program Visual MINTEQ,[28] while k_d was computed according to the Eigen model.[29] The model shows a very short transient (not experimentally accessible) with a very fast increase of the accumulation. After the

transient, the theoretical rate of increase in the accumulation declines and approaches the experimentally observed constant effluent concentration that we identify as the (quasi) steady state. As in DGT, the regime cannot be rigorously termed "steady state" because of the increasing accumulation in the resin, but, for the sake of simplicity in the notation, we will use here the acronym "SS" to indicate this regime. This SS is also consistent with the linear accumulation shown for the initial Cu-IDA trajectory in Fig. 5.2. For this reason, we suggest labelling this regime, just after the transient regime and with shorter or longer duration, as the "SS plateau".

5.3.4.2. Steady-state model of metal uptake in the column (Model IV)

As seen in Model III, a quasi steady-state regime settles for the concentrations of the species in the column at the early stages. This SS implies an approximate stable flux of metal from solution to the resin (responsible for the initial linear accumulation in the trajectories) and an approximate constant effluent concentration (the SS plateau). The fundamental equation for column SS Model IV can be derived from Eq. (5.11), by applying the diffusive steady state (dSS) approximation (see Section 5.5.4). However, for SS to be valid all along the column (*i.e.* for different *z*), we must also assume that the concentrations of M and ML at the bead surface are constant, *e.g.* 0 for M and a fixed value for ML. Of course, ξ is expected to be independent from *z*, as in Eq. (5.7). On the other hand, Model IV relaxes the condition of ligand-excess and can use lability degrees derived from bead models other than Model II.

As detailed in the next subsections, the differences in mathematical treatment between complexes of different charge are minimum (they just concern the interpretation of ξ, which may be analysed in a second stage).

NEUTRAL COMPLEXES

As detailed in Section 5.3.4.2, the ratio between effluent and feed concentrations can be expressed as:

$$\ln\frac{c_{\mathrm{T,M}}^{\mathrm{eff,SS}}}{c_{\mathrm{T,M}}} = -\frac{z_{\max}}{z_{\mathrm{char}}} \tag{5.15}$$

where the superscript "eff, SS" indicates the SS-plateau concentration of the effluent (*i.e.* at $z=z_{\max}$) and

$$z_{\mathrm{char}} = \frac{Q\delta\left(1+K'\right)}{D_{\mathrm{M}}\alpha\left(1+K'\xi\right)} \tag{5.16}$$

z_{char} can be interpreted as the resin bed length that reduces the feed concentration by a factor e= 2.718, so that the lower z_{char}, the lower will be the effluent total concentration (for a constant z_{max}).

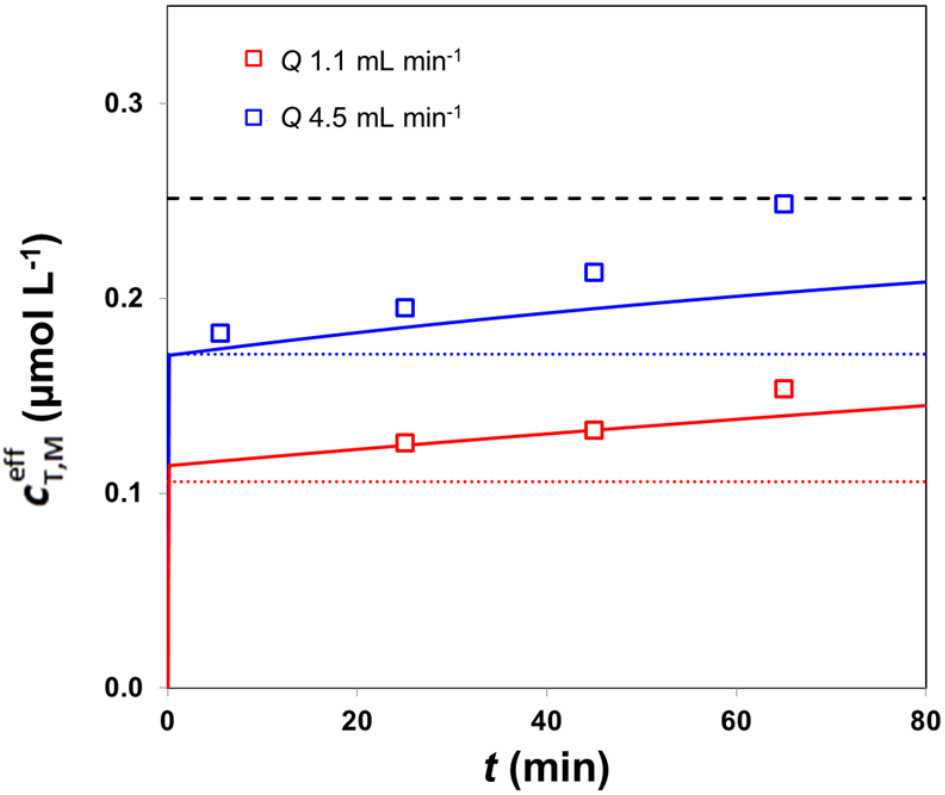

Figure 5.6. Impact of flow rate on breakthrough curves solutions of Cu(II) in absence of ligand. $c_{T,M}$= 2.5×10^{-7} M, Q= 4.5 and 1.1 mL min^{-1} a) Markers: experimental data; b) Continuous line: Model III; c) Dotted line: Model IV. Upper dashed line for the eventual equilibrium value.

By taking K'=0, previous equations are also valid for experiments where metal is present mostly as the free ion. The ratio of the z_{char} values of two experiments in absence of ligand with different flow rates (see Fig. 5.6) yielded 0.32, which is reasonably close to the expected value for the ratio of flow rates (0.25), especially if we take into account that δ might decrease with an increasing flow rate.

If we compare two column runs, with and without the ligand, one can derive

$$\frac{\left(\ln\frac{c_{T,M}^{eff,SS}}{c_{T,M}}\right)_{\text{with complex}}}{\left(\ln\frac{c_{T,M}^{eff,SS}}{c_{T,M}}\right)_{\text{absence of ligand}}}=\frac{1+K'\xi}{1+K'} \qquad (5.17)$$

from which the ξ value could be retrieved (see below).

A conclusion of experimental interest is that the use of very small resin sizes (*e.g.* microChelex) and long columns would improve method sensitivity (when using Eq. (5.17)), but, on the other hand, small particle sizes can lead to too low ratios $\frac{c_{\mathrm{T,M}}^{\mathrm{eff,SS}}}{c_{\mathrm{T,M}}}$, with consequent difficulty in determining the height of the plateau.

As shown in Section 5.3.4.2, the initial accumulation in a trajectory follows:

$$n^{\mathrm{SS}} = Q\, c_{\mathrm{T,M}} \left[1 - \mathrm{e}^{-\frac{z_{\max}}{z_{\mathrm{char}}}} \right] t \tag{5.18}$$

For small $z_{\max}$ / z_{char} ratios, the previous expression simplifies to

$$n^{\mathrm{SS}} \approx c_{\mathrm{T,M}} \frac{D_{\mathrm{M}} \alpha}{\delta} \frac{\left(1 + K'\xi\right)}{\left(1 + K'\right)} z_{\max} t \tag{5.19}$$

which could alternatively be derived from Model II neglecting any *z*-dependence of the accumulation in the column.

Note that a completely inert system with a large conditional binding constant would yield a very small slope of the trajectory, which could be mistaken by a situation of sample-resin equilibrium. In principle, both situations could be distinguished by running experiments with varying column bed length.

From Eq. (5.18), the initial slope of the trajectories (which could be identified with the initial rate of accumulation R_{acc} in previous DIET literature) can be described by

$$slope = Q\, c_{\mathrm{T,M}} \left[1 - \mathrm{e}^{-\frac{z_{\max}}{z_{\mathrm{char}}}} \right] = Q\, c_{\mathrm{T,M}} \left[1 - \frac{c_{\mathrm{T,M}}^{\mathrm{eff,SS}}}{c_{\mathrm{T,M}}} \right] = Q\ c_{\mathrm{T,M}}\ \Xi \tag{5.20}$$

where Ξ could be called the “system retention degree” (or “apparent column lability degree”) which, for fixed total metal and ligand concentrations, increases when the lability degree of the formed complex increases. This Ξ bears some analogy to the the fraction *X* used by some authors.[7,10,30] One difference is that Ξ is computed only from the SS plateau concentrations, while *X* is sometimes taken after a fixed volume of sample has gone through the column.

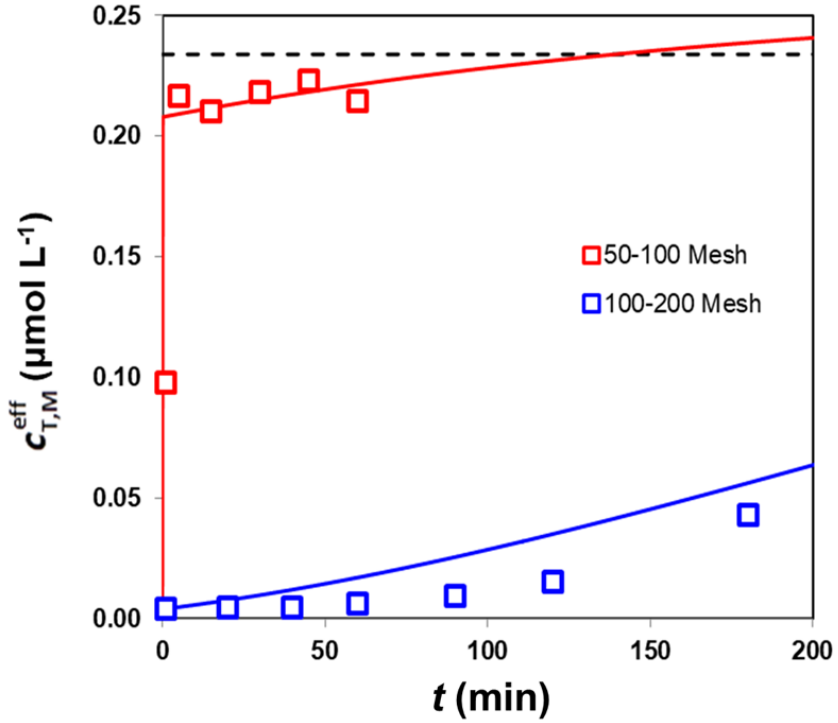

Figure 5.7. Breakthrough curves of Cu(II) in absence of ligand with very different levels of the SS plateau due to different resin size (red squares for 50-100 Mesh, blue squares for 100-200 Mesh). The solid lines were computed with Model III. The horizontal dashed line stands for the influent total concentration $c_{T,M}$.

Notice that Ξ and X can be used even for a case without ligands. For instance, for the case in absence of ligand shown in Fig. 5.7 as red square markers, Ξ=0.1, because these global parameters are not only dependent on ML characteristics. Ξ values in Tab. 5.2, computed using:

$$\Xi = 1 - \frac{c_{T,M}^{eff,SS}}{c_{T,M}} \tag{5.21}$$

are correlated to the lability degree of the complexes according to Model II. Those in Tab. 5.3 cannot be usually compared with ξ_{theo} due to the attainment of equilibrium or other reasons.

The lability degree of a complex can be computed from the difference in the initial slopes of two trajectories (with and without ligand):

$$\xi = \left(1+\frac{1}{K'}\right)\frac{\left(\ln\left[1-\frac{slope}{Qc_{T,M}}\right]\right)_{\text{with complex}}}{\left(\ln\left[1-\frac{slope}{Qc_{T,M}}\right]\right)_{\text{absence of ligand}}} - \frac{1}{K'} \qquad (5.22)$$

A trajectory with slope $Q\,c_{T,M}$ would correspond to complete retention of the metal. This ideal situation is approximated quite closely in the here-probed cases of metal accumulation in absence of ligand. A direct consequence, and a possible drawback of this computation method for ξ, is that the denominator of Eq. (5.22) may not be estimated with enough accuracy.

POSITIVELY CHARGED COMPLEXES

Expressions of the SS Model IV for $z_{ML}>0$ can be derived from the case of neutral complexes with the additional change of $\xi = 1$, whenever the lability degree is involved. So, z_{char} could be computed with Eq. (5.15) expecting to obtain, in this case, the same value with or without ligand. Obviously, no information on the complex kinetics could be extracted from the effluent concentration (Eq. (5.17)) or from the initial slope of the trajectories (Eq. (5.18)). The initial slope will be directly proportional to the total metal concentration, as already observed for Sm-malate (charge +1).[4]

NEGATIVELY CHARGED COMPLEXES

As there is practically no penetration of the negative complexes into the beads at the relatively low ionic strength of the experiments, the accumulation will proceed from the flux of free metal partially supported by the dissociation of the complex just in the diffusion layer. This means a very low ξ. However, all the derivations of analytical SS expressions for neutral species apply with no other variation than the sign of the charge.

Table 5.2. Compilation of studied systems corresponding to neutral complexes. All the experiments were carried out with columns packed with ∼0.1 g of Dowex 50x4 100-200 mesh. For computations, the average bead radius is r_0 = 5.6×10^{-5} m, the diffusion layer thickness δ= 7×10^{-6} m, the section of the column S = 3.85 ×10^{-5} m^2 and the length of the column z_{max} = 6.0×10^{-3} m.

System	$c_{T,L}$ (M)	$c_{T,M}$ (M)	ξ_{theo} computed according to Model II Eq. (5.7)	ξ from initial slope trajectory according to Model IV Eq. (5.22)	ξ from effluent concentration according to Model IV Eq (5.17)	z_{char} (m) Eq. (5.16)	Ξ Eq. (5.21)	c_{DIET} (M) Eq. (5.24)	c_{DIET} (M) Eq. (5.25)	c_M (M) computed with Visual MINTEQ
Cu-Glutamate	5×10^{-4}	2.34×10^{-7}	0.70	0.86	0.63	2.3×10^{-3}	0.92	1.49×10^{-7}	2.02×10^{-7}	3.09×10^{-9}
Cu-IDA	5×10^{-7}	2.34×10^{-7}	0.17	0.10	0.05	1.0×10^{-2}	0.44	3.37×10^{-8}	4.35×10^{-8}	2.47×10^{-8}
	5×10^{-6}	2.38×10^{-7}	0.16	0.10	0.08	1.8×10^{-2}	0.28	1.97×10^{-8}	2.44×10^{-8}	1.58×10^{-9}
Cu-Malate	1.5×10^{-4}	2.79×10^{-7}	1.00	≈1[b]	---[a]	---[a]	≈1	---[a]	≈c_{TM}[b]	7.81×10^{-8}
	1×10^{-3}	2.49×10^{-7}	1.00	≈1[b]	---[a]	---[a]	≈1	---[a]	≈c_{TM}[b]	1.49×10^{-8}
Cu-Malonate	1×10^{-3}	2.56×10^{-7}	0.99	≈1[b]	---[a]	---[a]	≈1	---[a]	≈c_{TM}[b]	7.32×10^{-10}
Cu-Salicylate	5×10^{-3}	2.34×10^{-7}	1.00[c]	≈1[b]	0.95	1.6×10^{-3}	≈1	2.23×10^{-7}	≈c_{TM}[b]	1.60×10^{-8}
Ni-Malonate	5×10^{-4}	2.46×10^{-7}	0.86	≈1[b]	---[d]	6.6×10^{-3}	≈1	---[d]	≈c_{TM}[b]	6.94×10^{-8}
	1×10^{-3}	2.39×10^{-7}	0.86	≈1[b]	---[d]	2.1×10^{-3}	≈1	---[d]	≈c_{tm}[b]	4.12×10^{-8}

[A] The plateau corresponding to the steady state could not be clearly observed in the breakthrough curve.

[b] The initial slope of the trajectory practically coincides with the one of metal in absence of ligand.

[c] ξ computed assuming that the reactive species is LH^-, instead of L^{2-} as in the other cases.

[d] The equation cannot be implemented, as we do not have results of Ni(II) in absence of ligands. The initial slope of Ni(II) trajectory has been assumed equal to the one of Cu(II).

Table 5.3. Compilation of studied systems corresponding to charged complexes. All the experiments were carried out with columns packed with ∼0.01 g of Dowex 50x2 resin, 200-400 mesh. The average bead radius r_0 is 2.8×10^{-5} m, the diffusion layer thickness δ is 5×10^{-6} m, the section of the column S is 1.96×10^{-5} m^2 and the length of the column z_{max} is 1.0×10^{-3} m.

System	Charge	$C_{T,L}$ (M)	$C_{T,M}$ (M)	ξ_{theo} computed according to Model II Eq. (5.7)	ξ from initial slope trajectory according to Model IV Eq. (5.22)	Ξ Eq. (5.21)	c c_{DIET} (M) Eq. (5.25)	c_M (M) computed with Visual MINTEQ
Cu-Citrate	-1	5.00×10^{-5}	2.50×10^{-7}	0.78	---[a]	≈0[a]	---[a]	1.51×10^{-9}
	-2	6.30×10^{-8}	2.42×10^{-7}	0.00[b]	≈0[c]	0.79	1.61×10^{-7}	1.73×10^{-7}
		1.25×10^{-7}	2.33×10^{-7}	0.00 [b]	≈0[c]	0.56	8.25×10^{-8}	1.04×10^{-7}
Cu-EDTA		1.88×10^{-7}	2.50×10^{-7}	0.00[b]	≈0[c]	0.30	3.83×10^{-8}	5.98×10^{-8}
	+2	1.00×10^{-6}	2.50×10^{-7}	1.00[b]	≈1[d]	≈1	$\approx c_{TM}$[d]	1.81×10^{-7}
		2.70×10^{-6}	2.50×10^{-7}	1.00[b]	≈1[d]	≈1	$\approx c_{TM}$[d]	1.25×10^{-7}
Cu-en		7.80×10^{-6}	2.50×10^{-7}	1.00[b]	≈1[d]	≈1	$\approx c_{TM}$[d]	6.18×10^{-8}
Ni-Citrate	-1	5.00×10^{-4}	2.44×10^{-7}	0.003	---[a]	≈0[a]	---[a]	8.39×10^{-10}
	-2	5.93×10^{-8}	2.37×10^{-7}	0.00[b]	≈0[c]	0.83	1.81×10^{-7}	1.76×10^{-7}
		1.33×10^{-7}	2.65×10^{-7}	0.00 [b]	≈0[c]	0.48	7.56×10^{-8}	1.31×10^{-7}
Ni-EDTA		1.94×10^{-7}	2.59×10^{-7}	0.00[b]	≈0[c]	0.33	4.48×10^{-8}	6.44×10^{-8}

[a] The equilibrium is attained almost instantaneously.

[b] The system was not under ligand excess conditions, so Model II does not hold strictly.

[c] As a consequence of uncertainties on the slopes and on K', Eq. (5.22) give slightly negative values of ξ.

[d] The slope of the accumulation curve practically coincides with the one of the metal in absence of ligand.

5.3.5. The DIET-labile fraction (c_{DIET})

As stated throughout this thesis, the "concentration" measured with the DGT sampler is not, strictly speaking, *the* labile fraction, but rather an effective free metal concentration defined as "DGT concentration".[15,16] In analogy, for a set of complexes denoted with index *i*, we can introduce a "DIET concentration" defined as:

$$c_{DIET} \equiv c_M \left(1 + \sum_i \frac{D_i}{D_M} K_i' \xi_i \right) \tag{5.23}$$

which is a measure of the labile fraction probed by a particular column.

For systems of one complex with $D_i = D_M$, c_{DIET} can be evaluated by comparing the height of the SS-plateau with the one of an experiment in absence of ligand, performed with the same column in identical conditions (see Section 5.3.4.2):

$$c_{DIET} = c_{T,M} \frac{\left(\ln \frac{c_{T,M}^{eff,SS}}{c_{T,M}} \right)_{\text{with complex}}}{\left(\ln \frac{c_{T,M}^{eff,SS}}{c_{T,M}} \right)_{\text{absence of ligand}}} \tag{5.24}$$

A limitation of this method is that $c_{T,M}^{eff,SS}$ for experiments in absence of ligand may be too close to the limit of detection to be accurately determined. Alternatively, c_{DIET} can be computed from the initial slopes of the trajectories:

$$c_{DIET} = c_{T,M} \frac{\left(\ln \left[1 - \frac{slope}{Q c_{T,M}} \right] \right)_{\text{with complex}}}{\left(\ln \left[1 - \frac{slope}{Q c_{T,M}} \right] \right)_{\text{absence of ligand}}} \tag{5.25}$$

Neither definition is free from disadvantages, as the same considerations drawn for Eq. (5.22) hold here.

5.3.6. The SS plateau in the breakthrough curve

The experimental SS plateau for a system with a complex appears extremely clear for Cu-IDA at both concentrations of ligand assayed (see Fig. 5.8). The SS plateau can be regarded as the initial period within the second phase of the biphasic behaviour, while the transient (*i.e.* before SS settles) is the first phase of the biphasic behaviour. For instance, in Fig. 5.8, after the sudden initial rise, the effluent concentration stays fixed to around 57% of the total sample concentration for at least 1500 s. Given that the height

of the plateau for an experiment in absence of ligand, in identical conditions, is not higher than 1.7% (see blue squares in Fig. 5.7), it can be safely concluded that the IDA complexes have a reduced lability.

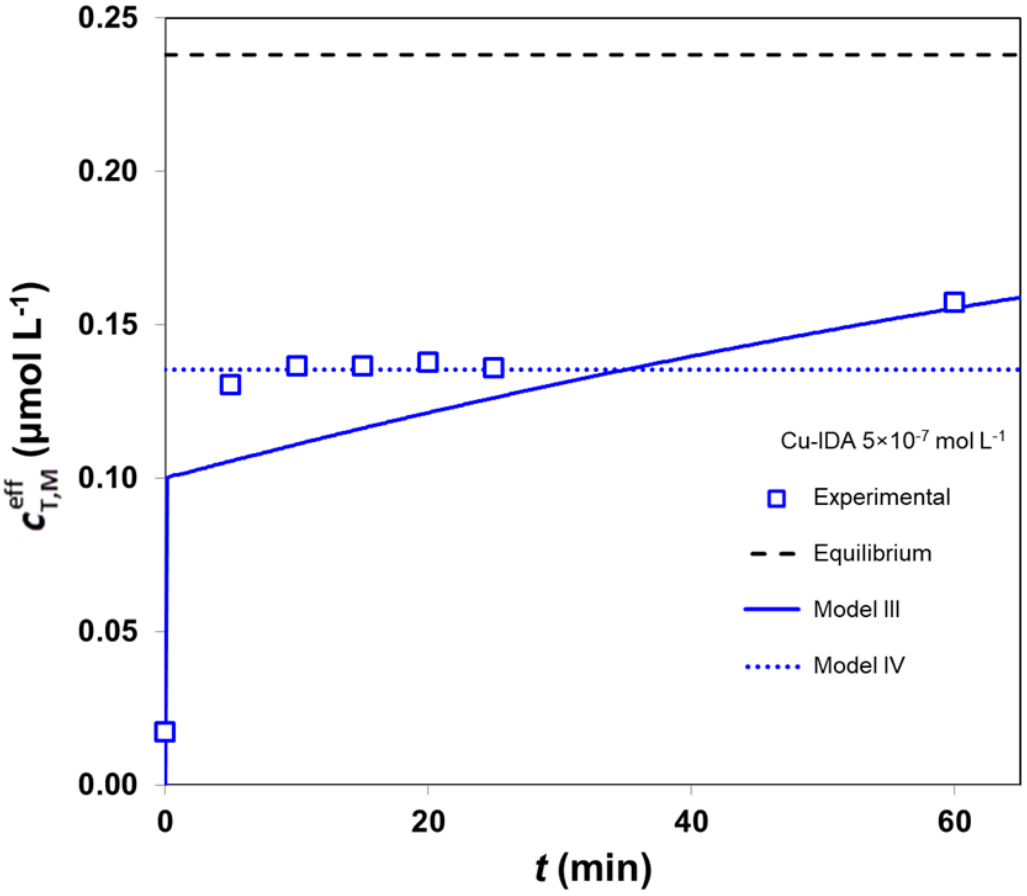

Figure 5.8. Breakthrough curve of total concentration $c^{eff}_{T,M}$ for the system Cu-IDA, with $c_{T,IDA}$= 5×10^{-7} M. Markers: experimental data; continuous line: Model III; dotted line: Model IV. Upper black dashed line stands for the eventual equilibrium value. $c_{T,Cu}$= 2.47×10^{-7} M, Q= 4.5 mL min^{-1}.

Lower plateaus (at about 10% of $c_{T,M}$) can be spotted in the curves of salicylate and glutamate. Clear SS plateaus have been observed also in the case of Ni-malonate, although at concentrations too low to be safely quantified.

The SS plateau is more apparent when the initial depletion of the metal along the column is not so intense *i.e.* when $c^{eff}_{T,M}$ is not negligible in front of $c_{T,M}$. Let us compare, for instance, in Fig. 5.7, the series for small (blue squares) and large resin (red squares) both with similar flow rates in a solution with just Cu. In the limit of very low effluent concentrations (*e.g.* series of blue squares), the SS plateau concentration may be indistinguishable from the baseline (background signal).

Previously, this biphasic behaviour was observed only at low I and with trivalent cations.[5] This can be explained considering that the duration of the SS-plateau is related to the time along which the beads act as a perfect sink for M. Increasing the electrostatic partitioning factor χ or the ion charge z_M makes these terms to drop down, and as a consequence the beads tend to behave as perfect sink for M during longer periods.

Also, by comparing the two Ni-only breakthrough curves in Fig. 5.4b, one concludes that the SS plateau is clearer in those cases where the accumulation rate is lower (*i.e.* lower initial slope in the trajectory).

5.3.7. Retrieval of lability parameters and c_{DIET}

NEUTRAL COMPLEXES

Lability degrees for neutral complexes are gathered in Tab. 5.2. The theoretical lability degree ξ_{theo} has been computed according to Model II, Eq. (5.7) and needed parameters from Tab. 5.1. Lability degrees from the SS plateau, Eq. (5.17), or from the slope of the trajectory, Eq. (5.22), could not be computed for systems with the ligands malate and malonate, but for the rest of the systems both values were reasonably close to each other and to the theoretical ξ value. This is also partially due to r_1 having being fitted to 61.6 μm to obtain such similarity. The agreement between ξ from Eq. (5.17) and (5.22), albeit anticipated, lends support to model IV. Given that the experimental concentrations of the SS plateau were not completely constant, the value of $c_{T,M}^{eff}$ used in Eq. (5.17) was taken from the intercept of the linear regression of the first points.

c_{DIET} concentrations for Cu(II) systems with malate or malonate from the SS plateau could not be computed, as the plateau was not observed. As the accuracy of our measurements did not allow to distinguish the slope of the trajectory of such systems from the one in absence of ligand, we suggest full lability (as theoretically expected by ξ_{theo}) and estimate $c_{DIET}=c_{T,M}$. For the rest of complexes in Tab.5.2, c_{DIET} values look quite reasonably in between the fully labile case when $c_{DIET}=c_{T,M}$ (practically reached for Cu-salicylate) and the completely inert case when $c_{DIET}=c_M$ (approached by the Cu-IDA system).

POSITIVE COMPLEXES

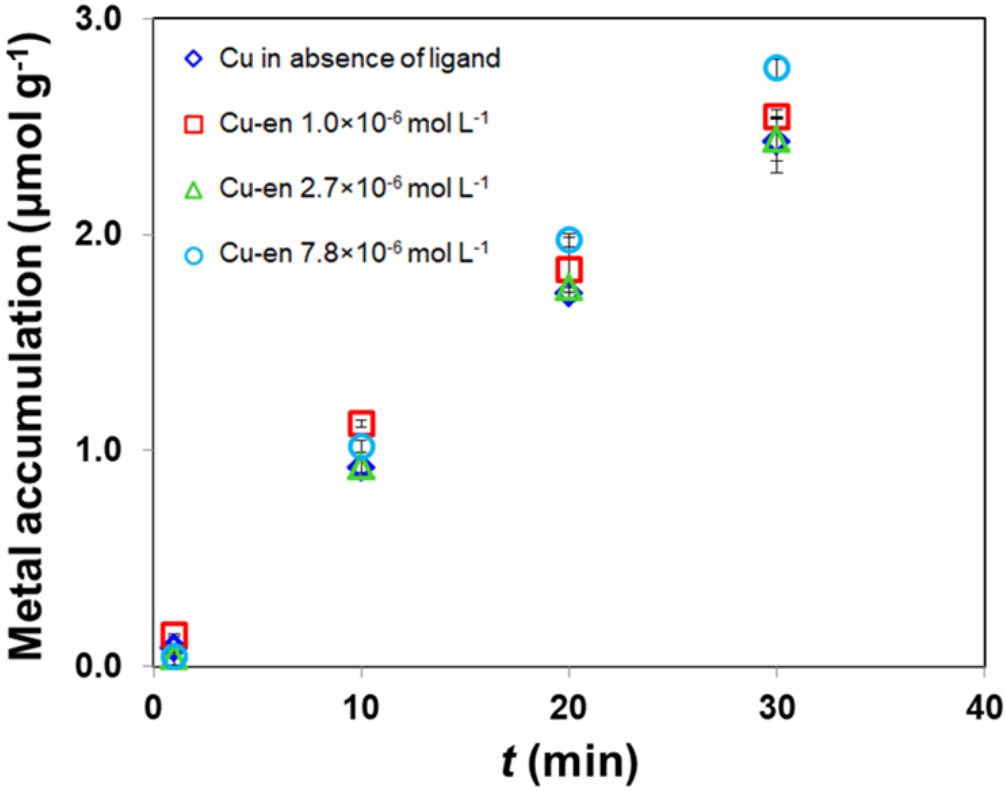

Figure 5.9. Trajectories related to Cu(II) accumulation on Dowex 50x4 (200-400 mesh) in presence of three different concentrations of en, which forms positively charged complexes. Each series corresponds to a different free Cu^{2+} concentration, reported in the legend (as M). The points stand for the average of three independent columns. $c_{T,Cu}$= 2.5×10^{-7} M, Q= 4.5 mL min^{-1}.

Theoretical lability degrees for the systems with Cu-en computed with Eq. (5.7) yielded a value of 1 (see Tab. 5.3). The initial slope of the trajectories is just proportional to the total metal concentration (see Fig. 5.9) and, accordingly, the labile fraction c_{DIET} is equal to the total metal concentration. The eventual equilibrium (total metal) accumulation for positive complexes is $\chi^{z_M} c_M + \chi^{z_{ML}} c_{ML}$, so, much higher than that of neutral complexes (for a common bulk free metal concentration).

NEGATIVE COMPLEXES

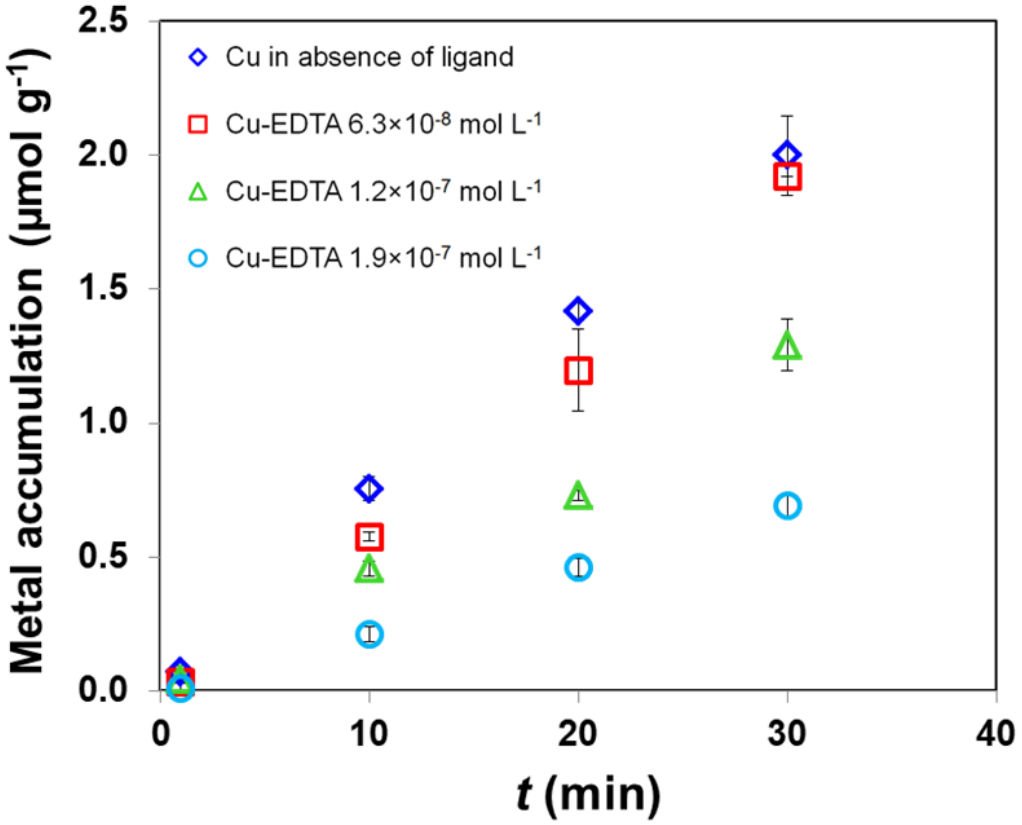

Figure 5.10. Trajectories related to Cu(II) accumulation on Dowex 50x4 (200-400 mesh) in presence of three different concentrations of EDTA, which forms negatively charged complexes. Each series corresponds to a different free Cu^{2+} concentration, reported in the legend (as M). The points stand for the average of three independent columns. $c_{T,Cu}$= 2.5×10 ^{7} M, Q= 4.5 mL min^{-1}.

In Tab. 5.3, the theoretical lability degree is computed with Eq. (5.7), even if only the citrate systems are under clear excess of ligand conditions. For these systems no determinations are possible due to the fast attainment of equilibrium (see Fig. 5.4). Theoretical ξ values for negative complexes with EDTA are practically 0, as expected from the repulsion of the complex from the resin and the strong affinity constant. Consequently, the slopes of the trajectories are clearly different from the solutions where the metal is present almost exclusively as free ion (see Fig. 5.3 or Fig. 5.10). The values of ξ retrieved from the initial slopes using Eq. (5.22) are slightly negative, which we attribute to experimental uncertainties, but in agreement with a practically totally inert behaviour. The values of c_{DIET} are, accordingly, usually slightly lower than (or almost equal to) the theoretical free fraction. So, in the Cu-EDTA systems, DIET is measuring just the free fraction of the metal in the sample.

5.4. Conclusions

The (practically) constant effluent concentration, described as "SS plateau", seen at short enough times in the breakthrough curves, is associated to a steady-state regime where the beads act as perfect sink for free metal (*i.e.* they are far away from equilibrium). This (quasi) steady-state regime also explains the initial linear accumulations having a lower slope than that for metal solutions in absence of ligand or solutions of completely labile complexes (that in the probed systems showed an almost complete retention of the metal, so that the slope of these trajectories approximates $Q\,c_{T,M}$).

c_{DIET}, as defined in Eq. (5.23), quantifies the labile concentration of a system in DIET measurements using ion exchange or chelating resins (such as Chelex). A simple and general model for the initial SS stages of the uptake in a DIET experiment (Model IV) leads to the practical Eqs. (5.24) and (5.25) for c_{DIET} computation when assuming common diffusion coefficients of metal and complexes.

If the SS plateau in the breakthrough curve is clear enough, the lability degree can be computed from Eq. (5.17) and c_{DIET} from Eq. (5.24). Otherwise, one has to resort to the initial slope of the trajectory by applying Eq. (5.18), provided that the difference with the product $Q\,c_{T,M}$ is above the experimental error. The same *caveat* has to be taken into account for computing c_{DIET} with Eq. (5.25).

Most of the complexes considered were found to be completely labile, in some cases contrasting with previous voltammetric studies.[31] This tendency for DIET to "labilise" the complexes, not dissimilar to the one of DGT,[12,30,32,33] is a consequence of the beads radii being relatively large, in comparison with typical voltammetric reaction layer thicknesses. As it happened with IET,[20] DIET cannot be applied to the study of positively charged complexes, as they accumulate inside the resin at a rate close to the free metal ions; on the other hand, it proved to be particularly effective for studying the dissociation of neutral complexes

The resin bed volume has a key role in the retrieved global lability parameter Ξ. The longer the column, the higher the lability seen by DIET. This means that each column has an analytical window of labilities, so that future work with columns packed with different amounts of resin and/or different flow rates[7] might prove very useful. For the range of columns analysed so far, smaller bed volumes had allowed better effluent analysis. Larger amount of resin improved the limit of detection of the technique (in the

eluate analysis) and allowed more frequent sampling of accumulations at short times, but hindered the detection of the SS-plateau regime (*e.g.* slopes of trajectories practically undistinguishable from $Q\,c_{T,M}$, leading to ξ=1 and c_{DIET}=$c_{T,M}$).

The use of the effluent total metal concentration evolution (*i.e.* breakthrough curves), though promising when a clear SS plateau is detected, might be of more limited use in natural systems where the concentrations of the target ions (especially after flushing through the column) are too low for an accurate determination.

5.5. Appendices

In this section it will be presented the formal derivation of the models. All of them are based on the common assumptions listed in Section 5.3.3.1.

5.5.1. Model I: time dependent accumulation in one bead

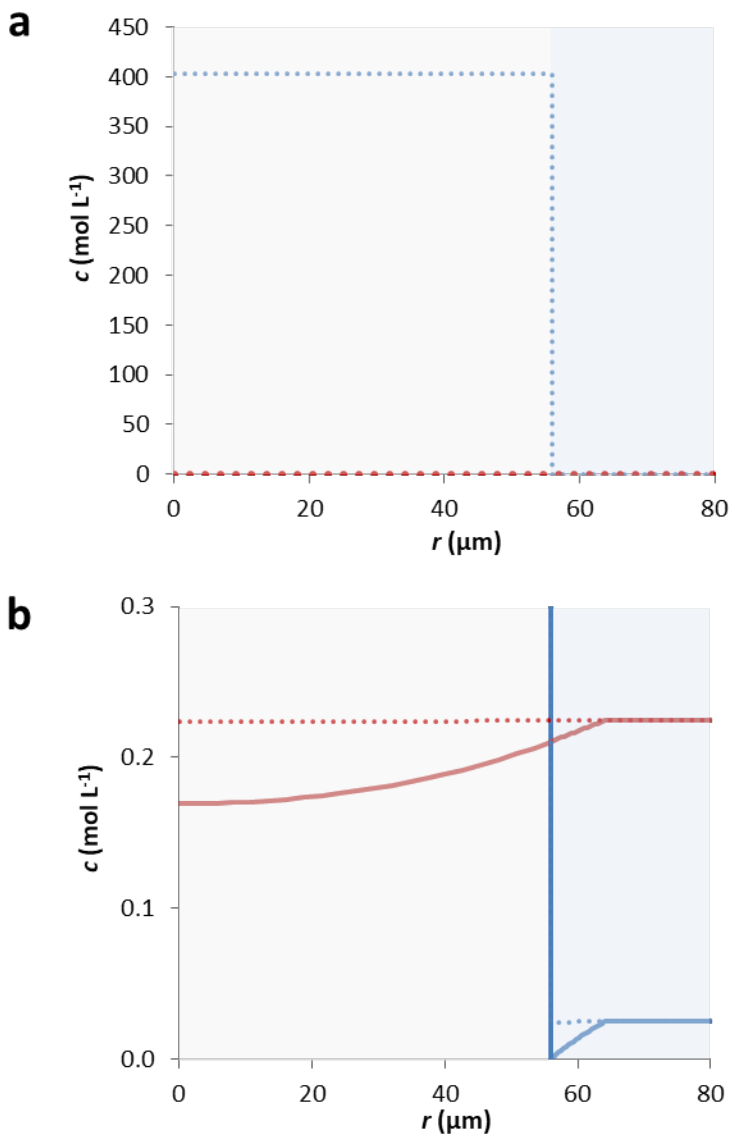

Figure A5.1. Concentration profiles of M (blue) and ML (red) in one bead at t= 100 s (continuous line) and at equilibrium (dotted lines) for the system Cu-IDA 5×10^{-7} M (computed with Model I). Panel b *is a magnification of panel* a *highlighting the profiles at short time and in the diffusion layer. Parameters as in Tab. 5.1.*

In Model I, both metal species, M and ML can penetrate inside the resin, where the complex can dissociate and be generated again. The problem will be split into two parts: resin and solution domain.

SOLUTION DOMAIN ($r_0<r<r_1$)

The continuity equations for free and complexed metal can be written, respectively, as:

$$\frac{\partial c_{\mathrm{M}}(r,t)}{\partial t} = D_{\mathrm{M}}\nabla^2 c_{\mathrm{M}}(r,t) + k_{\mathrm{d}}\, c_{\mathrm{ML}}(r,t) - k'_{\mathrm{a}}\, c_{\mathrm{M}}(r,t) \tag{A5.1}$$

and:

$$\frac{\partial c_{\mathrm{ML}}(r,t)}{\partial t} = D_{\mathrm{M}}\nabla^2 c_{\mathrm{ML}}(r,t) - k_{\mathrm{d}}\, c_{\mathrm{ML}}(r,t) + k'_{\mathrm{a}}\, c_{\mathrm{ML}}(r,t) \tag{A5.2}$$

where D_{M} is the diffusion coefficient of the metal species, k_{d} is the dissociation rate constant of the complex and k'_{a} is the effective association rate constant, defined as:

$$k'_{\mathrm{a}} = k_{\mathrm{a}} c_{\mathrm{L}} \tag{A5.3}$$

RESIN DOMAIN ($r<r_0$)

The continuity equations for the free and the complexed metal can be written, respectively, as:

$$\frac{\partial \tilde{c}_{\mathrm{M}}(r,t)}{\partial t} = \tilde{D}_{\mathrm{M}}\nabla^2 \tilde{c}_{\mathrm{M}}(r,t) + \tilde{k}_{\mathrm{d}}\, \tilde{c}_{\mathrm{ML}}(r,t) - \tilde{k}'_{\mathrm{a}}\, \tilde{c}_{\mathrm{M}}(r,t) \tag{A5.4}$$

and:

$$\frac{\partial \tilde{c}_{\mathrm{ML}}(r,t)}{\partial t} = \tilde{D}_{\mathrm{M}}\nabla^2 \tilde{c}_{\mathrm{ML}}(r,t) - \tilde{k}_{\mathrm{d}}\, \tilde{c}_{\mathrm{ML}}(r,t) + \tilde{k}'_{\mathrm{a}}\, \tilde{c}_{\mathrm{ML}}(r,t) \tag{A5.5}$$

where tilde ~ indicates concentrations or parameters inside the resin bead.

This system of equations can be solved with the following boundary conditions:

i) at the centre of the bead (r= 0) :

$$\left(\frac{\partial \tilde{c}_{\mathrm{M}}(r,t)}{\partial r}\right)_{r=0} = 0 \tag{A5.6}$$

and:

$$\left(\frac{\partial \tilde{c}_{\mathrm{ML}}(r,t)}{\partial r}\right)_{r=0} = 0 \tag{A5.7}$$

ii) the partitioning of the metal species at the bead surface ($r = r_0$):

$$\tilde{c}_{\mathrm{M}}\left(r_0^-,t\right) = \chi^{z_{\mathrm{M}}}\; c_{\mathrm{M}}\left(r_0^+,t\right) \tag{A5.8}$$

and:

$$\tilde{c}_{\mathrm{ML}}\left(r_0^-,t\right) = \chi^{z_{\mathrm{ML}}}\; c_{\mathrm{ML}}\left(r_0^+,t\right) \tag{A5.9}$$

iii) from the continuity of fluxes at the bead surface:

$$\left(\frac{\partial \tilde{c}_{\mathrm{M}}(r,t)}{\partial r}\right)_{r=r_0^-} = \left(\frac{\partial c_{\mathrm{M}}(r,t)}{\partial r}\right)_{r=r_0^+} \tag{A5.10}$$

and:

$$\left(\frac{\partial \tilde{c}_{\mathrm{ML}}(r,t)}{\partial r}\right)_{r=r_0^-} = \left(\frac{\partial c_{\mathrm{ML}}(r,t)}{\partial r}\right)_{r=r_0^+} \tag{A5.11}$$

iv) at the limits of the diffusion layer ($r = r_1$):

$$c_{\mathrm{M}}\left(r_1,t\right) = c_{\mathrm{M}}^{*}\left(t\right) \tag{A5.12}$$

and:

$$c_{\mathrm{ML}}\left(r_1,t\right) = c_{\mathrm{ML}}^{*}\left(t\right) \tag{A5.13}$$

Now, by introducing the variables

$$\mu_{\mathrm{M}}(r,t) \equiv r\; c_{\mathrm{M}}\left(r,t\right) \tag{A5.14}$$

and:

$$\mu_{\mathrm{ML}}(r,t) \equiv r\; c_{\mathrm{ML}}\left(r,t\right) \tag{A5.15}$$

The continuity equations in the SOLUTION DOMAIN (A5.1) and (A5.2) can be rewritten as:

$$\frac{\partial \mu_{\mathrm{M}}(r,t)}{\partial t} = D_{\mathrm{M}}\frac{\partial^2 \mu_{\mathrm{M}}(r,t)}{\partial r^2} + k_{\mathrm{d}}\;\mu_{\mathrm{ML}}(r,t) - k_{\mathrm{a}}'\;\mu_{\mathrm{M}}(r,t) \tag{A5.16}$$

and (as we have assumed that $D_{\mathrm{M}} = D_{\mathrm{ML}}$):

$$\frac{\partial \mu_{\mathrm{ML}}(r,t)}{\partial t} = D_{\mathrm{M}}\frac{\partial^2 \mu_{\mathrm{ML}}(r,t)}{\partial r^2} - k_{\mathrm{d}}\;\mu_{\mathrm{ML}}(r,t) + k_{\mathrm{a}}'\;\mu_{\mathrm{M}}(r,t) \tag{A5.17}$$

Similarly, the continuity equations in the RESIN DOMAIN (A5.4) and (A5.5) can be rewritten as:

$$\frac{\partial \tilde{\mu}_{\mathrm{M}}(r,t)}{\partial t} = D_{\mathrm{M}}\frac{\partial^2 \tilde{\mu}_{\mathrm{M}}(r,t)}{\partial r^2} + k_{\mathrm{d}}\;\tilde{\mu}_{\mathrm{ML}}(r,t) - \tilde{k}_{\mathrm{a}}'\;\tilde{\mu}_{\mathrm{M}}(r,t) \tag{A5.18}$$

and

$$\frac{\partial \tilde{\mu}_{\mathrm{ML}}(r,t)}{\partial t} = D_{\mathrm{M}} \frac{\partial^2 \tilde{\mu}_{\mathrm{ML}}(r,t)}{\partial r^2} - k_{\mathrm{d}}\, \tilde{\mu}_{\mathrm{ML}}(r,t) + \tilde{k}'_{\mathrm{a}}\, \tilde{\mu}_{\mathrm{M}}(r,t) \tag{A5.19}$$

as we also assume that diffusion coefficients in the resin are equal to those in the solution.

In this work, we assume that the rate constants inside the resin are equal to those outside the resin (k_{d} and k_{a}).

The boundary conditions (A5.6) and (A5.7) become:

$$\tilde{\mu}_{\mathrm{M}}(0,t) = 0 \tag{A5.20}$$

and:

$$\tilde{\mu}_{\mathrm{ML}}(0,t) = 0 \tag{A5.21}$$

while, with simple algebra (A5.10) and (A5.11) become:

$$\left(\frac{\partial \tilde{\mu}_{\mathrm{M}}(r,t)}{\partial r}\right)_{r=r_0^-} - \frac{\tilde{\mu}_{\mathrm{M}}\left(r_0^-,t\right)}{r_0} = \left(\frac{\partial \mu_{\mathrm{M}}(r,t)}{\partial r}\right)_{r=r_0^+} - \frac{\mu_{\mathrm{M}}\left(r_0^+,t\right)}{r_0} \tag{A5.22}$$

and:

$$\left(\frac{\partial \tilde{\mu}_{\mathrm{ML}}(r,t)}{\partial r}\right)_{r=r_0^-} - \frac{\tilde{\mu}_{\mathrm{ML}}\left(r_0^-,t\right)}{r_0} = \left(\frac{\partial \mu_{\mathrm{ML}}(r,t)}{\partial r}\right)_{r=r_0^+} - \frac{\mu_{\mathrm{ML}}\left(r_0^+,t\right)}{r_0} \tag{A5.23}$$

Let us first solve the continuity equation relative to the free metal (A5.18). Here we will broadly follow the treatment found in Crank[34] and in the example by Chávez (http://demonstrations.wolfram.com/TransientDiffusionInABilayerSystem/), as well as the nomenclature used by the latter.

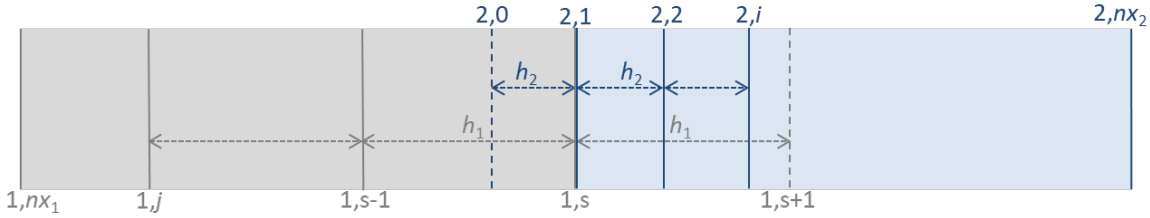

Figure A5.2. Discretization of the space domain. Grey solid lines: resin grid; blue solid lines: solution grid. Dashed lines: virtual nodes. Pairs of numbers in blue above indicate the indices of the solution grid, while the grey ones below indicate those of the resin grid. Some nodes (as 2,1/1,s) belong to both grids.

Let us now discretize Eq. (A5.18) in the space domain. To account for the presence of two phases, we will start by considering two grids for each subdomains one for the resin

(subscript 1) and one for the solution (subscript 2). Let each grid be divided into nx_1 or nx_2 intervals of equal width h_1 or h_2. By adapting Eq. (8.11) of Crank's book,[34] the continuity equation Eq. (A5.18) in a generic node j of the grid can be rewritten as:

$$\frac{\partial \tilde{\mu}_{\mathrm{M}_{1,j}}(t)}{\partial t} = D_{\mathrm{M}} \frac{\tilde{\mu}_{\mathrm{M}_{1,j+1}}(t) - 2\tilde{\mu}_{\mathrm{M}_{1,j}}(t) + \tilde{\mu}_{\mathrm{M}_{1,j-1}}(t)}{h_1^2} + k_{\mathrm{d}}\, \tilde{\mu}_{\mathrm{ML}_{1,j}}(t) - \tilde{k}'_{\mathrm{a}}\, \tilde{\mu}_{\mathrm{M}_{1,j}}(t) \qquad \text{(A5.24)}$$

for the resin subdomain, and as:

$$\frac{\partial \mu_{\mathrm{M}_{2,i}}(t)}{\partial t} = D_{\mathrm{M}} \frac{\mu_{\mathrm{M}_{2,i+1}}(t) - 2\mu_{\mathrm{M}_{2,i}}(t) + \mu_{\mathrm{M}_{2,i-1}}(t)}{h_2^2} + k_{\mathrm{d}}\, \mu_{\mathrm{ML}_{2,i}}(t) - k'_{\mathrm{a}}\, \mu_{\mathrm{M}_{2,i}}(t) \qquad \text{(A5.25)}$$

for the solution domain (node i, Eq. (A5.18)).

Similarly, the equation corresponding to the first unknown node (j=2) of the resin subdomain (r=0) will be:

$$\frac{\partial \tilde{\mu}_{\mathrm{M}_{1,2}}(t)}{\partial t} = D_{\mathrm{M}} \frac{\tilde{\mu}_{\mathrm{M}_{1,3}}(t) - 2\tilde{\mu}_{\mathrm{M}_{1,2}}(t)}{h_1^2} + k_{\mathrm{d}}\, \tilde{\mu}_{\mathrm{ML}_{1,2}}(t) - \tilde{k}'_{\mathrm{a}}\, \tilde{\mu}_{\mathrm{M}_{1,2}}(t) \qquad \text{(A5.26)}$$

while the one for the last (unknown) node of the solution subdomain will be:

$$\frac{\partial \mu_{\mathrm{M}_{2,nx_2-1}}(t)}{\partial t} = D_{\mathrm{M}} \frac{\mu^*_{\mathrm{M}} - 2\mu_{\mathrm{M}_{2,nx_2-1}}(t) + \mu_{\mathrm{M}_{2,nx_2-2}}(t)}{h_2^2} + k_{\mathrm{d}}\, \mu_{\mathrm{M}_{2,nx_2-1}}(t) - k'_{\mathrm{a}}\, \mu_{\mathrm{M}_{2,nx_2-1}}(t) \qquad \text{(A5.27)}$$

Let us now focus on the interface between the two phases. For simplicity we also label s=nx_1. The interface point will be called (1,s) if expressed using the coordinates of the resin subdomain and (2,1) using those of the solution one. In order to compute the difference quotient of Eq. (A5.18) across the interface, let us add to each grid a "virtual" node (indicated by superscript ν) located in the other subdomain, and let their coordinates be (1,s+1) and (2,0), respectively.

The boundary condition at the interface (A5.22) can be discretized as:

$$\frac{\mu^{\nu}_{\mathrm{M}_{1,s+1}}(t) - \tilde{\mu}_{\mathrm{M}_{1,s\text{-}1}}(t)}{2h_1} - \frac{\tilde{\mu}_{\mathrm{M}_{1,s}}(t)}{r_0} = \frac{\mu_{\mathrm{M}_{2,2}}(t) - \tilde{\mu}^{\nu}_{\mathrm{M}_{2,0}}(t)}{2h_2} - \frac{\mu_{\mathrm{M}_{2,1}}(t)}{r_0} \qquad \text{(A5.28)}$$

If, following the notation of Crank,[34] p.149, the value of the difference (A5.28) is called F (as it is proportional to the flux crossing the interface), the first virtual point of the resin subdomain can be expressed as:

$$\mu^{\nu}_{\mathrm{M}_{1,s+1}}(t) = 2h_1 F + 2h_1 \frac{\tilde{\mu}_{\mathrm{M}_{1,s}}(t)}{r_0} + \tilde{\mu}_{\mathrm{M}_{1,s\text{-}1}}(t) \qquad \text{(A5.29)}$$

The continuity equation at point (1,s) will therefore be:

$$\frac{\partial \tilde{\mu}_{\mathrm{M}_{1,s}}(t)}{\partial t} = D_{\mathrm{M}} \frac{\mu^{v}_{\mathrm{M}_{1,s+1}}(t) - 2\tilde{\mu}_{\mathrm{M}_{1,s}}(t) + \tilde{\mu}_{\mathrm{M}_{1,s-1}}(t)}{h_1^2} + k_{\mathrm{d}}\ \tilde{\mu}_{\mathrm{ML}_{1,s}}(t) - k'_{\mathrm{a}}\ \tilde{\mu}_{\mathrm{M}_{1,s}}(t) \tag{A5.30}$$

The substitution of (A5.29) in (A5.30) with further rearrangements yields:

$$h_1 \frac{\partial \tilde{\mu}_{\mathrm{M}_{1,s}}}{\partial t} = 2D_{\mathrm{M}}F + \frac{2D_{\mathrm{M}}}{h_1}\left(\tilde{\mu}_{\mathrm{M}_{1,s-1}}(t) - \tilde{\mu}_{\mathrm{M}_{1,s}}(t) + h_1 \frac{\tilde{\mu}_{\mathrm{M}_{1,s}}(t)}{r_0}\right) + h_1\left(k_{\mathrm{d}}\ \tilde{\mu}_{\mathrm{ML}_{1,s}}(t) - k'_{\mathrm{a}}\ \tilde{\mu}_{\mathrm{M}_{1,s}}(t)\right) \tag{A5.31}$$

A similar reasoning can be followed to rewrite the continuity equation at point (2,1) in the coordinates of the solution subdomain:

$$h_2 \frac{\partial \mu_{\mathrm{M}_{2,1}}(t)}{\partial t} = -2D_{\mathrm{M}}F + \frac{2D_{\mathrm{M}}}{h_2}\left(\mu_{\mathrm{M}_{2,2}}(t) - \mu_{\mathrm{M}_{2,1}}(t) - h_2 \frac{\mu_{\mathrm{M}_{2,1}}(t)}{r_0}\right) + h_2\left(k_{\mathrm{d}}\ \mu_{\mathrm{ML}_{2,1}}(t) - \tilde{k}'_{\mathrm{a}}\ \mu_{\mathrm{M}_{2,1}}(t)\right) \tag{A5.32}$$

By adding (A5.31) to (A5.32), the F terms cancel out:

$$\begin{aligned} h_1 \frac{\partial \tilde{\mu}_{\mathrm{M}_{1,s}}(t)}{\partial t} + h_2 \frac{\partial \mu_{\mathrm{M}_{2,1}}(t)}{\partial t} = {} & \frac{2D_{\mathrm{M}}}{h_1}\left(\tilde{\mu}_{\mathrm{M}_{1,s-1}}(t) - \tilde{\mu}_{\mathrm{M}_{1,s}}(t) + h_1 \frac{\tilde{\mu}_{\mathrm{M}_{1,s}}(t)}{r_0}\right) + h_1\left(k_{\mathrm{d}}\ \tilde{\mu}_{\mathrm{ML}_{1,s}}(t) - k'_{\mathrm{a}}\ \tilde{\mu}_{\mathrm{M}_{1,s}}(t)\right) + \\ & + \frac{2D_{\mathrm{M}}}{h_2}\left(\mu_{\mathrm{M}_{2,2}}(t) - \mu_{\mathrm{M}_{2,1}}(t) - h_2 \frac{\mu_{\mathrm{M}_{2,1}}(t)}{r_0}\right) + h_2\left(k_{\mathrm{d}}\ \mu_{\mathrm{ML}_{2,1}}(t) - \tilde{k}'_{\mathrm{a}}\ \mu_{\mathrm{M}_{2,1}}(t)\right) \end{aligned} \tag{A5.33}$$

This is the discretized version of the flux boundary condition at the interface.

The concentration boundary conditions at the interface (A5.8) relate $\mu_{\mathrm{M}_{1,s}}$ and $\mu_{\mathrm{M}_{2,1}}$:

$$\tilde{\mu}_{\mathrm{M}_{1,s}}(t) = \chi^{z_{\mathrm{M}}}\mu_{\mathrm{M}_{2,1}}(t) \tag{A5.34}$$

and $\mu_{\mathrm{ML}_{1,s}}$ and $\mu_{\mathrm{ML}_{1,s}}$:

$$\tilde{\mu}_{\mathrm{ML}_{1,s}}(t) = \chi^{z_{\mathrm{ML}}}\mu_{\mathrm{ML}_{2,1}}(t) \tag{A5.35}$$

The substitution of (A5.34) and (A5.35) in (A5.33) leads to:

$$\frac{\partial \tilde{\mu}_{\mathrm{M}_{1,s}}(t)}{\partial t} = \frac{1}{h_1 + \frac{h_2}{\chi^{z_{\mathrm{M}}}}}\left[\begin{aligned} & \frac{2D_{\mathrm{M}}}{h_1}\left(\tilde{\mu}_{\mathrm{M}_{1,s-1}}(t) - \tilde{\mu}_{\mathrm{M}_{1,s}}(t) + h_1 \frac{\tilde{\mu}_{\mathrm{M}_{1,s}}(t)}{r_0}\right) + h_1\left(k_{\mathrm{d}}\ \tilde{\mu}_{\mathrm{ML}_{1,s}}(t) - k'_{\mathrm{a}}\ \tilde{\mu}_{\mathrm{M}_{1,s}}(t)\right) + \\ & + \frac{2D_{\mathrm{M}}}{h_2}\left(\mu_{\mathrm{M}_{2,2}}(t) - \frac{\tilde{\mu}_{\mathrm{M}_{1,s}}(t)}{\chi^{z_{\mathrm{M}}}} - \frac{h_2}{\chi^{z_{\mathrm{M}}}}\frac{\tilde{\mu}_{\mathrm{M}_{1,s}}(t)}{r_0}\right) + h_2\left(k_{\mathrm{d}}\ \frac{\tilde{\mu}_{\mathrm{ML}_{1,s}}(t)}{\chi^{z_{\mathrm{ML}}}} - \tilde{k}'_{\mathrm{a}}\ \frac{\tilde{\mu}_{\mathrm{M}_{1,s}}(t)}{\chi^{z_{\mathrm{M}}}}\right) \end{aligned}\right] \tag{A5.36}$$

By analogy, a similar equation can be written for the ML complex:

$$\frac{\partial \tilde{\mu}_{\mathrm{ML}_{1,s}}(t)}{\partial t} = \frac{1}{h_1 + \frac{h_2}{\chi^{z_{\mathrm{ML}}}}} \left[\begin{array}{l} \frac{2D_{\mathrm{M}}}{h_1}\left(\tilde{\mu}_{\mathrm{ML}_{1,s-1}}(t) - \tilde{\mu}_{\mathrm{ML}_{1,s}}(t) + h_1 \frac{\tilde{\mu}_{\mathrm{ML}_{1,s}}(t)}{r_0} \right) + h_1 \left(k'_{\mathrm{a}}\ \tilde{\mu}_{\mathrm{M}_{1,s}}(t) - k_{\mathrm{d}}\ \tilde{\mu}_{\mathrm{ML}_{1,s}}(t) \right) + \\ \quad + \frac{2D_{\mathrm{M}}}{h_2}\left(\mu_{\mathrm{ML}_{2,2}}(t) - \frac{\tilde{\mu}_{\mathrm{ML}_{1,s}}(t)}{\chi^{z_{\mathrm{ML}}}} - \frac{h_2}{\chi^{z_{\mathrm{ML}}}} \frac{\tilde{\mu}_{\mathrm{ML}_{1,s}}(t)}{r_0} \right) + h_2 \left(\tilde{k}'_{\mathrm{a}}\ \frac{\tilde{\mu}_{\mathrm{M}_{1,s}}(t)}{\chi^{z_{\mathrm{M}}}} - k_{\mathrm{d}}\ \frac{\tilde{\mu}_{\mathrm{ML}_{1,s}}(t)}{\chi^{z_{\mathrm{ML}}}} \right) \end{array} \right] \tag{A5.37}$$

The system of differential equations (A5.24), (A5.25), (A5.26), (A5.27), (A5.36) and (A5.37) can be solved numerically in the time variable (for each spatial position) by imposing the following initial conditions:

$$\tilde{\mu}_{\mathrm{M}_{1,j}}(0) = 0\ ,\ \tilde{\mu}_{\mathrm{ML}_{1,j}}(0) = 0 \qquad \text{for}\ \ j=2,\ldots, nx_1 \tag{A5.38}$$

and:

$$\mu_{\mathrm{M}_{2,\mathrm{i}}}(0) = 0\ ,\ \mu_{\mathrm{ML}_{2,\mathrm{i}}}(0) = 0 \qquad \text{for}\ \ j=2,\ldots, nx_2\text{-}1 \tag{A5.39}$$

and the boundary conditions:

$$\tilde{\mu}_{\mathrm{M}_{1,1}}(t) = 0,\ \tilde{\mu}_{\mathrm{ML}_{1,1}}(t) = 0 \qquad \forall t \tag{A5.40}$$

and:

$$\mu_{\mathrm{M}_{2,nx_2}}(t) = r_1 c^*_{\mathrm{M}}(t),\ \mu_{\mathrm{ML}_{2,nx_2}}(t) = r_1 c^*_{\mathrm{ML}}(t) \qquad \forall t \tag{A5.41}$$

In the computations, we typically used 21 points for each grid, corresponding to $h_1 = 2.7\times10^{-6}$ m and $h_2 = 2.6\times10^{-7}$ m.

As seen in Fig. A5.1, for typical values in the considered systems, the current metal concentration inside the beads at 100 s is negligible in front of the final equilibrium concentration of M in the resin. This observation is used in Model II. On the other hand, the practical constancy of ML concentration profile inside the resin will be used in Model III.

5.5.2. Model II: accumulation in one bead at steady state

This model is similar to those developed for DGT,[21] with the main difference that we are now in spherical geometry.

Apart from the general assumptions common to all models, in Model II it is also assumed that the concentration of free metal in the resin phase is negligible in comparison to its equilibrium value (*i.e.* we are in the initial accumulation stage, far away from equilibrium), so that only the dissociation of ML (and not its re-association) needs to be taken into account. This is a reasonable assumption, as illustrated in Fig. A5.1a. Due to the huge value of the partitioning factor for M, this steady state also

implies that the resin acts as a perfect sink for the free metal (c_M drops to 0 at the resin/solution interface), as shown in the schematic representation given in Fig. A5.3

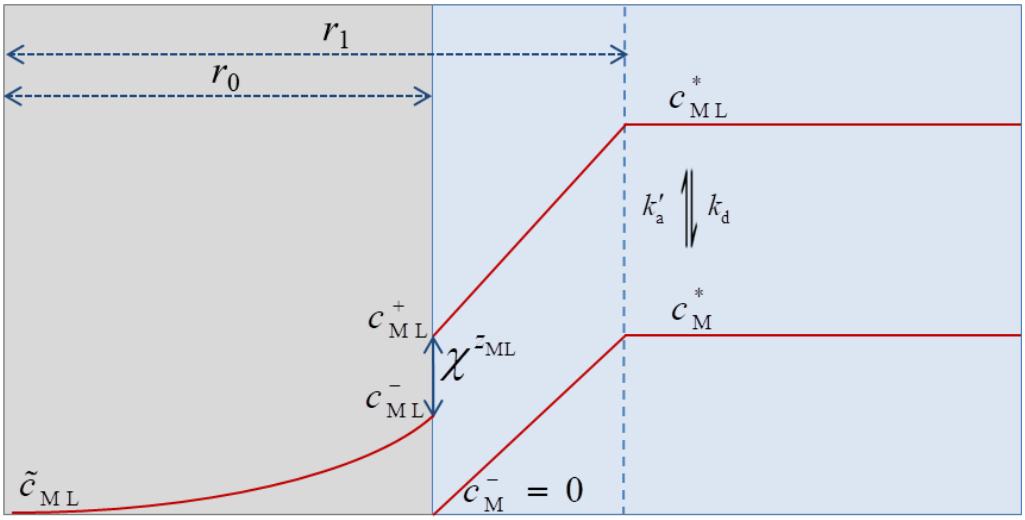

Figure A5.3. Schematic representation of the concentration profiles inside one bead and in its diffusion (boundary) layer according to Model II. The interface acts as perfect sink for the metal. The Boltzmann factor rules the partitioning of ML at the interface.

The problem will be split into two parts: resin and solution domain.

RESIN DOMAIN ($0<r<r_0$)

From assumptions 1 and 2, the continuity equation for the metal complex inside the bead can be written as follows:

$$0 = D_M\left(\frac{d^2\tilde{c}_{ML}(r)}{dr^2}+\frac{2}{r}\frac{d\tilde{c}_{ML}(r)}{dr}\right)-k_d\,\tilde{c}_{ML}(r) \qquad 0<r<r_0 \tag{A5.42}$$

The change of variable given by (A5.15), allows reaching:

$$\frac{d^2\tilde{\mu}_{ML}(r)}{dr^2}=\frac{k_d}{D_M}\tilde{\mu}_{ML}(r)=\frac{1}{\lambda^2}\tilde{\mu}_{ML}(r) \tag{A5.43}$$

where

$$\lambda=\sqrt{\frac{D_M}{k_d}} \tag{A5.44}$$

can be called the penetration parameter.

The solution of Eq. (A5.43) is known to be in the form of:

$$\tilde{\mu}_{ML}(r)=E\sinh\left(\frac{r}{\lambda}\right)+F\cosh\left(\frac{r}{\lambda}\right) \tag{A5.45}$$

from boundary condition (A5.21) it can be readily deduced that

$$E = 0 \tag{A5.46}$$

which leads to:

$$\tilde{\mu}_{\mathrm{ML}}(r) = F \cosh\left(\frac{r}{\lambda}\right) \tag{A5.47}$$

At the surface of the bead, Eq. (A5.47) becomes:

$$\tilde{\mu}_{\mathrm{ML}}(r_0) = r_0 \tilde{c}_{\mathrm{ML}}(r_0) = F \cosh\left(\frac{r_0}{\lambda}\right) \tag{A5.48}$$

By dividing (A5.47) by (A5.48) and solving for c_{ML}, we finally obtain:

$$\tilde{c}_{\mathrm{ML}}(r) = \frac{r_0}{r} \tilde{c}_{\mathrm{ML}}(r_0) \frac{\sinh\left(\frac{r}{\lambda}\right)}{\sinh\left(\frac{r_0}{\lambda}\right)} \tag{A5.49}$$

which describes the concentration profile in the resin domain. The derivative of (A5.49) at the inner side of the resin/solution interface becomes (considering boundary condition (A5.9)) reads:

$$\left(\frac{d\tilde{c}_{\mathrm{ML}}(r)}{dr}\right)_{r=r_0^-} = \frac{\chi^{z_{\mathrm{ML}}} c_{\mathrm{ML}}^+}{\lambda} \coth\left(\frac{r_0}{\lambda}\right) \tag{A5.50}$$

where, for simplicity of notation, we define

$$c_{\mathrm{ML}}^+ \equiv c_{\mathrm{ML}}(r_0^+) \tag{A5.51}$$

SOLUTION DOMAIN ($r_0<r<r_1$)

Since both the free and the complexed metal are present in the solution, we write a continuity equation for each of them:

$$0 = D_{\mathrm{M}}\left(\frac{d^2 c_{\mathrm{M}}(r)}{dr^2} + \frac{2}{r}\frac{dc_{\mathrm{M}}(r)}{dr}\right) + k_{\mathrm{d}}\, c_{\mathrm{ML}}(r) - k_{\mathrm{a}}'\, c_{\mathrm{ML}}(r) \tag{A5.52}$$

$$0 = D_{\mathrm{M}}\left(\frac{d^2 c_{\mathrm{ML}}(r)}{dr^2} + \frac{2}{r}\frac{dc_{\mathrm{ML}}(r)}{dr}\right) - k_{\mathrm{d}}\, c_{\mathrm{ML}}(r) + k_{\mathrm{a}}'\, c_{\mathrm{ML}}(r) \tag{A5.53}$$

we can define the new combination variables:

$$c_{\mathrm{T,M}}(r) \equiv c_{\mathrm{M}}(r) + c_{\mathrm{ML}}(r) \tag{A5.54}$$

$$\phi(r) \equiv c_{\mathrm{ML}}(r) - K' c_{\mathrm{M}}(r) \tag{A5.55}$$

By adding (A5.52) and (A5.53) and substituting (A5.54), the following equation is obtained:

$$0 = D_{\mathrm{M}}\left(\frac{d^2 c_{\mathrm{T,M}}(r)}{dr^2} + \frac{2}{r}\frac{dc_{\mathrm{T,M}}(r)}{dr}\right) \tag{A5.56}$$

In a similar fashion, subtracting *K*' times Eq. (A5.53) from Eq. (A5.52), while substituting (A5.55) leads to:

$$0 = D_{\mathrm{M}}\left(\frac{d^2\phi(r)}{dr^2} + \frac{2}{r}\frac{d\phi(r)}{dr}\right) - k_{\mathrm{d}}\, c_{\mathrm{ML}}(r) + k'_{\mathrm{a}}\, c_{\mathrm{M}}(r) - K'\left(k_{\mathrm{d}}\, c_{\mathrm{ML}}(r) - k'_{\mathrm{a}}\, c_{\mathrm{M}}(r)\right) \tag{A5.57}$$

which can be further simplified into:

$$0 = \frac{d^2\phi(r)}{dr^2} + \frac{2}{r}\frac{d\phi(r)}{dr} - \frac{\phi(r)}{m^2} \tag{A5.58}$$

where

$$m = \sqrt{\frac{D_{\mathrm{M}}}{k'_{\mathrm{a}} + k_{\mathrm{d}}}} \tag{A5.59}$$

We now introduce two new variables:

$$\mu_{\mathrm{T,M}}(r) \equiv r c_{\mathrm{T,M}}(r) = r\left(c_{\mathrm{M}}(r) + c_{\mathrm{ML}}(r)\right) \tag{A5.60}$$

$$f(r) \equiv r\phi(r) = r\left(c_{\mathrm{ML}}(r) - K' c_{\mathrm{M}}(r)\right) \tag{A5.61}$$

By substituting (A5.60) in (A5.56) :

$$0 = \frac{d^2\mu_{\mathrm{T,M}}(r)}{dr^2} \tag{A5.62}$$

and using (A5.61), Eq. (A5.58) becomes:

$$\frac{d^2 f(r)}{dr^2} = \frac{f(r)}{m^2} \tag{A5.63}$$

Let us focus now on Eq. (A5.62). Its general solution is known to be in the form of:

$$\mu_{\mathrm{T,M}}(r) = A + Br \tag{A5.64}$$

By recalling the boundary conditions

$$\mu_{\mathrm{T,M}}\left(r_0^+\right) \equiv \mu^+_{\mathrm{T,M}} = c^+_{\mathrm{ML}} r_0 \tag{A5.65}$$

and

$$\mu_{\mathrm{T,M}}(r_1) \equiv \mu^*_{\mathrm{T,M}} = \left(c^*_{\mathrm{ML}} + c^*_{\mathrm{M}}\right) r_1 \tag{A5.66}$$

Eq. (A5.64) can be rewritten as:

$$\mu_{\mathrm{T,M}}(r) = \mu^+_{\mathrm{T,M}} + \frac{\mu^*_{\mathrm{T,M}} - \mu^+_{\mathrm{T,M}}}{r_1 - r_0}\left(r - r_0\right) \tag{A5.67}$$

Let us move to Eq. (A5.63). Its solution is known (see SI-24 in Puy *et al.*[21]) to be in the form of:

$$f\left(r\right)=E\sinh\left(\frac{r_1-r}{m}\right)+F\cosh\left(\frac{r_1-r}{m}\right) \tag{A5.68}$$

Being the boundary conditions:

$$f\left(r_0^+\right)\equiv f^+=rc_{\mathrm{ML}}(r_0) \tag{A5.69}$$

and:

$$f\left(r_1\right)=0 \tag{A5.70}$$

We then obtain:

$$f\left(r\right)=r_0c_{\mathrm{ML}}^+\frac{\sinh\left(\frac{r_1-r}{m}\right)}{\sinh\left(\frac{r_1-r_0}{m}\right)} \tag{A5.71}$$

So as to invert the change of variables, we solve for $c_{\mathrm{ML}}(r)$ in (A5.60) and (A5.61):

$$c_{\mathrm{ML}}(r)=\frac{f\left(r\right)+K'\mu_{\mathrm{T,M}}(r)}{r\left(1+K'\right)} \tag{A5.72}$$

Substituting (A5.71) and (A5.67) in (A5.72) and differentiating at $r=r_0$ yields:

$$\left(\frac{dc_{\mathrm{ML}}\left(r\right)}{dr}\right)_{r=r_0^+}=-\frac{c_{\mathrm{ML}}^+}{\left(1+K'\right)r_0}\left(\frac{r_0}{m}\coth\left(\frac{r_1-r_0}{m}\right)+1\right)+\frac{K'}{1+K'}\frac{r_1\left(c_{\mathrm{T,M}}^*-c_{\mathrm{ML}}^+\right)}{r_0\left(r_1-r_0\right)} \tag{A5.73}$$

Boundary condition (A5.11) allows us to equate (A5.50) and (A5.73). Solving for c_{ML}^+ leads to:

$$c_{\mathrm{ML}}^+=\frac{\left(1+K'\right)c_{\mathrm{ML}}^*}{K'+\frac{r_0\left(r_1-r_0\right)}{r_1m}\coth\left(\frac{r_1-r_0}{m}\right)+\frac{r_1-r_0}{r_1}+\frac{r_0\left(r_1-r_0\right)\left(1+K'\right)\chi^{z_{\mathrm{ML}}}}{r_1\lambda}\coth\left(\frac{r_0}{\lambda}\right)} \tag{A5.74}$$

The lability degree ξ can be expressed, as demonstrated in Galceran *et al.*,[23] as:

$$\xi=1-\frac{c_{\mathrm{ML}}^+}{c_{\mathrm{ML}}^*} \tag{A5.75}$$

The following formula for the lability degree can, then, be derived:

$$\xi=1-\frac{1+K'}{K'+\frac{r_0\left(r_1-r_0\right)}{r_1m}\coth\left(\frac{r_1-r_0}{m}\right)+\frac{r_1-r_0}{r_1}+\frac{r_0\left(r_1-r_0\right)\left(1+K'\right)\chi^{z_{\mathrm{ML}}}}{r_1\lambda}\coth\left(\frac{r_0}{\lambda}\right)} \tag{A5.76}$$

One can check that, if $r_1 \to \infty$, $r_0 \to \infty$, $r_1 - r_0 \to g$ (thickness of the gel layer), but r_0 is taken as r_{planar} (thickness of the planar resin disc) when compared to λ, one almost retrieves the formula for ξ in planar DGT:

$$\xi = 1 - \frac{1+K'}{K' + \frac{g}{m}\coth\left(\frac{g}{m}\right) + \frac{g(1+K')\chi^{z_{ML}}}{\lambda}\coth\left(\frac{r_{planar}}{\lambda}\right)} \qquad \text{(A5.77)}$$

which is Eq (13) in Puy *et al.*[21] (for $D_M = D_{ML}$), except for the coth or tanh of r_{planar}/λ, which suggests a different convergence of both geometries.

5.5.3. Model III: time-dependent accumulation in a packed column

This approach follows the treatment found in Bird's treatise[14] for the metal uptake on a packed column not at steady state, extended here to include the contribution of the ML complexes.

Let the column be a cylinder of total bed length z_{max} and S its cross-section area. Let ε be the fraction of the column volume occupied by the mobile phase (the solution), *i.e.* that not occupied either by the beads or by the diffusion layer around the beads. Let us call α the effective surface area of the solid phase (the resin) per unit length of bed, and ρ the volume of the solid phase per unit length of bed. Let the mobile phase flow through at a rate Q. We assume that in each of the layers of infinitesimal length dz there is diffusive steady state (dSS). We assume perfect mixing of the solution beyond r_1.

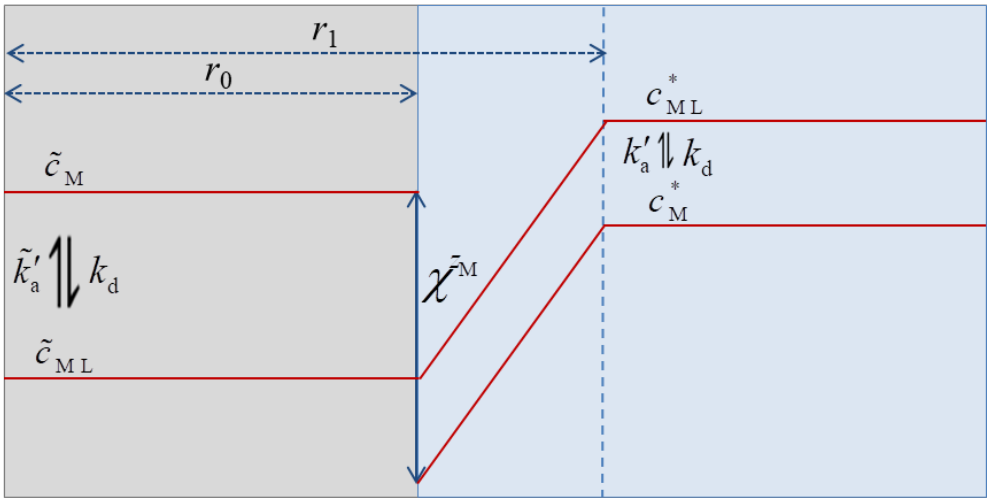

Figure A5.4. Schematic representation of the concentration profiles inside one bead and in its diffusion (boundary) layer in Model III (later on to be integrated within the column characteristics) for a neutral complex. The interface does not necessarily act as a perfect sink for the metal. The Boltzmann factor rules the partitioning of both, M and ML, at the interface.

To simplify the problem, let us assume flat concentration profiles inside the resin phase. Contrary to Model II, we do not assume perfect sink condition for the free metal nor steady state inside the bead (see outline in Fig. A5.4) but a simple kinetics of interconversion between M and ML.

Like in Model II, we can write the continuity equations in the solution phase as in (A5.62) and (A5.63). The boundary conditions at $r=r_1$ are (A5.66) and (A5.70) and those at $r=r_0$ are:

$$\mu_{\mathrm{T,M}}\left(r_0^+\right) \equiv \mu_{\mathrm{T,M}}^+ = r_0\left(c_{\mathrm{ML}}^+ + c_{\mathrm{M}}^+\right) \tag{A5.78}$$

and:

$$f\left(r_0^+\right) \equiv f^+ = r_0\left(c_{\mathrm{ML}}^+ - K'c_{\mathrm{M}}^+\right) \tag{A5.79}$$

The solution of (A5.62) is formally identical to (A5.67) (albeit with $\mu_{\mathrm{T,M}}^+$ now including a metal concentration not necessarily negligible):

$$\mu_{\mathrm{T,M}}(r) = \frac{c_{\mathrm{M}}^* + c_{\mathrm{ML}}^* - c_{\mathrm{M}}^+ - c_{\mathrm{ML}}^+}{r_1 - r_0} r_0 r_1 + \frac{r_1\left(c_{\mathrm{M}}^* + c_{\mathrm{ML}}^*\right) - r_0\left(c_{\mathrm{M}}^+ - c_{\mathrm{ML}}^+\right)}{r_1 - r_0} r \tag{A5.80}$$

Following a similar reasoning to that below Eq. (A5.68) , Eq. (A5.63) can be solved in Model III to give:

$$f\left(r\right) = r_0\left(c_{\mathrm{ML}}^+ - K'c_{\mathrm{M}}^+\right)\frac{\sinh\left(\frac{r_1 - r}{m}\right)}{\sinh\left(\frac{r_1 - r_0}{m}\right)} \tag{A5.81}$$

Let us invert the change of variables as done in (A5.72) to solve for $c_{\mathrm{ML}}(r)$. The substitution of (A5.81) and (A5.80) in (A5.72) leads to an equation for $\left(\frac{dc_{\mathrm{ML}}(r)}{dr}\right)_{r=r_0^+}$ analogue to (A5.73), where the flux of ML across the interface can be then expressed as:

$$J_{\mathrm{ML}} = -\frac{D_{\mathrm{M}}}{r_0\left(1+K'\right)}\left[\left(c_{\mathrm{ML}}^+ - K'c_{\mathrm{M}}^+\right)\left(\frac{r_0}{m}\coth\left(\frac{r_1 - r_0}{m}\right)+1\right) - \frac{K'r_1}{\left(r_1 - r_0\right)}\left(c_{\mathrm{ML}}^* + c_{\mathrm{M}}^* - c_{\mathrm{ML}}^+ - c_{\mathrm{M}}^+\right)\right] \tag{A5.82}$$

Similarly, $c_{\mathrm{M}}(r)$ can be isolated from (A5.60) and (A5.61):

$$c_{\mathrm{M}}(r) = \frac{\mu_{\mathrm{T,M}}(r) - f\left(r\right)}{r\left(1+K'\right)} \tag{A5.83}$$

Following the same approach applied to the ML case, we can write an expression for the flux of M across the interface:

$$J_{\mathrm{M}}=\frac{D_{\mathrm{M}}}{r_0\left(1+K'\right)}\left[\left(c_{\mathrm{ML}}^{+}-K'c_{\mathrm{M}}^{+}\right)\left(\frac{r_0}{m}\coth\left(\frac{r_1-r_0}{m}\right)+1\right)+\frac{r_1}{\left(r_1-r_0\right)}\left(c_{\mathrm{ML}}^{*}+c_{\mathrm{M}}^{*}-c_{\mathrm{ML}}^{+}-c_{\mathrm{M}}^{+}\right)\right] \quad \text{(A5.84)}$$

The summation of (A5.84) and (A5.82) gives the total flux across the interface:

$$J_{\mathrm{T,M}}=-\frac{D_{\mathrm{M}}}{\delta}\left(c_{\mathrm{ML}}^{*}+c_{\mathrm{M}}^{*}-c_{\mathrm{ML}}^{+}-c_{\mathrm{M}}^{+}\right) \quad \text{(A5.85)}$$

where δ is the effective thickness of the diffusion layer.

Once found the metal transfer in a single bead, let us consider the metal transfer in the whole column.

The variation (per unit of time) of the total metal number of moles in the volume of a generic infinitesimal layer of the mobile phase at position *z* is:

$$S\varepsilon dz\frac{\partial c_{\mathrm{T,M}}^{*}\left(z,t\right)}{\partial t}=-J_{\mathrm{T,M}}\alpha dz-Qdc_{\mathrm{T,M}}^{*}\left(z,t\right) \quad \text{(A5.86)}$$

where the first r.h.s. term accounts for the diffusion towards the beads and the last term describes the difference between the input and output of metal to the infinitesimal volume (due to the flow of liquid).

Eq. (A5.86), combined with (A5.85), (A5.8) and (A5.9), can be rewritten as:

$$S\varepsilon\frac{\partial c_{\mathrm{T,M}}^{*}\left(z,t\right)}{\partial t}=-\frac{D_{\mathrm{M}}\alpha}{\delta}\left(c_{\mathrm{T,M}}^{*}\left(z,t\right)-\frac{\tilde{c}_{\mathrm{ML}}\left(z,t\right)}{\chi^{z_{\mathrm{ML}}}}-\frac{\tilde{c}_{\mathrm{M}}\left(z,t\right)}{\chi^{z_{\mathrm{M}}}}\right)-S\varepsilon v\frac{\partial c_{\mathrm{T,M}}^{*}\left(z,t\right)}{\partial z} \quad \text{(A5.87)}$$

Similarly, the continuity equations for M and ML in the resin phase can be written as:

$$\rho\frac{\partial\tilde{c}_{\mathrm{M}}\left(z,t\right)}{\partial t}=J_{\mathrm{M}}\alpha+\rho\left(k_{\mathrm{d}}\tilde{c}_{\mathrm{ML}}\left(z,t\right)-\tilde{k}_{\mathrm{a}}'\tilde{c}_{\mathrm{M}}\left(z,t\right)\right) \quad \text{(A5.88)}$$

(where the term in between brackets describes the reaction inside the resin) and:

$$\rho\frac{\partial\tilde{c}_{\mathrm{ML}}\left(z,t\right)}{\partial t}=J_{\mathrm{ML}}\alpha-\rho\left(k_{\mathrm{d}}\tilde{c}_{\mathrm{ML}}\left(z,t\right)-\tilde{k}_{\mathrm{a}}'\tilde{c}_{\mathrm{M}}\left(z,t\right)\right) \quad \text{(A5.89)}$$

The substitution of the equations of the fluxes (A5.84) and (A5.82) in (A5.88) and (A5.89) finally leads to:

$$\rho\frac{\partial\tilde{c}_{\mathrm{M}}\left(z,t\right)}{\partial t}=\frac{D_{\mathrm{M}}\alpha}{r_0\left(1+K'\right)}\left[\left(\frac{\tilde{c}_{\mathrm{ML}}\left(z,t\right)}{\chi^{z_{\mathrm{ML}}}}-\frac{K'\tilde{c}_{\mathrm{M}}\left(z,t\right)}{\chi^{z_{\mathrm{M}}}}\right)\left(\frac{r_0}{m}\coth\left(\frac{r_1-r_0}{m}\right)+1\right)+\frac{r_1}{r_1-r_0}\left(c_{\mathrm{T,M}}^{*}\left(z,t\right)-\frac{\tilde{c}_{\mathrm{ML}}\left(z,t\right)}{\chi^{z_{\mathrm{ML}}}}-\frac{\tilde{c}_{\mathrm{M}}\left(z,t\right)}{\chi^{z_{\mathrm{M}}}}\right)\right]+$$
$$+\rho\left(k_{\mathrm{d}}\tilde{c}_{\mathrm{ML}}\left(z,t\right)-k_{\mathrm{a}}\tilde{c}_{\mathrm{L}}\tilde{c}_{\mathrm{M}}\left(z,t\right)\right) \quad \text{(A5.90)}$$

and:

$$\rho\frac{\partial\tilde{c}_{\mathrm{ML}}\left(z,t\right)}{\partial t}=\frac{D_{\mathrm{M}}\alpha}{r_0\left(1+K'\right)}\left[-\left(\frac{\tilde{c}_{\mathrm{ML}}\left(z,t\right)}{\chi^{z_{\mathrm{ML}}}}-\frac{K'\tilde{c}_{\mathrm{M}}\left(z,t\right)}{\chi^{z_{\mathrm{M}}}}\right)\left(\frac{r_0}{m}\coth\left(\frac{r_1-r_0}{m}\right)+1\right)+\frac{K'r_1}{r_1-r_0}\left(c_{\mathrm{T,M}}^{*}\left(z,t\right)-\frac{\tilde{c}_{\mathrm{ML}}\left(z,t\right)}{\chi^{z_{\mathrm{ML}}}}-\frac{\tilde{c}_{\mathrm{M}}\left(z,t\right)}{\chi^{z_{\mathrm{M}}}}\right)\right]-$$
$$-\rho\left(k_{\mathrm{d}}\tilde{c}_{\mathrm{ML}}\left(z,t\right)-k_{\mathrm{a}}\tilde{c}_{\mathrm{L}}\tilde{c}_{\mathrm{M}}\left(z,t\right)\right) \quad \text{(A5.91)}$$

The equations to be solved are (A5.87), (A5.90) and (A5.91).

5.5.4. Model IV: accumulation in a packed column at steady state

DERIVATION OF THE EFFLUENT CONCENTRATION IN MODEL IV

In Model IV we assume that the whole column is at steady state (at each *z*). While all the other general assumptions hold, assumption 5 (ligand excess conditions) is not strictly necessary.

From the definition of ξ,[23] it follows that for spherical geometry –even in absence of ligand excess conditions-, the flux to the bead surfaces (at a certain column height *z*) can be computed as

$$J_{\mathrm{T,M}}(z)=\frac{D_{\mathrm{M}}c_{\mathrm{M}}^{*}(z)}{\delta}(1+\xi K') \tag{A5.92}$$

The SS in the diffusion layer can also apply with a non-null (but fixed) concentration of ML at the bead surface (as in Model II).

Given that, from (5.5), the total concentration in the flowing solution of the column can be related to the free one as

$$c_{\mathrm{T,M}}^{*}(z)=(1+K')c_{\mathrm{M}}^{*}(z) \tag{A5.93}$$

one obtains

$$J_{\mathrm{T,M}}(z)=\frac{D_{\mathrm{M}}}{\delta}\left(\frac{1+\xi K'}{1+K'}\right)c_{\mathrm{T,M}}^{*}(z) \tag{A5.94}$$

Taking into account the steady state of the column (*i.e.* no varitation with time), Eq. (A5.86) becomes:

$$J_{\mathrm{T,M}}(z)\alpha dz=-Qdc_{\mathrm{T,M}}^{*}(z) \tag{A5.95}$$

Substituting (A5.94) into (A5.95) yields:

$$\frac{dc_{\mathrm{T,M}}^{*}(z)}{c_{\mathrm{T,M}}^{*}(z)}=-\frac{D_{\mathrm{M}}\alpha}{Q\delta}\left(\frac{1+\xi K'}{1+K'}\right)dz \tag{A5.96}$$

which, after integration between z=0 and z=$z_{\max}$, results in:

$$\ln\frac{c_{\mathrm{T,M}}^{\mathrm{eff,SS}}}{c_{\mathrm{T,M}}}=-\frac{D_{\mathrm{M}}\alpha}{Q\delta}\left(\frac{1+\xi K'}{1+K'}\right)z_{\max} \tag{A5.97}$$

where $c_{\mathrm{T,M}}^{\mathrm{eff,SS}}$ is the total metal concentration in the effluent at steady state (*i.e.* what we measure at the end of the column).

The introduction of the characteristic resin bed length z_{char}, defined as:

$$z_{\mathrm{char}}=\frac{Q\delta(1+K')}{D_{\mathrm{M}}\alpha(1+K'\xi)} \tag{A5.98}$$

allows (A5.97) to be rewritten as:

$$\ln\frac{c_{\mathrm{T,M}}^{\mathrm{eff,SS}}}{c_{\mathrm{T,M}}}=-\frac{z_{\max}}{z_{\mathrm{char}}} \tag{A5.99}$$

One can find $c_{\mathrm{M,T}}^{*}(z)$ at a generic *z* by integration

$$c_{\mathrm{T,M}}(z)=c_{\mathrm{T,M}}(0)e^{-\frac{z_{\max}}{z_{\mathrm{char}}}} \tag{A5.100}$$

In the case where no ligands are present, Eq. (A5.97) becomes:

$$\ln\frac{c_{\mathrm{T,M}}^{\mathrm{eff,SS}}}{c_{\mathrm{T,M}}}=-\frac{D_{\mathrm{M}}\alpha}{Q\delta}z_{\max} \tag{A5.101}$$

from which the value of parameter α can be readily estimated:

$$\alpha=-\frac{\delta Q\ln\dfrac{c_{\mathrm{T,M}}^{\mathrm{eff,SS}}}{c_{\mathrm{T,M}}}}{D_{\mathrm{M}}z_{\max}} \tag{A5.102}$$

RETRIEVING THE LABILITY DEGREE FROM MODEL IV

Dividing (A5.97) by (A5.99) leads to:

$$\frac{\left(\ln\dfrac{c_{\mathrm{T,M}}^{\mathrm{eff,SS}}}{c_{\mathrm{T,M}}}\right)_{\text{with complex}}}{\left(\ln\dfrac{c_{\mathrm{T,M}}^{\mathrm{eff,SS}}}{c_{\mathrm{T,M}}}\right)_{\text{absence of ligand}}}=\frac{1+K'\xi}{1+K'} \tag{A5.103}$$

thus allowing the estimation of the lability degree ξ.

The amount of metal accumulated in the whole resin at time *t* can be computed by integrating the fluxes (times the effective area) given by Eq. (A5.94) with the total metal concentration given in Eq. (A5.100) for the different layers of the columns from *z*=0 to $z=z_{\max}$:

$$n^{\mathrm{SS}}=t\int_{z=0}^{z_{\max}}J_{\mathrm{T,M}}(z)\alpha dz=tQc_{\mathrm{T,M}}^{*}\left[1-\mathrm{e}^{-\frac{z_{\max}}{z_{\mathrm{char}}}\left(\frac{1+K'\xi}{1+K'}\right)}\right] \tag{A5.104}$$

Notice that, due to the steady state of the whole column, we have multiplied the number of moles accumulated per unit time (the integral factor) directly by the elapsed time. The first three factors in the rightmost hand side of Eq. (A5.104) give the rate of metal accumulation in the resin, which corresponds to the initial slope of the "trajectories" (R_{acc} in previous literature[4,6]):

$$slope=Q\,c_{\mathrm{T,M}}\left[1-\mathrm{e}^{-\frac{z_{\max}}{z_{\mathrm{char}}}}\right]=Q\,c_{\mathrm{T,M}}\left[1-\frac{c_{\mathrm{T,M}}^{\mathrm{eff,SS}}}{c_{\mathrm{T,M}}}\right]=Q\;\;c_{\mathrm{T,M}}\;\Xi \tag{A5.105}$$

where we have introduced the "system retention degree" Ξ.

The fractional height of the plateau can, then, be expressed as a function of the rate of accumulation:

$$\frac{c_{\mathrm{T,M}}^{\mathrm{eff,SS}}}{c_{\mathrm{T,M}}} = 1 - \frac{slope}{Qc_{\mathrm{T,M}}} \tag{A5.106}$$

Then, by substituting (A5.106) in (A5.103) and isolating ξ, we arrive to:

$$\xi = \left(1 + \frac{1}{K'}\right) \frac{\left(\ln\left[1 - \frac{slope}{Qc_{\mathrm{T,M}}}\right]\right)_{\text{with complex}}}{\left(\ln\left[1 - \frac{slope}{Qc_{\mathrm{T,M}}}\right]\right)_{\text{absence of ligand}}} - \frac{1}{K'} \tag{A5.107}$$

which is a practical way to retrieve the values of the lability degree from the accumulation results.

DEFINITION OF c_{DIET}

In analogy to what has been done in the literature about the DGT we can introduce a "DIET concentration", a measure of the labile fraction probed by a particular column, defined as:

$$c_{\mathrm{DIET}} \equiv c_{\mathrm{M}} \left(1 + \sum_i \frac{D_i}{D_{\mathrm{M}}} K_i' \xi_i\right) \tag{A5.108}$$

for a set of complexes denoted with index *i*.

In the case of just one complex and common diffusion coefficients:

$$c_{\mathrm{DIET}} \equiv c_{\mathrm{M}} \left(1 + K' \xi\right) \tag{A5.109}$$

Multiplying both terms of Eq. (A5.103) by $c_{\mathrm{T,M}}$ and applying the relationship (A5.93) (applied to the inlet, where $c_{\mathrm{T,M}}^{*}\left(z=0\right) = c_{\mathrm{T,M}}$) we obtain:

$$c_{\mathrm{DIET}} = c_{\mathrm{T,M}} \frac{\left(\ln \frac{c_{\mathrm{T,M}}^{\mathrm{eff,SS}}}{c_{\mathrm{T,M}}}\right)_{\text{with complex}}}{\left(\ln \frac{c_{\mathrm{T,M}}^{\mathrm{eff,SS}}}{c_{\mathrm{T,M}}}\right)_{\text{absence of ligand}}} \tag{A5.110}$$

Analogously, the following expression can be derived from (A5.107):

$$c_{\mathrm{DIET}} = c_{\mathrm{T,M}} \frac{\left(\ln\left[1 - \frac{slope}{Qc_{\mathrm{T,M}}}\right]\right)_{\text{with complex}}}{\left(\ln\left[1 - \frac{slope}{Qc_{\mathrm{T,M}}}\right]\right)_{\text{absence of ligand}}} \tag{A5.111}$$

5.6. References

(1) Cantwell, F. F.; Nielsen, J. S.; Hrudey, S. E. Free nickel ion concentration in sewage by an ion exchange column-equilibration method. *Anal. Chem.* **1982**, *54* (9), 1498–1503.

(2) Fortin, C.; Campbell, P. G. G. An ion-exchange technique for free-metal ion measurements (Cd^{2+}, Zn^{2+}): Applications to complex aqueous media. *Int. J. Environ. Anal. Chem.* **1998**, *72* (3), 173–194.

(3) Zhao, C. M.; Campbell, P. G. C.; Wilkinson, K. J. When are metal complexes bioavailable? *Environ. Chem.* **2016**, *13*, 425–433.

(4) Nduwayezu, I.; Mostafavirad, F.; Hadioui, M.; Wilkinson, K. J. Speciation of a lanthanide (Sm) using an ion exchange resin. *Anal. Methods* **2013**, *8*, 6774–6781.

(5) Leguay, S.; Campbell, P. G. C.; Fortin, C. Determination of the free-ion concentration of rare earth elements by an ion-exchange technique: Implementation, evaluation and limits. *Environ. Chem.* **2016**, *13* (3), 478–488.

(6) Rowell, J. A.; Fillion, M. A.; Smith, S.; Wilkinson, K. J. Determination of the speciation and bioavailability of Samarium to Chlamydomonas Reinhardtii in the presence of natural organic matter. *Environ. Toxicol. Chem.* **2018**, *37*, 1623–1631.

(7) Bowles, K. C.; Apte, S. C.; Batley, G. E.; Hales, L. T.; Rogers, N. J. A rapid Chelex column method for the determination of metal speciation in natural waters. *Anal. Chim. Acta* **2006**, *558* (1–2), 237–245.

(8) Figura, P.; McDuffie, B. Determination if labilities of soluble trace-metal species in aqueous environmental samples by Anodic Stripping Voltammetry and Chelex column and batch methods. *Anal. Chem.* **1980**, *52*, 1433–1439.

(9) Alvarez, M. B.; Malla, M. E.; Batistoni, D. A. Performance evaluation of two chelating ion-exchange sorbents for the fractionation of labile and inert metal species from aquatic media. *Anal. Bioanal. Chem.* **2004**, *378* (2), 438–446.

(10) Procopio, J. R.; Viana, M. D. M.; Hernandez, L. H. Microcolumn ion-exchange method for kinetic speciation of copper and lead in natural waters. *Environ. Sci. Technol.* **1997**, *31*, 3081–3085.

(11) Herrin, R. T.; Andren, A. W.; Armstrong, D. E. Determination of silver speciation in natural waters. 1. Laboratory test of Chelex-100 chelating resin as a competing ligand. *Environ. Sci. Technol.* **2001**, *3*, 1953–1958.

(12) Mongin, S.; Uribe, R.; Puy, J.; Cecilia, J.; Galceran, J.; Zhang, H.; Davison, W. Role of the resin layer thickness in the lability of complexes measured by DGT. *Environ. Sci. Technol.* **2011**, *45*, 4869–4875.

(13) Uribe, R.; Mongin, S.; Puy, J.; Cecilia, J.; Galceran, J.; Zhang, H.; Davison, W. Contribution of partially labile complexes to the DGT metal flux. *Environ. Sci. Technol.* **2011**, *45*, 5317–5322.

(14) Bird, R. B.; Stewart, W. E.; Lightfoot, E. N. *Transport Phenomena*; Wiley & Sons: New York, 1960.

(15) Galceran, J.; Puy, J. Interpretation of diffusion gradients in thin films (DGT) measurements: A systematic approach. *Environ. Chem.* **2015**, *12* (2), 112–122.

(16) Puy, J.; Galceran, J.; Rey-Castro, C. Diffusive Gradient in Thin-films for environmental measurements; Davison, W., Ed.; Cambridge University Press: Cambridge (UK), 2016.

(17) Fortin, C.; Campbell, P. G. G. Thiosulfate enhances silver uptake by a green alga: role of anion transporters in metal uptake. *Environ. Sci. Technol.* **2001**, *35*, 2214.

(18) Pesavento, M.; Sturini, M.; D'Agostino, G.; Biesuz, R. Solid phase extraction of copper(II) by fixed bed procedure on cation exchange complexing resins. *J. Chromatogr. A* **2010**, *1217* (8), 1208–1218.

(19) Fortin, C.; Couillard, Y.; Vigneault, B.; Campbell, P. G. C. Determination of free Cd, Cu and Zn concentrations in lake waters by in situ diffusion followed by column equilibration ion-exchange. *Aquat. Geochemistry* **2010**, *16* (1), 151–172.

(20) Sweileh, J. A.; Lucyk, D.; Kratochvil, B.; Cantwell, F. F. Specificity of the ion exchange/atomic absorption method for free copper(II) species determination in natural waters. *Anal. Chem.* **1987**, *59* (4), 586–592.

(21) Puy, J.; Galceran, J.; Cruz-González, S.; David, C. A.; Uribe, R.; Lin, C.; Zhang, H.; Davison, W. Measurement of metals using DGT: Impact of ionic strength and kinetics of dissociation of complexes in the resin domain. *Anal. Chem.* **2014**, *86* (15), 7740–7748.

(22) Quattrini, F.; Galceran, J.; David, C. A.; Puy, J.; Alberti, G.; Rey-Castro, C. Dynamics of trace metal sorption by an ion-exchange chelating resin described by a mixed intraparticle/film diffusion transport model. The Cd/Chelex case. *Chem. Eng. J.* **2017**, *317*, 810–820.

(23) Galceran, J.; Puy, J.; Salvador, J.; Cecília, J.; van Leeuwen, H. P. Voltammetric lability of metal complexes at spherical microelectrodes with various radii. *J.*

Electroanal. Chem. **2001**, *505* (1–2), 85–94.

(24) Buffle, J.; Startchev, K.; Galceran, J. Computing steady-state metal flux at microorganism and bioanalogical sensor interfaces in multiligand systems. A reaction layer approximation and its comparison with the rigorous solution. *Phys. Chem. Chem. Phys.* **2007**, *9*, 2844–2855.

(25) Galceran, J.; Puy, J.; Salvador, J.; Cecília, J.; Mas, F.; Garcés, J. L. Lability and mobility effects on mixtures of ligands under steady-state conditions. *Phys. Chem. Chem. Phys.* **2003**, *5*, 5091–5100.

(26) Salvador, J.; Puy, J.; Cecília, J.; Galceran, J. Lability of complexes in steady-state finite planar diffusion. *J. Electroanal. Chem.* **2006**, *588* (2), 303–313.

(27) Galceran, J.; van Leeuwen, H. P. Physicochemical kinetics and transport at chemical-biological surfaces. In *IUPAC series on analytical and physical chemistry of environmental systems, vol.9*; van Leeuwen, H. P., Koester, W., Eds.; John Wiley & Sons Ltd: Chichester (UK), 2004.

(28) Gustafsson, J. P. Visual MINTEQ. Stockholm 2013.

(29) Eigen, M.; Wilkins, R. G. The kinetics and mechanism of formation of metal complexes. In *Mechanisms of inorganic reactions*; Kleinberg, J., Murmann, R. K., Fraser, R. T. M., Bauman, J., Eds.; America Chemical Society: Washington (DC), 1965; 55–80.

(30) Figura, P.; McDuffie, B. Use of Chelex resin for determination of labile trace-metal fractions in aqueous ligand media and comparison of the method with anodic-stripping votammetry. *Anal. Chem.* **1979**, *51*, 120–125.

(31) Agraz, R.; Sevilla, M. T.; Hernandez, L. H. Copper speciation analysis using a chemically-modified electrode. *Anal. Chim. Acta* **1993**, *283*, 650–656.

(32) van Leeuwen, H. P.; Town, R.; Buffle, J.; Cleven, R.; Davison, W.; Puy, J.; van Riemsdijk, W.; Sigg, L. Dynamic speciation analysis and bioavailabilty of metals in aquatic systems. *Environ. Sci. Technol.* **2005**, *39* (22), 8545–8556.

(33) Puy, J.; Uribe, R.; Mongin, S.; Galceran, J.; Cecilia, J.; Levy, J. L.; Zhang, H. Lability criteria in diffusive gradients in thin films. *J. Phys. Chem. A* **2012**, *116*, 6564–6573.

(34) Crank, J. *The Mathematics of Diffusion*; Oxford University Press: Oxford, 1975.

6. Towards eDGT – extracting and interpreting information from DGT at equilibrium

6.1. DGT and equilibrium – possibility of a complementary approach

One of the main assumptions of the DGT design is that the sampler acts as a perfect sink with respect to the metals and there is a linear relationship between accumulation and deployment time. This is generally reasonable at short times, as the number of free sites is in large excess with respect to the moles of bound metal. While several corrections[1] have been implemented to take into account the deviations from the perfect-sink hypothesis, in practice they are not always easy to apply. As time passes, however, the overall rate of metal uptake by the resin decreases and its behaviour is farther and farther from ideal, until in the end it approaches equilibrium with the bulk metal. In summary, the DGT sensors evolves from a transient regime to the steady-state regime (the one sought until now), then to a decreasing-flux regime and finally to equilibrium (see Fig. 1.2).[2]

Alternative information to that usually conveyed by the DGT (*i.e.* the labile fraction) could be extracted by moving away from the dynamic regime and focus instead on the system once it has already attained equilibrium. In this regime, we expect to retrieve a thermodynamic information: the free metal ion concentration.[3,4]

It was in the work of Mongin *et al.*[5] that the idea of an "equilibrium operation mode" of the DGT appeared for the first time. In this chapter, we will expand on it and propose a specifically optimised design of the passive sampler, as well as a simple model that accounts for the influence of several parameters on the metal partitioning. This new technique, labelled eDGT (for equilibrium DGT), will be applied to study the speciation of several trace metals in synthetic freshwater in presence of a competing ligand.

6.2. Designing the eDGT

Our aim is to develop a passive sampler to target the free metal ions. This requires not only building a practical and effective device, but also finding the right interpretation of the results. As indicated in Section 1.2.3, an ideal EPS (Equilibrium Passive Sampler) should:

- reach equilibrium in the shortest time possible, not only to speed the sampling up, but also to reduce the chance of fouling and damaging.
- have a well-defined distribution coefficient between the two phases for every analyte, or at least an easy way to determine it.
- take up an amount of analyte above the limit of quantification of the complementary technique.

The equilibration time depends on the geometry of the sampler, namely its contact surface area, its volume and the thickness of the barrier. The determination of the distribution coefficients, on the contrary, is much trickier, and it derives directly from the chemical properties of the collecting phase.

6.2.1. Building the sampler

The exploitation of the equilibrium regime of DGT devices can be obviously done with standard DGT devices, but the equilibration time might be too long (especially when carrying out preliminary experiments). On the other hand, due to the commercial availability and popularity of DGT devices, it would be useful for the new technique to be implemented with materials familiar to DGT-users. Ideally, DGT and eDGT devices could be even deployed side by side and retrieved at different times, providing complementary information. The first challenge is then to keep the equilibration time under reasonable limits, possibly hours or days. This can be achieved by increasing as much as possible the contact area, while thinning the DBL (diffusive boundary layer) to a minimum.

In our case, we modified the classical DGT setup by eliminating the gel layer covering the Chelex resin disc (so reducing the length of the DBL from 0.93 to 0.13 mm) and by opening a further hole in the DGT piston (as shown in Fig. 6.1).

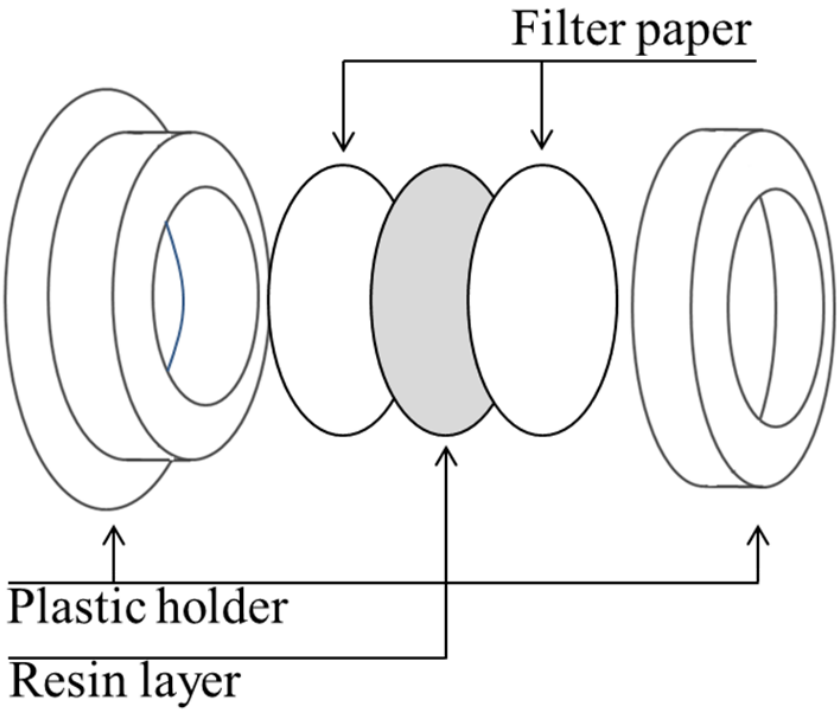

Figure 6.1. Exploded view drawing of the eDGT device.

The receiving phase, the resin disc, was sandwiched between two cellulose nitrate filters (Whatman, diameter 25 mm, pore size 0.45 μm). Although the thickness of the ensemble filter/resin/filter setup is quite smaller than the resin/diffusive gel/filter one, and consequently held more loosely, the filters are stiff enough to keep the resin in place, without adding a further spacer to tighten it up. Some further care had to be taken, though, in the act of retrieving the sampler from water, as well as choosing a deployment site where the stream is slow, so as not to let the membrane slip out.

6.2.2. Modelling the uptake

In order to interpret the results produced by the sampler, we need to find the distribution coefficient that relates the amount of metal accumulated in the Chelex resin to the concentration of the corresponding free species in solution. As a first approximation, the functional groups of the resin can be modelled using the stability constant of similar ligands like IDA[6] or MIDA,[7] but in this way we would neglect the fact that the inside of the resin presents very different conditions if compared to the bulk solutions: relatively large ionic strength, high density of charges, steric hindrance, etc. A classical approach to describe metal binding to resin can be found in the work of what could be called the school of Pavia.[7–10] In their interpretation, generally referred to as the "Gibbs-Donnan model", the sorbent is represented as a liquid phase separated from the external solution

by an interface through which water, neutral molecules and ions can diffuse, while the active groups, permanently linked to the resin, cannot; as a consequence of the separation of charge, a Donnan potential arises at the interface. The main facts about the Gibbs-Donnan model have been summarised in Section 3.7.5. Here we would like to add that the iminodiacetic groups of Chelex were found to form complexes with stoichiomietries not normally observed for the dissolved iminodiacetic acid, as a consequence of geometrical constriction.

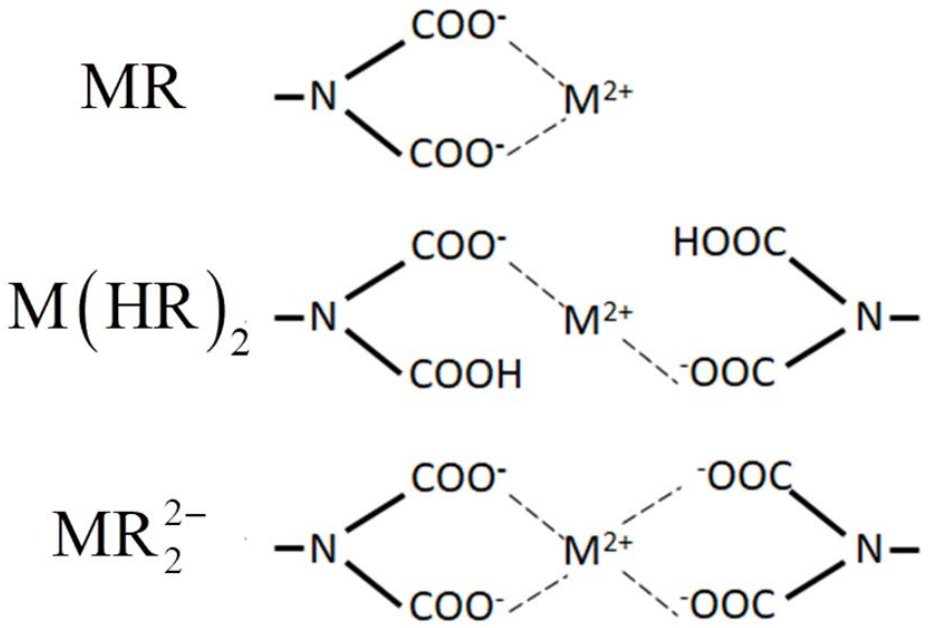

*Figure 6.2. Several possible stoichiometries of the complexes formed by a divalent cation (*M*) and the iminodiacetic functionalities of the resin Chelex 100 according to Pesavento et al.*[8,11]

According to the literature, the prevalent Chelex-metal complexes are those represented in Fig. 6.2, with stoichiometry MR, MR_2 and $M(HR)_2$; R stands for the whole iminodiacetic functionality. The intrinsic complexation constants (see A3.68 for their definition) for several metal cations of environmental interest are reported in Tab. 6.1. To simplify the notation, here and throughout this chapter the oxidation state of the metal ions will be omitted, as all of them are divalent.

Table 6.1. Values of the logarithm of the intrinsic complexation constants (β_{1npi}) for several M(II)-Chelex complexes. In the literature these constants appear under the names of β_{110i} (MR complexes), β_{122i} ($M(HR)_2$) and β_{120i} (MR_2). Charges are omitted for the sake of simplicity.

Metal	**MR**	**$M(HR)_2$**	**MR_2**
Ca	-7.87[11]	-4.72[11]	---
Mg	---	-4.94[11]	---
Mn	---	-4.08[11] -4.20[8]	-14.50[11] -14.50[8]
Cd	---	-3.13[11] -3.47[8]	-11.00[11] -11.7[8]
Zn	-4.66[8]	-3.44[8]	-9.54[8]
Ni	-2.28[11] -2.90[8]	---	-10.74[11]
Cu	-0.79[11] -0.75[8]	---	-5.76[11] -6.70[8]

As a general observation, it can be said that the metals that are bound more strongly tend to form MR complexes, while higher stoichiometries are expected for the weaker ones. Thus, instead of considering in detail the behaviour of each metal, for the sake of simplicity we will make two major assumptions:

- The MR_2 complexes exist in negligible amount. This is reasonable, as the formation of tetrahedral complexes is likely to be limited by sterical constraints, and at neutral-mildly acidic pH (as explored in this chapter) the resin sites tend to be at least partially protonated.
- Only one of the remaining two species (either MR and $M(HR)_2$) is relevant. This assumption is safe for all metals, with the significant exception of Zn.

We can, then, lump the metal cations together on the basis of the complex they are more likely to form: $M(HR)_2$ for the weaker ones (Ca, Mg, Mn and Cd) and MR for the others (Ni, Cu). Zn is an intermediate case, and it will be decided in which group it fits better by comparing its behaviour with the other cations. Metals whose intrinsic constant were not found in the literature can be assigned to one group or the other by comparing their relative selectivity for Chelex: it is safe to assume, for example, that Co will behave as Cd. Pb, on the other hand, was found to form several complexes with different number of water molecules (MHR, MROH);[12] since in all of them only one resin group is involved, it is safe to let Pb join Cu in the MR group. The groups are schematised in Tab. 6.2 below.

Table 6.2. Metal cations grouped according the kind of complex they are more likely to form.

MR	**$M(HR)_2$**
Cu, Ni, Pb, (Zn)	Ca, Cd, Co, Mg, Mn, (Zn)

Let us start considering the case of the cations that form MR complexes. To keep the notation simple, let the conditional (dependent on *I*) complexation constant be called K_{MR}:

$$K_{MR} = \frac{\tilde{c}_{MR}}{\tilde{c}_M \tilde{c}_R} \tag{6.1}$$

where the tilde refers to the concentrations in the gel phase. The number of moles of metal chemically bound to the resin is given by the difference between the total metal in the resin disc ($\tilde{n}_{T,M}$), the metal electrostatically bound in the resin beads and the metal diffused inside the gel:

$$\tilde{n}_{MR} = \tilde{n}_{T,M} - V_R \left(\chi_R^2 c_{M^{2+}}^* \right) - c_M^* \left(V_{disc} - V_R \right) \tag{6.2}$$

where χ_R is the electrostatic partitioning factor referred to the resin beads and V_R and V_{disc} are the volumes of the beads and of the resin disc, respectively.

The metal concentration in the bulk solution can be related to the amount bound to the resin through the relationship:

$$c_M^* = \frac{\tilde{n}_{MR}}{V_R K_{MR} \chi_R^2 \tilde{c}_R} \tag{6.3}$$

Such a relationship cannot be practically used as K_{MR} is not exactly known and the number of resin sites changes from sampler to sampler, depending on the manufacture. To circumvent this problem, the concentrations can be normalised with respect to a reference cation of the same charge, chosen among those that form complexes with similar stoichiometry:

$$c_{Ref}^* = \frac{\tilde{n}_{RefR}}{V_R K_{RefR} \chi_R^2 \tilde{c}_R} \tag{6.4}$$

Combining (6.4) and (6.3) yields:

$$c_{\mathrm{M}}^{*} = \frac{\tilde{n}_{\mathrm{MR}}}{\tilde{n}_{\mathrm{RefR}}} c_{\mathrm{Ref}}^{*} \frac{K_{\mathrm{RefR}}}{K_{\mathrm{MR}}} \tag{6.5}$$

This equation, which will be referred to as the "key eDGT equation", allows to compute the free metal concentration from the number of moles of M and Ref chemically bound, the free metal concentration of the reference cation and a ratio of constants that can be calibrated for a given *I*. By cancelling $\tilde{c}_{\mathrm{R}}$ the normalisation with respect to Ref accounts for the effects of competition by other metal cations and by protons as well. As a consequence, the calibration is independent from the pH. It is worth noting that this model corresponds to a competitive Langmuir isotherm.

Analogous reasoning can be applied to the case of $M(HR)_2$ complexes. Given the relationship:

$$K_{\mathrm{M(HR)_2}} = \frac{\tilde{c}_{\mathrm{M(HR)_2}}}{\tilde{c}_{\mathrm{M}} \tilde{c}_{\mathrm{HR}}^{2}} \tag{6.6}$$

an equation formally identical to (6.5) can be written

$$c_{\mathrm{M}}^{*} = \frac{\tilde{n}_{\mathrm{M(HR)_2}}}{\tilde{n}_{\mathrm{Ref(HR)_2}}} c_{\mathrm{Ref}}^{*} \frac{K_{\mathrm{Ref(HR)_2}}}{K_{\mathrm{M(HR)_2}}} \tag{6.7}$$

provided that the chosen reference cation forms complexes of similar stoichiometry.

The proportionality parameters (to be obtained in suitable calibrations) in Eqs. (6.5) and (6.7) are

$$\frac{K_{\mathrm{MR}}}{K_{\mathrm{RefR}}} = \frac{c_{\mathrm{Ref}}^{*}}{c_{\mathrm{M}}^{*}} \frac{\tilde{n}_{\mathrm{MR}}}{\tilde{n}_{\mathrm{RefR}}} \tag{6.8}$$

and

$$\frac{K_{\mathrm{M(HR)_2}}}{K_{\mathrm{Ref(HR)_2}}} = \frac{c_{\mathrm{Ref}}^{*}}{c_{\mathrm{M}}^{*}} \frac{\tilde{n}_{\mathrm{M(HR)_2}}}{\tilde{n}_{\mathrm{Ref(HR)_2}}} \tag{6.9}$$

While the moles of analyte and reference accumulated can be determined by eluting the resin (and discounting the electrostatically bound fraction), the free concentration of the reference cation in the bulk solution has to be measured directly with a complementary analytical technique, such as ISE or AGNES.

This model shares some formal similarities with the classical IET[13] (see Section 1.2.2), but it presents the major advantages of not needing an exactly known amount of resin

and of being independent from pH. In addition, the chelating resin Chelex 100 guarantees much higher pre-concentration factors than Dowex 50.

Clearly the choice of the reference cation is crucial for the successful application of the technique. Ideally, the reference should comply with the following characteristics:

1- It must be ubiquitously present in the environment in measurable amounts.

2- Its free fraction should be easily measurable with an independent technique.

3- It must be bound by the resin mainly through specific interactions (*i.e.* forming complexes with fixed stoichiometry describable with a stability constant, instead of a Boltzmann factor just related to charges).

4- It must form complexes with the same stoichiometry as the metals for which it will be used as a reference.

Considering only the first two conditions, the best choice would have probably been Ca, a metal present at high concentrations in freshwater and easily measurable with an ISE. Unfortunately our preliminary experiments clearly showed that, at low ionic strength, Ca is bound to the resin mainly through electrostatic interactions (as it will be shown in Section 6.6 of this chapter). For the normalization to be effective, it is paramount to know exactly the amount of reference metal bound, but any attempts of accurately separating the electrostatic and chemical contributions of Ca has met with failure due to the uncertainty on the estimated value of χ. As a consequence, we had to resort to other references: for the metals of the MR group the best one would probably be Zn, widespread in the natural environment and detectable even at very low concentration with AGNES. On the other hand this option is a suitable one only if Zn complexation as $Zn(HR)_2$ is negligible. As this assumption is not necessarily granted, the safest choice would be probably Pb, which surely forms complexes of stoichiometry 1:1 and for which both ISE and AGNES methods are available. The choice for the $M(HR)_2$ group is not straightforward either, since most of the possible candidates (Ca, Mg and Mn) were found to be bound, for a significant fraction, through electrostatic interactions. In this case, the best option is probably Cd, which forms strong chemical bounds with the resin and can be measured by ISE and AGNES. On the down side, Cd is not as ubiquitous as Pb. Zn could serve as an alternative, given its intermediate behaviour; it would be interesting to verify whether Zn could be used as a reference for the metals of both groups.

6.3. Experimental part

A long-term application of our work is the analysis of metal speciation in the streams of the Pyrenees mountains, an area of relevant interest that has already been subjected to numerous studies.[14,15] Before moving to sample or on-field analysis, though, it is necessary to calibrate the technique and evaluate its performance in a controlled environment. Our starting point was to use a synthetic freshwater following the recipe given in Parat *et al.*,[15] which is based on the composition of the rivers Garonne and Gave de Pau (see Tab. 6.3):

Table 6.3. Major components of the synthetic freshwater (adapted from Parat *et al.*[15]).

	Conc (M)
$NaHCO_3$	1.0×10^{-3}
$MgSO_4$	1.0×10^{-4}
KNO_3	5.0×10^{-5}
$CaCl_2\cdot2H_2O$	2.0×10^{-4}

The resulting ionic strength is about 4 mM. Even though the pH of the real medium is about 7.5, we chose to work at slightly more acidic conditions (pH 6.4±0.5). According to the model (see Eqs. (6.5) and (6.7)) the pH does not affect the calibration of the technique, and lowering the pH allows us to work in a wider range of concentrations, reducing the risk of precipitation of metal hydroxides. As a reference of the trace metal concentration, we took the following average values, obtained from analyses of the water of the river Ebro:

Table 6.4. Reference values of the trace metal concentrations in synthetic freshwater.

	Conc (M)
Mn[16]	1.6×10^{-7}
Cd[17]	1.2×10^{-9}
Co[18]	4.6×10^{-9}
Zn[17]	6.1×10^{-7}
Ni[17]	4.9×10^{-8}
Pb[17]	4.8×10^{-9}
Cu[17]	3.2×10^{-8}

In a typical eDGT experiment, several aliquots of heavy metal standards were added to 5 L of synthetic freshwater. A first sample of the solution was taken to measure the total

metal concentration; then, a small number of eDGT devices (3 or 4) were deployed and left hanging from plastic wires (see Fig. 6.3). The reduced number of eDGT devices was intended to minimise the depletion of the metal ions in the sample solution (even though only the equilibrium concentration was used in the computations). Care had to be taken to ensure that the flow kept them completely submerged, to allow the metal to diffuse inside the resin from both sides.

Figure 6.3. Picture of a typical experimental setup, showing three samplers suspended from plastic wires, left free to float in a stirred solution.

The solution was stirred throughout the experiment by means of an overhead stirrer. The pH was adjusted with small additions of concentrated HNO_3 and NaOH standard solutions. The sample solutions were left at the open air and the exchange of the atmospheric CO_2 caused a slow, but noticeable pH drift that had to be corrected. Preliminary experiments showed that equilibrium is reached in the first 48 hours. To ensure its attainment, nevertheless, we retrieved the first sampler three days after the stabilization of the pH; two days more were left to pass before retrieving the remaining ones. Once equilibrium is attained and the samplers are retrieved, the number of bound moles of M and Ref is found by eluting the resin in acidic conditions and subsequently analysing the eluates, while the ratio of stability constants (we will use $\frac{K_{\mathrm{M}}}{K_{\mathrm{Ref}}}$ to refer to both $\frac{K_{\mathrm{MR}}}{K_{\mathrm{RefR}}}$ and $\frac{K_{\mathrm{M(HR)_2}}}{K_{\mathrm{Ref(HR)_2}}}$ see Eqs. (6.8) and (6.9)) can be determined by calibrating the system in a solution of known composition at the *I* of interest.

6.4. Results

A sound, reproducible calibration is the first, necessary step. The calibration, apart from obtaining the values of the ratio of constants $\frac{K_{MR}}{K_{RefR}}$, serves two main purposes: it confirms that the metals accumulate in the resin with a coverage ruled by a competitive Langmuir isotherm, and that the normalisation with respect to a reference cation is an acceptable way to deal with the differences between samplers.

FIRST APPROACH: HIGH CONCENTRATION CALIBRATION

A possible limitation of the eDGT is its reliance on another experimental technique for measuring the concentration of the reference metal in the bulk solution, which *de facto* defines its limit of detection. If the reference is chosen among the majoritarian cations (*e.g.* Ca) this may not constitute a problem, but the same cannot be said for the trace metals. Moreover, the calibration requires good estimates for the free concentration of all targeted and reference trace metals. For this reason, we initially chose to calibrate the technique in solutions where the trace metal were at higher concentrations than the environmental ones; for those like Cd, naturally present at very low levels, the concentration was increased up to three orders of magnitude.

A series of four experiments (here called 1H, 2H, 3H and 4H) was performed, using solutions of different trace-metal compositions and concentrations (see Tab. A6.1).

When deciding the composition of the solutions, we were at first reluctant to work with Cu, as its large complexation constants with the ligand MIDA[19] suggested that this metal may be bound so strongly by Chelex that, even at environmental concentrations, may lead to resin saturation. Although Eqs. (6.5) and (6.7) do hold even in the proximity of full saturation, the accuracy in the determination might be greatly compromised. These experiments, though, showed that Cu binding, albeit strong, is not as overwhelming as we thought in the first place (see the ratio of constants in Tab. 6.5).

As previously explained in Section 6.2.2, we will use Pb as a reference cation for group MR, and Cd for group $M(HR)_2$, but due to its interesting features (ubiquity, ease of measuring) we will also explore the possibility of using Zn for all the cations irrespective of their group, even if it might form complexes of different stoichiometries with the iminodiacetic binding groups. Since the fraction of Mn specifically bound, as computed with Eq. (6.2), is very small and potentially affected by a large uncertainty, this metal may not be suitable for the analysis. Conversely, for all the other trace metals

the fraction electrostatically bound is negligible. The ratio of constants obtained for each metal in these high-concentration calibration experiments are reported in the three plots below (Fig. 6.4), using as reference Cd, Pb and Zn. All the values are listed in Tab. A6.5, A6.6 and A6.7 in the appendices.

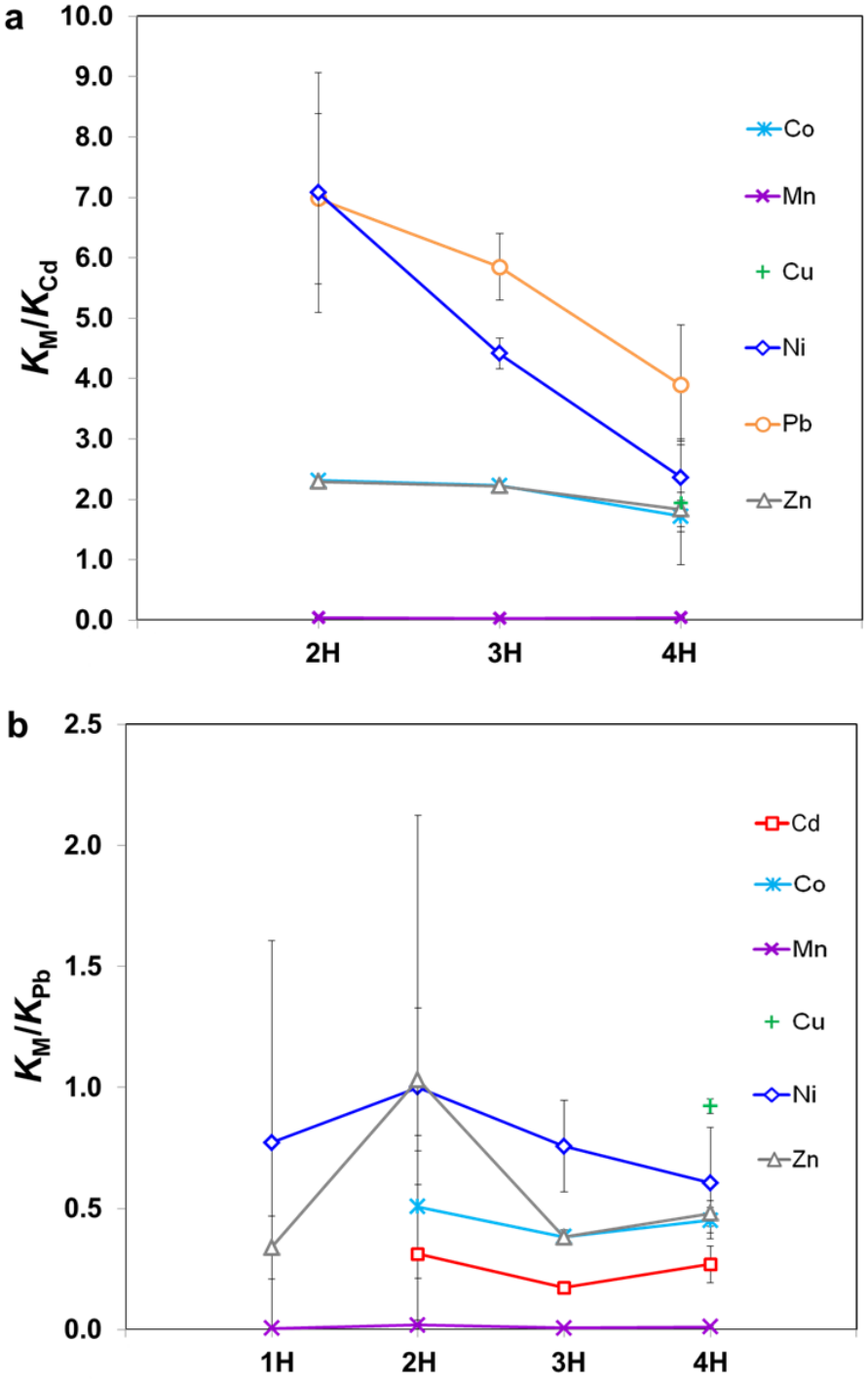

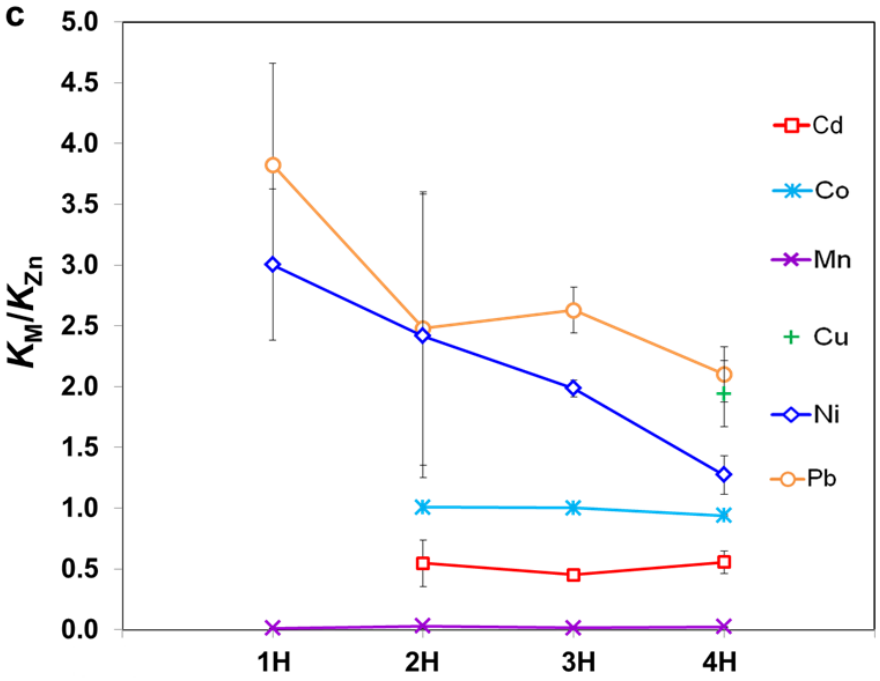

Figure 6.4. High-concentration calibration of the eDGT passive sampler. For each experiment (1H to 4H) it is given the ratio of constants K_M/K_{Ref}, with Ref being Cd (Panel a*), Pb (*b*) and Zn (*c*). Every point is the average of three replicates (three samplers deployed in the same solution), the error bars represent the standard deviation. All the values are listed in Tab. A6.5, A6.6 and A6.7 in the appendices.*

A few observations about the calibrations can be now drawn:

1- there is quite a large variability among the samplers of each experiment, in particular for 1H and 2H
2- independently from the choice of the reference, the reproducibility of the results of Cd, Co and Mn is good for all the experiments
3- Ni and Pb show poor reproducibility when normalised with respect to Cd and Zn, but the reproducibility of Ni improves considerably when the reference is Pb

Point 3 seems to confirm the hypothesis that Ni and Pb form complexes with the same stoichiometry, while Zn does not; on the other hand, it is unclear why Cd, Co and Mn, which should form $M(HR)_2$ complexes, should perform well when using Pb as a reference. The readiest conclusion is that our distinction in two groups does not hold very tightly, and the choice of the reference can be made simply following some broad, semi-empirical rules: Zn could be a safe choice for Cd and Co, while Ni needs to be normalised with respect to Pb. A deeper insight in this phenomenon is hindered by the large uncertainty on the results (mentioned in Point 1). For the sake of comparison, the values of the ratios of constants (with respect to Zn) are reported in Tab. 6.5.

Table 6.5. Values of the ratios of constants as determined in the calibrations.

K_{Mn}/K_{Zn}	K_{Cd}/K_{Zn}	K_{Co}/K_{Zn}	K_{Ni}/K_{Zn}	K_{Pb}/K_{Zn}	K_{Cu}/K_{Zn}
0.02(1)	0.52(6)	0.98(4)	2.2(7)	2.8(7)	1.9[a]

[a] The ratio K_{Cu}/K_{Zn} comes without error as only one replicate was available.

It can be seen that the ratios of constants roughly follow the order of selectivity of Chelex 100 for these metals as reported by the manufacturer[20] (Mn<Cd<Co<Ni<Pb<<Cu) although the value of K_{Cu}/K_{Zn} seems underestimated (Chelex should be 30 times more selective for Cu than for Ni).

SPECIATION MEASUREMENTS IN PRESENCE OF SYNTHETIC LIGANDS – NTA

As the series of calibrations described in the previous paragraph gave, for some metals, rather satisfactory results, eDGT was tested in a speciation analysis experiment. A candidate for the ligand was Nitrilotriacetic Acid (NTA), a strong complexant with which we had already worked in Chapter 4 and whose constants with most of the heavy-metal cations are well documented. A potential drawback of NTA is that the dissociation of the M-NTA complexes may be very slow, so requiring extremely long times to reach equilibrium. For this reason, the target metals were chosen among the fastest to dissociate, such as Cd. As a reference we could have used Co, but it forms rather inert complexes[21] and lacks a complementary technique for measuring the free cation. We resorted then to Zn, as the calibrations showed that it is a good reference for Cd and it has the benefit of forming a relatively labile complex with NTA.

We worked at two levels of NTA concentration, 8×10^{-7} M and 2.8×10^{-6} M, while the metal concentration was kept constant in both experiments ($c_{T,Cd}= 1\times10^{-7}$ M, $c_{T,Zn}= 2\times10^{-7}$ M). A third experiment, performed with the same metal concentration, but in absence of ligand, served as a term of comparison and as a kind of punctual calibration.

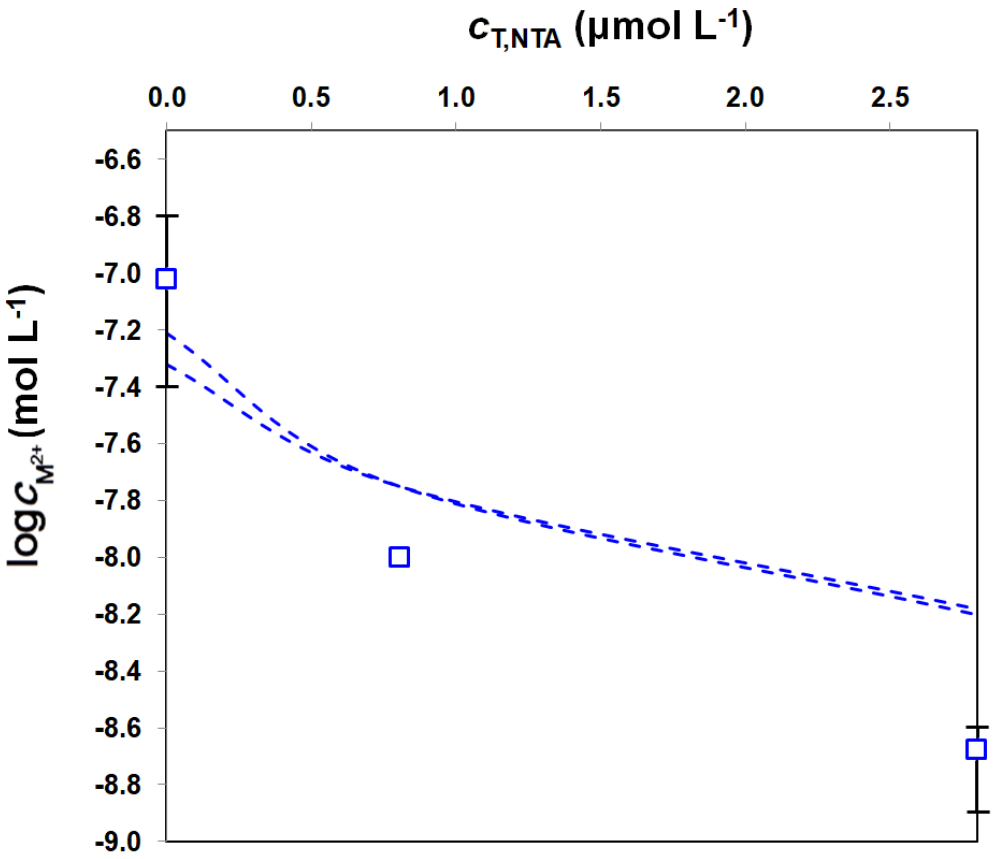

Figure 6.5. Free Cd concentration as a function of the total NTA added. Dashed lines: free concentration computed with Visual MINTEQ; Symbols: concentration computed from the metal accumulated in the eDGT, using K_{Cd}/K_{Zn} *= 0.52 (see Tab. 6.5).The experiments at* $c_{T,NTA}$ *= 0 and 2.8×10^{-6} M were performed in duplicate.*

From the results of this first eDGT measurement, represented in Fig. 6.5, we can draw two main considerations: first, although the results from the eDGT do not exactly coincide with the predictions from Visual MINTEQ, the general trend is respected; second, the new "calibration point", (the experiment performed in absence of ligand), gave a value of the ratio of constants quite far away from the one previously obtained (Tab. 6.5). The blame for the discrepancies in Fig 6.5 can be put on several factors, such as the error on the complexation constants (notwithstanding that their reliability was key in the choice of NTA) or the long dissociation time (not so long, however, that equilibrium cannot be reached in the experimental timescale). These hypotheses, though, cannot account for the difference in the experiment in absence of ligand, which should simply be a replicate of the calibrations. It comes as a logic conclusion that the error does not arise from the ligand, but is intrinsic to the system: for example the calibration may not be suitable because it was done in conditions too different from

those of the experiments, the stochiometries of the metal-resin complexes of Zn and Cd are too different, or the technique has a very large uncertainty, for reasons not yet clear. This last possibility, if proved true, would drastically reduce the precision of the eDGT and would clearly pose a serious threat to its application.

Let us start from the first hypothesis, that the calibration and the speciation measurement have not been performed in the same conditions. A first hint in this direction comes from the values of the Boltzmann factor (see Section 6.6.4 below). If the average χ_{resin} value obtained from the calibration is 128±23, the value retrieved from the K^+ partitioning in the NTA experiments is 49±5. As the composition of the solutions for the two series were roughly the same (identical pH and *I*, just different trace metals) the reason of this discrepancy probably resides in the samplers themselves. This hypothesis is not too wild, as the resin layers used for the two series of experiments came from different batches (those employed in the calibration had been synthesized in our laboratory, while we purchased those to be used for the measurements in presence of NTA from DGT Research Ltd.). Perhaps an incomplete washing of the gels left some charged monomers stuck in the polymeric matrix, or the volume of the two polymers was different (the gels prepared in Lleida tend to swell more than the commercial ones). Anyway, as said before, the contribution of electrostatic binding is negligible for both Cd and Zn, and even though the composition of the gels may be different, this can hardly be the reason for the discrepancy.

Another point that ought to be considered is the coverage of the resin sites. The total number of iminodiacetic sites of a DGT Chelex layer was estimated to be 1.8×10^{-5} mol per disc.[5] Assuming that all the metals form complexes with only one stoichiometry and discounting the electrostatic contribution, we find that the average number of occupied sites over the whole series of calibrations is 3×10^{-6} mol, much larger than the accumulation in the experiments in presence of NTA (less than 1×10^{-6} mol). Let now hypothesize that different kinds of sites are present: some of them stronger than the others, some more prone to form complexes of particular stoichiometries, and others that, once occupied, can affect the affinity of the surrounding sites (Fig. 6.6). If this were true, the accumulation would not be always linear with the bulk concentration. As a consequence, relationships of the kind of (6.8) may hold only within a limited range of concentrations.

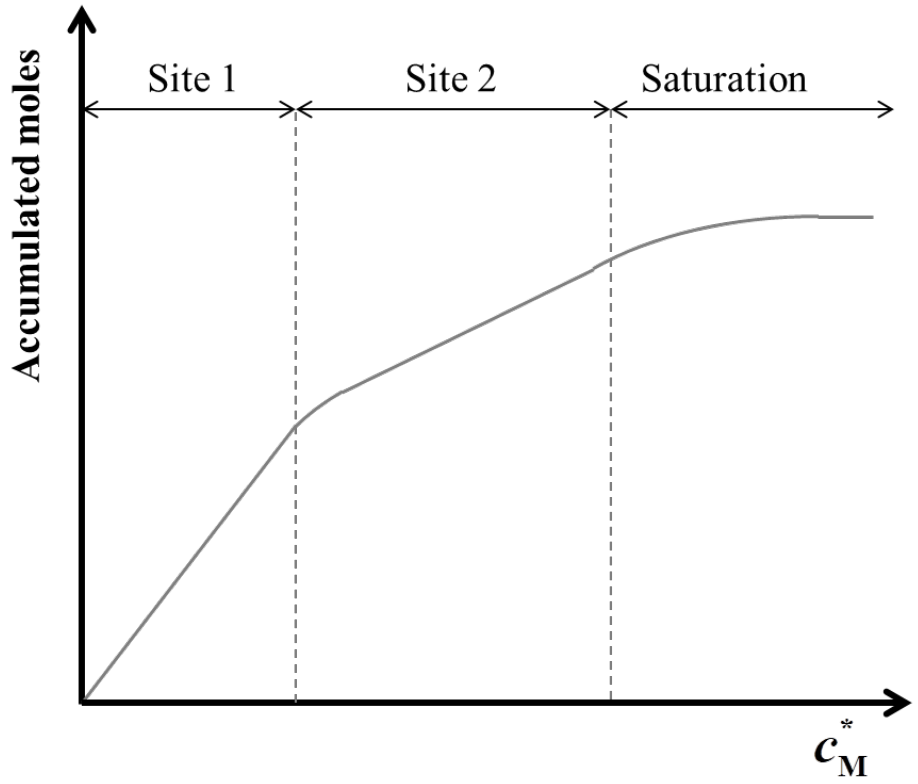

Figure 6.6. Scheme of the hypothetical relationship between c^*_M, the free metal bulk concentration, and the moles accumulated in the resin. The two types of resin sites show different affinities for the metals, reflected by the changing slope of the curve.

As a consequence, for the calibration to be effective, we decided to perform it in a range of concentrations as close as possible to the expected sample values (*e.g.* environmental concentrations).

SECOND APPROACH: LOW CONCENTRATION CALIBRATION

The previous series of calibrations strongly hinted at the fact that working with excessively high concentrations may lead to erratic performances, most likely because some kind of saturation of the resin, apparent heterogeneity or the formation of complexes with different stoichiometries. For this reason we decided to work with total metal concentrations at most ten times larger than those reported in Tab. 6.4. As a further way to check our hypotheses about the complex stoichiometries, as well as the presence of interactions or competition between the ions, three series of calibrations were performed: one with the metal of the MR group, one with those of the $M(HR)_2$ group and one with all the metals of Tab. 6.4. Each series is constituted by 4 experiments (with names 1iiL, 2iiL, 3iiL and 4iiL for the $M(RH)_2$ group, 1iL, 2iL, 3iL

and 4iiL for the MR group and 1L, 2L, 3L and 4L for all the metals); the total metal concentrations at equilibrium for each of them are given in Tab. A6.2, A6.3 and A6.4. Again, the choice of an adequate reference cation is crucial for a sound and reproducible calibration; as done for the calibration at high concentration, we will select Pb for the MR group and Cd for the $M(RH)_2$ group, while testing Zn as well. As the previous calibration most likely failed, the main objective of this one is to confirm that the normalisation works, at least in a certain range of concentrations. In particular, by comparing results coming from solutions at different composition, we want to verify that there is no interference among the ions.

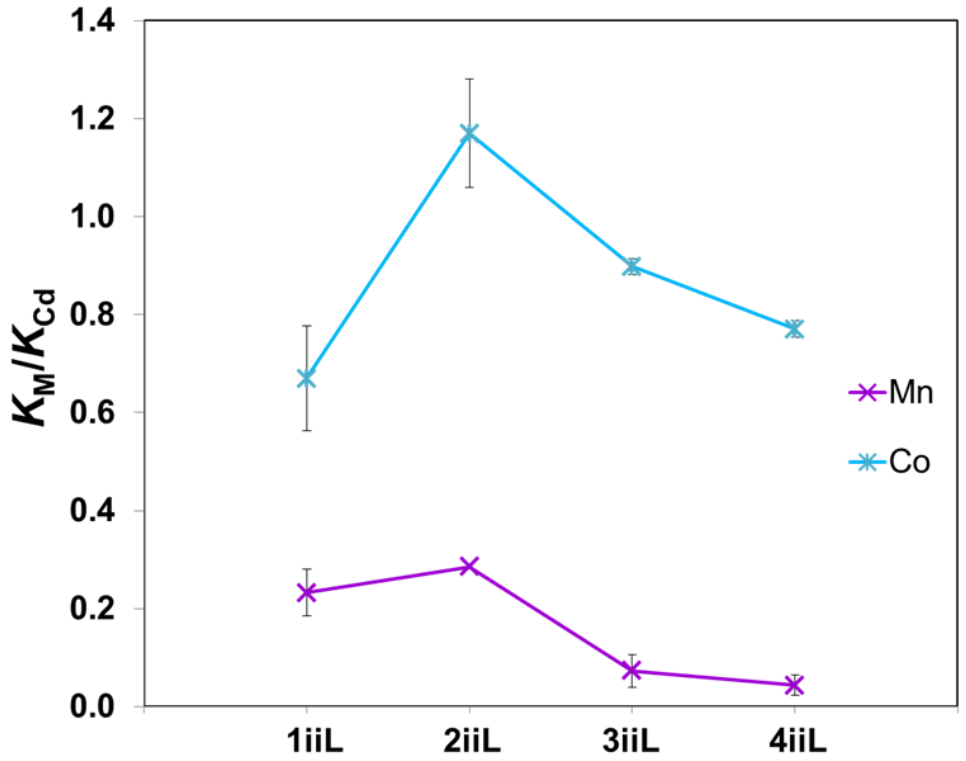

Figure 6.7. Calibration at low concentrations of the eDGT passive sampler for Co and Mn, using Cd as reference. The majoritarian components of the solution are given in Tab. 6.3, while the trace metal concentrations are given in Tab. A6.5. The values of the constants are given in Tab. A6.12.

The results regarding the metals of the $M(RH)_2$ group are given in Fig. 6.7. Those of Mn are discrete, although their reliability is debatable as a very large fraction of this metal is electrostatically bound and had to be subtracted from the total, increasing the uncertainty on the results and even leading to negative values (these replicates, present in particular in experiment "2iiL", were discarded). This means that the accuracy of Mn measurements will probably be very poor, at least in low-ionic strength media when the

electrostatic binding is preponderant. Co, on the contrary, is very well correlated with Cd, as reflected by the good reproducibility of the ratio of constants across the replicates (note the different scales of the vertical axis in the plots of the low-concentration calibrations and the high-concentration one).

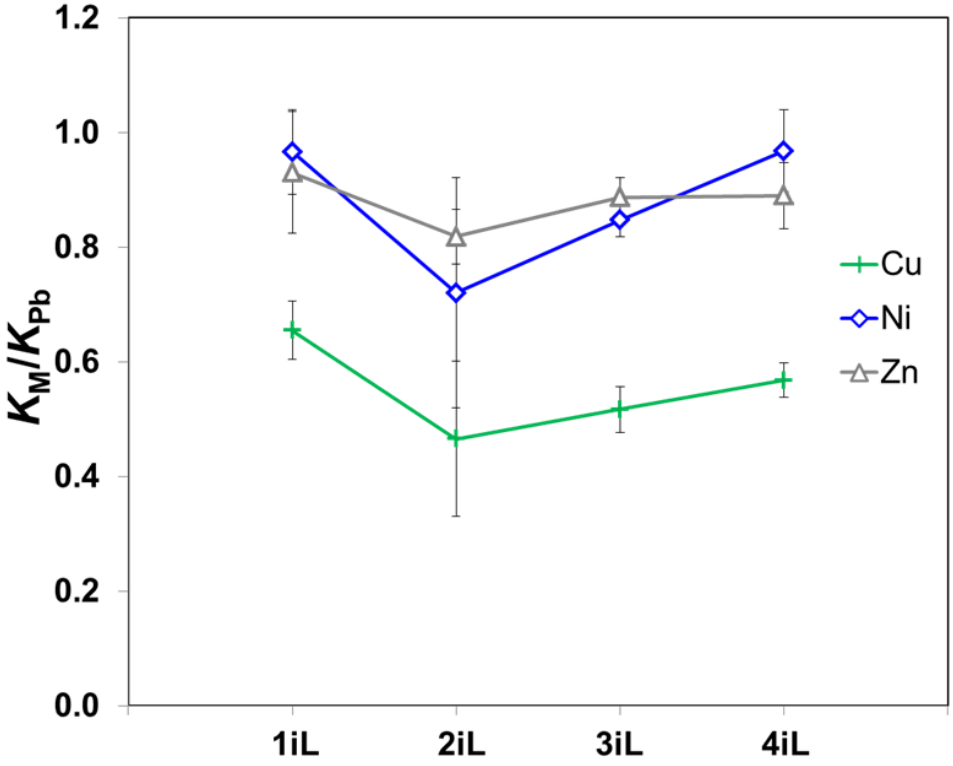

Figure 6.8. Calibration at low concentrations of the eDGT passive sampler for Pb, Ni and Cu, using Zn as reference. The major components of the solution are given in Tab. 6.3, while the trace metal concentrations are listed in Tab. A6.4. The values of the constants are given in Tab. A6.13.

The reproducibility improves when moving on to the cations that form monodentate complexes, as Fig. 6.8 makes clear. There is some residual variability, (as in the replicate "2iL"), but this is likely to arise from occasional errors, not infrequent when working with trace-level concentrations. It will be interesting to investigate more closely the behaviour of Cu, since in the high-concentration series this metal was used only once, and its reproducibility could not be studied. It is worth remembering that Cu is a special case among the ions considered, as it binds much more strongly with the resin than any other cation,[20] and preliminary eDGT experiments (data not shown) hinted at the fact that, at large concentrations, this ion can give particularly erratic results. In the calibration at low concentration, though, Cu behaves very much in line with the other ions and its affinity is not nearly as high as expected.

The three panels of Fig. 6.9 present the results of the last series of calibrations, the one with solutions of cations coming from both groups. If in panels “a” and “b” the reference cations are the already tried Cd and Pb, in panel “c” we finally test whether Zn is a suitable reference for the ions of both groups.

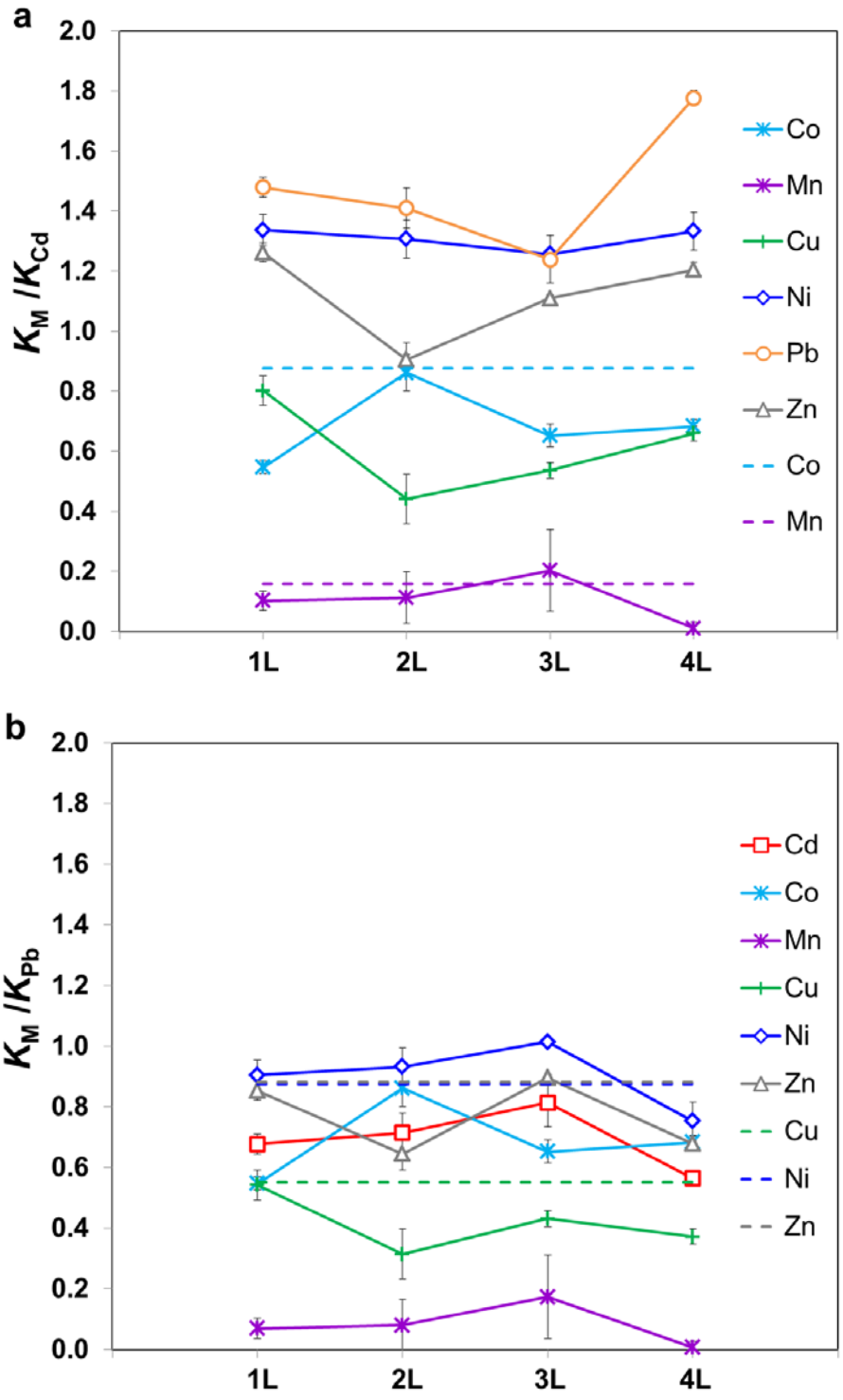

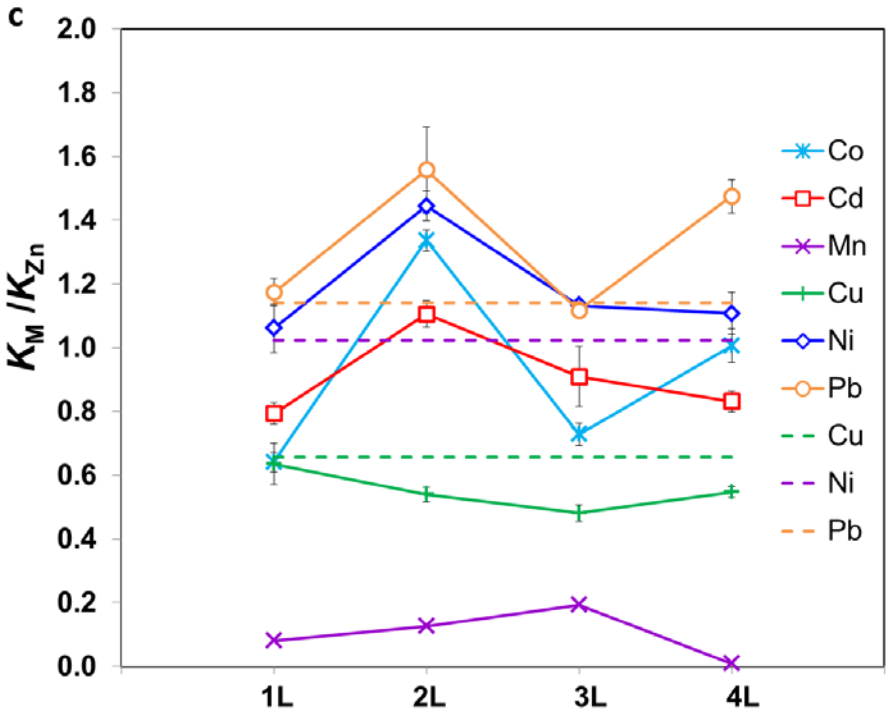

Figure 6.9. Calibration of the eDGT passive sampler for Co, Cd, Pb, Ni and Cu, using Cd (Panel a), Pb (b) and Zn (c) as references. The dashed lines correspond to the average values of the ratio of constants as found in the experiments reported in Fig. 6.7 and 6.8. The majoritarian components of the solution are given in Tab. 6.3, while the trace metal concentrations are as in Tab. A6.6.

By calibrating the eDGT using both the metals of the MR and $M(HR)_2$ group, we aim at answering a double-sided question: first, whether we can discard the interaction between cations of the two groups in the resin phase; second, whether it is necessary to work with different reference cations depending on the stoichiometry of the formed complex (*i.e.*, according to its group). Regarding the first part of the question, Fig. 6.9a and b substantially confirms the values of K_M/K_{Ref} obtained in the series of calibrations of Fig. 6.7 and 6.8 (represented as dashed lines), proving that, in this conditions, there is no interaction between the ions. As previously stated, having a unique reference for all the metals, like Zn, would be a significant step forward for the practical application of the technique. In fact, the values of K_M/K_{Zn} reported in Fig. 6.9c are quite reproducible (and in line with those obtained in the experiments of Fig. 6.7 and 6.8), although the uncertainty is larger than in the other cases. No clear patterns can be detected, since the ions with the poorest performance, Pb and Co, come from different groups, just like the two best do (Cu and Mn). Lacking any further information, we can assume that the main source of variance in this case is not the presence in the resin of

complexes of different stoichiometry, but rather the experimental error. In Tab. 6.6 we compare the values of K_M/K_{Ref} computed with Cd, Pb or Zn as a reference, while in Tab. 6.7 the respective average errors are reported.

Table 6.6. Values of the ratios of constants as determined in the low-concentration calibrations, normalised with respect to Cd, Pb and Zn. For each ratio it is reported the average value (over the four experiments of Fig. 6.9) and the average percentage error.

	K_{Co}/K_{Cd}	K_{Mn}/K_{Cd}	K_{Cu}/K_{Cd}	K_{Ni}/K_{Cd}	K_{Pb}/K_{Cd}	K_{Zn}/K_{Cd}
Average	1.01	0.11	0.61	1.31	1.48	1.12
% Error	23	73	26	3	15	14

	K_{Cd}/K_{Pb}	K_{Co}/K_{Pb}	K_{Mn}/K_{Pb}	K_{Cu}/K_{Pb}	K_{Ni}/K_{Pb}	K_{Zn}/K_{Pb}
Average	0.69	0.69	0.08	0.41	0.90	0.77
% Error	15	19	83	24	12	16

	K_{Cd}/K_{Zn}	K_{Co}/K_{Zn}	K_{Mn}/K_{Zn}	K_{Cu}/K_{Zn}	K_{Ni}/K_{Zn}	K_{Pb}/K_{Zn}
Average	0.91	0.93	0.10	0.55	1.19	1.33
% Error	15	34	75	12	15	16

Table 6.7. Values of the average percentage errors over the metals of the same group of the reference, over those of the other group and over all the metals.

% Error	**Same group**	**Other group**	**All metals**[a]
K_M/K_{Cd}	19	14	16
K_M/K_{Pb}	17	17	17
K_M/K_{Zn}	---	---	18

[a] Mn excluded.

Several important conclusions can be drawn by observing the values in the tables: first, the dispersion of the ratios seems to be independent from the reference cation. In fact, the values of the percentage errors in Tab. 6.7 are all roughly constant, regardless of whether they are referred only to the metals belonging to the group of the reference ion (first column), to all the metals (third column) or even only to those that allegedly form complexes of different stoichiometry (second column). From a practical point of view, this justifies the use of Zn, the most convenient option, as a reference for all the ions.

Second, these values of K_M/K_{Zn} are clearly different from those obtained in the high-concentration calibration (Tab. 6.5), with the exception of Co (the values of K_{Co}/K_{Zn}

obtained in the previous calibration was 0.98). As the two series of experiments were performed in the same conditions, apart from the total concentration of trace metals, this finding strongly hints that our hypothesis about the presence of different sites may well be true.

From the values of K_M/K_{Zn}, it is also evident that the resin roughly shows the same affinity towards all the ions, with the exception of Mn and Cu. As a first approximation, the ratio of constants could be taken equal to 1 for all metals but Mn and Cu, so obviating the need for a previous calibration. The reduced binding of Mn comports high uncertainty on the results, as made evident by Tab. 6.6, and probably will not permit using eDGT to target this metal.

It must be pointed out that, even if the calibration results are positive and will allow using eDGT for speciation measurements, they also substantially disprove the model of MR binding on which we have based our reasoning so far, suggesting as they do that all the ions form complexes of similar stoichiometry (*e.g.* all 1:1). As a tentative hypothesis we could imagine that, due to steric constraints, the number of sites that can form complexes with higher stoichiometry is limited. If this were true, only a small fraction of the metal ions will be involved in 1:2 complexes, while the majority of them would be bound by a single resin site. The discrepancy caused by the different stoichiometries will pass unnoticed because of the experimental error.

SPECIATION MEASUREMENT IN PRESENCE OF SYNTHETIC LIGANDS - CITRATE

Once proved that the low-concentration calibration gives better performances, we apply again eDGT to the measurement of free metal in presence of a competing ligand, this time focusing on the metals of the MR group. Since we need a complementary technique to verify the results given by the eDGT, the best option for an analyte is probably Pb, whose free concentration could be measured by AGNES or Pb-ISE. In addition to Pb and Zn, possible reference cations, we work also with Ni; in this case, since we lack an analytical technique specific for it we will have to resort to Visual MINTEQ to compute the free concentration. Instead of working with NTA, this time our choice fell on citrate, a relatively strong complexant that is labile enough, so as not to endure extremely long equilibration times; in this way we will exclude any possible problem arising from the incomplete attainment of equilibrium. We worked at two levels of citrate concentration, 1.0×10^{-4} M and 5.0×10^{-4} M (each of the two experiments was run in duplicate) and carried out a further calibration point in absence of ligand.

The composition of the solutions and the expected free metal concentration (as computed with Visual Minteq) are given, respectively, in Tab. A6.2 and Tab. A6.3.
The total metal concentrations in Tab. A6.2 was measured with ICP-MS, while an enzymatic test (Megazyme Citric Acid Assay Kit) was used to check the exact concentration of citrate present in solution ($5.1(2)\times10^{-4}$ and $1.1(2)\times10^{-4}$ M).
The results of this last series are reported in Fig. 6.10; as in Fig. 6.5 above, the dashed lines were computed with Visual MINTEQ while the markers stand for the experimental results. The free Pb concentration was computed using Zn as a reference (green), free Zn using Pb as a reference (red), while both Pb and Zn were used as a reference for Ni (blue).

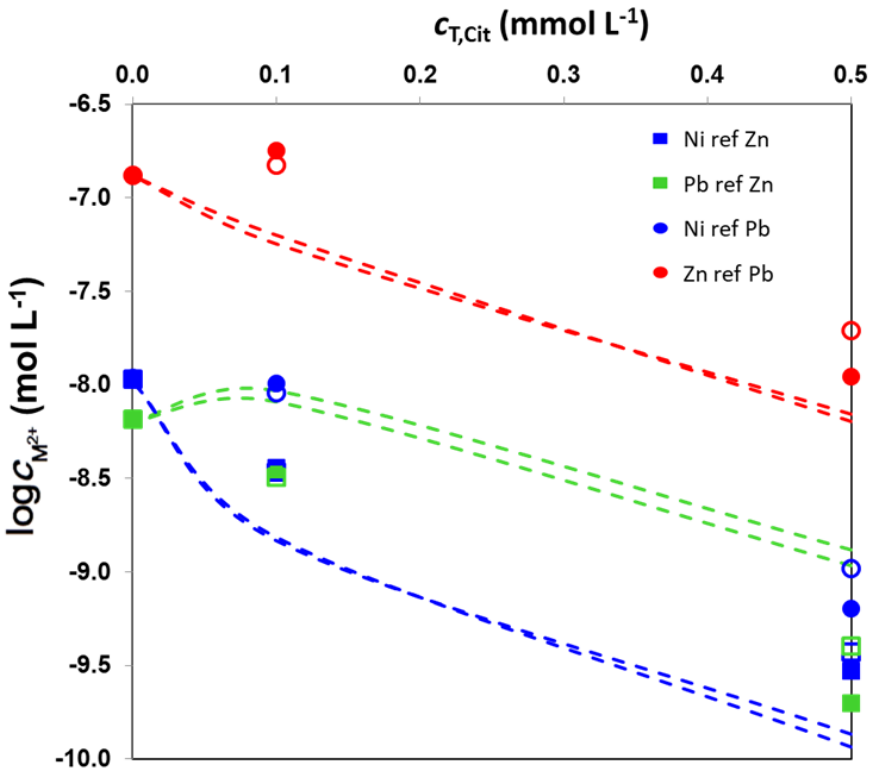

Figure 6.10. Free metal concentration as a function of the total citrate added. Dashed lines: computed free (each line corresponds to one of the replicates); markers: experimental results (full and empty markers correspond to the two replicates). Square markers indicate that the reference cation is Zn, while circle indicates that the reference cation is Pb.

As a first possible observation, the results are quite reproducible, but also far from the predictions of Visual Minteq, not dissimilarly to what happened in the series of experiments with NTA. Then, unlike this last case, the experiment in absence of ligand now actually gave results consistent with the calibrations, proving again that working at

lower concentrations was a significant improvement and that our hypothesis of the different type of sites is not without foundation.

It seems than that the method is clearly less accurate when working in presence of a ligand. We can formulate several hypotheses: first, the eDGT responds to the free fraction, whose real value is different from the estimate of Visual MINTEQ due to error on the constants. Second, some sort of interaction between the ligand and the resin takes place (*e.g*. direct binding of the complexes to the resin, with formation of ternary complexes). This source of error, already observed with the Gellyfish,[22] could be eliminated by calibrating the eDGT in presence of the same ligand. Third, the same considerations on the heterogeneity of the resin binding sites which affected the calibrations may well be true even in this last series of experiments.

6.5. Conclusions

A new equilibrium passive sampling device, originating from DGT, has been devised and tested in a controlled environment. If properly calibrated, eDGT displays discrete reproducibility and it is able to estimate the free fraction of several analytes at once with an uncertainty lower than 20%. If compared to the dynamic version of the technique, equilibrium DGT is of similar operation and should provide a clear thermodynamic quantity: the free ion concentration. Under the approximation that the ratio of constant is equal to 1, the technique does not even require to be calibrated in the experimental conditions.

It is undeniable that the technique, being still a prototype, leaves much room for improvement. A major drawback is the contribution of non-specific binding, difficult to estimate and, in cases like Ca, Mg and Mn, so large that it *de facto* invalidates the measurements for this cations. Probably this problem would not appear in a medium with higher ionic strength, such as seawater or estuarine water, where the electrostatic effect is negligible.

Further work is, then, needed to fully understand the preliminary results shown in this chapter. Perhaps, a systematic approach could be followed by building up isotherms for individual cations and, then, combinations of various cations. Even if the models reported in the literature have proved successful in describing the accumulation on Chelex at equilibrium, they could be improved by taking into consideration aspects as the sterical constraints imposed by the resin structure and the presence of different kinds of sites.

Perhaps eDGT, more than a physical device, could find its application as a theoretical framework to interpret the data obtained with the traditional DGT when equilibrium is approached. The study of this kind of systems in the light of the work presented in this chapter would probably provide a complementary interpretation of the results.

6.6. Appendices

6.6.1. Composition of the solutions

Table A6.1. Trace metal concentrations in the sample solution at equilibrium (in M) used for the calibration of the eDGT passive sampler (high concentration calibration), as measured by ICP-MS. The horizontal dashed lines stand for experiments where the metal was absent.

	Cd	**Co**	**Mn**	**Cu**	**Ni**	**Pb**	**Zn**
1H	---	---	5.0×10^{-6}	---	2.0×10^{-7}	3.9×10^{-8}	5.3×10^{-6}
2H	8.5×10^{-7}	8.3×10^{-7}	4.7×10^{-6}	---	2.3×10^{-7}	3.8×10^{-8}	5.0×10^{-6}
3H	6.9×10^{-7}	6.3×10^{-7}	4.4×10^{-6}	---	1.9×10^{-7}	4.1×10^{-8}	6.7×10^{-6}
4H	2.0×10^{-6}	2.0×10^{-6}	1.5×10^{-5}	6.9×10^{-7}	7.2×10^{-7}	1.2×10^{-7}	3.0×10^{-6}

Table A6.2. Total metal concentrations in the deployment solutions (in M) used for the series of experiments in presence of NTA.

c_{NTA} **(M)**	**Ca**	**K**	**Mg**	**Na**	**Rb**	**Cd**	**Zn**
$\mathbf{2.8\times10^{-6}}$	1.9×10^{-4}	2.1×10^{-4}	1.0×10^{-4}	---	---	8.3×10^{-8}	2.1×10^{-7}
	1.8×10^{-4}	6.6×10^{-5}	1.0×10^{-4}	---	---	9.0×10^{-8}	1.7×10^{-7}
$\mathbf{8.0\times10^{-7}}$	1.9×10^{-4}	2.0×10^{-4}	1.0×10^{-4}	---	---	7.1×10^{-8}	1.8×10^{-7}
0.00	1.8×10^{-4}	4.9×10^{-5}	1.0×10^{-4}	1.3×10^{-3} [a]	8.7×10^{-6} [b]	7.5×10^{-8}	1.4×10^{-7}
	1.7×10^{-4}	6.1×10^{-5}	9.8×10^{-5}	---	---	5.7×10^{-8}	1.3×10^{-7}

[a] Na was present in all the solutions, but was measured only in this case

[b] Rb was present only in this solution

Table A6.3. Free metal concentrations (in M) corresponding to the experiments in presence of NTA, computed with Visual MINTEQ.

c_{NTA} **(M)**	**Ca**	**K**	**Mg**	**Na**	**Rb**	**Cd**	**Zn**
$\mathbf{2.8\times10^{-6}}$	1.8×10^{-4}	2.1×10^{-4}	9.5×10^{-5}	---	---	6.3×10^{-9}	2.7×10^{-9}
	1.7×10^{-4}	6.6×10^{-5}	9.5×10^{-5}	---	---	6.6×10^{-9}	2.1×10^{-9}
$\mathbf{8.0\times10^{-7}}$	1.8×10^{-4}	2.0×10^{-4}	9.5×10^{-5}	---	---	1.8×10^{-8}	9.7×10^{-9}
0.00	1.8×10^{-4}	4.9×10^{-5}	9.9×10^{-5}	1.3×10^{-3} [a]	8.7×10^{-6} [b]	7.2×10^{-8}	1.4×10^{-7}
	1.7×10^{-4}	6.1×10^{-5}	9.7×10^{-5}	---	---	5.4×10^{-8}	1.3×10^{-7}

[a] Na was present in all the solutions, but was measured only in this case

[b] Rb was present only in this solution

Table A6.4. Trace metal concentrations at equilibrium (in M) used for the calibration of the eDGT passive sampler (low concentration calibration, cations that allegedly form MR complexes), as measured by ICP-MS.

	Cu	Ni	Pb	Zn
1iL	1.7×10^{-8}	3.0×10^{-8}	2.5×10^{-9}	3.8×10^{-7}
2iL	2.1×10^{-8}	3.4×10^{-8}	4.9×10^{-9}	4.4×10^{-7}
3iL	1.6×10^{-8}	4.0×10^{-8}	2.0×10^{-8}	3.8×10^{-7}
4iL	2.0×10^{-8}	3.1×10^{-7}	6.4×10^{-9}	4.5×10^{-7}

Table A6.5. Trace metal concentrations at equilibrium (in M) used for the calibration of the eDGT passive sampler (low concentration calibration, cations that allegedly form $M(HR)_2$ complexes), as measured by ICP-MS.

	Cd	Co	Mn
1iiL	1.6×10^{-9}	3.0×10^{-9}	1.6×10^{-7}
2iiL	1.1×10^{-8}	4.1×10^{-8}	2.2×10^{-6}
3iiL	7.1×10^{-9}	3.5×10^{-9}	2.0×10^{-6}
4iiL	1.8×10^{-9}	3.2×10^{-8}	2.0×10^{-6}

Table A6.6. Trace metal concentrations at equilibrium (in M) used for the calibration of the eDGT passive sampler (low concentration calibration, all cations) as measured by ICP-MS.

	Cd	Co	Mn	Cu	Ni	Pb	Zn
1L	3.1×10^{-9}	8.5×10^{-9}	1.7×10^{-7}	2.3×10^{-7}	4.6×10^{-8}	1.2×10^{-8}	6.8×10^{-7}
2L	2.4×10^{-9}	5.0×10^{-8}	1.6×10^{-6}	4.0×10^{-8}	4.8×10^{-7}	4.9×10^{-8}	7.3×10^{-8}
3L	1.3×10^{-8}	6.4×10^{-9}	1.9×10^{-7}	3.2×10^{-7}	4.8×10^{-7}	6.8×10^{-9}	6.6×10^{-8}
4L	1.2×10^{-8}	4.6×10^{-8}	1.5×10^{-6}	3.1×10^{-7}	4.5×10^{-8}	4.6×10^{-8}	6.1×10^{-7}

Table A6.7. Total metal concentrations in the deployment solutions (in M) used for the series of experiments in presence of citrate.

c_{Cit} (M)	Mg	Ca	Zn	Pb	Ni
5.0×10^{-4}	9.91×10^{-5}	1.89×10^{-4}	4.86×10^{-7}	3.24×10^{-8}	3.79×10^{-8}
	9.20×10^{-5}	1.87×10^{-4}	5.68×10^{-7}	4.89×10^{-8}	4.09×10^{-8}
1.0×10^{-4}	9.70×10^{-5}	1.74×10^{-4}	4.28×10^{-7}	3.20×10^{-8}	3.79×10^{-8}
	9.32×10^{-5}	1.89×10^{-4}	4.67×10^{-7}	3.52×10^{-8}	3.94×10^{-8}
0.00	9.46×10^{-5}	1.80×10^{-4}	1.43×10^{-7}	8.04×10^{-9}	1.13×10^{-8}

Table A6.8. Free metal concentrations (in M) corresponding to the experiments in presence of citrate, as computed with Visual MINTEQ.

c_{Cit} (M)	Mg	Ca	Zn	Pb	Ni
5.0×10^{-4}	1.74×10^{-5}	3.44×10^{-5}	6.97×10^{-9}	1.08×10^{-9}	1.36×10^{-10}
	1.32×10^{-5}	2.83×10^{-5}	6.38×10^{-9}	1.31×10^{-9}	1.16×10^{-10}
1.0×10^{-4}	6.48×10^{-5}	1.14×10^{-4}	5.67×10^{-8}	8.12×10^{-9}	1.47×10^{-9}
	6.42×10^{-5}	1.33×10^{-4}	6.31×10^{-8}	9.30×10^{-9}	1.53×10^{-9}
0.00	9.00×10^{-5}	1.69×10^{-4}	1.31×10^{-7}	6.35×10^{-9}	1.04×10^{-8}

6.6.2. Values of the ratio of constants

Table A6.9. Values of the ratio of constants K_M/K_{Cd} obtained from the calibrations at high concentration (Cd was absent from the solution used for calibration 1H). The horizontal dashed lines stand for experiments where the metal was absent.

	Co	Mn	Cu	Ni	Pb	Zn
2H	2.3(1)	0.040(1)	---	7(2)	7(1)	2.3(1)
3H	2.23(5)	0.0317(1)	---	4.4(2)	5.8(6)	2.22(5)
4H	1.7(3)	0.040(3)	4(1)	2.4(6)	4(1)	1.8(3)

Table A6.10. Values of the ratio of constants K_M/K_{Pb} obtained from the calibrations at high concentration. The horizontal dashed lines stand for experiments where the metal was absent.

	Cd	Co	Mn	Cu	Ni	Zn
1H	---	---	0.004(2)	---	0.77(3)	0.3(1)
2H	0.3(3)	0.5(3)	0.02(2)	---	1.00(7)	1.0(3)
3H	0.17(2)	0.38(3)	0.0054(5)	---	0.76(3)	0.38(3)
4H	0.3(1)	0.45(5)	0.011(4)	0.92(3)	0.60(1)	0.5(1)

Table A6.11. Values of the ratio of constants K_M/K_{Zn} obtained from the calibrations at high concentration. The horizontal dashed lines stand for experiments where the metal was absent.

	Cd	Co	Mn	Cu	Ni	Pb
1H	---	---	0.012(2)	---	3.0(6)	3.8(8)
2H	0.5(2)	1.01(1)	0.03(2)	---	2(1)	2(1)
3H	0.45(1)	1.002(4)	0.0143(4)	---	2.0(1)	2.6(2)
4H	0.6(1)	0.939(5)	0.022(5)	1.9(3)	1.3(2)	2.1(2)

Table A6.12. Values of the ratio of constants K_M/K_{Cd} obtained from the calibrations at low concentration for the cations that allegedly form $M(HR)_2$ complexes.

	Co	Mn
1iiL	0.7(1)	0.23(5)
2iiL	1.2(1)	0.29[a]
3iiL	0.90(2)	0.07(3)
4iiL	0.77(2)	0.04(2)

[a] Only one point was available.

Table A6.13. Values of the ratio of constants K_M/K_{Pb} obtained from the calibrations at low concentration for the cations that allegedly form MR complexes.

	Cu	Ni	Zn
1iL	0.65(5)	0.97(7)	0.9(1)
2iL	0.4(1)	0.7(2)	0.82(5)
3iL	0.52(4)	0.85(3)	0.89(3)
4iL	0.57(3)	0.97(7)	0.89(6)

6.6.3. Moles accumulated in the resin disc

Table A6.14. Total moles accumulated in the resin disc for each experiment of the high concentration calibration. Each line represents one sampler (three samplers were used for each experiment). The last column reports the values of the Boltzmann factor referred to the resin beads, computed from the partitioning of Ca and Mg. The horizontal dashed lines stand for experiments where the metal was absent or was present but not measured (the case of Ca in 3H).

	Ca	Mg	Cd	Co	Mn	Cu	Ni	Pb	Zn	χ_R
1H	6.4×10^{-7}	8.8×10^{-8}	---	---	2.5×10^{-8}	---	1.1×10^{-7}	3.0×10^{-8}	2.0×10^{-6}	12.8
	5.8×10^{-7}	9.2×10^{-8}	---	---	1.9×10^{-8}	---	1.8×10^{-7}	4.5×10^{-8}	1.9×10^{-6}	12.4
	3.8×10^{-7}	6.6×10^{-8}	---	---	1.1×10^{-8}	---	1.1×10^{-7}	2.7×10^{-8}	8.5×10^{-7}	10.4
2H	7.0×10^{-7}	3.1×10^{-7}	1.8×10^{-7}	2.3×10^{-7}	6.5×10^{-8}	---	8.2×10^{-8}	1.2×10^{-8}	1.4×10^{-6}	17.6
	5.2×10^{-7}	2.5×10^{-7}	1.3×10^{-7}	2.9×10^{-7}	2.9×10^{-8}	---	3.0×10^{-7}	4.6×10^{-8}	1.8×10^{-6}	15.2
	4.6×10^{-7}	2.3×10^{-7}	1.2×10^{-7}	2.7×10^{-7}	2.8×10^{-8}	---	1.9×10^{-7}	3.2×10^{-8}	1.6×10^{-6}	14.4
3H	---	2.4×10^{-7}	1.0×10^{-7}	2.0×10^{-7}	2.1×10^{-8}	---	1.1×10^{-7}	3.1×10^{-8}	2.1×10^{-6}	14.0
	---	2.0×10^{-7}	9.0×10^{-8}	1.8×10^{-7}	1.9×10^{-8}	---	1.1×10^{-7}	3.3×10^{-8}	2.0×10^{-6}	13.2
	---	2.3×10^{-7}	1.0×10^{-7}	2.1×10^{-7}	2.1×10^{-8}	---	1.2×10^{-7}	3.7×10^{-8}	2.2×10^{-6}	13.6
4H	5.3×10^{-7}	2.1×10^{-7}	2.5×10^{-7}	4.9×10^{-7}	8.0×10^{-8}	3.9×10^{-7}	2.6×10^{-7}	7.2×10^{-8}	7.8×10^{-7}	16.4
	6.5×10^{-7}	2.3×10^{-7}	3.9×10^{-7}	5.7×10^{-7}	1.3×10^{-7}	3.4×10^{-7}	2.4×10^{-7}	6.7×10^{-8}	8.9×10^{-7}	17.6
	6.4×10^{-7}	2.4×10^{-7}	3.6×10^{-7}	6.6×10^{-7}	1.1×10^{-7}	4.7×10^{-7}	3.3×10^{-7}	8.9×10^{-8}	1.1×10^{-6}	17.6

Table A6.15. Total moles accumulated in the resin disc for the series of experiments in presence of NTA. Each line represents one of the samplers used for each experiment. The last column reports the values of the Boltzmann factor referred to the resin beads, computed from the partitioning of K, Na and Rb (in the first replicate of the experiment at $c_{T,NTA}$= 0) and K (in all the others).

$c_{T,NTA}$ (M)	Replicate	Ca	K	Mg	Na	Rb	Cd	Zn	χ_R
2.8×10^{-6}	I	2.7×10^{-6}	4.9×10^{-8}	6.6×10^{-7}	---	---	1.2×10^{-8}	2.6×10^{-8}	5.2
		1.9×10^{-6}	5.8×10^{-8}	4.7×10^{-7}	---	---	1.8×10^{-8}	3.4×10^{-8}	6.2
		2.8×10^{-6}	6.3×10^{-8}	7.2×10^{-7}	---	---	1.4×10^{-8}	2.9×10^{-8}	6.7
	II	2.4×10^{-6}	1.9×10^{-7}	6.2×10^{-7}	---	---	1.4×10^{-8}	2.4×10^{-8}	65.0
		2.3×10^{-6}	1.1×10^{-7}	6.0×10^{-7}	---	---	1.6×10^{-8}	2.7×10^{-8}	38.6
		2.2×10^{-6}	9.1×10^{-8}	5.8×10^{-7}	---	---	1.8×10^{-8}	3.1×10^{-8}	30.9
8.0×10^{-7}		2.0×10^{-6}	5.2×10^{-8}	4.7×10^{-7}	---	---	3.0×10^{-8}	5.7×10^{-8}	5.9
		3.2×10^{-6}	5.5×10^{-8}	7.5×10^{-7}	---	---	2.0×10^{-8}	4.1×10^{-8}	6.2
0	I	1.7×10^{-6}	5.0×10^{-8}	4.1×10^{-7}	---	---	2.9×10^{-8}	5.2×10^{-8}	5.7
		2.6×10^{-6}	1.6×10^{-8}	6.9×10^{-7}	2.8×10^{-7}	1.9E-09	3.1×10^{-8}	5.8×10^{-8}	5.7
		2.4×10^{-6}	1.7×10^{-8}	6.5×10^{-7}	2.9×10^{-7}	1.9E-09	3.1×10^{-8}	5.7×10^{-8}	6.0
		2.2×10^{-6}	1.8×10^{-8}	6.1×10^{-7}	3.0×10^{-7}	2.0E-09	3.0×10^{-8}	5.6×10^{-8}	6.2
	II	2.7×10^{-6}	6.2×10^{-8}	7.6×10^{-7}	---	---	7.8×10^{-8}	1.8×10^{-7}	22.7

Table A6.16. Total moles accumulated in the resin disc for each experiment of the low concentration calibration. Each line represents one sampler (at least three samplers were used for each experiment). The last column reports the values of the Boltzmann factor referred to the resin beads, computed from the partitioning of K.

	Ca	K	Mg	Cu	Ni	Pb	Zn	χ_R
1iL	3.5×10^{-7}	2.7×10^{-8}	1.4×10^{-7}	3.5×10^{-9}	8.7×10^{-9}	8.1×10^{-10}	1.0×10^{-7}	10.4
	1.4×10^{-6}	3.1×10^{-8}	4.3×10^{-7}	7.7×10^{-9}	1.9×10^{-8}	1.6×10^{-9}	2.3×10^{-7}	11.6
	1.6×10^{-6}	3.9×10^{-8}	4.8×10^{-7}	8.1×10^{-9}	1.9×10^{-8}	1.7×10^{-9}	2.4×10^{-7}	14.8
	2.8×10^{-6}	4.1×10^{-8}	7.9×10^{-7}	6.2×10^{-9}	1.5×10^{-8}	1.2×10^{-9}	1.9×10^{-7}	15.6
2iL	1.4×10^{-6}	3.6×10^{-8}	4.1×10^{-7}	3.9×10^{-9}	9.3×10^{-9}	1.5×10^{-9}	1.2×10^{-7}	13.6
	1.3×10^{-6}	2.8×10^{-8}	3.9×10^{-7}	4.6×10^{-9}	1.0×10^{-8}	1.8×10^{-9}	1.3×10^{-7}	10.4
	1.6×10^{-6}	3.5×10^{-8}	4.8×10^{-7}	5.6×10^{-9}	1.3×10^{-8}	3.9×10^{-9}	1.6×10^{-7}	13.2
	1.9×10^{-6}	3.5×10^{-8}	5.6×10^{-7}	4.8×10^{-9}	1.1×10^{-8}	1.8×10^{-9}	1.3×10^{-7}	13.2
3iL	1.4×10^{-6}	2.8×10^{-8}	4.0×10^{-7}	3.5×10^{-9}	1.3×10^{-8}	7.4×10^{-9}	1.4×10^{-7}	10.8
	1.4×10^{-6}	3.2×10^{-8}	3.9×10^{-7}	4.7×10^{-9}	1.7×10^{-8}	9.8×10^{-9}	1.7×10^{-7}	12.0
	1.3×10^{-6}	2.9×10^{-8}	3.7×10^{-7}	5.6×10^{-9}	2.0×10^{-8}	1.1×10^{-8}	1.9×10^{-7}	11.2
	1.6×10^{-6}	5.0×10^{-8}	4.5×10^{-7}	6.9×10^{-9}	2.4×10^{-8}	1.4×10^{-8}	2.4×10^{-7}	19.2
4iL	1.9×10^{-6}	3.7×10^{-8}	5.2×10^{-7}	4.7×10^{-9}	1.1×10^{-7}	2.3×10^{-9}	1.5×10^{-7}	13.6
	4.8×10^{-7}	3.4×10^{-8}	1.6×10^{-7}	8.5×10^{-9}	1.4×10^{-7}	3.6×10^{-9}	1.2×10^{-7}	12.8
	1.4×10^{-6}	3.1×10^{-8}	4.0×10^{-7}	6.5×10^{-9}	1.5×10^{-7}	3.2×10^{-9}	1.9×10^{-7}	11.6
	4.0×10^{-7}	4.0×10^{-8}	1.5×10^{-7}	7.4×10^{-9}	1.3×10^{-7}	2.9×10^{-9}	9.4×10^{-8}	14.8

	Ca	K	Mg	Cd	Co	Mn	χ_R
1iiL	1.6×10^{-6}	5.0×10^{-8}	4.6×10^{-7}	6.9×10^{-10}	8.2×10^{-10}	2.8×10^{-8}	14.4
	1.4×10^{-6}	4.2×10^{-8}	4.2×10^{-7}	1.7×10^{-9}	2.3×10^{-9}	3.6×10^{-8}	12.0
	1.3×10^{-6}	3.5×10^{-8}	3.6×10^{-7}	9.7×10^{-10}	1.4×10^{-9}	3.0×10^{-8}	10.0
2iiL	1.5×10^{-6}	4.3×10^{-8}	4.2×10^{-7}	2.2×10^{-9}	9.0×10^{-9}	1.4×10^{-7}	13.2
	1.4×10^{-6}	3.1×10^{-8}	3.9×10^{-7}	2.2×10^{-9}	9.9×10^{-9}	1.9×10^{-7}	9.60
	4.8×10^{-7}	3.4×10^{-8}	1.9×10^{-7}	2.7×10^{-9}	1.3×10^{-8}	6.1×10^{-8}	10.4
3iiL	1.4×10^{-6}	5.4×10^{-8}	4.3×10^{-7}	3.6×10^{-9}	1.6×10^{-9}	2.5×10^{-7}	15.6
	4.4×10^{-7}	3.5×10^{-8}	1.7×10^{-7}	2.8×10^{-9}	1.3×10^{-9}	4.9×10^{-8}	10.4
	1.2×10^{-6}	3.9×10^{-8}	2.9×10^{-7}	4.2×10^{-9}	1.9×10^{-9}	2.1×10^{-7}	11.6
4iiL	1.4×10^{-6}	5.1×10^{-8}	3.4×10^{-7}	8.8×10^{-10}	1.3×10^{-8}	1.9×10^{-7}	14.0
	1.2×10^{-6}	4.5×10^{-8}	3.4×10^{-7}	2.0×10^{-8}	1.8×10^{-8}	2.0×10^{-7}	12.4
	1.2×10^{-6}	3.8×10^{-8}	3.9×10^{-7}	1.9×10^{-9}	2.7×10^{-8}	2.1×10^{-7}	10.4

	Ca	K	Mg	Cd	Co	Mn	Cu	Ni	Pb	Zn	χ_R
1L	1.6×10^{-6}	3.1×10^{-8}	5.0×10^{-7}	4.8×10^{-10}	1.8×10^{-9}	2.1×10^{-8}	9.6×10^{-9}	2.1×10^{-8}	2.6×10^{-9}	2.4×10^{-7}	14.0
	1.6×10^{-6}	3.6×10^{-8}	5.0×10^{-7}	6.5×10^{-10}	2.3×10^{-9}	2.3×10^{-8}	1.2×10^{-8}	2.6×10^{-8}	3.2×10^{-9}	3.0×10^{-7}	16.4
	1.4×10^{-6}	2.7×10^{-8}	4.6×10^{-7}	3.9×10^{-10}	1.4×10^{-9}	2.1×10^{-8}	6.2×10^{-9}	1.5×10^{-8}	1.9×10^{-9}	1.9×10^{-7}	12.4
	2.7×10^{-6}	3.2×10^{-8}	7.3×10^{-7}	6.9×10^{-10}	2.5×10^{-9}	3.2×10^{-8}	1.3×10^{-8}	2.8×10^{-8}	3.4×10^{-9}	3.4×10^{-7}	14.4
2L	1.6×10^{-6}	3.1×10^{-8}	5.2×10^{-7}	4.2×10^{-10}	1.7×10^{-8}	1.4×10^{-7}	9.4×10^{-9}	1.7×10^{-7}	7.9×10^{-9}	2.2×10^{-8}	14.0
	1.3×10^{-6}	2.9×10^{-8}	4.4×10^{-7}	6.2×10^{-10}	2.4×10^{-8}	1.4×10^{-7}	1.3×10^{-8}	2.5×10^{-7}	1.0×10^{-8}	3.2×10^{-8}	12.8
	2.9×10^{-6}	3.0×10^{-8}	8.0×10^{-7}	2.2×10^{-10}	8.7×10^{-9}	1.8×10^{-7}	4.1×10^{-9}	8.6×10^{-8}	3.6×10^{-9}	1.1×10^{-8}	13.2
	1.3×10^{-6}	2.7×10^{-8}	4.4×10^{-7}	4.0×10^{-10}	1.5×10^{-8}	1.2×10^{-7}	7.9×10^{-9}	1.6×10^{-7}	6.4×10^{-9}	2.0×10^{-8}	12.0
3L	1.5×10^{-6}	2.8×10^{-8}	5.0×10^{-7}	3.3×10^{-9}	1.4×10^{-9}	3.0×10^{-8}	7.2×10^{-8}	1.4×10^{-7}	1.3×10^{-9}	1.9×10^{-8}	12.4
	2.7×10^{-6}	2.7×10^{-8}	7.1×10^{-7}	4.6×10^{-9}	1.9×10^{-9}	5.0×10^{-8}	9.5×10^{-8}	2.0×10^{-7}	1.9×10^{-9}	2.5×10^{-8}	12.0
	1.3×10^{-6}	3.8×10^{-8}	4.3×10^{-7}	6.8×10^{-9}	3.0×10^{-9}	2.1×10^{-8}	1.9×10^{-7}	3.5×10^{-7}	3.4×10^{-9}	4.6×10^{-8}	16.8
	1.4×10^{-6}	3.1×10^{-8}	4.7×10^{-7}	5.1×10^{-9}	2.1×10^{-9}	2.8×10^{-8}	1.1×10^{-7}	2.2×10^{-7}	2.1×10^{-9}	2.9×10^{-8}	13.6
4L	1.2×10^{-6}	3.4×10^{-8}	4.2×10^{-7}	3.5×10^{-9}	1.5×10^{-8}	9.9×10^{-8}	8.7×10^{-8}	1.4×10^{-8}	1.3×10^{-8}	2.0×10^{-7}	14.4
	1.2×10^{-6}	3.1×10^{-8}	4.4×10^{-7}	4.2×10^{-9}	1.8×10^{-8}	1.2×10^{-7}	1.1×10^{-7}	1.9×10^{-8}	1.5×10^{-8}	2.4×10^{-7}	12.8
	1.8×10^{-6}	3.6×10^{-8}	5.9×10^{-7}	6.3×10^{-9}	2.6×10^{-8}	2.0×10^{-7}	1.5×10^{-7}	2.8×10^{-8}	2.2×10^{-8}	3.5×10^{-7}	14.8
	1.1×10^{-6}	2.9×10^{-8}	4.0×10^{-7}	6.4×10^{-9}	2.9×10^{-8}	7.7×10^{-8}	1.7×10^{-7}	3.0×10^{-8}	2.3×10^{-8}	3.9×10^{-7}	12.4

Table A6.17. Total moles accumulated in the resin disc for the series of experiments in presence of citrate. Each line represents one of the four samplers used for each experiment. The last column reports the values of the Boltzmann factor referred to the resin beads, computed from the partitioning of K.

$c_{T,Cit}$ (M)	Replicate	Ca	K	Mg	Ni	Pb	Zn	χ_R
5.0×10^{-4}	I	1.0×10^{-6}	3.6×10^{-8}	2.6×10^{-7}	6.6×10^{-9}	9.4×10^{-9}	1.4×10^{-7}	13.7
		1.8×10^{-6}	4.9×10^{-8}	5.3×10^{-7}	9.7×10^{-9}	1.2×10^{-8}	1.7×10^{-7}	18.7
		2.4×10^{-6}	5.0×10^{-8}	7.1×10^{-7}	1.0×10^{-8}	1.2×10^{-8}	1.8×10^{-7}	19.1
		1.0×10^{-6}	3.9×10^{-8}	2.8×10^{-7}	6.8×10^{-9}	8.6×10^{-9}	1.3×10^{-7}	14.9
	II	2.6×10^{-6}	1.6×10^{-7}	4.6×10^{-8}	8.9×10^{-10}	8.7×10^{-10}	3.1×10^{-8}	64.6
		1.0×10^{-6}	3.8×10^{-8}	2.7×10^{-7}	8.4×10^{-9}	1.3×10^{-8}	1.8×10^{-7}	15.4
		1.2×10^{-6}	4.1×10^{-8}	3.1×10^{-7}	1.0×10^{-8}	1.6×10^{-8}	2.1×10^{-7}	16.8
		1.1×10^{-6}	3.4×10^{-8}	3.0×10^{-7}	6.8×10^{-9}	8.8×10^{-9}	1.2×10^{-7}	13.8
1.0×10^{-4}	I	1.5×10^{-6}	3.7×10^{-8}	4.8×10^{-7}	7.3×10^{-9}	8.4×10^{-9}	1.2×10^{-7}	14.1
		1.3×10^{-6}	3.4×10^{-8}	4.1×10^{-7}	1.1×10^{-8}	1.2×10^{-8}	1.8×10^{-7}	13.1
		1.5×10^{-6}	4.2×10^{-8}	4.8×10^{-7}	9.4×10^{-9}	1.1×10^{-8}	1.6×10^{-7}	16.0
		1.8×10^{-6}	4.3×10^{-8}	5.7×10^{-7}	8.7×10^{-9}	9.8×10^{-9}	1.4×10^{-7}	16.3
	II	1.9×10^{-6}	5.0×10^{-8}	5.4×10^{-7}	8.4×10^{-9}	9.8×10^{-9}	1.4×10^{-7}	19.4
		1.6×10^{-6}	4.9×10^{-8}	4.7×10^{-7}	1.3×10^{-8}	1.6×10^{-8}	2.5×10^{-7}	19.1
		1.6×10^{-6}	4.5×10^{-8}	4.5×10^{-7}	1.2×10^{-8}	1.5×10^{-8}	2.2×10^{-7}	17.5
		1.5×10^{-6}	4.0×10^{-8}	4.3×10^{-7}	1.0×10^{-8}	1.3×10^{-8}	1.8×10^{-7}	15.6
0.00	I	2.3×10^{-6}	3.5×10^{-8}	6.7×10^{-7}	3.5×10^{-8}	2.4×10^{-8}	4.2×10^{-7}	12.9
		2.0×10^{-6}	4.2×10^{-8}	6.1×10^{-7}	2.0×10^{-8}	1.5×10^{-8}	2.6×10^{-7}	15.3
		2.3×10^{-6}	4.6×10^{-8}	6.7×10^{-7}	4.5×10^{-8}	3.1×10^{-8}	5.2×10^{-7}	16.9
		2.2×10^{-6}	4.1×10^{-8}	6.6×10^{-7}	3.5×10^{-8}	2.5×10^{-8}	4.1×10^{-7}	14.8

6.6.4. Determination of χ_R

A direct way to determine the value of χ_R is from the partitioning of an ion known to display no chemical interaction with the resin, as done for the Chelex beads in Section 4.6.2. Data about the partitioning factor of the DGT resin gel at different *I* were provided in Altier *et al.*[23] and they had been obtained by studying the partitioning of Rb^+, a cation that also presents the advantage of not being prone to contamination due to its scarcity in the natural environment. Here, we did not deem it necessary to spike any further metal ion, and we instead relied on the partitioning of K^+. Although the chances of contamination are higher, we have always been working in a range of concentrations high enough to be safe (5×10^{-5} – 5×10^{-6} M).

A reliable estimate of the volume of the gel resin disc (V_{disc}) and of the resin beads (V_R) embedded in the gel itself is needed for the computation of χ_{disc} and χ_R.. V_{disc} was taken equal to 1.8×10^{-7} m^3, a value determined in the Lleida laboratory from experimental water content data.[5] V_R was estimated to be around 4.5×10^{-8} m^3, computed from the average number of sites per DGT disc[5] and the density of sites in the resin beads as provided by the manufacturer.[20]

All the eDGT experiments were performed in the same conditions, so we expect to find only relatively small differences between different resin gels. Recall that χ_R strongly depends not only on *I* but also on the pH, as it affects the fraction of protonated sites in the resin. The average value of χ_{disc} at *I*= 4 mM and pH 6.4 is 3.4±0.6 (computed over the 52 samplers used in both series of calibrations). We noticed that resin layers coming from different batches, such as those prepared in Lleida and the purchased ones, sometimes presented quite different partitioning factors, probably as a consequence of residual charges left in the polymer. The average χ_{disc} is quite close to 5.8, the one given in the cited work[23] at *I*= 10 mM and pH 7.5. The different number of charged sites at the two pHs can probably account for the discrepancy between the two values.

As we know, the polyacrylamide matrix should be completely uncharged, while all the charge is concentrated inside the Chelex beads. Strictly speaking, the partitioning factor should be referred to the volume of said beads. From the estimated V_R we can compute an average value of χ_R equal to 14±2. This is the value that will be later used to compute $\tilde{n}_{MR}$, the fraction of metal chemically bound, *via* Eq. (6.2). It must be remembered, though, that the contribution of electrostatic binding was found to be negligible for the majority of cations, with the exception of Ca, Mg and Mn.

6.7. References

(1) Puy, J.; Galceran, J.; Rey-Castro, C. Interpreting the DGT Measurement. In *Diffusive Gradients in Thin-Films for Environmental Measurements*; Davison, W., Ed.; Cambridge University Press: Cambridge (UK), 2016; 93–122.

(2) Jiménez-Piedrahita, M.; Altier, A.; Cecilia, J.; Puy, J.; Galceran, J.; Rey-Castro, C.; Zhang, H.; Davison, W. Extending the use of Diffusive Gradients in Thin Films (DGT) to solutions where competition, saturation, and kinetic effects are not negligible. *Anal. Chem.* **2017**, *89* (12), 6567–6574.

(3) Galceran, J.; Salvador, J.; Puy, J.; Mas, F.; Gimenez, D.; Esteban, M. Amalgamation effects in reverse pulse polarography at spherical electrodes. Influence on speciation measurements. *J. Electroanal. Chem.* **1998**, *442*, 151–167.

(4) Quattrini, F.; Galceran, J.; David, C. A.; Puy, J.; Alberti, G.; Rey-Castro, C. Dynamics of trace metal sorption by an ion-exchange chelating resin described by a mixed intraparticle/film diffusion transport model. The Cd/Chelex case. *Chem. Eng. J.* **2017**, *317*, 810–820.

(5) Mongin, S. Contribution to the availability of metal ions in aquatic systems. Doctoral thesis, Universitat de Lleida, 2012.

(6) Senn, D. B.; Griscom, S. B.; Lewis, C. G.; Galvin, J. P.; Chang, M. W.; Shine, J. P. Equilibrium-based sampler for determining Cu^{2+} concentrations in aquatic ecosystems. *Environ. Sci. Technol.* **2004**, *38* (12), 3381–3386.

(7) Pesavento, M.; Biesuz, R.; Gallorini, M.; Profumo, A. Sorption mechanism of trace amounts of divalent metal ions on a chelating resin containing iminodiacetate groups. *Anal. Chem.* **1993**, *65* (18), 2522–2527.

(8) Pesavento, M.; Biesuz, R. Characterization and applications of chelating resins as chemical reagents for metal ions, based on the Gibbs-Donnan model. *React. Funct. Polym.* **1998**, *36* (2), 135–147.

(9) Pesavento, M.; Biesuz, R.; Alberti, G.; Sturini, M. Separation of copper (II) and aluminium (III) from fresh waters by solid phase extraction on a complexing resin column. *J. Sep. Sci.* **2003**, *26*, 381–386.

(10) Alberti, G.; Amendola, V.; Pesavento, M.; Biesuz, R. Beyond the synthesis of novel solid phases: Review on modelling of sorption phenomena. *Coord. Chem. Rev.* **2012**, *256* (1–2), 28–45.

(11) Pesavento, M.; Biesuz, R.; Baffi, F.; Gnecco, C. Determination of metal ions concentration and speciation in seawater by titration with an iminodiacetic resin. *Anal. Chim. Acta* **1999**, *401* (1–2), 265–276.

(12) Biesuz, R.; Alberti, G.; Pesavento, M. Sorption of lead(II) on two chelating resins: From the exchange coefficient to the intrinsic complexation constant. *J. Solution Chem.* **2008**, *37* (4), 527–541.

(13) Cantwell, F. F.; Nielsen, J. S.; Hrudey, S. E. Free nickel ion concentration in sewage by an ion exchange column-equilibration method. *Anal. Chem.* **1982**, *54* (9), 1498–1503.

(14) Zavarise, F.; Companys, E.; Galceran, J.; Alberti, G.; Profumo, A. Application of the new electroanalytical technique AGNES for the determination of free Zn concentration in river water. *Anal. Bioanal. Chem.* **2010**, *397* (1), 389–394.

(15) Parat, C.; Authier, L.; Castetbon, A.; Aguilar, D.; Companys, E.; Puy, J.; Galceran, J.; Potin-Gautier, M. Free Zn^{2+} determination in natural freshwaters of the Pyrenees: towards\non-site measurements with AGNES. *Environ. Chem.* **2015**, *12* (3), 329–337.

(16) Vilavert, L.; Sisteré, C.; Schuhmacher, M.; Nadal, M.; Domingo, J. L. Environmental Concentrations of Metals in the Catalan Stretch of the Ebro River, Spain: Assessment of Temporal Trends. *Biol. Trace Elem. Res.* **2015**, *163* (1–2), 48–57.

(17) Roig, N.; Sierra, J.; Moreno-Garrido, I.; Nieto, E.; Gallego, E. P.; Schuhmacher, M.; Blasco, J. Metal bioavailability in freshwater sediment samples and their influence on ecological status of river basins. *Sci. Total Environ.* **2016**, *540*, 287–296.

(18) Ferré-huguet, N.; Domingo, J. L. Nivells de metalls al Riu Ebre en la comarca de la Ribera d'Ebre. *Miscel·lània del CERE* **2008**, *19*, 93–114.

(19) Schwarzenbach, G.; Anderegg, G.; Schneider, W.; Senn, H. Komplexone XXVI. Über die Koordinationstendenz von N-substituierten Iminodiessigsäuren. *Helv. Chim. Acta* **1955**, *38* (5), 1147–1170.

(20) Biorad. *Chelex® 100 and Chelex 20 Chelating Ion Exchange Resin Instruction Manual*; Hercules, CA.

(21) Puy, J.; Galceran, J.; Cruz-González, S.; David, C. A.; Uribe, R.; Lin, C.; Zhang, H.; Davison, W. Measurement of metals using DGT: Impact of ionic strength and kinetics of dissociation of complexes in the resin domain. *Anal. Chem.* **2014**, *86*

(15), 7740–7748.

(22) Dong, Z.; Lewis, C. G.; Burgess, R. M.; Shine, J. P. The Gellyfish: An in situ equilibrium-based sampler for determining multiple free metal ion concentrations in marine ecosystems. *Environ. Toxicol. Chem.* **2015**, *34* (5), 983–992.

(23) Altier, A.; Jiménez-Piedrahita, M.; Rey-Castro, C.; Cecilia, J.; Galceran, J.; Puy, J. Accumulation of Mg to Diffusive Gradients in Thin Films (DGT) devices: kinetic and thermodynamic effects of the ionic strength. *Anal. Chem.* **2016**, *88* (20), 10245–10251.

7. General discussion and conclusions

7.1. General discussion

Assessing the concentration of heavy metals in natural media is key to understanding their toxicity, and is the preliminary step to the application of bioavailability models such as FIAM or BLM. As stated in numerous places throughout this thesis, the behaviour of a specific analyte is not defined by only one concentration, but by several: for example (*i*) the total one; (*ii*) the free concentration at equilibrium, the most classic predictor of toxicity; and (*iii*) the various labile concentrations, which in some cases may describe more accurately the uptake, but with the *caveat* that, being often purely operationally defined, heavily depend on the technique applied. This demands the development of models with a strong physical basis, which should allow a more general interpretation of the results and a deeper understanding of the underlying processes.

Methods of analysis based on chelating resins such as Chelex 100 have been successfully employed in speciation studies in the recent past, by studying both metal partitioning at equilibrium[1–3] and the rate of its accumulation.[4,5] Being Chelex a weakly acidic resin, its degree of ionization is sensitive to changes in pH and, to a lesser extent, ionic strength.[6] These parameters condition, in fact, the fraction of available binding sites, the volume of the resin beads (that swell because of the repulsion of charges) and the partitioning factor at the particle/solution interface; they also affect the effective diffusion coefficient in the resin phase.[7] Since these factors control metal transport both in the stagnant layer surrounding the beads and inside the beads themselves, a full understanding of their effects requires taking into consideration the contributions of internal and external diffusion together. Most of the previous works[8] that modelled the uptake rate to chelating resins starting from similar premises (*i.e.* metal transport purely under the control of diffusion) only considered the contribution of film diffusion. It is true that this approach may lead to semi-quantitative results of good quality – good enough, for example, to have a general idea of the equilibration times – and, in many cases, it can describe well the first stages of the uptake. It must be said, though, that

only the more complete model developed here can account for the dependence of the uptake rate on pH, a rather complex phenomenon controlled by several factors of similar importance. Even if the new model performs well in its current applications, there is plenty of room for improvement: in particular two aspects that had to be neglected were the limited loading of the resin (the outer layers of the beads are saturated first, the basic hypothesis of the shrinking core model[9]) and the charge variation due to the progressive binding, which have repercussions on many parameters, first of all on the partitioning coefficient.

Vast though it may be, the study of metal uptake by Chelex in absence of ligands represents a prelude to the application of the resin to the assessment of dynamic metal speciation in metal-ligand mixtures. In this latter case, the rate of accumulation in the resin can readily provide a good estimate of the dissociation rate constant of the complexes. The complexes studied in this work, Cd-NTA and Ni-NTA, are two interesting cases – one fairly labile, the other inert – that well represent the variety found in natural media. For Cd-NTA, a good correspondence was found between the values of the dissociation rate constant obtained from the resin accumulation data and those predicted by the Eigen model, while for Ni-NTA the resin measurements implied a much faster dissociation than expected. This confirms the observation previously made with a related technique, the DGT passive sampler,[10] which led to postulate that relatively inert complexes may directly react with the sites of the resin, instead of dissociating first. Further evidence of this alternative mechanism was obtained by studying the dependence of the dissociation rate constant with the ionic strength. This effect, though, was partially hidden by the high concentration of charges in the resin phase, which buffers the ionic strength. A possible improvement could be to work at lower pH, in conditions where the majority of sites are protonated and the charge, as a consequence, is lower.

Many speciation techniques exploit the advantageous features of ion-exchange resins, either in stirred vessels operating in batch (or continuous) mode, as in the cases detailed in the previous paragraphs, or in fixed-bed mode, held in a solid support of some sort, embedded in gel matrices (as in the DGT) or packed in a column as in the IET[11] or in the recently developed DIET.[12] While IET is known to respond to the free metal fraction (with the potential interference of positively-charged complexes) it has been demonstrated in this work that DIET provides information about a range of complexes of different lability. The width of this range (the “analytical window” of tested labilities)

can be tuned by acting on parameters such as the bed length of the column and the particle size of the resin. In addition, while in the traditional IET and in the early experiments with DIET, the chemical information could be extracted only by eluting the metal accumulated in the resin, we found that analysing the amount of metal remaining in the effluent (the breakthrough curve) could provide complementary and sometimes more meaningful data. This finding is of particular interest, because it also provides a coherent explanation to the evolution of metal concentration in the effluent, which sometimes exhibits a long-lasting plateau of difficult interpretation (a consequence of the system being at steady state). This new mode of analysis, though promising, does not benefit from the pre-concentration of the metal in the resin, and has higher limits of detection.

Among the application of chelating resins, we have mentioned the DGT passive sampler. As done with many other techniques,[13–15] which could be adapted to work in equilibrium or dynamic mode, the possibility of using the DGT at equilibrium has been explored. As the amount of sorbent in the commercial DGT is not exactly known, we suggest normalising it with respect to a reference ion. An additional challenge presented by the equilibrium DGT is its reliance on the chelating resin Chelex, whose mechanism of binding is of more difficult interpretation than, for example, the purely electrostatic interaction of the sulfonic ion-exchange resin Dowex 50 employed in IET. Although more refined models, *e.g.* based on the Gibbs-Donnan theory,[16] could be applied, we found that acceptably good results could be obtained by choosing Zn(II) as reference ion, an element ubiquitously found in natural waters and whose free concentration is easily quantified with AGNES.[17] The eDGT response is linear only in a limited range of concentrations and, as a consequence, it has to be calibrated in conditions as close as possible to the experimental ones. The eDGT gives reliable results for Cd(II), Co(II), Cu(II), Ni(II), Pb(II) and Zn(II); it cannot be applied to the measurement of Ca(II) and Mg(II) (and, to a lesser extent, of Mn(II)) as they are retained mainly by electrostatic interactions.

7.2. Conclusions

The present thesis focused on the study of metal availability in aqueous media, and it developed both new theoretical frameworks, aimed at modelling the dynamic evolution of systems of environmental interest, and new analytical techniques. The most relevant conclusions of this work are:

- A model (MCM) was developed to describe the rate of metal ion sorption by a chelating sorbent in finite volume conditions (for the sample solution), under the possible co-limitation of both internal and external diffusion. This model improves classical solutions by taking into account the intraparticle diffusion, an aspect generally overseen in the literature about this type of resin, but crucial to fully describe the effects of pH. The comparison of the metal fluxes at the particle/solution interface also allows determining which step (either internal or external diffusion) is limiting.
- Monitoring the accumulation rate in a sorbent material is an effective way to study the dissociation kinetics of a complex. While this is rather common practice in speciation studies, the application of a sound theoretical framework constituted a novelty in this field and allowed the determination of parameters of relevant interest such as the dissociation rate constant. Further research is needed, however, to clarify the mechanism of uptake when working with extremely labile complexes.
- The non-Eigen dissociative behaviour observed with inert metal complexes accumulating in the DGT was confirmed by parallel experiments with loose resin beads. The variation of $\tilde{k}_d$ with the ionic strength supports the ligand-assisted mechanism hypothesis, postulated to explain the non-Eigen dissociative behaviour.[10]
- DIET (Dynamic Ion Exchange Technique), a recently proposed use of a minicolumn of cation exchange resin beads, can be effectively used to study the dissociation of metal complexes and to retrieve its lability degree ξ. It must be noted that DIET does not measure the free metal concentration, as suggested by some scientists,[12,15] but a DIET-labile fraction, here defined as c_{DIET} by analogy with c_{DGT}. Only for sufficiently inert complexes, c_{DIET} approaches the free metal concentration.
- Our theoretical framework relates DIET lability to parameters such as the resin-bed length, resin mesh and flow rate, which can be varied accordingly to study the behaviour of complexes of different lability. Besides, it allows extracting information from the effluent metal concentrations (*i.e.* from the breakthrough curve), a promising novelty provided that a sufficiently sensitive complementary technique is employed for their analysis.

- A model with a relatively short number of assumptions suggests extracting relevant information from the DGT at equilibrium, whose practical implementation consists in simple changes in the standard sampler. Care has to be taken to calibrate the sampler in conditions as close as possible to the experimental ones, since alternative stoichiometries and interactions difficult to predict may arise at different levels of metal concentration. In addition, at low ionic strength, the binding of metal ions like Mg(II) and Ca(II) becomes completely non-specific (electrostatic).
- The DGT at equilibrium (eDGT) was used to perform speciation studies on systems of several metals in presence of synthetic ligands. The obtained preliminary results, though indicating that the method might work, are not sufficiently satisfactory and more work should be devoted to its development, especially to the theoretical framework of equilibrium binding in the eDGT resin discs.

7.3. References

(1) Pesavento, M.; Biesuz, R.; Gallorini, M.; Profumo, A. Sorption mechanism of trace amounts of divalent metal ions on a chelating resin containing iminodiacetate groups. *Anal. Chem.* **1993**, *65* (18), 2522–2527.

(2) Pesavento, M.; Biesuz, R. Sorption of divalent metal ions on an iminodiacetic resin from artificial seawater. *Anal. Chim. Acta* **1997**, *346* (3), 381–391.

(3) Alberti, G.; Biesuz, R.; Huidobro, C.; Companys, E.; Puy, J.; Galceran, J. A comparison between the determination of free Pb(II) by two techniques: Absence of Gradient and Nernstian Equilibrium Stripping and Resin Titration. *Anal. Chim. Acta* **2007**, *599*, 41–50.

(4) Chakraborty, P.; Gopalapillai, Y.; Murimboh, J.; Fasfous, I. I.; Chakrabarti, C. L. Kinetic speciation of nickel in mining and municipal effluents. *Anal. Bioanal. Chem.* **2006**, *386* (6), 1803–1813.

(5) Yapici, T.; Fasfous, I. I.; Zhao, J.; Chakrabarti, C. L. Effects of various competing ligands on the kinetics of trace metal complexes of Laurentian Fulvic Acid in model solutions and natural waters. *Anal. Chim. Acta* **2009**, *636* (1), 6–12.

(6) Biorad. *Chelex® 100 and Chelex 20 Chelating Ion Exchange Resin Instruction Manual*; Hercules, CA.

(7) Quattrini, F.; Galceran, J.; David, C. A.; Puy, J.; Alberti, G.; Rey-Castro, C. Dynamics of trace metal sorption by an ion-exchange chelating resin described by a mixed intraparticle/film diffusion transport model. The Cd/Chelex case. *Chem. Eng. J.* **2017**, *317*, 810–820.

(8) Alberti, G.; Biesuz, R. EmporeTM membrane vs. Chelex 100: Thermodynamic and kinetic studies on metals sorption. *React. Funct. Polym.* **2011**, *71* (5), 588–598.

(9) Liberti, L.; Passino, R. Ion-exchange kinetics in selective systems. In *Ion-exchange and solvent extraction, Vol 9*; Marinsky, J. A., Marcus, Y., Eds.; Marcel Dekker, Inc.: New York.

(10) Puy, J.; Galceran, J.; Cruz-González, S.; David, C. A.; Uribe, R.; Lin, C.; Zhang, H.; Davison, W. Measurement of metals using DGT: Impact of ionic strength and kinetics of dissociation of complexes in the resin domain. *Anal. Chem.* **2014**, *86* (15), 7740–7748.

(11) Cantwell, F. F.; Nielsen, J. S.; Hrudey, S. E. Free nickel ion concentration in sewage by an ion exchange column-equilibration method. *Anal. Chem.* **1982**, *54* (9), 1498–1503.

(12) Rowell, J. A.; Fillion, M. A.; Smith, S.; Wilkinson, K. J. Determination of the speciation and bioavailability of Samarium to Chlamydomonas Reinhardtii in the presence of natural organic matter. *Environ. Toxicol. Chem.* **2018**, *37*, 1623–1631.

(13) Marang, L.; Reiller, P.; Pepe, M.; Benedetti, M. F. Donnan membrane approach:From equilibrium to dynamic speciation. *Environ. Sci. Technol.* **2006**, *40* (17), 5496–5501.

(14) Stephens, B. S.; Kapernick, A. P.; Eaglesham, G.; Mueller, J. F. Event monitoring of herbicides with naked and membrane-covered Empore disk integrative passive sampling devices. *Mar. Pollut. Bull.* **2009**, *58* (8), 1116–1122.

(15) Nduwayezu, I.; Mostafavirad, F.; Hadioui, M.; Wilkinson, K. J. Speciation of a lanthanide (Sm) using an ion exchange resin. *Anal. Methods* **2016**, *8*, 6774–6781.

(16) Pesavento, M.; Biesuz, R. Characterization and applications of chelating resins as chemical reagents for metal ions, based on the Gibbs-Donnan model. *React. Funct. Polym.* **1998**, *36* (2), 135–147.

(17) Companys, E.; Cecília, J.; Codina, G.; Puy, J.; Galceran, J. Determination of Zn^{2+} concentration with AGNES using different strategies to reduce the deposition time. *J. Electroanal. Chem.* **2005**, *576* (1), 21–32.